

**Synthesis and characterization of new Discotic
Polycyclic Aromatic Hydrocarbons
and related pyrolytic nanostructures**

Dissertation

zur Erlangung des Grades
“Doktor der Naturwissenschaften”

am Fachbereich Chemie, Pharmazie und Geowissenschaften der

Johannes Gutenberg-Universität Mainz

vorgelegt von

Bassem El Hamaoui

geboren in Tripoli, Libanon

Mainz, 2007

Decan:

1. Berichterstatter:

2. Berichterstatter:

Tag der mündlichen Prüfung:

Die vorliegende Arbeit wurde in der Zeit von januar 2003 bis januar 2007 im Max-Planck-Institut für Polymerforschung in Mainz unter Anleitung von Herrn Prof. Dr. Klaus Müllen ausgeführt.

Ich danke Herrn Prof. Dr. K. Müllen für seine wissenschaftliche und persönliche Unterstützung sowie für seine ständige Diskussionsbereitschaft.

Dedicated to my mother, my sister
and to the memory of my father

Table of contents

1. Introduction	1
1.1 Polycyclic Aromatic Hydrocarbons (PAHs).....	1
1.2 Carbon Nanotubes (CNTs): general overview on synthesis, properties and applications..	5
1.2.1 Definition of CNTs.....	5
1.2.2 Synthesis and properties.....	6
1.2.2.1 Electric Arc discharge.....	6
1.2.2.2 Laser Ablation.....	7
1.2.2.3 Chemical Vapor Deposition.....	9
1.2.3 Potential applications of CNTs.....	9
1.2.4 From graphitic CNTs to graphenic Discotic Liquid Crystals(LCs).....	10
1.3 Liquid Crystals: definition, bulk properties and applications.....	10
1.3.1 Synthesis and phase behavior of discotic LCs.....	13
1.3.2 Amphiphile discotic LCs.....	17
1.3.3 Charge carrier mobility and related electronic properties of graphite discs.....	18
1.3.4 FETs.....	20
1.3.5 Photovoltaic cells.....	21
1.4 Motivation and objectives.....	22
2. Time-resolved spectroscopic study of phosphorescent platinated and alkylated hexa-<i>peri</i>-hexabenzocoronenes	30
2.1 Introduction.....	30
2.2 Synthesis.....	32
2.3 Photophysical properties.....	36
2.4 Photoluminescence study of HBC-Ph-C ₁₂ (25).....	43
2.5 In-Solution HBC supramolecular chemistry.....	45
2.6 Summary.....	50
3. Self-assembly of amphiphilic hexa-<i>peri</i>-hexabenzocoronenes into supramolecular nanostructures	52
3.1 Introduction.....	52
3.2 Synthesis and structural characterization.....	54
3.3 Results and discussion.....	58
3.3.1 UV-Vis and fluorescence spectra.....	58
3.3.2 Solid-state self-assembly investigated by X-ray scattering.....	61
3.3.3 Infrared spectroscopy.....	67
3.3.4 Self-assembled nanostructures studied by electron microscopy.....	69
3.3.5 Discussion.....	71
3.4 Conclusion.....	77
4. Control of the homeotropic order of discotic hexa-<i>peri</i>-hexabenzocoronenes	81
4.1 Processability and alignment on surfaces	81
4.2 Synthesis.....	84
4.3 Thermal properties of compounds 45a and 45b	87
4.4 Structure investigation by X-ray scattering of compounds 45a and 45b	88

4.5 Homeotropic arrangement of compounds 45a and 45b	93
4.6 Synchrotron radiation Microfocus diffractometry of the dendritic morphology.....	99
4.7 Discussion.....	102
4.8 Conclusion.....	106
5. Solid-state synthesis of carbon nanotubes and other carbon nanostructures by thermolysis of 2D and 3D cobalt complexes	110
5.1 Introduction.....	111
5.2 Preparation and solid-state pyrolysis of complex 50 as a model compound.....	112
5.2.1 Synthesis and characterization of complex 50	112
5.2.2 Results and discussion.....	115
5.3 Cobalt complexes with various structures and geometries.....	121
5.3.1 Synthesis and characterization.....	123
5.3.2 Results and discussion.....	130
5.3.3 Conclusion.....	141
6. Uniform carbon and carbon-cobalt nanostructures by solid-state thermolysis of polyphenylene dendrimer-cobalt complexes	144
6.1 Introduction.....	144
6.2 Synthesis and characterization.....	146
6.3 Solid-state thermolysis of cobalt complex 71	149
6.3.1 Results and discussion.....	149
6.3.2 Acidic treatment and magnetic properties of cobalt nanoparticles of 71 prepared at 800 °C.....	153
6.4 Thermolysis of the higher generation dendrimer cobalt complexes 72 and 73	159
6.5 Summary.....	161
7. Summary and Outlook	164
8. Experimental Section	172
8.1 General methods.....	172
8.2 Materials.....	174
8.3 Synthesis.....	175
9. Appendix	208
List of Publications	212

Index of Abbreviations

DCM	dichloromethane
DSC	differential scanning calorimetry
EA	elemental analysis
FD MS	field desorption mass spectroscopy
FET	field effect transistor
g	gram
HBC	hexa- <i>peri</i> -hexabenzocoronene
LED	light emitting diode
MALDI-TOF	matrix-assisted laser desorption ionization –time of flight
FT-IR	Fourier transform infrared
NMR	nuclear magnetic resonance
PE	petroleum ether
POM	polarized optical microscopy
PAH	polycyclic aromatic hydrocarbons
RT	room temperature
SEM	scanning electron microscopy
TEM	transmission electron microscopy
TCNQ	7,7,8,8-tetracyanoquinodimethane
THF	tetrahydrofuran
TMS	trimethylsilyl
Tolane	diphenylacetylene
UV-vis	ultraviolet/visible
EDX	energy dispersive x-ray spectroscopy
HPB	hexaphenylbenzene

Chapter

1

Introduction

1.1 Polycyclic Aromatic Hydrocarbons (PAHs)

Polycyclic aromatic hydrocarbons (PAHs), more simply known as polyarenes, constitute an extraordinarily large and diverse class of organic molecules. The major sources of PAHs are crude oil, coal and oil shale. The fuels produced from these fossil sources constitute the primary source of energy for the industrial nations of the world, and the petrochemicals produced from these raw materials are the basis of synthetic fibers and plastic industries. Coal tars and petroleum residues produced in the refining process contain high percentages of PAHs, representing a wide range of molecular sizes and structural types. Also present in these sources are large quantities of the equally diverse polycyclic aromatic heterocyclic analogs containing one or more nitrogen, oxygen or sulfur atoms. Together the PAHs and their heterocyclic analogs constitute an enormous resource of chemical raw materials that remain relatively underutilized in relation to their potential.¹

PAHs are ubiquitous environmental contaminants. They derive principally from combustion of fossil fuels in heat and power generation, refuse burning and coke ovens. These sources together contribute more than 50% of the nationwide emissions of benzopyrene, the widely employed hydrocarbon as a standard for PAH emissions. Vehicle emissions are another major source particularly in urban areas of industrialized countries contributing as much as 35% to the total PAHs emissions in the USA.² The patterns of polyarenes produced in pyrolytic

reactions vary considerably with temperature.³ At high temperatures under anaerobic conditions, the products consist of relatively simple mixtures of unsubstituted PAHs. At intermediate temperatures, unsubstituted and alkyl-substituted PAHs are formed. Fundamental contributions to the direct synthesis and characterization of polycyclic aromatics were made by the pioneering work of R. Scholl,⁴ E. Clar,⁵ and M. Zander,⁶ who achieved the synthesis of numerous aromatic compounds under drastic conditions at high temperatures in strongly oxidizing reaction melts. Recently, a synthetic breakthrough has been achieved as a result of progress of analytical techniques and has made possible the selective synthesis of various PAHs, with a broad range of sizes and shapes and under mild conditions.^{6c}

Carbon based materials, clusters, and molecules are unique in many ways. One distinction relates to the many possible configurations of the electronic states of the carbon atom, which is known as the hybridization of the atomic orbitals and relates to the bonding of carbon atoms to their nearest neighbors.⁷ Three possible hybridizations occur in carbon : sp , sp^2 and sp^3 , while other elements in group IV such as Si and Ge exhibit primarily sp^3 hybridization. The various bonding states are connected with certain structural arrangements, so that sp bonding gives rise to chain structures, sp^2 bonding to planar structures and sp^3 bonding to tetrahedral structures.

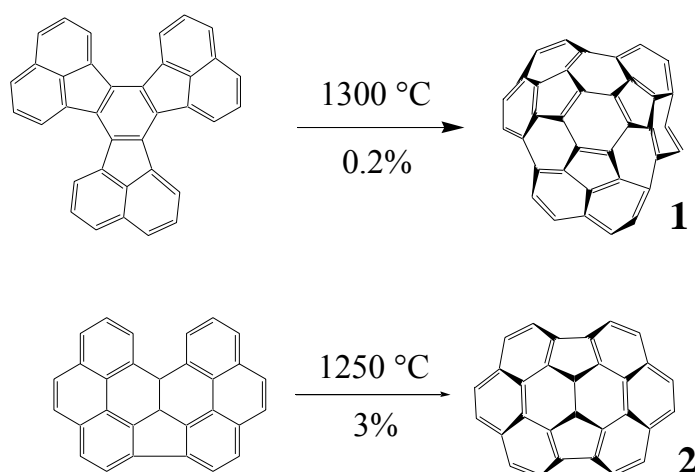
While sp^2 bonded graphite is the ground state phase of carbon under ambient conditions, at higher temperatures and pressures, sp^3 bonded diamond is stable. It is believed that a variety of novel π -electron carbon bulk phases remain to be discovered and explored.

The physical reason why these nanostructures form is that a graphene layer (defined as a single 2D layer of 3D graphite) of finite size has many edge atoms with dangling bonds corresponding to high energy states. Therefore, the total energy of a small number of carbon atoms (30-100) is reduced by eliminating dangling bonds, even at the expense of increasing the

strain energy, thereby promoting the formation of closed cage clusters such as fullerenes and carbon nanotubes.

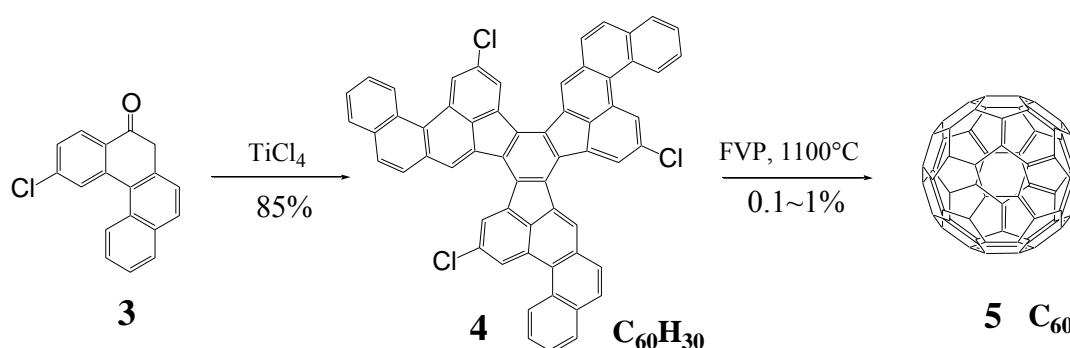
The conversion of appropriate precursors to condensed PAHs at elevated temperature is the classic synthetic method toward various pure polycyclic aromatics. A typical experimental process is referred to as flash vacuum pyrolysis (FVP), in which the pyrolysis of the precursor is carried out, in a very short time (tens of ms to several seconds). The key point is the design of the precursors, which should have a good thermal stability and reactive sites. The selectivity and yield can be improved by optimization of the pyrolysis techniques.

The classic reaction is the thermal cyclodehydrogenation, in which ring formation and hydrogen abstraction can take place in a consecutive fashion. Six or five membered rings can be formed during the pyrolysis. Representative examples are shown in Scheme 1. Bowl shaped fullerene fragments **1-2** could be obtained for the first time by high temperature thermal pyrolysis even though the yield is low due to steric hindrance.⁸



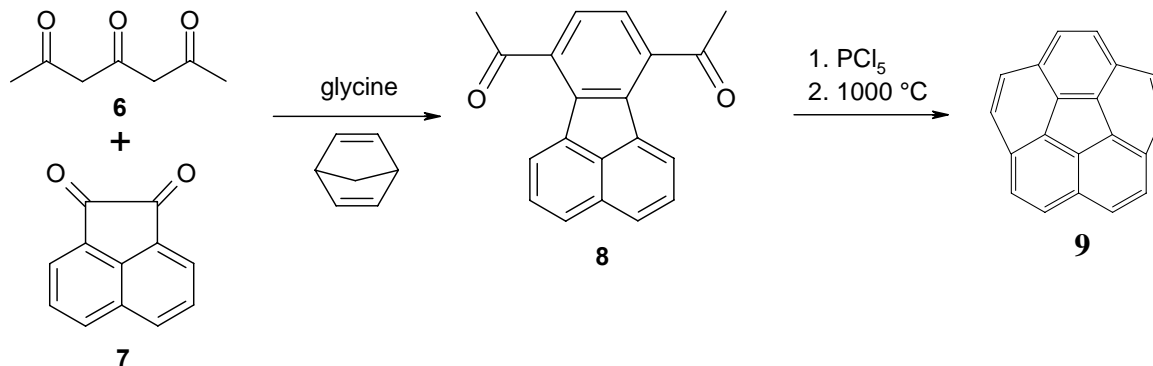
Scheme 1: Synthesis of bowl-shaped fullerene fragments (**1**, **2**) by thermal cyclodehydrogenation.

The incorporation of halogen atoms or other functionality that could generate radical intermediates at high temperatures in the gas phase would be essential to get curvature started in the pi system. For the rest of the “zipping up” to form C₆₀, appropriate precursors with halogen substituents in the fjord regions or at *ortho* positions have been applied to synthesize PAH in significantly higher yield because the C-X (X=halogens) bonds have lower dissociation enthalpies than Caryl-H bonds. A most successful example is the quantitative synthesis of C₆₀ fullerene as shown in Scheme 2. Catalyzed trimerization of precursor of the alkyl aryl ketone **3** using TiCl₄, yielded precursor from which the Buckminster fullerene C₆₀ **5** was made for first time in preparative scale by a total chemical synthesis.



Scheme 2: Synthesis of the bucky-bowl-shaped fullerene (**5**) by thermal cyclodehydrogenation.

The utility of FVP can be also illustrated by the synthesis of corannulene in only three steps from commercially available starting materials *via* route of involving, in the key step, FVP of 7,10-bis(1-chlorovinyl)fluoranthene obtained from 7,10-diacetylfluoranthene (**8**) by reaction with PCl₅ (Scheme 3).⁹ The classical synthesis of corannulene (**9**) by Barth and Lawton entailed 16 steps and provided the hydrocarbon in low overall yield.¹⁰ The thermal cyclodehydrogenation provides PAH substrates with the large activation energy needed to effect endothermic cyclization to form a strained polycyclic carbon framework, making it valuable for the synthesis of large non-polar polyarenes.¹¹



Scheme 3: synthesis of corannulene (9) in only two steps

1.2 Carbon Nanotubes (CNTs): general overview on synthesis, properties and applications.

1.2.1 Definition of CNTs

A carbon nanotube consists of concentric shells of graphite formed by one or more sheet of conventional graphite rolled up into a cylinder. The lattice of carbon atoms remains continuous around the circumference. They can be distinguished into: SWNTs (single-wall nanotubes), i.e. a cylinder with only one external wall; MWNTs (multi-wall nanotubes), made of multiple coaxial cylinders. An ideal SWNT is a carbon cylinder made of one graphite layer rolled up around one axis, with hemi-spherical end caps. The main body of a SWNT is made purely of hexagons (no defects). The endcaps correspond to half a fullerene molecule, hence they are made of hexagons and pentagons. SWNTs are essentially a one-dimensional structure.

The SWNT parameters are the diameter and the chiral vector (n,m) or helicity, i.e. the graphite rollup direction with respect to the cylinder axis. On the other hand, a MWNT is made of coaxial SWNTs. Notice that possible interactions between walls may stabilize the NT growth.

It is convenient to specify a general carbon nanotube in terms of the tubule diameter d_t , and the chiral angle θ , which are shown in figure 1. The chiral vector C_h is defined in terms of the integers (n,m) and the basis vectors \mathbf{a}_1 , and \mathbf{a}_2 of the honeycomb lattice. The circumference of any carbon nanotube is expressed in terms of the chiral vector $C_h = n\hat{\mathbf{a}}_1 + m\hat{\mathbf{a}}_2$ which connects two crystallographically equivalent sites on a 2D graphene sheet.¹² The construction in figure 1 depends uniquely on the pair of integers (n,m) which specify the chiral vector.

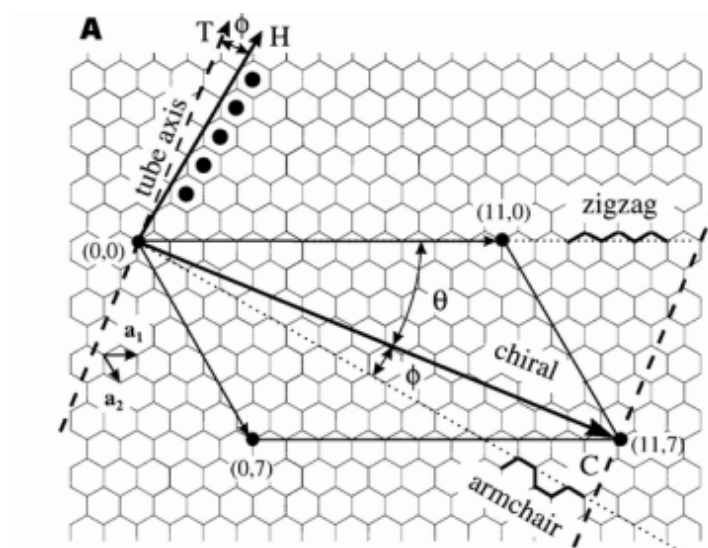


Figure 1: Relation between the hexagonal carbon lattice and the chirality of carbon nanotubes.

1.2.2 Synthesis and properties

Several techniques have been developed to produce carbon nanotubes in sizeable quantities, including arc discharge, laser ablation, and chemical vapor deposition (CVD). These three methods will be introduced as following.

1.2.2.1 Electric Arc discharge

One of the most widely used techniques to produce nanotubes is the electric arc discharge, the same as used to prepare fullerene molecules¹³. Indeed carbon nanotubes were found for the

first time during the examination of fullerene materials produced by the arc technique.¹⁴ The principle of this method is based on an electric arc discharge generated between two graphite electrodes under an inert atmosphere of helium or argon.¹⁵ The high temperature occurring between the two rods during the process allows the sublimation of carbon (Figure 2).

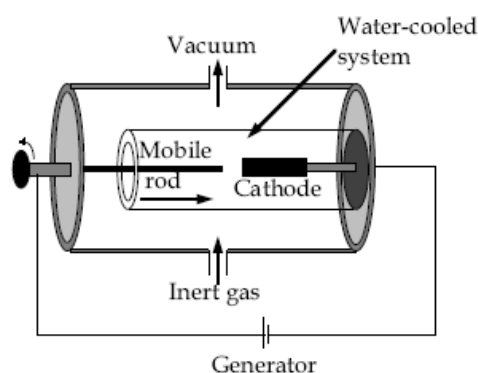


Figure 2: Schematic representation of the electric-arc apparatus used at the University of Montpellier.

α -Evaporation of pure graphite: In this case, two kinds of products are formed in the reactor, a deposit which grows on the end of the cathode during the arc process¹⁴ and soot on the reactor walls.¹⁵

β -Co-evaporation of graphite and a metal: By drilling a hole in the centre of the anode and filling it with a mixture of a metal catalyst and graphite powders, another element is introduced and co-evaporated with the carbon during the arc discharge process.^{16,17}

1.2.2.2 Laser Ablation

A second very useful and powerful technique for producing carbon nanotubes is the laser ablation method. A piece of graphite is vaporized by laser irradiation under an inert atmosphere.¹⁸ Carbon is vaporized at 1200 °C from the surface of a solid disk of graphite into a high-density helium (or argon) flow, using a focused pulsed laser (Figure 3).¹⁹

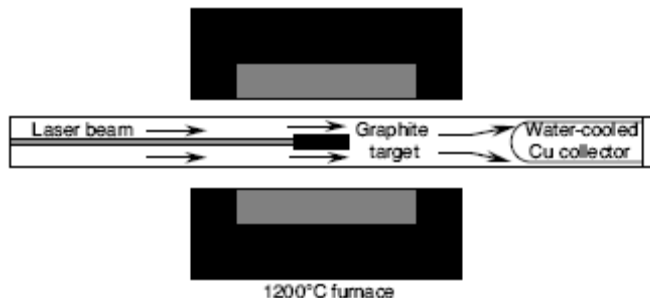


Figure 3: Schematic representation of the oven laser-vaporization apparatus used at Rice University (Houston, Texas, USA)

Yields of SWNTs are always seen to increase with temperature. These SWNTs have remarkably uniform diameter and self-organize into rope-like crystallites 5–20 nm in diameter (Figure 4a,b) and tens to hundreds of mm long, consisting of 100–500 SWNTs depending on the metal catalyst (Figure 4c).¹⁹

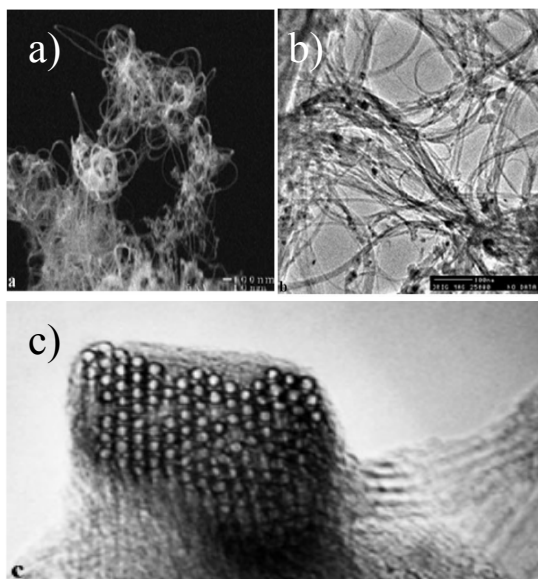


Figure 4: Microscopy images of single-walled nanotubes obtained by laser ablation¹⁷: a) SEM picture of carbon fibriles tangled together. b) TEM image of bundles of SWNTs. c) HRTEM image of one SWNT bundle bent in such a way that it is seen edge-on.

1.2.2.3 Chemical Vapor Deposition

A schematic experimental setup for CVD growth is depicted in Figure 5. The growth process involves heating a catalyst material to relatively low temperatures (500-1000 °C)²⁰ in a tube furnace and flowing a hydrocarbon gas through the tube reactor for a period of time. Materials grown over the catalyst are collected upon cooling the system to room temperature. The key parameters in nanotube CVD growth are the hydrocarbons, catalysts and growth temperature. CVD methods have come a long way from producing carbon fibers, filaments, and multiwalled carbon nanotubes to the synthesis of SWNTs^{21,22} with high crystallinity and perfection comparable to those of arc¹⁸ and laser^{19a,b} materials.

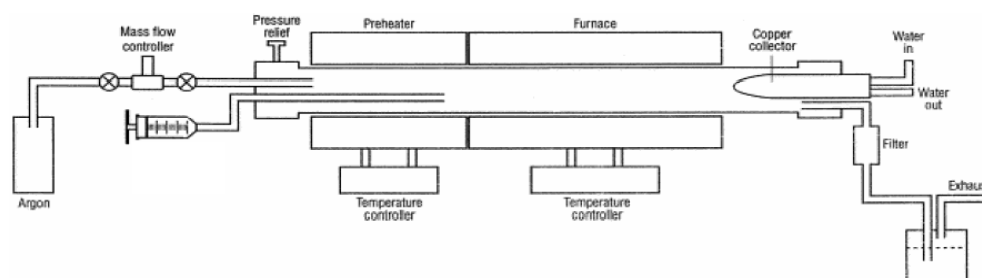


Figure 5: Schematic representation of CVD reactor for synthesis of carbon nanotubes

1.2.3 Potential applications of CNTs

Many potential applications have been proposed for carbon nanotubes, including conductive and high strength composites²³, lithium storage²⁴, field emission displays and radiation sources²⁵, hydrogen storage media²⁶ and nanometer-sized semiconductor devices and interconnects.²⁷

1.2.4 From graphitic CNTs to graphenic Discotic Liquid Crystals(LCs)

Carbon nanotubes serve as novel graphitic materials and are of interest because of their electronic and mechanical properties. In similarity with CNTs, PAHs possess also graphenic cores where their electronic and optoelectronic properties studied. Limitations of PAHs for good processing and solubility can be overcome by introducing flexible alkyl (or alkyl ether) chains around the rigid cores as well as to render the substituted PAHs into columnar liquid crystalline phase.

1.3 Liquid Crystals: definition, bulk properties and applications

Liquid crystals are substances that exhibit a phase of matter that has properties between those of a conventional liquid, and those of a solid crystal. For instance, a liquid crystal (LC) may flow like a liquid, but have the molecules in the liquid arranged and oriented in a crystal-like way. It is a well known state of matter lying between solid and isotropic liquid phases. It was discovered in 1888 by REINITZER²⁸ and since then immense efforts in research and development have made this field an important part of today's electronics. Liquid crystals can be divided into thermotropic and lyotropic LCs. Thermotropic LCs exhibit a phase transition into the LC phase as temperature is changed, whereas lyotropic LCs exhibit phase transitions as a function of concentration, e.g. an ordered phase is achieved by aggregation of the solute depending upon its concentration. In the crystal phase, the molecules have a high degree of order unlike the isotropic liquid phase where only a short range of order dominates, mobile and non-oriented molecules with respect to each others.

The first LC phase was discovered by Chandrasekhar S. in 1977 in the benzene- hexa-n-alkanes.²⁹ Since then, discotic liquid crystals have become a topic of interest to many research groups all around the world. The number of known discotic mesogens is growing continuously; currently more than 1500 different discotics are known.³⁰ In figure 6 are presented several examples of the most common discotics. With a few exceptions, these mesogens consist of a flat or nearly flat core with an axis of symmetry perpendicular to the plane of molecule.

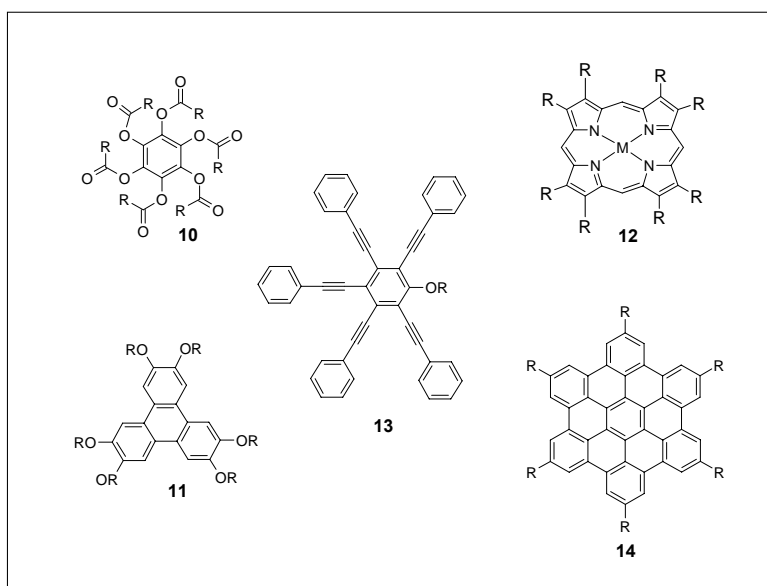


Figure 6: Discotic liquid crystalline materials – some common examples

Molecules that exhibit liquid crystal phases are called *mesogens*. They consist of a planar, rigid core to which flexible side chains are attached. There are three different distinct ways in which the mesogens can be ordered (Figure 7): nematic-discotic (N_D), nematic-columnar (N_{Col}) columnar hexagonal ordered (Col_{ho}) and columnar-disordered (Col_d). While the nematic-discotic phase only exhibits a long range orientational order of the mesogens, the molecules in the columnar discotic liquid crystalline state are arranged in columns, similar to coins in a stack. Several variations of the columnar structure have been identified: columns with a hexagonal lattice (Col_h), rectangular lattice (Col_r) and with an oblique lattice (Col_{ob}).

Additionally the degree of established organization within the column can be denoted with ordered (o) or disordered (d).³¹

The largest example, hexakis(*p*-dodecyl)-*peri*-hexabenzocoronene (**15b**), forms hexagonal discotic mesophases with exceptionally large phase widths. The high thermal stability of the mesophase is attributed to the large π - π -overlap areas of the aromatic cores.³²

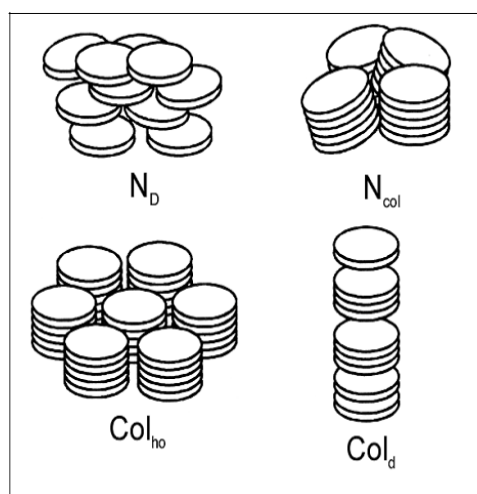


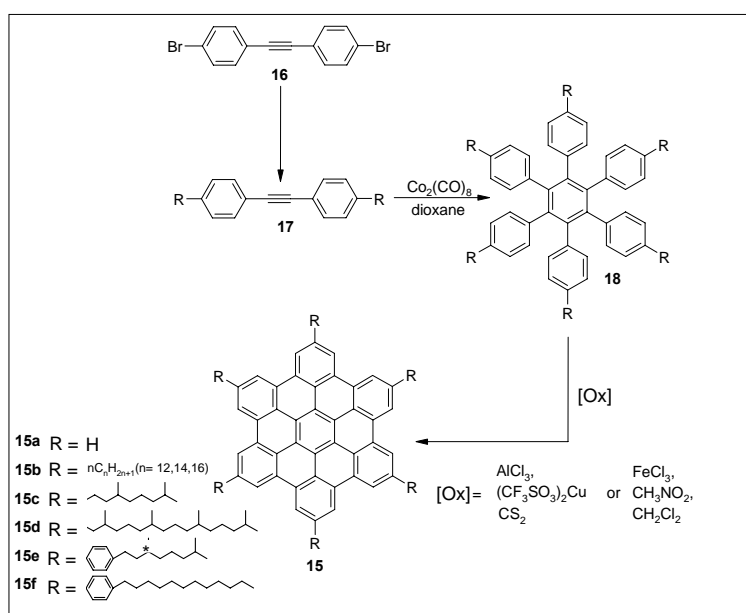
Figure 7: Schematic illustration of different discotic mesophases: nematic-discotic (N_D), nematic-columnar (N_{col}), hexagonal ordered (Col_{ho}) and columnar-disordered (Col_d).

The combination of sub-units with an additional intramolecular functionality offers a powerful tool to design molecular architectures which are characterized by the fact that their self-organization results from a complex interplay and/or competition between different factors and driving forces of structure formation. The configurations of the optoelectronic devices place specific requirements on the physical properties of the LC material to be used. Three main physical parameters to control the columnar organization can be mentioned: stability of the mesophase, supramolecular order of the mesophase and photophysical electronic properties of the LC material. Triphenylenes (**11**)³³, porphyrins (**12**)³⁴, and hexabenzocoronenes (**14**)³⁵ are the most widely investigated classes of discotic LC for use in optoelectronic devices.

1.3.1 Synthesis and phase behavior of discotic LCs

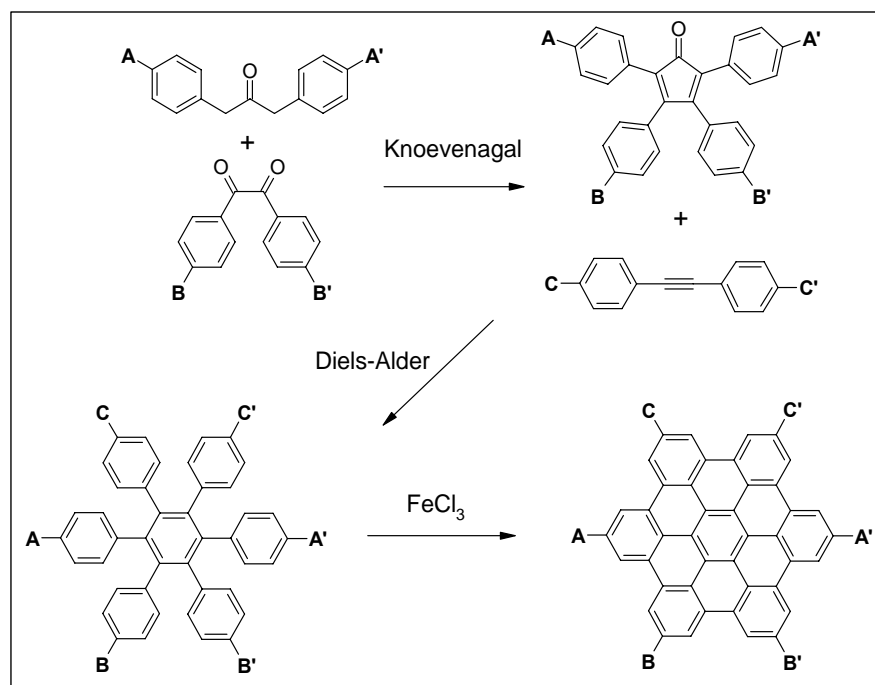
Hexa-*peri*-hexabenzocoronene (HBC) **15a** possesses a large aromatic core with C₆ symmetry, and their derivatives were intensively studied in the Müllen group.³⁶ The larger core size and high symmetry allows an efficient π - π overlap of the HBC discs in the self-assembled columns, leading to a high order in the mesophase with large phase width. The synthesis of the branched oligophenylenes is based on the cyclotrimerization reaction. Attachment of flexible chains on these discs increased vastly the latter's solubility and rendered them into ordered columnar liquid crystalline phases. The six-fold symmetric HBC derivatives **15** were prepared as shown in scheme 4 and their phase behavior was adjusted by varying the peripheral functions.

In the group of Prof. MÜLLEN, a synthetic method was developed in recent years which selectively made PAHs accessible in a size previously not thought possible.



Scheme 4: Synthesis of symmetrical HBC.

The cyclotrimerization offers a preparatively convenient route to all-benzenoid hydrocarbons with hexagonal symmetry, and the possibility of introducing solubilizing substituents, and further derivatization due to the possibility of attaching a variety of substituents such as alkyl or halogen (Scheme 4). The low symmetric HBC derivatives were synthesized by an alternative way (scheme 5). The key step is the Diels- Alder cycloaddition between suitable tetraphenylcyclopentadienone derivatives and substituted diphenylacetylenes to afford hexaphenylbenzene bearing different substituents. It has to be observed however, that only symmetrical tolans lead to isomerically pure hexaphenylbenzenes. The most effective reagent for the oxidative cyclodehydrogenation of alkyl substituted hexaphenylbenzenes to the corresponding hexabenzocoronenes has turned out to be iron (III) chloride, pre-dissolved in nitromethane.³⁷ This reagent does not lead to the cleavage or migration of alkyl side chains, unlike the stronger LEWIS-acid aluminium (III) chloride, where this problem can occur as a side-reaction.



Scheme 5: Synthesis of unsymmetrical HBC.

Study of the liquid crystalline and the thermal behaviour of HBCs were achieved using differential scanning calorimetry (DSC), polarized optical microscopy (POM), two-dimensional wide and small angle X-ray scattering (2D-WAXS and 2D-SAXS) and thermogravimetric analysis (TGA) as necessary tools for structure characterization. TGA gives information about thermal stability of the material (under inert atmosphere). Indeed, hexaalkyl-substituted HBCs show that the decomposition starts above 300 °C by cleavage of alkyl chains. The unsubstituted HBC disc **15a** (R = H) is stable up to 700 °C and sublimates between 500 and 600 °C. The temperatures of phase transitions of the materials are determined by DSC. For example, the thermal compoment of hexakis(*p*-dodecyl)-*peri*-hexabenzocoronene HBC- C_{12} **15b** shows a crystalline phase (D_h) until isotropic melting at about 417 °C. In the crystalline phase, the molecules are three-dimensionally ordered with a low mobility of the discs and the discs are tilted with respect to the columnar axis (Figure 8). In the D_h phase, the rotation of HBC discs around the column axis is possible, and the discs are now perpendicular to the columnar axis. In the isotropic phase, the molecules behave like a normal liquid, i.e. no anisotropy exists. Such phase structure was studied by 2D wide-angle X-ray diffraction (WAXD) combined with solid state NMR techniques.³⁸ The transition to the mesophase is often accompanied by birefringence and the formation of characteristic textures. These textures, which can be observed by polarized optical microscopy, provide an indication of the type of the mesophase.



Figure 8: Schematic representation of “crystal” – liquid crystal and liquid crystal – isotropic transitions for HBC **15b**.

X-ray diffractometry is a powerful tool regarding the structure analysis. As some information regarding the nature of the phases can be gained by the powder X-ray diffractometry, one can not distinguish reflections arising from intercolumnar and intracolumnar order. For this reason, extrusion of macroscopically oriented samples suitable for structural analysis is required.

Wide angle X-ray scattering (WAXS) measurements recorded with vertical orientation of filaments perpendicular with respect to the incident X-ray beam (Figure 9) provide two dimensional diffractograms with information pertaining to the stacking within columns and the 2D packing of those columns, partitioned along the vertical and horizontal directions, respectively. When some 3D correlation exists, then reflexes appear along diagonals.

The recorded scattered intensity distributions can be analyzed along various directions (*e.g.* equatorial (e) or meridional (m)) or integrated over the azimuthal angle. The results of intensity distributions are presented as functions of the scattering vector ($s = 2\sin\theta/\lambda$), where θ is the scattering angle. A schematic representation of a diffractogram where the information related to the stacking within the columns and the intercolumnar packing can be obtained (Figure 9). The common Bragg reflections from the columnar packing of the fiber lie in the equator (a) and the diffuse scattering of the unoriented aliphatic side chains appear as a ring (b). The meridional reflections in (c) correspond to the discs belonging to the same columns and are parallel to the fiber axis. If these discs are tilted, within the column, then the additional reflections appear along the diagonal (c').

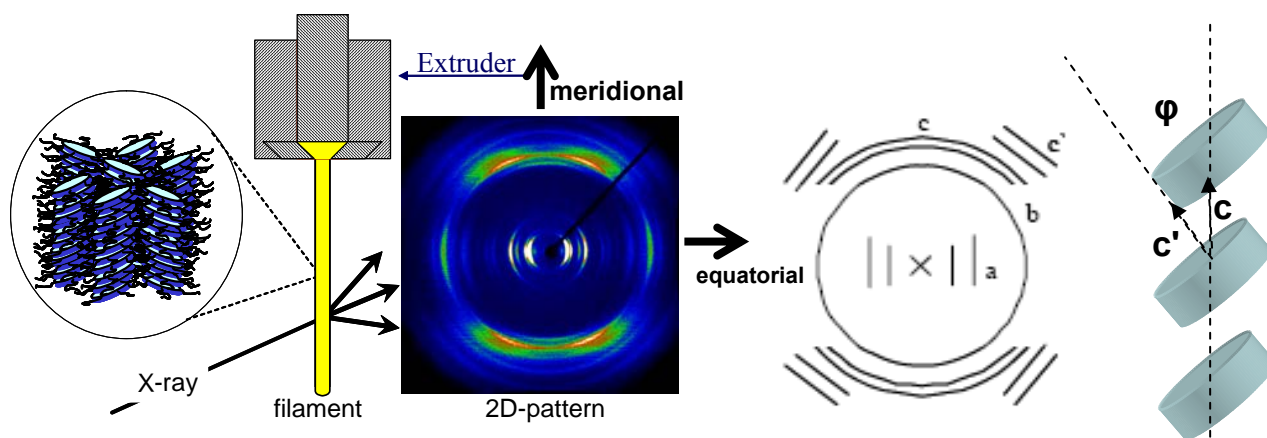


Figure 9: A diagram of experimental set up and principle for 2D WAXD measurements on extruded filaments of **15b**.

Experimental data regarding WAXS and DSC measurements of the behaviour of HBC derivatives are available in reference.³⁹

1.3.2 Amphiphile discotic LCs

Until today, amphiphilic triphenylenes and very few amphiphilic HBC molecules have been prepared (figure 10).⁴⁰ Their hydrophobic-hydrophilic character has an influence on the bulk properties and the self-organization of the materials. Triphenylene **19a** exhibits a hexagonal columnar ordered mesophase (D_{ho}) and the two-fold hydroxy terminated compound **19b** forms a monotropic lamellar LC phase with a well defined double-layer packing of associated pairs of discs (arising from partial overlapping of the OH-containing tails) and local columnar intra-layer ordering.⁴¹ For hexa-*peri*-hexabenzocoronenes with one or two hydrophilic functions **20a-d**, the amphiphilic effect is not greatly pronounced in the bulk due to the large π - π overlapping interaction which is dominant over all other factors in controlling their supramolecular organization in the bulk.

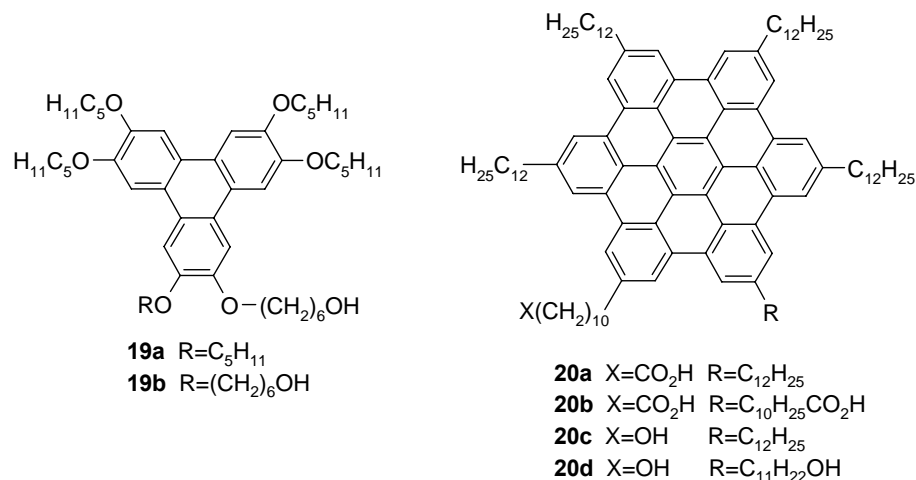


Figure 10: Amphiphilic discotic molecules.

All these compounds exhibit a hexagonal columnar (D_h) phase at temperatures higher than 100 °C, all 10-20 °C higher than for hexaalkyl-HBC(dodecyl).⁴² At the air-water interface, the amphiphilic HBC **120a** forms well-defined Langmuir monolayers with lamellar organization in the low-pressure phase and hexagonal lattices in the high pressure phase.⁴³ In this last phase, coherence from the π stacks is lost and the organization is driven by crystallization of the substituent alkyl chains.⁴⁴ Thin films can also be transferred onto a solid support.

1.3.3 Charge carrier mobility and related electronic properties of graphite disks.

Discotic liquid crystals have already found applications as active components in organic light-emitting diodes,⁴⁵ photovoltaic cells^{35,46} and field effect transistors.⁴⁷ Common features that impact on the device performance are charge injection or collection at the electrodes and charge transport in the bulk material. The latter depends on the degree of order within the columnar stack and thus on the overlap between the π -orbitals, thus providing co-axially insulated conductive pathways which offer a unique possibility for the one-dimensional

transport of charge. When large PAHs are used as rigid cores, the strong overlap of π^* orbitals of adjacent aromatic rings results in a high one-dimensional charge carrier mobility along the columnar axis. Time of flight (TOF) photoconductivity and pulse radiolysis time-resolved microwave conductivity (PR-TRMC) are the ways to estimate the mobility of charge carriers in standard devices configurations.⁴⁸ The mobility values for the LC phases of HBCs, recorded by PR-TRMC are the highest ever found for discotic materials, and are well in excess of the value of $0.1 \text{ cm}^2\text{V}^{-1}\text{s}^{-1}$ found by both PR-TRMC and TOF techniques for the helical columnar phase of 2,3,6,7,10,11-hexahexylthiotriphenylene.⁴⁹ The "crystalline" phases exhibit the highest values ($1.13 \text{ cm}^2\text{V}^{-1}\text{s}^{-1}$), while transition to the mesophases coincides with a distinct decrease in mobilities ($0.17\text{-}0.46 \text{ cm}^2\text{V}^{-1}\text{s}^{-1}$).^{36b} As an example, the temperature dependence of one-dimensional charge carrier mobility for HBC- C_{12} is depicted in figure 11.

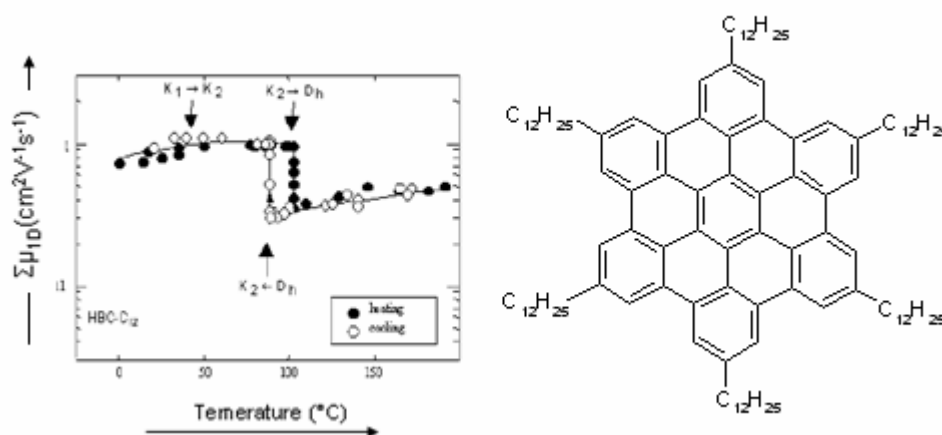


Figure 11: The temperature dependence of one-dimensional charge carrier mobility of HBC- C_{12} 15b.

Applications of discotic liquid crystals as active functional materials components, due to their charge carrier mobility as compared to conventional conjugated polymers, have found interest for field effect transistors (FET), photovoltaic cells and organic light emitting diodes (OLED). Furthermore, their liquid crystalline properties offer the possibility of obtaining extensive,

well-organized layers in which the columnar orientation can be controlled and self-healing of structural defects can occur. They also have the advantage that they can be processed extremely cheaply over large areas at low temperatures by processing directly from solution.

1.3.4 FETs

The control of the order and orientation of discotic liquid crystalline materials is a crucial point for the successful device application. Bao et al.⁵⁰ obtained high field effect mobility by controlling the morphology and order of metallophthalocyanines when using highly ordered vacuum-deposited thin films for FET fabrication. Van de Craats et al. found recently that direct processing of HBC based discotic materials on the oriented film such as rubbed polytetrafluoroethane (PTFE) substrate provided high ordered thin films with the columnar axis of discs parallel to the orientation axis. Figure 12 shows highly oriented HBC film used in the fabrication of FET devices. High FET mobility up to $10^{-3} \text{ cm}^2\text{V}^{-1}\text{s}^{-1}$ and high on/off ratio of 10^4 was achieved.⁴⁸

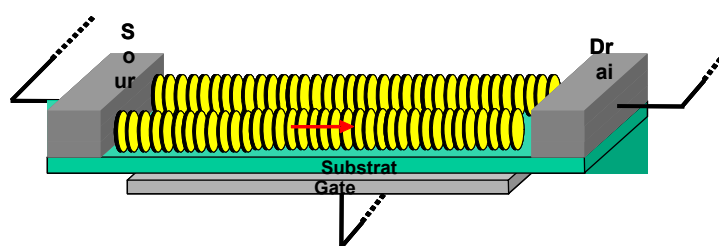


Figure 12: Schematic representation of discotic LC materials in FETs.

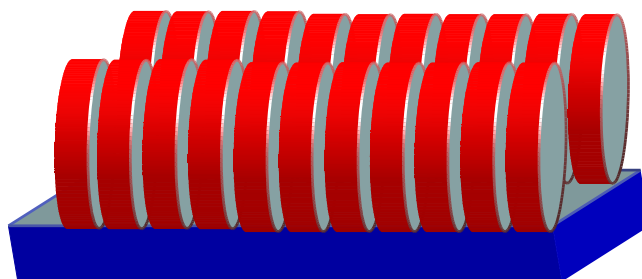


Figure 13: Schematic representation of supramolecular arrangement on surfaces with: edge-on orientation of the molecules, where the columnar axis is oriented parallel to the substrate.

The main charge transport in field-effect transistors takes place parallel to the insulating substrate and therefore requires an edge-on arrangement (schematic representation in Figure 13) of the discotic molecules with uniaxial columnar orientation in charge transport direction. Langmuir-Blodgett,⁵¹ zone-casting technique,⁵² zone-crystallization⁵³ or solution casting onto pre-oriented PTFE⁵¹ as well as mechanical forces (shear) are suitable methods to obtain highly ordered surface layers with the desired columnar orientation. In general, edge-on arrangement results from a minimization of the surface contact of molecules with the substrate of different polarity.

1.3.5 Photovoltaic cells

Discotic liquid crystalline materials have been proposed as potential candidates for the active layer in organic based optoelectronic devices such as light-emitting diodes (LEDs), photovoltaic cells (PVCs), and field-effect transistors (FETs). High-efficient organic photovoltaic devices derive their performance from two basic elements: (i) the dissociation within the active semiconductor layers of the photogenerated excited state, and (ii) the transport of the resulting separated charges to the electrodes. Optimized photovoltaic devices require, in addition to an optimal acceptor-donor interaction, a migration of charges foremost perpendicular to the substrate. Schmidt-Mende et al.³⁵ made a big progress by constructing a p-

n type photovoltaic solar cell using discotic liquid crystal HBC-PhC₁₂ as the hole transporting layer and crystalline perylene diimide (PDI) dye as electron transporting layer in solution by spin-coating on an ITO substrate. The obtained photodiodes exhibited an extremely high external quantum efficiency (EQE = 34% at 490 nm) and 2% as power efficiency. Such simple but highly efficient methods are very promising for the practical solar cell application using discotic LCs.

1.4 Motivation and objectives

Discotic liquid crystals (HBCs) as molecularly defined graphite subunits have long been recognized as ideal graphenic model compounds for delocalized π -systems. Therefore, the size, the topology of the ring fusion (cyclodehydrogenation reaction), and the periphery are crucial not only for the electronic properties at the molecular and supramolecular level, but also for packing in two dimensions, thus yielding phase behavior and promising applications in thin film devices and supramolecular scale devices. Despite the recent advances, some more improvements are desirable:

The construction of precisely defined molecular materials, designed to perform specific interactions, requires the incorporation of hydrophobic-hydrophilic, hydrogen-bonding or electrostatic interactive functional building blocks and a control of the supramolecular assembly process. Owing to their extended flat hydrophobic aromatic surface, HBC molecules can self-assemble into ordered columnar structures via π -stacking interaction. Appropriate structural modification of the HBC alkyl chains, by insertion of N-methyl-imidazole motifs at their ends, can be employed for the constructions of nanosized supramolecular architectures based on the HBC flat hydrophobic core and the hydrophilic imidazolium property, thus leading to nano-ordered supramolecular aggregation in both solution and solid state.

Insertion of heavy metal to the HBC disc periphery would enhance radiative emission from triplet excited state to the singlet ground state with enhancement of the emission life time. This would also afford fast inter-system crossing by increasing spin-orbit coupling which lead exclusively to the emission of phosphorescence ($T_1 \rightarrow S_0$) at low and room temperatures. Nevertheless, a thorough understanding of triplet photophysics is essential if one intends to develop a full picture of basic excitations in HBC π -systems, where very few detailed studies toward this purpose were performed before. An understanding of such issues is also necessary for further progress in the technological development of opto-electronic devices.

Improving HBC synthesis by diversion of the peripheral substituents enhanced their solubility and processability making them suitable for commercial applications in optoelectronic technologies where the adaptability, simplicity and low cost of manufacturing are extremely attractive. Additionally, lowering the melting temperature by introduction of branched alkyl chains containing heteroatoms provides the possibility of homeotropically aligning HBC aggregates on surfaces and making them candidates for electronic application, such as solar cells.

From a topological standpoint, single-walled and multi-walled carbon nanotubes can be regarded as a family of graphite. Their tubular architectures, in which curved graphene sheets are stacked perpendicularly to the longer axis of the tubes, are characteristic of graphite structures. Actually, thermal treatment, of commercially available cobalt-carbon frameworks, may yield interesting and easily-made carbon materials that could be more expensive when compared to traditional methods like arc discharge or chemical vapor deposition which use pre-deposited metallic catalyst on substrates and produces carbon nanostructures at high temperatures. On the other hand, jet printing of the organo-cobalt precursors followed by thermal treatment under inert atmosphere would lead to high yields of aligned carbon

nanotubes making them candidates for electronic applications, as well as using the metallic properties of embedded cobalt toward heterogeneous catalysis such as production of carbon nanostructures at high temperature in the presence of additional carbon source.

In this thesis work, newly prepared series of HBC materials as well as carbon ordered nanomaterials will be presented as follows:

1) Incorporating Pt into the para-position of the HBC shell should enhance the spin-orbit coupling and thus increase the ISC between S_1 and T_n (Figure 14). The synthesis of large soluble PAHs has recently been developed in our group,⁵⁴ therefore allowing us to conduct a detailed time-resolved photoluminescence study on this type of chromophores with and without platinum metal.

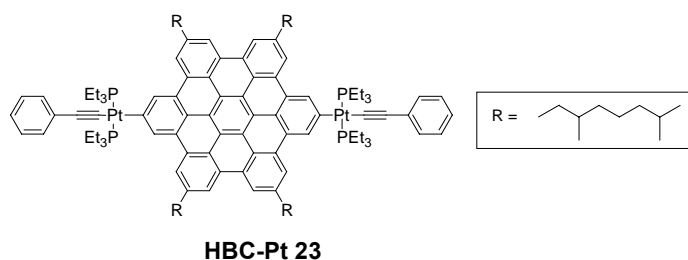


Figure 14: HBC-Pt 23 complex structure.

2) Self-assembly for materials applications can be controlled by appropriate structural modification at the core periphery. Attachment of flexible hydrophilic imidazolium units to the HBC core should induce amphiphilicity which is expected to affect the self-assembly behavior in different solvents and under different conditions (Figure 15). This should reveal the basic relationship between structure and nano-organization in both solution and on a substrate.

4) Controllable solid-state pyrolysis of organometallic precursors has recently emerged as an alternative method for preparing carbon nanostructures such as CNTs and carbon onions. The catalytic decomposition of hydrocarbons is a promising way for the production of carbon nanotubes and nanostructures on large scales. The choice of the organometallic precursor appears as a key issue for controlling the morphologies (shape and uniformity) of the carbon structures and the conversion yield. Thus, ethynyl functionalized polyphenylene dendrimers can serve as precursors because of their carbon-rich character and facile complexation with cobalt carbonyl at the peripheries. Moreover, hexa-*peri*-hexabenzocoronene and diphenylacetylene-cobalt nanocluster derivatives should allow the formation of well-ordered carbon nanostructures at high temperatures (Figure 17).

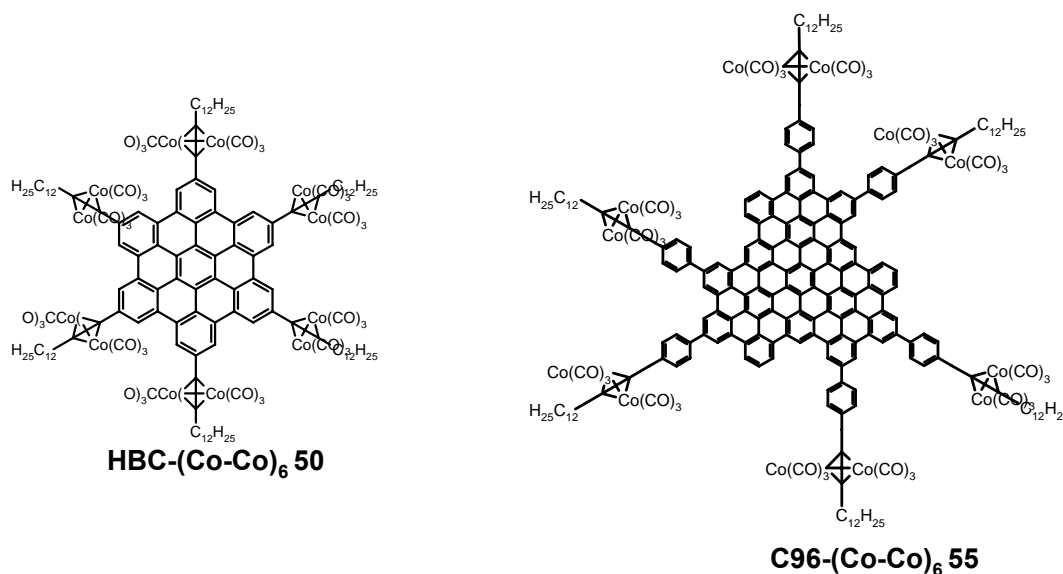


Figure 17: HBC 50 and C96 55 cobalt complexes as precursors for solid-state thermolysis

¹ R. G. Harvey, Polycyclic Aromatic Hydrocarbons, 1996.

- ² a) A. Bjorseth, T. Ramdahl, Handbook of polycyclic aromatic hydrocarbons. Vol2, eds. A. Bjorseth & T. Ramdahl, Marcel Dekker: New York, 1985, pp.1-20; G. Grimmer, environmental carcinogens: Polycyclic aromatic hydrocarbons, CRC Press: Boca Raton, Fla., 1983.
- ³ M. Blumer, *Sci. Am.* **1976**, 234, 35.
- ⁴ a) R. Scholl, C. Seer, R. Weitzenböck, *Chem. Ber.* **1910**, 43, 2202; b) R. Scholl, C. Seer, *Liebigs Ann. Chem.* **1912**, 394, 111; c) R. Scholl, H. Neumann, *Chem. Ber.* **1922**, 55, 118-126 ; d) R. Scholl, C. Seer, *Chem. Ber.* **1922**, 55, 330.
- ⁵ a) E. Clar, *Nature* **1948**, 161, 238; b) E. Clar, *Chem. Ber.-Recl.* **1948**, 81, 52; c) E. Clar, D. G. Stewart, *J. Am. Chem. Soc.* **1953**, 75, 2667; d) E. Clar, *Chem. Ber.-Recl.* **1949**, 82, 495.
- ⁶ a) M. Zander, W. Franke, *Chem. Ber.-Recl.* **1958**, 91, 2794; b) M. Zander, *Chem. Ber.-recl.* **1959**, 92, 2744; c) S. Hagen, H. Hopf, *Top. Curr. Chem.* **1998**, 196, 44-89; d) M. Zander, *Angew. Chem. Int. Ed. Engl.* **1960**, 72, 513.
- ⁷ M. S. Dresselhaus, G. Dresselhaus, K. Sugihara, I. L. Spain, H. A. Goldberg, *Graphite Fibers and Filament, SpringerSer. Mater. Sci.*, Vol 5 (Springer, Berlin, Heilderberg 1988).
- ⁸ a) L. T. Scott, M. S. Bratcher, S. Hagen, *J. Am. Chem. Soc.* **1996**, 118, 8743; b) S. Hagen, M. S. Bratcher, M. S. Erickson, G. Zimmermann, L. T. Scott, *Angew. Chem. Int. Ed.* **1997**, 36, 406; *Angew. Chem.* **1997**, 109, 407.
- ⁹ L. T. Scott, M. M. Hashemi, D. T. Meyer, H. B. Waren, *J. Am. Chem. Soc.* **1991**, 113, 7082.
- ¹⁰ W. E. Barth, R. G. J. Lawton, *J. Am. Chem. Soc.* **1966**, 88, 380.
- ¹¹ P. W. Rabideau, *J. Am. Chem. Soc.* **1994**, 116, 7891.
- ¹² M. S. Dresselhaus, G. Dresselhaus, and R. Saito, *Phys. Rev.* **1992**, B 45, 6234.
- ¹³ W. Krätschmer, L.D. Lamb, K. Fostiropoulos, D.R. Huffman, *Nature* **1990**, 347, 354.
- ¹⁴ S. Iijima: *Nature* **1991**, 354, 56.
- ¹⁵ T.W. Ebbesen, P.M. Ajayan, *Nature* **1992**, 358, 220.
- ¹⁶ S. Iijima, T. Ichihashi, *Nature* **1993**, 363, 603.
- ¹⁷ a) P.M. Ajayan, J.M. Lambert, P. Bernier, L. Barbedette, C. Colliex, J.M. Planeix, *Chem. Phys. Lett.* **1993**, 215, 509; b) J.M. Lambert, P.M. Ajayan, P. Bernier, *Synth. Met.* **1995**, 70, 1475; c) C. Journet, W.K. Maser, P. Bernier, A. Loiseau, M. Lamy de la Chapelle, S. Lefrant, P. Deniard, R. Lee, J.E. Fischer, *Nature* **1997**, 388, 756; d) P.M. Ajayan, C. Colliex, J.M. Lambert, P. Bernier, L. Barbedette, M. Tence, O. Stephan, *Phys. Rev. Lett.* **1994**, 72, 1722; e) Y. Saito, K. Kawabata, M. Okuda, *J. Phys. Chem.* **1995**, 99, 16076.
- ¹⁸ H.W. Kroto, J.R. Heath, S.C. O'Brien, R.F. Curl, R.E. Smalley, *Nature* **1985**, 318, 162.
- ¹⁹ a) T. Guo, P. Nikolaev, A.G. Rinzler, D. Tomanek, D.T. Colbert, R.E. Smalley, *J. Phys. Chem.* **1995**, 99, 10694; b) T. Guo, P. Nikolaev, A. Thess, D.T. Colbert, R.E. Smalley, *Chem. Phys. Lett.* **1995**, 243, 49, c) A. Thess, R. Lee, P. Nikolaev, H. Dai, P. Petit, J. Robert, C. Xu, Y.H. Lee, S.G. Kim, A.G. Rinzler, D.T. Colbert, G. Scuseria, D. Tomanek, J.E. Fischer, R.E. Smalley, *Science*, **1996**, 273, 483.
- ²⁰ Dai, H. Nanotube Growth and Characterization. Carbon Nanotubes; Springer: Berlin, **2001**; pp 29-53.
- ²¹ a) J. Kong, H. Soh, A. Cassell, C. F. Quate, H. Dai, *Nature* **1998**, 395, 878; b) J. Hafner, M. Bronikowski, B. Azamian, P. Nikolaev, D. Colbert, *Chem. Phys. Lett.* **1998**, 296, 195; c) B. Satishkumar, A. Govindaraj, R. Sen,

- C. N. R. Rao, *Chem. Phys. Lett.* **1998**, 293, 47; d) J. -F. Colomer, C. Stephan, S. Lefrant, G. V. Tendeloo, I. Willems, *Chem. Phys. Lett.* **2000**, 317, 83.
- ²² N. Tyutyulkov, N. Ivanov, K. Müllen, A. Staykov, F. Dietz, *J. Phys. Chem. B* **2004**, 108, 4275.
- ²³ a) C. Bower, R. Rosen, and L. Jin, J. Han, O. Zhou, *Appl. Phys. Lett.* **1999**, 74, 3317 ; b) L. Jin, C. Bower, O. Zhou, *Appl. Phys. Lett.* **1998**, 73, 1197; c) B. I. Yakobson, C. J. Brabec, and J. Bernholc, *Phys. Rev. Lett.* **1996**, 76, 2511.
- ²⁴ a) B. Gao, A. Kelinhammes, X. P. Tang, C. Bower, Y. Wu, O. Zhou, *Chem. Phys. Lett.* **1999**, 307, 153; b) M. Wittingham (Ed.), recent advances in rechargeable Li batteries, *Solid State Ionics* **1994**, 69, (3,4).
- ²⁵ J. -M. Bonard, F. Meier, T. Stöckli, L. Forró, A. Chatelain, W. A. de Heer, J. -P. Salvetat, *Ultramicroscopy* **1998**, 77, 7.
- ²⁶ a) M. Pederson, J. Broughton, *Phys. Rev. Lett.* **1992**, 69, 2689; b) P. Chen, X. Wu, J. Lin, K. Tan, *Science*, **1999**, 285, 91; c) Y. Ye, C. C. Ahn, C. Witham, B. Fultz, J. Liu, A. G. Rinzler, D. Colbert, K. A. Smith, R. E. Smalley, *Appl. Phys. Lett.* **1999**, 74, 2307.
- ²⁷ a) Baughman, R. H., Zakhidov, A. A., and de Heer, W. A., *Science*, **2002**, 297, 787-792; b) D. Rotman, *Natur & Technik* **2002**, 70, 30.
- ²⁸ F. Reinitzer, *Monatsh. Chem.* **1888**, 9, 421.
- ²⁹ S. Chandrasekhar, B. K. Sadashiva, K. A. Suresh, *Pramana* **1977**, 9, 471.
- ³⁰ V. Vill, *LiqCryst - Database of Liquid Crystalline Compounds* **1995**, LCI Publisher GmbH, Hamburg, 1999.
- ³¹ S. Chandrasekhar, S. K. Prasad, *Contemp. Phys.* **1999**, 40, 237.
- ³² P. Herwig, C. W. Kayser, K. Müllen, H. W. Spiess, *Adv. Mater.* **1996**, 8, 510.
- ³³ J. Simmerer, B. Glusen, W. Paulus, A. Kettner, P. Schumacher, D. Adam, K. H. Etzbach, K. Siemensmeyer, K. J. H. Wendorff, H. Ringsdorf, D. Haarer, *Adv. Mater.* **1996**, 8, 815.
- ³⁴ C. Y. Liu, H. L. Pan, H. J. Tang, M. A. Fox, A. J. Bard, *J. Phys. Chem.* **1995**, 99, 7632.
- ³⁵ L. Schmidt-Mende, A. Fechtenkötter, K. Müllen, E. Moons, R. H. Friend, J. D. MacKenzie, *Science* **2001**, 293, 1119.
- ³⁶ a) M. Watson, A. Fechtenkötter, K. Müllen, *Chem. Rev.* **2001**, 101, 1267; b) A. Stabel, P. Herwig, K. Müllen, *Angew. Chem. Int. Ed.* **1995**, 34, 1609; *Angew. Chem.* **1995**, 107, 335; c) A. M. van de Craats, J. M. Warman, A. Fechtenkötter, J. D. Brand, M. A. Harbison, K. Müllen, *Adv. Mater.* **1999**, 11, 1469; d) A. Fechtenkötter, K. Saalwächter, M. A. Harbison, K. Müllen, H. W. Spiess, *Angew. Chem. Int. Ed.* **1999**, 38, 3039; *Angew. Chem.* **1999**, 111, 3224; e) A. Fechtenkötter, N. Tchebotareva, M. D. Watson, K. Müllen, *Tetrahedron Symp.* **2001**, 57, 3769; f) P. Samori, A. Fechtenkötter, F. Jäckel, T. Böhme, K. Müllen, J. P. Rabe, *J. Am. Chem. Soc.* **2001**, 123, 11462.
- ³⁷ S. Ito, M. Wehmeier, J. D. Brand, C. Kübel, R. Epsch, J. P. Rabe, K. Müllen, *Chem.-Eur. J.* **2000**, 6, 4327.
- ³⁸ a) S. P. Brown, I. Schnell, J. D. Brand, K. Müllen, H. W. Spiess, *J. Am. Chem. Soc.* **1999**, 121, 6712; b) I. Fischbach, T. Pakula, P. Minkin, A. Fechtenkötter, K. Müllen, H. W. Spiess, *J. Phys. Chem. B* **2002**, 106, 6408.
- ³⁹ a) N. Tchebotareva, Ph.D. thesis, Johannes Gutenberg Universität in Mainz, **2003**; b) S. Ito, M. Wehmeier, J. D. Brand, C. Kübel, R. Epsch, J. P. Rabe, K. Müllen, *Chem. Eur. J.* **2000**, 6, 4327; c) J. Wu, M. D. Watson, K.

Müllen, *Angew. Chem. Int. Ed.* **2003**, *42*, 5329; d) J. Wu, M. D. Watson, L. Zhang, Z. Wang, K. Müllen, *J. Am. Chem. Soc.* **2004**, *126*, 177.

⁴⁰ a) J. Wu, J. Li, U. Kolb, K. Müllen, *Chem. Comm.* **2006**, 48; b) J. P. Hill, W. Jin, A. Kosaka, T. Fukushima, H. Ichihara, T. Shimomura, K. Ito, T. Hashizume, N. Ishii, T. Aida, *Science* **2004**, *304*, 1481; c) W. Jin, T. Fukushima, A. Kosaka, M. Niki, N. Ishii, T. Aida, *J. Am. Chem. Soc.* **2005**, *127*, 8284.

⁴¹ O. Ringsdorf, H. Tsukruk, V. Wendorff, *Langmuir* **1992**, *8*, 9, 2279.

⁴² J. D. Brand, C. Kübel, S. Ito, K. Müllen, *Chem. Mater.* **2000**, *12*, 1638.

⁴³ a) S. Kubowicz, U. Pietsch, M. D. Watson, N. Tchebotareva, K. Müllen, A. F. Thuenemann, *Langmuir* **2003**, *19*, 5036; b) A. F. Thuenemann, S. Kubowicz, C. Burger, M. D. Watson, N. Tchebotareva, K. Müllen, *J. Am. Chem. Soc.* **2003**, *125*, 352.

⁴⁴ N. Reitzel, T. Hassenkam, K. Balashev, T. R. Jensen, P. B. Howes, K. Kjaer, A. Fechtenkötter, N. Tchebotareva, S. Ito, K. Müllen, T. Bjornholm, *Chem. Eur. J.* **2001**, *7*, 4894.

⁴⁵ a) M. O'Neill, S. M. Kelly, *Adv. Mater.* **2003**, *15*, 1135; b) I. Seguy, P. Jolinat, P. Destruel, J. Farenc, R. Mamy, H. Bock, J. Ip, T. P. Nguyen, *J. Appl. Phys.* **2001**, *89*, 5442.

⁴⁶ G. Lassem, J. H. Wendorff, *Polym. Adv. Technol.* **1998**, *9*, 443.

⁴⁷ A. M. van de Crass, N. Stutzmann, O. Bunk, M. M. Nielsen, M. D. Watson, K. Müllen, H. D. Chanzy, H. Sirringhaus, R. H. Friend, *Adv. Mat.* **2003**, *15*, 495.

⁴⁸ K. Ohta, K. Hatsuoka, M. Sugibayashi, M. Ariyoshi, K. Ban, F. Maeda, R. Naito, K. Nishizawa, A. M. van de Craats, J. M. Warman, *Mol. Cryst. Liq. Cryst.* **2003**, *396*, 325.

⁴⁹ A. M. van de Craats, J. M. Warman, *Adv. Mater.* **2001**, *13*, 130.

⁵⁰ Z. Bao, A. J. Lovinger, A. Dodabalapur, *Adv. Mater.* **1997**, *9*, 42.

⁵¹ N. Reitzel, T. Hassenkam, K. Balashev, T. R. Jensen, P. B. Howes, K. Kjaer, A. Fechtenkötter, N. Tchebotareva, S. Ito, K. Müllen, T. Bjornholm, *Chem.-Eur. J.* **2001**, *7*, 4894.

⁵² A. Tracz, J. K. Jeszka, M. D. Watson, W. Pisula, K. Müllen, T. Pakula, *J. Am. Chem. Soc.* **2003**, *125*, 1682.

⁵³ W. Pisula, M. Kastler, D. Wasserfallen, T. Pakula, K. Müllen, *J. Am. Chem. Soc.* **2004**, *126*, 8074.

⁵⁴ a) C. D. Simpson, J. Wu, M. D. Watson, K. Müllen, *J. Mater. Chem.* **2004**, 494; b) M. D. Watson, A. Fechtenkötter, K. Müllen, *Chem. Rev.* **2001**, *101*, 1267.

⁵⁵ C. Y. Liu, A. Fechtenkötter, M. D. Watson, K. Müllen, A. J. Bard, *Chem. Mater.* **2003**, *15*, 124.

⁵⁶ a) N. Terasawa, H. Monobe, K. Kiyohara, Y. Shimizu, *Chem. Commun.* **2003**, 1678; b) A. N. Cammidge, H. Gopee, *J. Mater. Chem.* **2001**, *11*, 2773.

⁵⁷ K. Hatusaka, K. Ohta, I. Yamamoto, H. Shirai, *J. Mater. Chem.* **2001**, *11*, 423.

Chapter 2

Time-resolved spectroscopic study of phosphorescent platinated and alkylated hexa-peri-hexabenzocoronenes

In this chapter, the photoluminescence properties of a series of photoactive HBC complexes have been studied. Introduction of platinum-phenylethynyl to the HBC core enhanced the spin-orbit coupling by three orders of magnitude and thus increased the inter-system crossing between the first excited state S_1 and the triplet excited state T_1 . This allowed the visualization of phosphorescence radiative emission at both low and room temperatures. It is therefore possible to access the singlet and triplet state by using conventional spectroscopic techniques. The triplet energy level has been tuned between 2.3 and 1.7 eV by varying the HBC core substituents. Alkylated HBCs did not show any triplet emission at room temperature, but only fluorescence type emission.

2.1 Introduction

The photophysics of triplet states in conjugated materials are of high scientific and industrial research interest since in electroluminescence devices based on small molecules, the majority of excited states formed upon recombination of charge carriers are triplets.¹ Theoretical and experimental studies suggested that triplet emission is more efficient if the molecules have rigid planar structures (e.g., the ladder-type poly-*para*-phenylenes).^{1c,2} Heavy atoms such as Pt,³ Au,⁴ and Hg⁵ were introduced into the organic π -systems to enhance the spin-orbit coupling and improved triplet emission was found in these organometallic complexes.

photoluminescence experiments on different HBC derivatives. Herein, a highly symmetric hexakis(3,7-dimethyloctyl)-*peri*-hexabenzocoronene (**HBC-C_{8,2}** **24**) and hexakis(4-phenyldodecyl) *peri*-hexabenzocoronene (**HBC-Ph-C₁₂** **25**) substituted with alkyl and phenyl-alkyl chains were chosen as the reference (Chart 1) compounds. In addition, to improve the phosphorescence yield of the compound and further elucidate the influence of heavy atoms on the triplet state of HBC, a double-substituted HBC-platinum complex *2,11-bis[trans-bis(triethylphosphine)-(phenylethynyl)platinum]-5,8,14,17-tetrakis(3,7-dimethyloctyl)hexa-*peri*-hexabenzocoronene* (**HBC-Pt** **23**) was prepared and its photophysical properties were compared to **HBC-C_{8,2}** (**24**) and **HBC-Ph-C₁₂** (**25**). Combination of both the heavy-atom effect and the increased intersystem crossing in the novel double platinum-substituted HBC leads to the exclusive emission of phosphorescence without any residues of fluorescence in the prompt and delayed emission spectra.

2.2 Synthesis

The **HBC-C_{8,2}** (**24**) and **HBC-Ph-C₁₂** (**25**) were prepared following the reported procedure.¹² 2,11-Dibromo-5,8,14,17-tetrakis(3,7-dimethyloctanyl)-hexa-*peri*-hexabenzocoronene (**21**) was prepared according to the literature procedure.¹³ A representative malid-tof spectrum is shown in figure 1. The phenylene-ethynyl-Pt moieties were substituted on the *para*-positions of precursor **21** according to the synthetic route shown in Scheme 1. Double oxidative addition of platinum to the *para*-dibromo-HBC (**21**)¹⁴ afforded the HBC-Pt complex (**22**) in 36% yield.¹⁵ CuI-catalyzed dehydrohalogenation reaction of compound (**22**) and phenylacetylene then gave the desired molecule HBC-Pt (**23**) in 44% yield. All these compounds were confirmed by mass spectroscopy, ¹H NMR, ¹³C NMR and ³¹P{¹H} NMR spectroscopy.

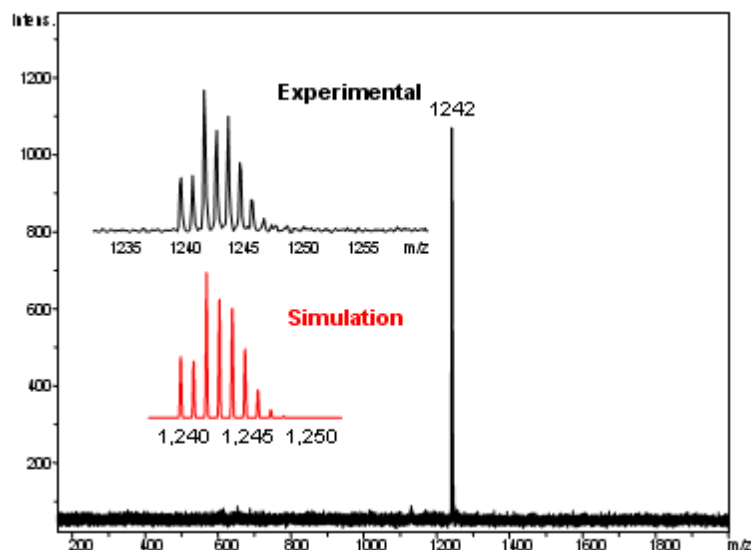
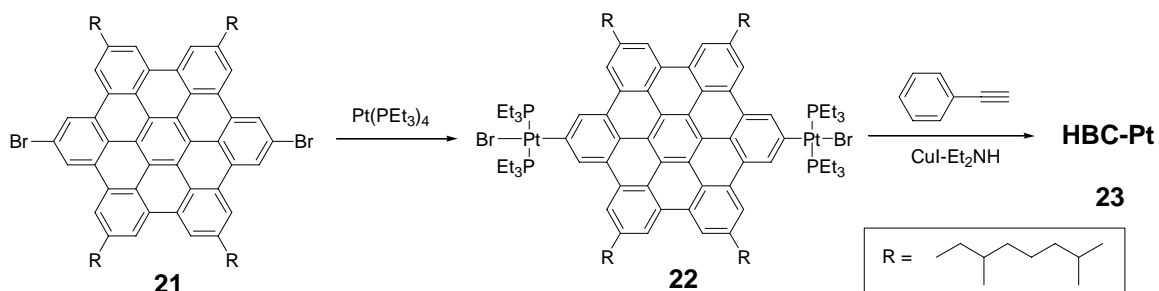


Figure 1: MALDI-ToF spectrum of **21**, calcd: m/z 1241.47 (100%, TCNQ as matrix). Inserted is a comparison of experimental results and simulated isotope distribution.

Examination of the ^1H NMR spectrum of **HBC-Pt (23)** showed that the phenylacetylene unit had been successfully incorporated by covalent bonding on to the platinum. Two broad signals and one triplet centered near 7.4 and 7.1 ppm respectively, were assigned to the protons of the phenyl (α -acetylene) moiety. (Figure 3)



Scheme 1: Synthesis of 2,11-bis[trans-bis(triethylphosphine)-(phenylethynyl)platinum]-5,8,14,17-tetrakis(3,7-dimethyloctyl)hexa-peri-hexabenzocoronene (**23**).

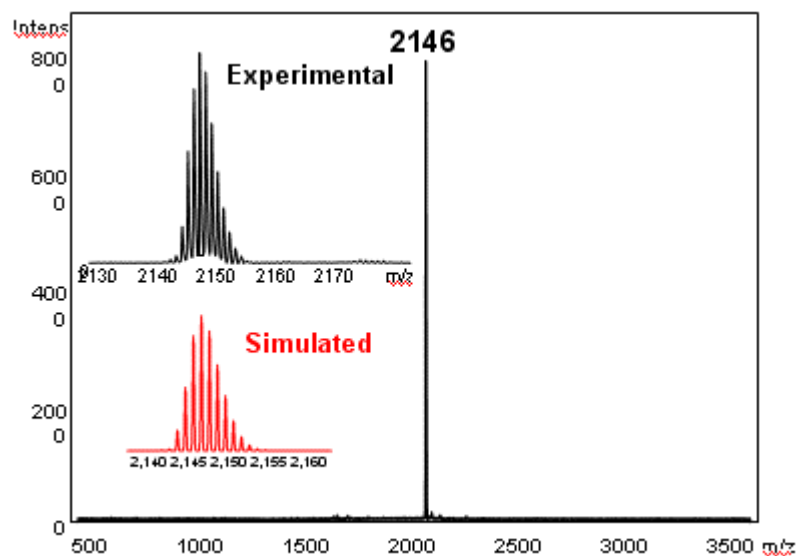


Figure 2: Maldi-Tof spectrum of complex **23**, an inset showing the experimental isotopic distribution in the top and the simulated isotopic distribution in the bottom.

A high resolution MALDI-MS spectrum for compound (**23**) was obtained after a solid-state sample preparation method. The spectrum revealed a single species with isotopic distribution in accord with its simulation (Figure 2).

$^{31}\text{P}\{^1\text{H}\}$ analysis of the final product (**23**) shows the formation of a single highly symmetrical species by the appearance of a sharp singlet with concomitant ^{195}Pt satellites (Figure 4). The small shift in the position of the phosphorous resonance in comparison to **HBC-Pt (22)** (1.854 ppm) is expected due to the exchange of the bromine with a π -conjugated group (figure 4) where $^1J_{\text{Pt-P}} = 1303.1$ Hz ($^1J_{\text{Pt-P}} = 1370.3$ Hz for **HBC-Pt (22)**). Maldi-tof, ^1H and $^{31}\text{P}\{^1\text{H}\}$ NMR measurements are in agreement with the phenyl-acetylene-platinum bonding on the HBC core (Figure 3 and 4).

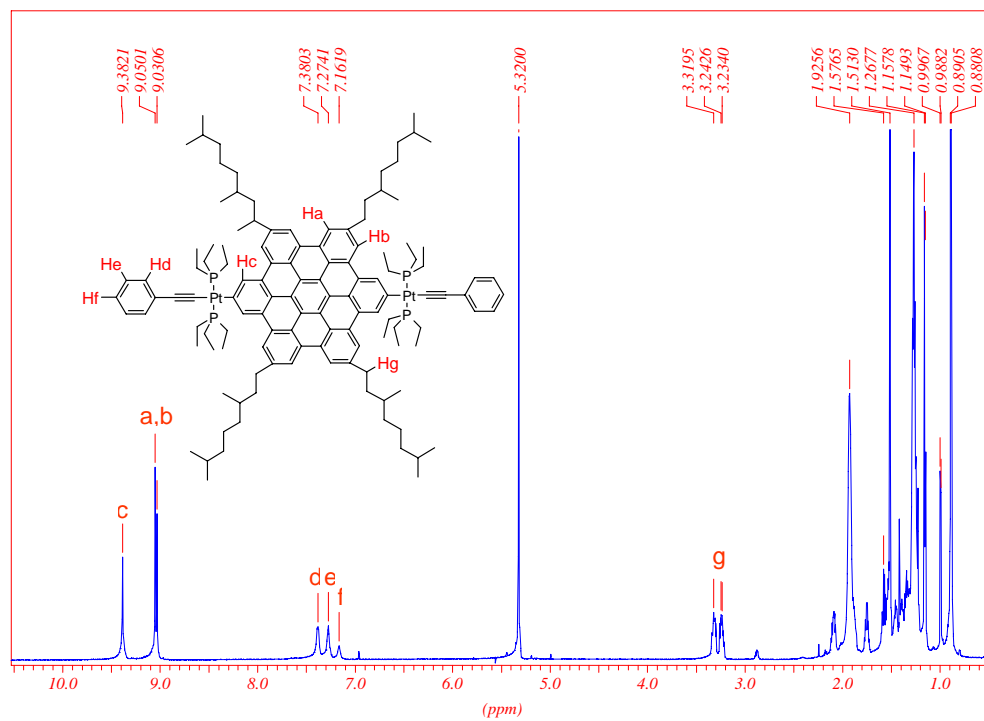


Figure 3: ^1H NMR spectrum of compound (23), an inset shows the molecule including differently labeled protons as correlated to the different peaks in the spectrum.

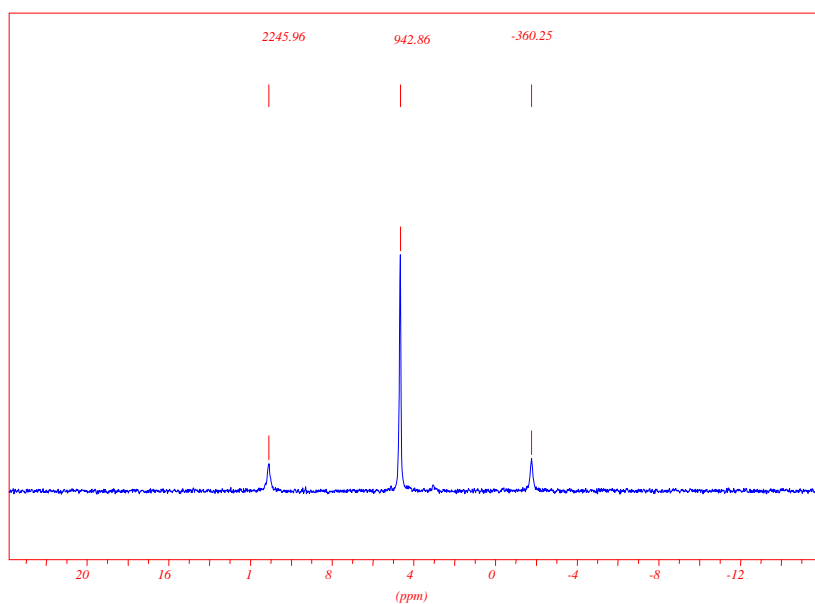


Figure 4: $^{31}\text{P}\{^1\text{H}\}$ spectrum of compound (23), showing a singlet at 4.65 ppm and the two ^{135}Pt satellites at -1.779 and 11.09 ppm respectively (triphenylphosphine as standard).

2.3 Photophysical properties

Steady-state UV-VIS absorption and photoluminescence spectra of both HBC compounds recorded in THF solutions are depicted in figure 5. The absorption spectrum of **HBC-Pt (23)** showed a slight red-shift (0.05 eV) compared to that of **HBC-C_{8,2} (24)** (Figure 5), indicating that π -conjugation of the HBC extends into the phenylacetylene sites through the platinum centers. The forbidden low energy α -band which was observed in the six-fold symmetric **HBC-C_{8,2} (24)** now appeared at 2.79 and 2.97 eV due to the symmetry breaking in **HBC-Pt (23)** and possibly a mixture with metal-to-ligand charge transfer (MLCT) transitions.¹¹

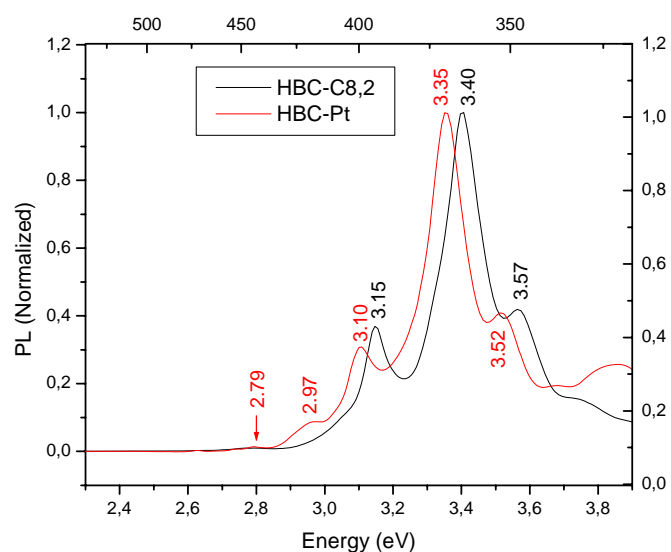


Figure 5: UV-Vis Absorption spectra of **HBC-C_{8,2} (24)** (black) and **HBC-Pt (23)** (red) in THF($1.0 \times 10^{-6} M$)

Cyclic voltammetry measurements on **HBC-Pt (23)** disclosed one reversible oxidation wave at 0.34V (vs Fc^+/Fc) for four-electron oxidations at the platinum centers (Figure 6), and the lack of stepwise oxidation indicated that the electron coupling through the large HBC spacer is

weak.¹⁶ A step wise multi-electron oxidation process was distinguished by DPV measurements.

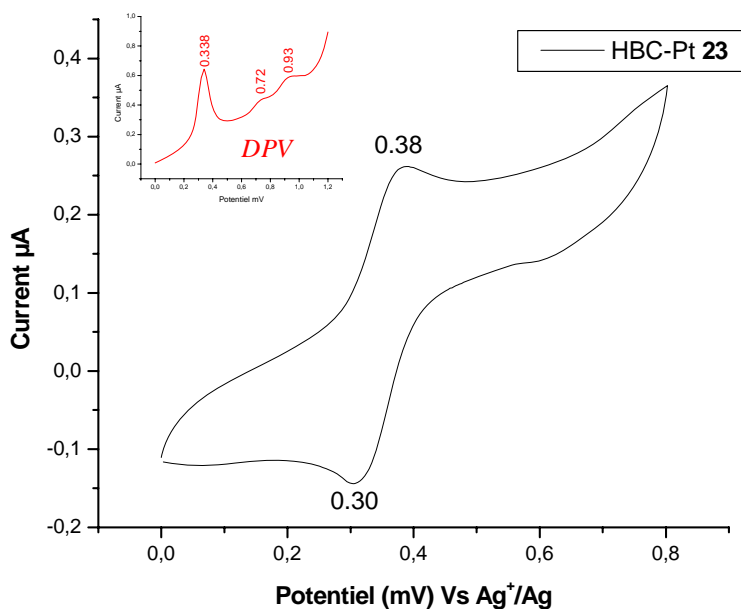


Figure 6: Cyclic voltammogram and inset differential pulse voltammogram of **HBC-Pt (23)** in CD_2Cl_2 and 0.1 M tetrabutylammonium hexafluorophosphate

Photoluminescence of both compounds (**23**) and (**24**) was measured in carefully degassed 2-methyl-tetrahydrofuran (MTHF) solutions at room temperature and 77 K using time-resolved photoluminescence spectroscopy (This measurement was done Dr. Frederik Laquai and Dr. Stanislav Balushev). As shown in Figure 7, time delayed photoluminescence measurements at room temperature on **HBC-C_{8,2} (24)** revealed delayed emission with the band structure and positions very similar to that of the prompt fluorescence. Thus, this band can be safely assigned to delayed fluorescence (DF) from the singlet state (S_1) which usually arises from triplet-triplet annihilation (TTA) as found in other π -conjugated polymers and organic crystals.¹

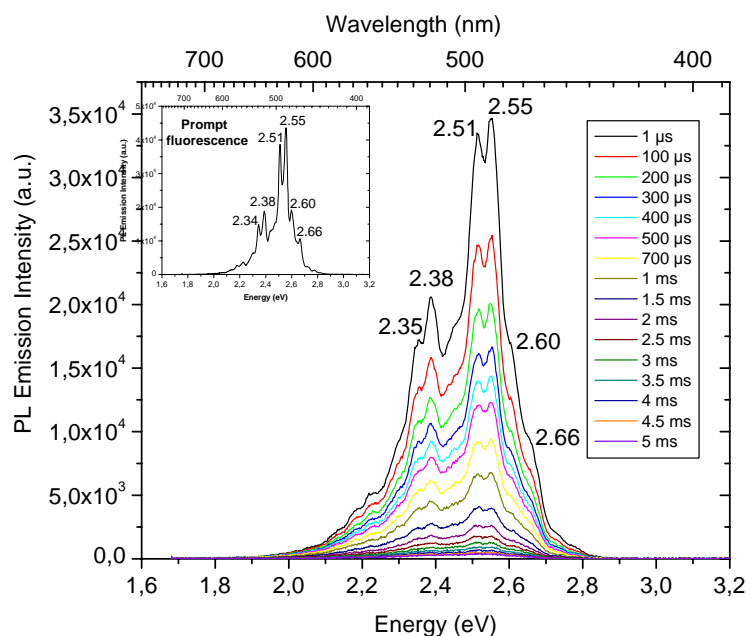


Figure 7: Time-resolved delayed fluorescence spectrum of **HBC-C_{8,2} (24)** at 296K (10 μ s gate). Inset is the prompt fluorescence spectrum at 296 K.

A complex spectrum with bands having main vibronic splittings of 40~50 meV was observed between 2.0 eV and 2.75 eV in both fluorescence and delayed fluorescence spectra due to the high symmetry of the compound which results in several forbidden transitions in the D_{6h} symmetric **HBC-C_{8,2} (24)**. Differences in shape of the delayed fluorescence spectrum with respect to the prompt (no delay time between excitation and acquisition) fluorescence spectrum result from the different sensitivity of the spectrometer setup that was used since DF is orders of magnitude weaker than prompt fluorescence. Figure 8 shows the decay kinetics of the delayed fluorescence in semi-logarithmic representation. The integration window was kept significantly smaller than the delay time, thus the true decay kinetic is observed. At longer delay times the DF decay approaches a single exponential decay with a lifetime of $\tau = 1.5$ ms indicating that the majority of triplet decay nonradiatively via the monomolecular decay channel at room temperature.

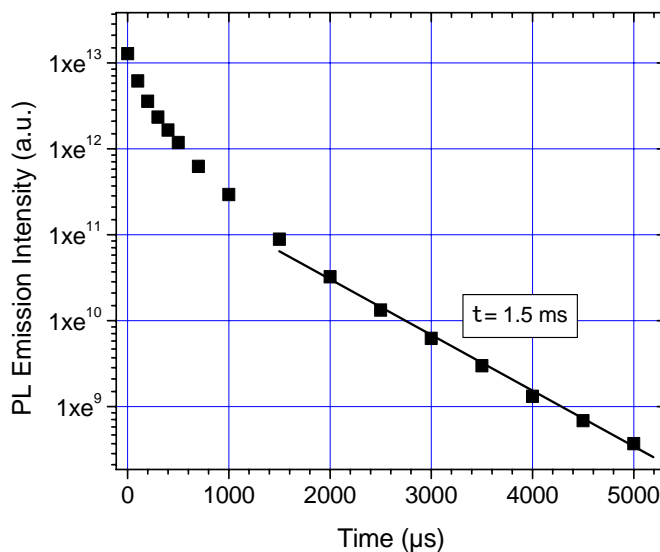


Figure 8: Delayed fluorescence decay of **HBC-C_{8,2} (24)** in dilute solution at room temperature in a semi-logarithmic plot. The line is a guide to the eye which indicates a lifetime of the DF of $\tau = 1.5 \text{ ms}$.

Long-range delayed photoluminescence measurements on **HBC-C_{8,2} (24)** at 77 K in highly diluted ($10 \mu\text{g/ml}$) frozen MTHF matrix revealed another well-resolved emission with its highest energy band at 2.16 eV and its maximum intensity centered at 1.98 eV (Figure 9a). This band is red-shifted compared to the fluorescence spectrum with a similar vibronic splitting (40~50 meV) and showed a mono-exponential decay with a long lifetime of $\tau = 8.9 \text{ s}$ after an initial faster decay probably caused by increased triplet-triplet-annihilation at high triplet concentrations (Figure 9b). This emission is assigned to phosphorescence from the T_1 state. The S_1 - T_1 energy gap is about 0.5 eV, which is smaller than the typically observed value of around 0.7 eV for aromatic hydrocarbons and 1.0 eV for organic crystals.^{1,2} It is interesting to note that the highest energy band of the phosphorescence is considerably smaller in intensity than the emission band at 1.98 eV indicating that the 0-0 transition from the first excited triplet state to the singlet ground state is less allowed than the lower energy transition. The lack of delayed fluorescence in the long time-range (spectrum after 100 ms) implies that DF has

already decayed in this time region. This is reasonable if one assumes that DF is caused by TTA and can only occur if two triplets occupy one disc. Hence, in the long time-delay the majority of triplets decay via the monoexponential decay channel, i.e. via phosphorescence or non-radiative deactivation.

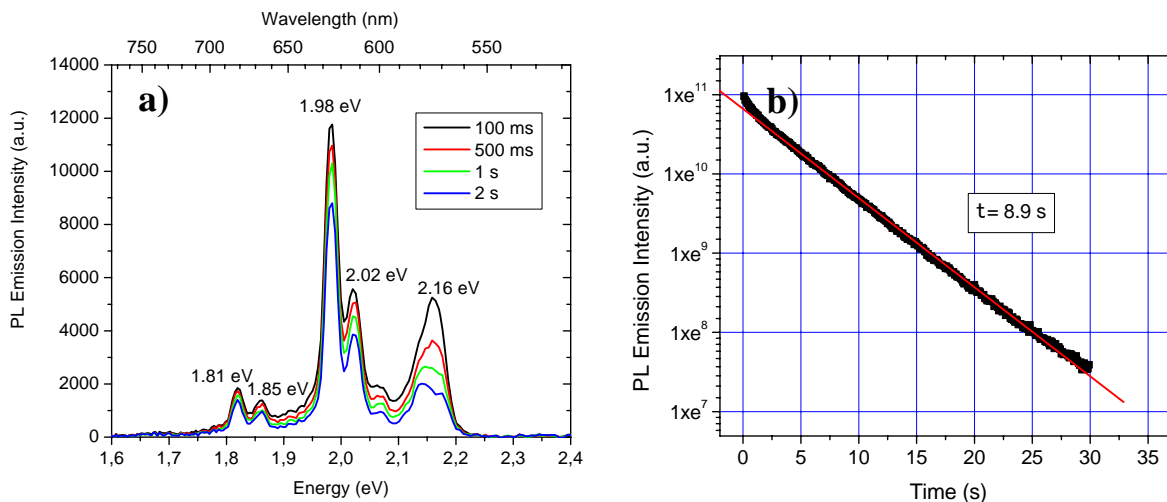


Figure 9: a) Plot phosphorescence spectrum in MTHF ($1.0 \times 10^{-6} M$) at 77K (10 ms gate) for **HBC-C_{8,2} (24)** and b) The phosphorescence decay plot and its corresponding life time.

This result also suggests a more efficient triplet emission from the large PAH molecules such as HBCs compared to other small hydrocarbon polymers or oligomers, in which usually both delayed fluorescence and phosphorescence can be observed at low temperature. The rigid planar and defect-free structure in the disc-like HBC molecules may decrease the non-radiative decay rates in comparison with other conjugated oligomers and polymers and increase the intersystem crossing.^{2a}

The **HBC-Pt (23)** complex showed a strong well-resolved emission band with its maximum intensity at 2.15 eV and a main vibronic splitting of 30~50 meV (Figure 10) in dilute solution at room temperature. All peaks displayed approximately mono-exponential decays with their lifetime being around 3.1 ms (Figure 12). Therefore, this band was assigned

to phosphorescence from the T_1 state. Since triplet states are highly sensitive to the presence of oxygen the MTHF was purified by refluxing over sodium for several days and successively degassed by five freeze-pump-thaw cycles. All solutions were prepared under glove box conditions and filled into sealed cuvettes for spectroscopical characterization. We have found that simple degassing of the solution by purging with argon leads to significantly shorter phosphorescence lifetimes (on the order of hundreds of μs) indicating quenching by residual oxygen. This effect decreased if the solutions were frozen since the oxygen diffusion is reduced in the frozen glassy solvent matrix. In comparison to the platinum-free **HBC-C_{8,2}** (**24**), the introduction of the heavy atom Pt dramatically enhanced the spin-orbital coupling and decreased the phosphorescence lifetime of the triplet state by three orders of magnitude. In addition, neither prompt nor delayed fluorescence could be observed, again suggesting a rapid intersystem crossing rate. The room temperature phosphorescence quantum yield (defined as the ratio of the number of photons emitted to the number of photons absorbed) of **HBC-Pt** (**23**) was determined to be $\Phi_{\text{ph}} \approx 1\%$ in toluene solution by plotting the integrated photoluminescence intensity versus the UV/vis absorbance at an excitation wavelength of 360 nm versus diphenylanthracene standard in cyclohexane solution. However, the phosphorescence spectrum of **HBC-Pt** (**23**) shows a remarkable difference if compared with that of **HBC-C_{8,2}** (**24**). The relative intensities of the phosphorescence bands changed dramatically towards the higher energy bands. It can be interpreted as a higher transition probability of the 0-0 phosphorescence band in the **HBC-Pt** (**23**) due to the symmetry breaking effect of the platinum-acetylide sidegroups. This is in good agreement with the observations of Kim et al.⁸ who observed an even stronger relative intensity of the 0-0 emission band in their phosphorescence spectrum, most probably because the symmetry in their compound is even lower (the HBC core bears only one platinum-acetylide substituents) than **HBC-Pt** (**23**).

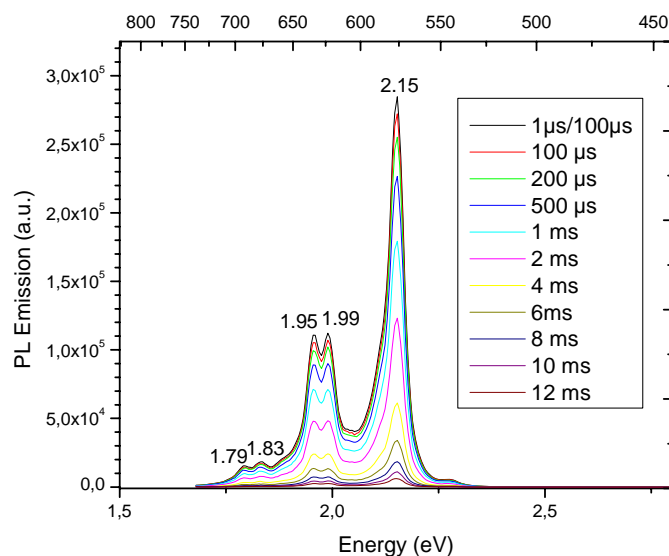


Figure 10: Time-resolved phosphorescence spectra of **HBC-Pt (23)** in MTHF ($1.0 \times 10^{-6} M$) at room temperature.

It is worthy to note that the reported hydrocarbon polymers and oligomers usually showed phosphorescence only at low temperature but rarely at room temperature, while **HBC-Pt (23)** emits phosphorescence at room temperature. When the solution was cooled down to 77 K, an even better resolved phosphorescence spectrum with the highest energy band centered at 2.17 eV was observed (Figure 11). The band exhibited a similar shape however slightly blue shifted as compared to the spectrum at room temperature. All peaks also showed mono-exponential decays with the phosphorescence lifetime being 8.7 ms (Figure 12). The intensity of the phosphorescence at low temperature is higher than that at room temperature. The more resolved structure and longer lifetime at low temperature are reasonable since at room temperature the thermal broadening masks the vibronic structure, the diffusion of the long-lived triplet excitons to quenching sites reduces the lifetime and triplets may be deactivated by collisional quenching with solvent molecules if the MTHF is not frozen.

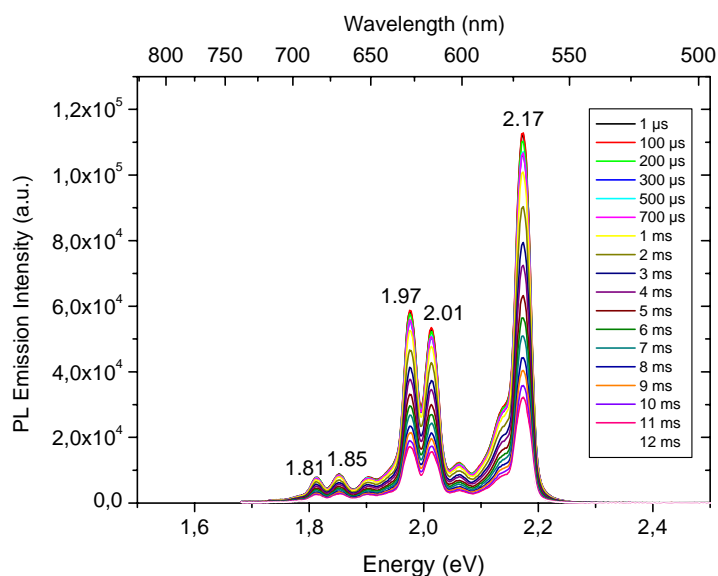


Figure 11: Time-resolved phosphorescence spectra of **HBC-Pt (23)** in *m*-THF ($1.0 \times 10^{-6} M$) at 77K.

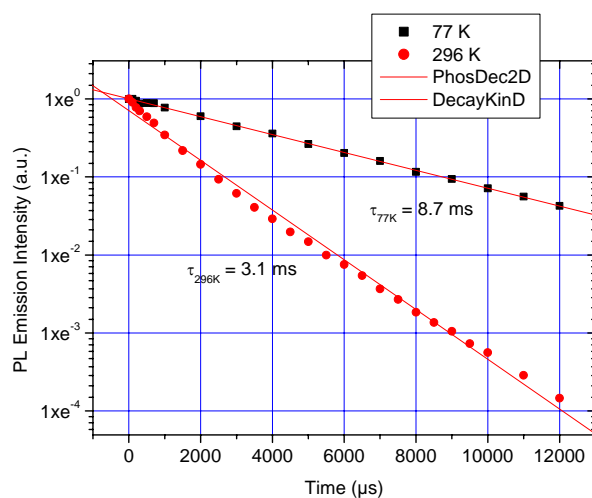


Figure 12: Phosphorescence decay plots for **HBC-Pt (23)** at room temperature and 77K.

2.4 Photoluminescence study of **HBC-Ph-C₁₂ (25)**

Absorption and photoluminescence measurements were conducted on the **HBC-Ph-C₁₂ (25)** yielding different behavior. The slight modification of **(25)** may seem trivial but in fact gives

rise to significant differences in the electronic and physical properties of the assembled materials when compared to **HBC-C_{8,2}** (**24**) and **HBC-Pt** (**23**). In this study, the absorption and photoluminescence spectra were recorded at a concentration of 10^{-6} M. The absorption maximum is around 371 nm for (**25**) and this is probably due to the aggregation effect in solution even at low concentration of about 10^{-6} M as previously reported.¹⁷ Prompt fluorescence measurements displayed the presence of broad signals. The luminescence spectrum for this material clearly shows that there are in fact two species contributing to the luminescence spectrum. The features from 2.1 to 2.6 eV are most likely due to aggregate emission, whereas the features from 2.6 to 3.0 eV can be attributed to the luminescence of *noncoupled(isolated)* molecules (Figure 13).¹⁷

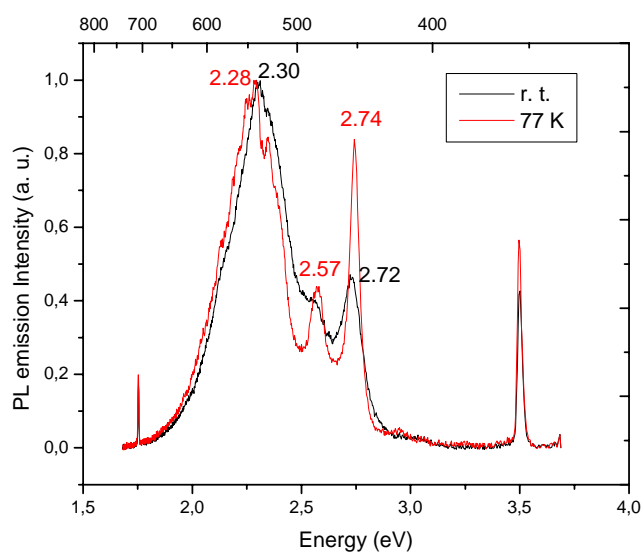


Figure 13: Prompt fluorescence spectrum of **HBC-Ph-C₁₂** (**25**) at room temperature and at 77 K

As shown in Figure 14, time delayed measurements at room temperature and at 77 K on **HBC-Ph-C₁₂** (**25**) revealed photoluminescence with the broad structure and positions similar to that of the prompt fluorescence. We can safely assign it as a delayed fluorescence from the first excited state (S_1) to the ground state (S_0) probably through a triplet-triplet annihilation process.

Several experiments toward visualization of low energy phosphorescence bands (if present) yielded only delayed fluorescence (DF). It seems that two probable mechanisms could take place, (i) triplet-triplet annihilation from yielding DF (The process in which the first excited singlet state is populated by interaction of two molecules in the triplet state thus producing one molecule in the singlet excited state), and (ii) non-radiative decay emission through the vibronic excited levels (internal conversion). At 77 K, we can see more vibronic splitting which is probably due to the decrease in the mobility of the disk molecules in the aggregates at low temperature and may favor the formation of an excimer electronic band.

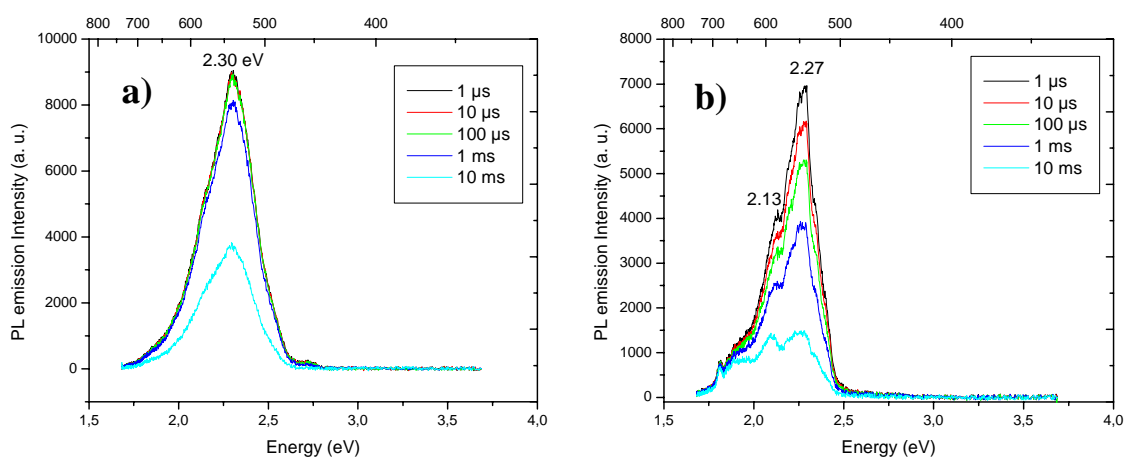


Figure 14: Time-resolved delayed fluorescence spectra of **HBC-Ph-C₁₂ (25)** a) at room temperature and b) 77 K.

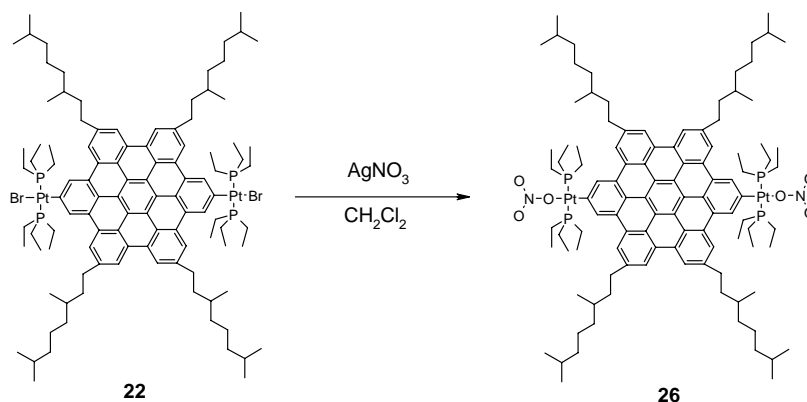
2.5 In-Solution HBC supramolecular chemistry

Metal-directed supramolecular self-assembly is a rapidly growing field, and recent years have witnessed enormous research activity in this area.¹⁸ This methodology has allowed the preparation of structurally well-defined grids, honeycombs, and cages.¹³ Among these, cages

have attracted much attention as a result of their important properties such as molecular recognition, inclusion phenomena, and catalysis.¹⁹ In metal-directed self-assembly, the simple combination of linkers owing 90° linkers in a 2:2 ratio to give cage molecules depends upon the size, bonding angles and rigidity of the building blocks.

The use of transition metals and coordination-based design allows the formation of a variety of self-organized nanosystems in a few highly convergent synthetic steps. The chemical bonding of the subunits must be relatively weak, thermodynamically stable, yet kinetically labile to allow the self-rearrangement of the subunits within the entire structure. A simple and general concept for generating ordered structures is based on the recognition-driven spontaneous assembly of complementary subunits. Since transition metals have co-ordination sites with specific geometries that depend upon their electronic structure they can serve as acceptor subunits. These can be linked together *via* donor building blocks that form the rigid frame of the assembled entity.²⁰

The synthesis of **HBC-Pt (22)** as depicted previously in Scheme 2, was carried out by twofold oxidative addition of $\text{Pt}(\text{PEt}_3)_4$ at 60°C in toluene for 40 hours. Later on, the bromine atoms of the latter precursor (**22**) were exchanged for more labile nitrates by reaction with AgNO_3 (Scheme 3). The resulting **ONO₂-Pt-HBC (26)** was isolated as a yellow crystalline compound, stable in air at room temperature. Characterization was carried out using ^1H , and $^{31}\text{P}\{^1\text{H}\}$ NMR spectroscopy.



Scheme 3: Synthesis of HBC-Pt-ONO₂ Complex (**26**)

Four equivalent phosphorus atoms in the molecule give rise to a sharp singlet at 13.46 ppm in the $^{31}\text{P}\{^1\text{H}\}$ spectrum, with accompanying ^{195}Pt satellites at 20.53 and 6.43 ppm respectively. The 8.81 ppm chemical shift difference from the precursor (**22**) towards low field indicates the coordination of the platinum to the nitrate group (Figure 15).

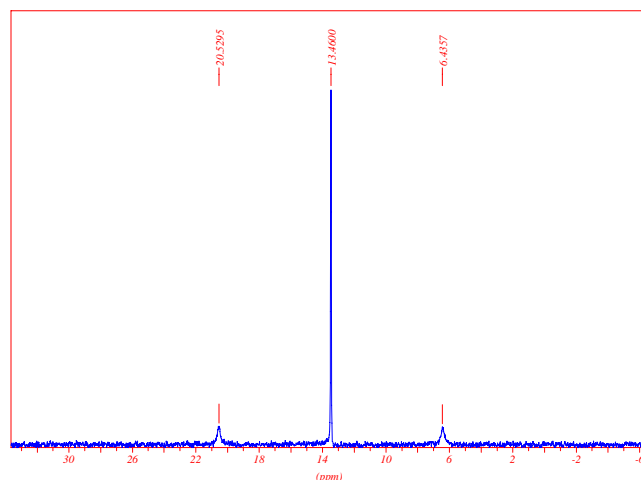
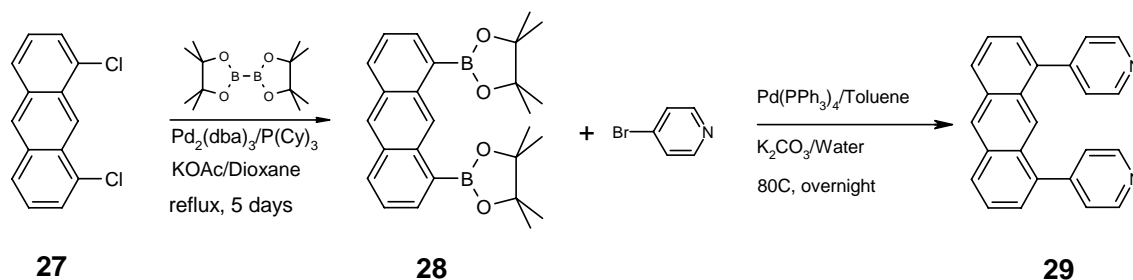


Figure 15: $^{31}\text{P}\{^1\text{H}\}$ NMR spectrum of HBC-Pt-ONO₂ (**26**)

Certain self-assembled structures call for the use of rigid tectons that have a 5-10° (or close) dihedral angle between their coordination vectors (pyridyl units and anthracene). The sole representative of this interesting class of compounds to date is the anthracene-based clip.¹⁵

Scheme 2 shows the synthesis of a complementary, pyridine-containing "clip" from 1,8-dichloroanthracene (**27**) converted to 1,8-bispyridylanthracene (**29**) in two steps.



Scheme 2: synthesis of 1,8-bispyridylanthracene (**29**)

Palladium catalyzed electrophilic substitution of the chlorine atoms of (**27**) with boronic ester pinacolates in refluxed dioxane afforded (**28**). The crude product was purified by column chromatography on silica gel using dichloromethane/hexane followed by dichloromethane to afford 60% pure compound. The latter reaction was followed by a Suzuki cross-coupling with 4-bromopyridine in toluene at 80 °C to yield the final compound (**29**) in 65 % yield after chromatographic workup with dichloromethane/triethylamine as eluents. The ^1H NMR spectrum is shown in Figure 16. The structural feature makes this molecule suited for supramolecular assembly as a donor clip by its coordination vectors which are not totally parallel to each other as the dihedral angle between the 4-pyridyl groups is around 5° but not flexible as 1,8-bis(4-pyridylethynyl)anthracene previously published¹⁵ where the dihedral angle is around 11° . The X-ray structure of 1,8-bispyridylanthracene (**29**) is shown in figure 17.

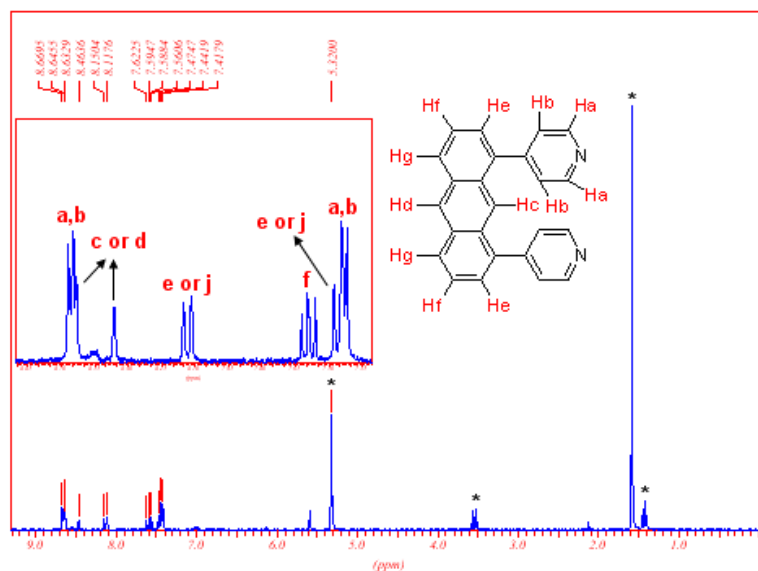


Figure 16: ^1H NMR of 1,8-bispyridylanthracene (**29**).

Herein, an effort for the above described combinational approach toward the synthesis of supramolecular cage was made by mixing the anthracene (**29**) and the HBC (**26**) units (2:2 ratio) in deuterated acetone and deuterated acetone/water mixtures but unfortunately all failed. The ^1H NMR spectrum did not show change but only the presence of the adducts similarly to the original spectra. Electro-spray mass spectroscopy did not provide any complex formation or any doubly-charged related complex.

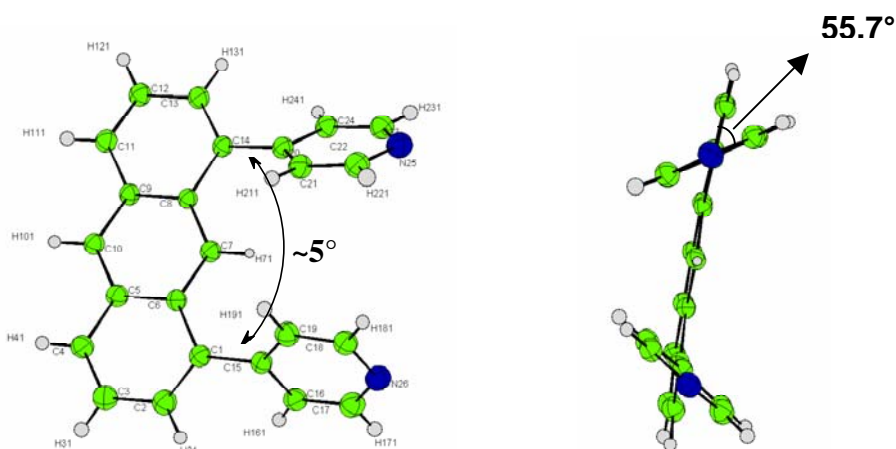


Figure 17: ORTEP representation of the X-ray structure of 1,8-bispyridylanthracene (**29**).

2.6 Summary

In conclusion, double phenyl-acetylene platinum substituted HBC materials were facilely synthesized via copper catalyzed cross coupling based on dibromo-HBC building block. Time-resolved photoluminescence measurements on the large polycyclic aromatic platinum complex **HBC-Pt (23)** visualized phosphorescence emission at low and room temperature whereas **HBC-C_{8,2} (24)** showed radiative triplet emission only at low temperature. In contrast, **HBC-Ph-C₁₂ (25)** yielded no triplet emission from the triplet excited state, neither at room temperature nor at 77K. This indicated that the inter-system crossing rate from the singlet excited state to the triplet excited was enhanced due to the spin-orbit coupling influenced by the presence of the platinum heavy metal. The rich family of large PAHs allows us to exploit the photophysics of other members and their complexes with different heavy metals in the future. Moreover, the fast charge transporting properties in large PAHs²¹ could also open the possibility of using the PAH-metal complexes as both the triplet emitting centers as well as charge transporting materials.

¹ a) M.A. Baldo, D.F. O'Brien, M.E. Thompson, S.R. Forrest, *Phys. Rev. B* **1999**, *60*, 14422; b) J.S. Wilson, A.S. Dhoot, A.J.A.B. Seeley, M.S. Khan, A. Köhler, R.H. Friend, *Nature* **2001**, *413*, 828; c) M. Pope, C. E. Swenberg, *Electronic Processes in Organic Crystals and Polymers* (Oxford University Press, Oxford 1999).

² a) J. S. Wilson, N. Chawdhury, M. R. Al-Mandhary, M. Younus, M. S. Khan, P. R. Raithby, A. Köhler, R. H. Friend, *J. Am. Chem. Soc.* **2001**, *123*, 9412; b) D. Beljonne, Z. Shuai, G. Pourtois, J. L. Brédas, *J. Phys. Chem. A* **2001**, *105*, 3899; c) Y. V. Romanovskii, A. Gerhard, B. Schweitzer, U. Scherf, R. I. Personov, H. Bässler, *Phys. Rev. Lett.* **2000**, *84*, 1027.

³ a) Y. Liu, S. Jiang, K. Glusac, D. H. Powell, D. F. Anderson, K. S. Schanze, *J. Am. Chem. Soc.* **2002**, *124*, 12412; b) J. S. Wilson, A. Köhler, R. H. Friend, M. K. Al-Suti, M. R. A. Al-Mandhary, M. S. Khan, P. R. Raithby, *J. Chem. Phys.* **2000**, *113*, 7627; c) N. Chawdhury, A. Köhler, R. H. Friend, W.-Y. Wong, J. Lewis, M. Younus, P. R. Raithby, T. C. Corcoran, M. R. A. Al-Mandhary, M. S. Khan, *J. Chem. Phys.* **1999**, *110*, 4963; d) D. Beljonne, H. F. Wittmann, A. Köhler, S. Gram, M. Younus, J. Lewis, P. R. Raithby, M. S. Khan, R. H. Friend, J. L. Brédas, *J. Chem. Phys.* **1996**, *105*, 3868; e) C.-H. Tao, N.-Y. Zhu, V. W.-W. Yam, *Chem. Eur. J.* **2005**, *11*, 1647.

- ⁴ a) W. Lu, H.-F. Xiang, N.-Y. Zhu, C.-M. Che, *Organometallics* **2002**, *21*, 2343 ; b) C.-M. Che, H.-Y. Chao, V. M. Miskowski, Y.-Q. Li, K.-K. Cheung, *J. Am. Chem. Soc.* **2001**, *123*, 4985.
- ⁵ a) W.-Y. Wong, L. Liu, J.-Y. Shi, *Angew. Chem. Int. Ed.* **2003**, *42*, 4064; b) W.-Y. Wong, L. Liu, S.-Y. Poon, K.-H. Choi, K.-W. Cheah, J.-X. Shi, *Macromolecules* **2004**, *37*, 4496.
- ⁶ a) A. Zweig, J. B. Gallivan, *J. Am. Chem. Soc.* **1969**, *91*, 260-264; b) A. Zweig, J. E. Lancaster, M. T. Neglia, *Tetrahedron* **1967**, *23*, 2577.
- ⁷ a) *Polycyclic Aromatic Hydrocarbons*, R. G. Harvey, Wiley-VCH, New York, **1997**; b) *The Aromatic Sextet*, E. Clar, Wiley-VCH, London, **1972**; c) R. J. Bushby, O. R. Lozman, *Curr. Opin. Solid. State Mater. Sci.* **2002**, *6*, 569.
- ⁸ K.-Y. Kim, S. Liu, M.E. Köse, K.S. Schanze, *Inorg. Chem.* **2006**, *45*, 2509.
- ⁹ a) D. Hertel, S. Setayesh, H.-G., Nothofer, U. Scherf, K. Müllen, H. Bässler, *Adv. Mater.* **2001**, *13*, 65; b) J. Partee, E. L., Frankevich, B. Uhlhom, J. Shinar, Y. Ding, J. T. Barton, *Phys. Rev. Lett.* **1999**, *82*, 3673; c) F. Laquai, C. Im, A. Kadashchuk, H. Bässler, *Chem. Phys. Lett.* **2003**, *375*, 286.
- ¹⁰ N. Chawdhury, A. Köhler, R. H. Friend, W.-Y. Wong, J. Lewis, M. Younus, P. R. Raithby, T. C. Corcoran, M. R. A. Al-Mandhary, M. S. Khan, *J. Chem. Phys.* **1999**, *110*, 4963.
- ¹¹ a) C. D. Simpson, J. Wu, M. D. Watson, K. Müllen, *J. Mater. Chem.* **2004**, 494; b) M. D. Watson, A. Fechtenkötter, K. Müllen, *Chem. Rev.* **2001**, *101*, 1267.
- ¹² A. Fechtenkötter, N. Tchebotareva, M. D. Watson, K. Müllen, *Tetrahedron* **2001**, *57*, 3769.
- ¹³ D. Wasserfallen, I. Fischbach, N. Chebotareva, M. Kastler, W. Pisula, F. Jaeckel, M. D. Watson, I. Schnell, J. P. Rabe, H. W. Spiess, K. Muellen, *Adv. Funct. Mater.* **2005**, *15*, 1585.
- ¹⁴ E. Clar, C. T. Ironside, *Proc. Chem. Soc.* **1958**, 150.
- ¹⁵ Y. K. Kryshenko, S. R. Seidel, D. C. Muddiman, A. I. Nepomuceno, P. J. Stang, *J. Am. Chem. Soc.* **2003**, *125*, 9647.
- ¹⁶ M. Sato, E. Mogi, M. Katada, *Organometallics* **1995**, *14*, 4837.
- ¹⁷ A. J. Fleming, J. N. Coleman, A. B. Dalton, A. Fechtenkötter, M. D. Watson, K. Müllen, H. J. Byrne, and W. J. Blau, *J. Phys. Chem. B* **2003**, *107*, 37.
- ¹⁸ a) S. Leininger, B. Olenyuk, P. J. Stang, *Chem. Rev.* **2000**, *100*, 853; b) D. L. Caulder, K. N. Raymond, *Acc. Chem. Res.* **1999**, *32*, 975.
- ¹⁹ a) M. Fujita, D. Ogura, M. Miyazawa, H. Oka, K. Yamaguchi, K. Ogura, *Nature* **1995**, *378*, 469; b) R. S. Meissner, J. D. Mendoza, J. Rebek, *Science* **1995**, *270*, 1485; c) J. Kang, J. Rebek, *Nature* **1997**, *385*, 50.
- ²⁰ a) B. Olenyuk, A. Fechtenkötter, P. J. Stang, *J. Chem. Soc.-Dalton Trans.* **1998**, 1707; b) B. Olenyuk, J. A. Whiteford, A. Fechtenkötter, P. J. Stang, *Nature* **1999**, *398*, 796.
- ²¹ A. M. van de Craats, J. M. Warman, A. Fechtenkötter, J. D. Brand, M. A. Harbison, K. Müllen, *Adv. Mater.* **1999**, *11*, 1469.

Chapter 3

*Self-assembly of amphiphilic hexa-*peri*-hexabenzocoronenes into nanostructures*

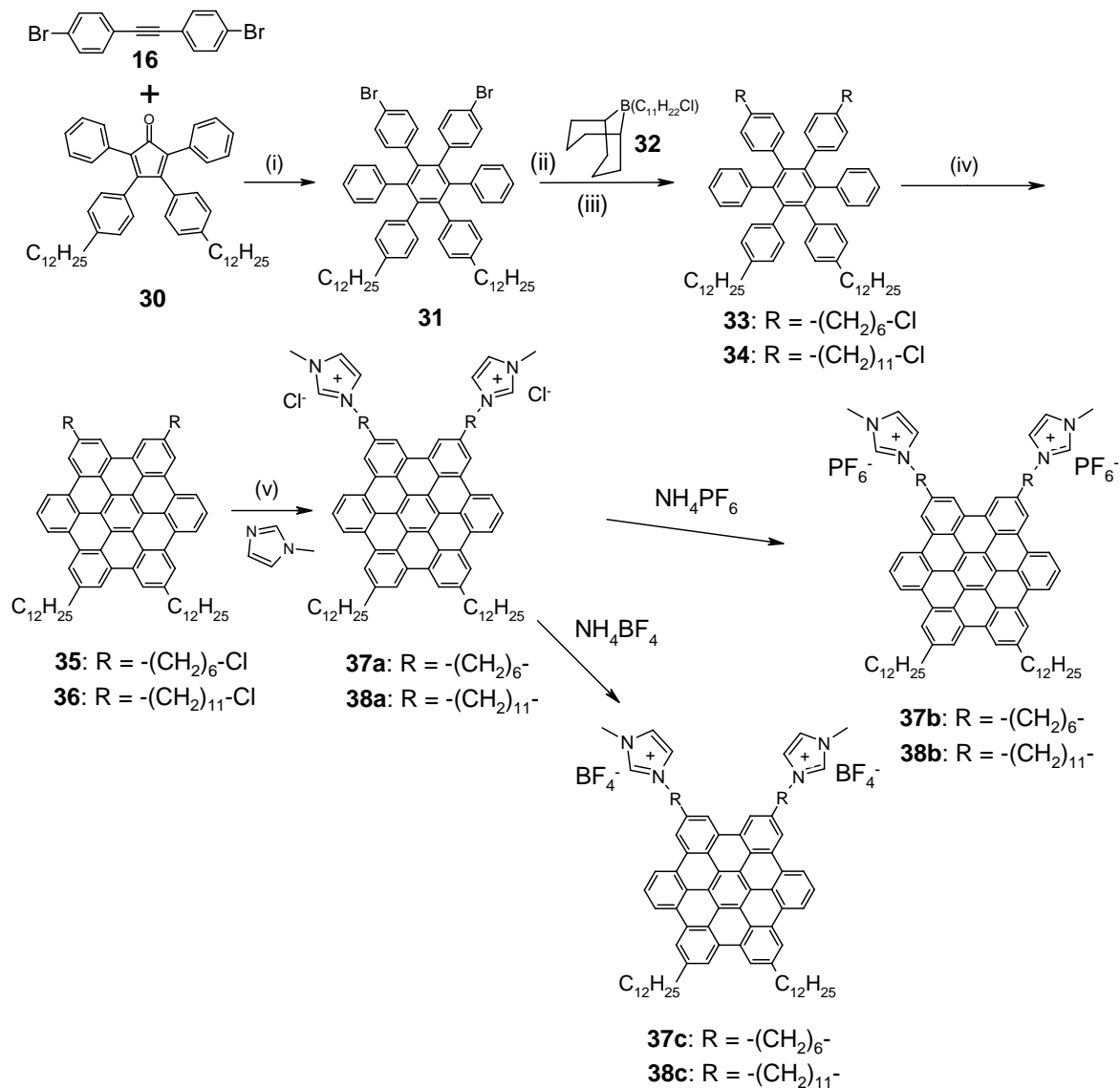
In this chapter, the synthesis of novel amphiphilic hexa-*peri*-hexabenzocoronenes is described. Solid-state wide-angle X-ray scattering (WAXS) of extruded fibers of these amphiphilic molecules revealed the formation of lamellar columnar structures. The self-assembly behavior in solution and in drop-cast thin-films was studied. On surfaces, scanning electron microscopy (SEM) and transmission electron microscopy (TEM) disclosed rod-like and fiber-like nanostructures, depending on the HBC's chemical structure and the solution processing conditions.

3.1 Introduction

Self-assembly is a valuable tool for building complex architectures on the nanoscale.¹ Non-covalent interactions such as hydrogen bonding, electrostatic (ion-ion and ion-dipole) interactions, van der Waals interactions, and hydrophobic-hydrophilic effects are used to construct nanofibers.² These combined interactions are fundamental for the future development of devices based on nanostructured organic materials,³ where long range order, high charge carrier mobilities and processability are prerequisites.⁴ Fibers⁵ have been reported, but the control of their shape and size is a big challenge.^{6,7} Hydrogen-bond interactions are one of the driving forces for the formation of ordered materials. Bis-urea functionalized oligothiophene derivatives were amenable to induce intermolecular hydrogen bonding and thereby provided a

framework for the formation of fibers.⁸ Furthermore, π -conjugated oligo(phenylenevinylene) generated hexameric conjugated "rosettes" that self-assembled in a chiral tubular fashion to give materials that can be used for opto-electronic purposes.⁹ In addition, disc-like molecules such as hexa-*peri*-hexabenzocoronene (HBC) have been considered as potentially useful materials¹⁰ because of their high charge carrier mobility along the self-assembled columns¹¹ and their pronounced aggregation in solution.^{12,13,14} Among them, water-soluble HBCs, in which the discotic core is substituted by six hydrophilic branched ethylene glycol chains, have been reported.^{14,15} The enhanced phase separation found in such systems induced strong self-assembly of the discs in both the solid-state and in solution. Aida's group recently reported an amphiphilic HBC molecule with C_{2v} symmetry that self-assembled into uniform nanotubes.¹⁶ Furthermore these nanotubes were cross-linked to form bundles via metathesis of the vinylene-ended TEG chains to enhance their robustness.¹⁷ Similar to ethylene glycol chains, imidazolium salts are also water solubilizing agents.¹⁸ They support the solubilization of hydrophobic entities in polar solvents. The functionalization of the HBC molecules with imidazolium salts has advantages over the "ethylene glycol" approach. One benefit is that the counter-ion can be easily exchanged and its effect on the supramolecular architecture either in bulk or in solution can be probed. Moreover, the presence of positive charges on the imidazolium units would favor the coupling of the HBC-imidazolium with other ionic species such as DNA. The formation of HBC-DNA complex would open an avenue toward materials that have electronic and optical properties for potential applications such as one-dimensional semiconductors and field effect transistors as well as gene delivery applications.¹⁹ Finally, the presence of hydrophobic and hydrophilic subunits would allow for the formation of nanostructures and improve the nanophase separation.

substitution reaction of *N*-methylimidazole with the chlorine atom yielding the final compounds 2,5-bis[6-(3-methyl-1-imidazoliumyl)]-11,14-didodecylhexa-*peri*-hexabenzocoronene dichloride (**37a**) and 2,5-bis[11-(3-methyl-1-imidazoliumyl)]-11,14-didodecylhexa-*peri*-hexabenzocoronene dichloride (**38a**) (Scheme 1).



Scheme 1: Synthesis 2,5-bis[6-(3-methyl-1-imidazoliumyl)]-11,14-didodecylhexa-*peri*-hexabenzocoronene dichloride (**37a**), 2,5-bis[6-(3-methyl-1-imidazoliumyl)]-11,14-didodecylhexa-*peri*-hexabenzocoronene bis(hexafluorophosphate) (**37b**), 2,5-bis[6-(3-methyl-

1-imidazoliumyl)]-11,14-didodecylhexa-*peri*-hexabenzocoronene bis(tetrafluoroborate) (**37c**), 2,5-bis[11-(3-methyl-1-imidazoliumyl)]-11,14-didodecylhexa-*peri*-hexabenzocoronene dichloride (**38a**), 2,5-bis[11-(3-methyl-1-imidazoliumyl)]-11,14-didodecylhexa-*peri*-hexabenzocoronene bis(hexafluorophosphate) (**38b**), 2,5-bis[11-(3-methyl-1-imidazoliumyl)]-11,14-didodecylhexa-*peri*-hexabenzocoronene bis(tetrafluoroborate) (**38c**), (i) *diphenylether*, reflux, 60% (ii) *11-chloroundecene*, 9-BBN, K_2CO_3 , $PdCl_2(dppf)$, 60% (iii) (*6-chlorohexyl*) zinc (II) bromide, $PdCl_2(dppf)$, 56% (iv) $FeCl_3$, CH_3NO_2 , CH_2Cl_2 51% and 55% for **35** and **36** respectively (v) 135 °C, quantitative yields.

The synthesis of the substituted tetraphenylcyclopentadienone (**30**) was done according to the literature.²⁰ A subsequent Diels-Alder reaction between **30** and bis(4-bromophenyl)acetylene (**16**) via [4+2] cycloaddition in refluxing diphenyl ether yielded 1,2-bis(4-bromophenyl)-3,6-diphenyl-4,5-bis(4-dodecylphenyl)benzene (**31**) as a colorless solid in 60% yield. First hydroboration of 11-chloroundecene with 9-borabicyclo[3.3.1]nonane (9-BBN) in THF at room temperature, overnight, gave the corresponding intermediate organoborane (**32**) which was then directly used in the subsequent Pd-catalyzed Suzuki cross-coupling reaction with **31** to afford 1,2-bis(4-[11-chloroundecyl]phenyl)-3,6-diphenyl-4,5-bis(4-dodecylphenyl)benzene (**34**) as a colorless waxy material in 60% yield. Alternatively, 6-chlorohexene was coupled to the HPB core (**31**) through Pd-catalyzed Negishi type cross-coupling reaction, whereby 1,2-bis(4-[6-chlorohexyl]phenyl)-3,6-diphenyl-4,5-bis(4-dodecylphenyl)benzene (**33**) was obtained as a colorless waxy solid in 56% yield. The cyclodehydrogenation reaction was achieved by adding a solution of $FeCl_3$ in nitromethane to solutions of precursors **33** and **34** in dichloromethane to afford the corresponding hexa-*peri*-hexabenzocoronenes **35** and **36** in 51% and 55% yields, respectively.

The second synthetic key step was the addition of the imidazolium functionality. HBC- C_6Cl (**33**) or HBCC₁₁Cl (**34**) was mixed with an excess of liquid *N*-methylimidazole and

heated to 135 °C overnight. After precipitation with hexane and washing with dichloromethane, the final compounds HBCC₆-Imd (**37a**) and HBCC₁₁-Imd (**38a**) were obtained as waxy orange materials in quantitative yields. Later, **37a** or **38a** were dissolved in a minimal amount of hot water. Solutions of NH₄PF₆ or NH₄BF₄ in water were then added resulting in yellow precipitates which were collected via filtration, washed with water several times and dried under reduced pressure. These materials were fully characterized by mass spectroscopy and NMR techniques. Figure 1 shows the ¹H NMR spectrum of compound **38a** (as an example) and its labeled protons.

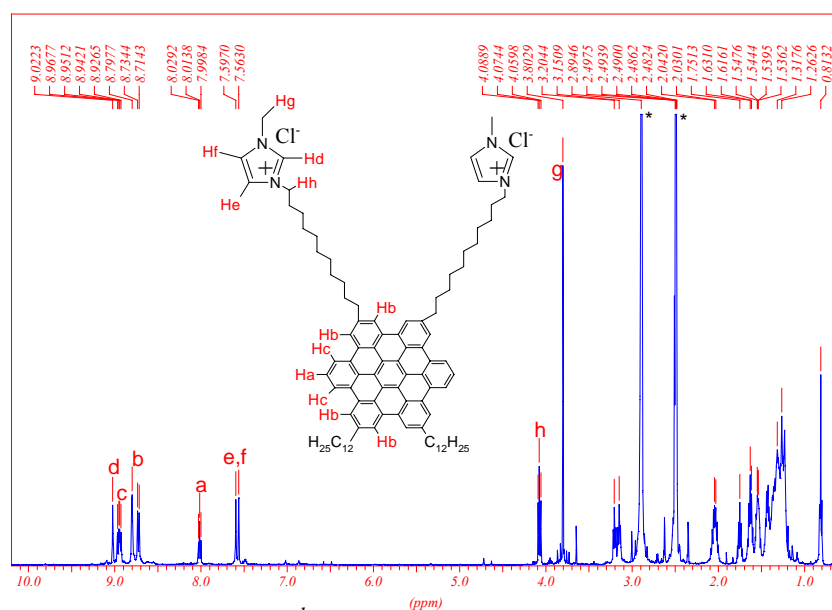


Figure 1: ¹H NMR spectrum of **38a** in DMSO.

To explore the effect of the counter ion on the chemical shift of the aromatic protons of the HBC core and the imidazolium cation, **38a**, **38b** and **38c** were dissolved in DMSO solution with a concentration of 1.3×10^{-3} mol/L and the ¹H NMR spectra were recorded at 353 K. The protons e, f, g and h (Figures 1 and 2) showed no chemical shift difference for the compounds **38a**, **38b** and **38c** indicating that there was no effect upon counter ion exchange. There was also no significant change in the chemical shift of the protons belonging to the HBC core and

the imidazolium ring. The only meaningful difference was observed for H(d) of **38a**, which appeared at lower field than those of **38b** and **38c** (Figure 2). Such behavior was also observed in alkyl imidazolium derivatives where the imidazolium ring hydrogens possessed the highest chemical shift in presence of chloride as counter ion when compared with other anions, due to the hydrogen bonding of the anions with the H(d) of the imidazolium cation ring.²¹

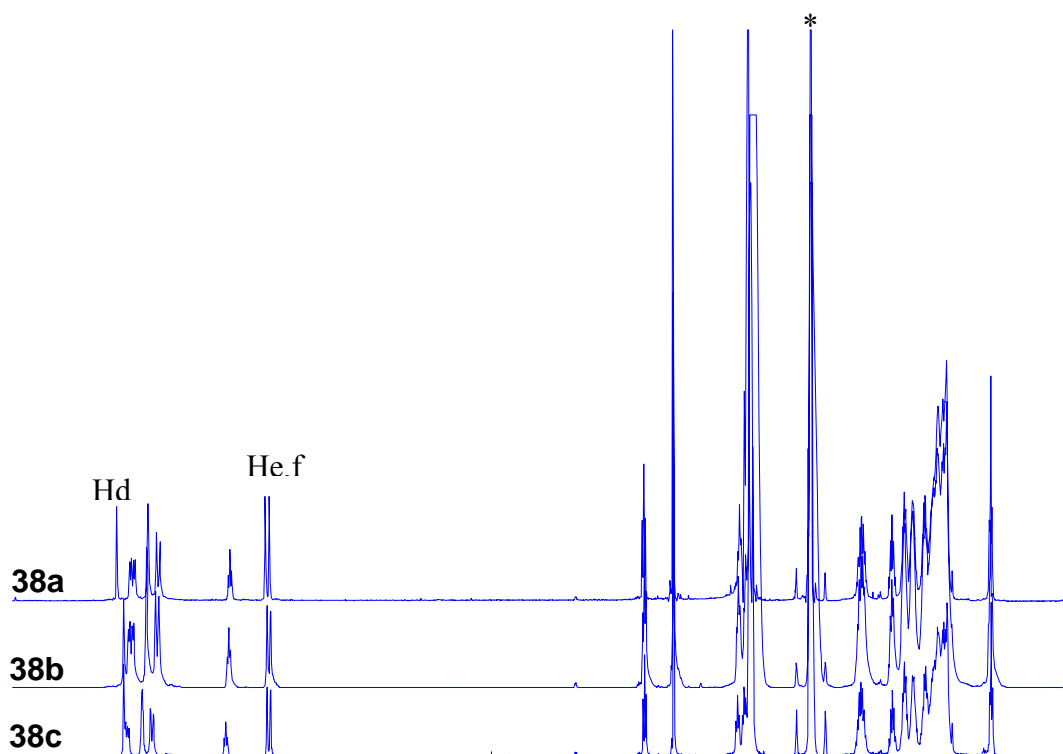


Figure 2: ^1H NMR spectra of **38a**, **38b** and **38c** in DMSO at 353 K ($C = 1.3 \times 10^{-3}$ mol/L).

3.3. Results and discussion

3.3.1. UV-Vis and fluorescence spectra

The attachment of hydrophilic imidazolium units rendered the amphiphilic HBC molecules soluble in water or other polar organic solvents. We found that **37a** and **38a** were soluble in both DMSO and H_2O and hence were suitable for self-assembly studies in both solvents.

To gain deeper insight into its aggregation behavior, concentration and solvent dependent UV-Vis-fluorescence spectra of the aggregated HBC **38a** in 9/1 water/DMSO were measured (Figures 3,4) with concentrations ranging from 2×10^{-5} to 8×10^{-7} M. The bands at 332, 361 and 412 were dependent on the concentration and lost intensity at concentrated solutions. At 2×10^{-5} M, a weak, broad band appeared at a wavelength around 450 nm, which could be assigned to absorption from the aggregates. The β -bands (361 nm) showed an increase in their extinction coefficients, while the bands at smaller and longer wavelengths exhibited a slight increase in intensity with decreasing concentration. A similar behavior has already been observed for other HBCs and C_{72} discs.^{12b,22} In DMSO, typical HBC absorption bands were found with $\lambda_{\text{max}} = 360$ nm for all **37a,b,c** and **38a,b,c**. Upon decreasing the DMSO/water solvent ratio, the band intensities (at 342, 360 and 389) dropped down and a broadening was observed, which is consistent with the formation of aggregates (Figure 3b). The presence of an isobestic point at a wavelength of 407 nm was consistent with a linear correlation between the monomer absorption at 390 nm and the absorption of aggregates at 418 nm, so that when the band at 390 nm decreases, the band at 418 nm increases. This indicated the formation of aggregates with an increasing proportion of water. This is also supported by the broadening of the bands in UV-vis spectra and by the decrease of the intensity bands at similar concentrations.

Aggregation was also apparent from fluorescence spectroscopy. The fluorescence spectra of **38a** in a mixture of DMSO and water with different volume ratios are shown in Figure 4b. In pure DMSO, a well-resolved fluorescence spectrum was observed. Upon incremental addition of water, the fluorescence intensity decreased and the emission maximum shifted to longer wavelength. When the DMSO/water ratio reached 4/6, a band centered at 515 nm was observed.

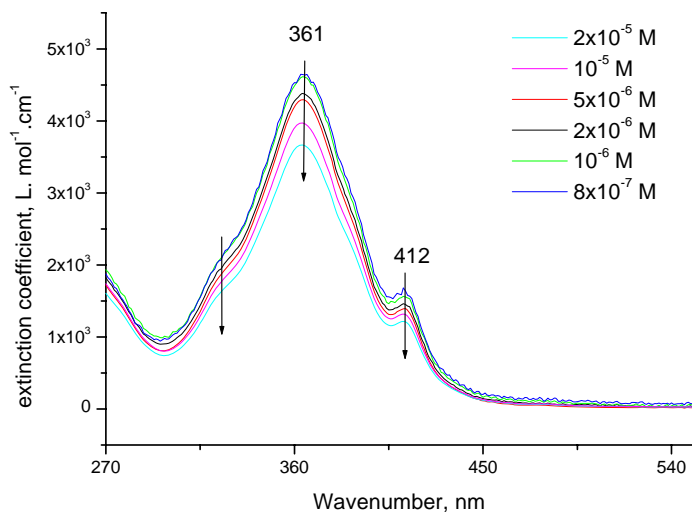


Figure 3: concentration dependent UV-vis absorption spectrum of **38a** in 9/1 water/DMSO mixture at room temperature.

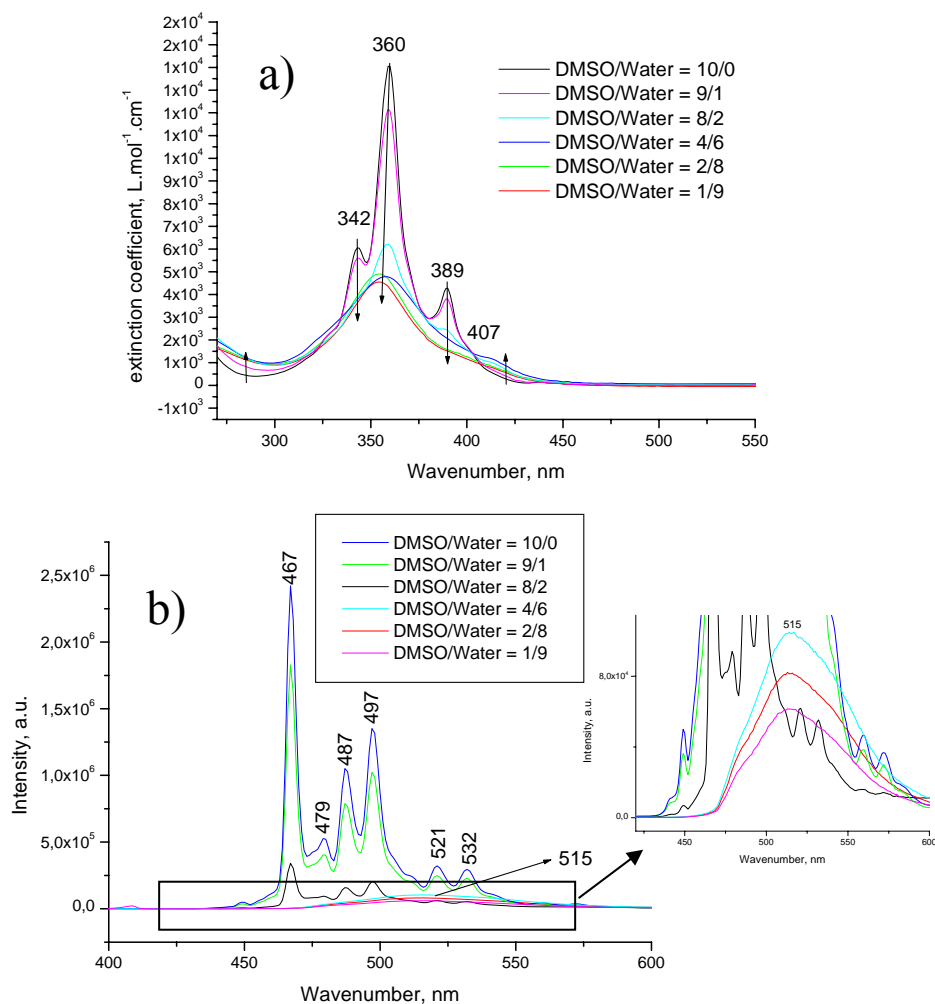


Figure 4: water/DMSO solvent dependent spectra a) UV-vis and b) fluorescence of **38a** at 10^{-6} M concentration, inset shows the bands at 515 nm.

This band typically arises from excimer emission, thus gradual addition of water enhances the hydrophobic interactions and leads to an increase of the size of aggregates. The red-shift of the emission spectrum could be explained as follows: solvent molecules assist in stabilizing and further lowering the energy level of the excited state by re-orienting themselves (termed solvent relaxation) around the excited HBCs aggregates. This has the effect of reducing the energy separation between the ground and excited states, which results in a red shift (to longer wavelengths) of the fluorescence emission.²³ The quenching of fluorescence intensity could be due to the high intermolecular interactions between the HBC derivatives among the aggregates. Both UV-vis and fluorescence measurements described above strongly supported the self-association of the imidazolium-HBC in solution.

3.3.2. Solid-state self-assembly investigated by X-ray scattering

The relation between molecular structure and the supramolecular organization has been investigated by two-dimensional wide-angle X-ray scattering (2D-WAXS) diffraction. In a home-built mini-extruder (Figure 9 in Chapter 1), the HBC material is heated up to a point at which it becomes plastically deformable and is extruded as thin filament by a constant-rate motion of the piston along the cylinder. This mechanical orientation, where discotic molecules are ordered due to shearing forces, was developed in our institute and has been used frequently.²⁴ To better understand the role of the imidazolium functionalization and the counter ions on the self-assembly of HBC core molecules, the HBC compounds **35-38** were dried under vacuum and mechanically extruded into filaments. All samples revealed a pronounced macroscopic alignment of columns along the filaments as indicated by intense and sharp reflections, which is typical for such structures.

Figure 5 presents the room temperature 2D-WAXS patterns for **35** and **36**. The positions of the equatorial reflections describe the intercolumnar arrangement and were fitted to a two-dimensional pseudo-hexagonal unit cell in both cases with the packing parameter of $a' = 3.78$ nm for **35** and $a' = 4.45$ nm for **36**. This is in good accordance with the difference of the side chain packing parameters ($a = 1.86$ nm and $b = 3.22$ for **35**; $a = 2.21$ nm and $b = 3.83$ nm for **36**) revealing the ratio of $\sqrt{3}$ to each other which is characteristic for the pseudo-hexagonal arrangement of columns. The columns, therefore, are not completely equivalent. This imperfection is possibly due to the side chain orientation so that the hexagonal unit cell is positionally superimposed onto a rectangular one. Because the less flexible aliphatic chains were attached to the aromatic core and a substitution with only four alkyl chains, a stronger interaction between the molecules was obtained and thus the higher intercolumnar order. As a consequence, the phase transition temperature of 207 °C for **35** and 195 °C for **36** to the mesophase is higher than the hexa-alkyl substituted HBCs (typically 130 °C for HBC-C₁₂). This behavior was also observed for HBCs possessing ether branched space-filling alkyl chains after cooling down from the isotropic phase to the liquid crystalline phase.²⁵

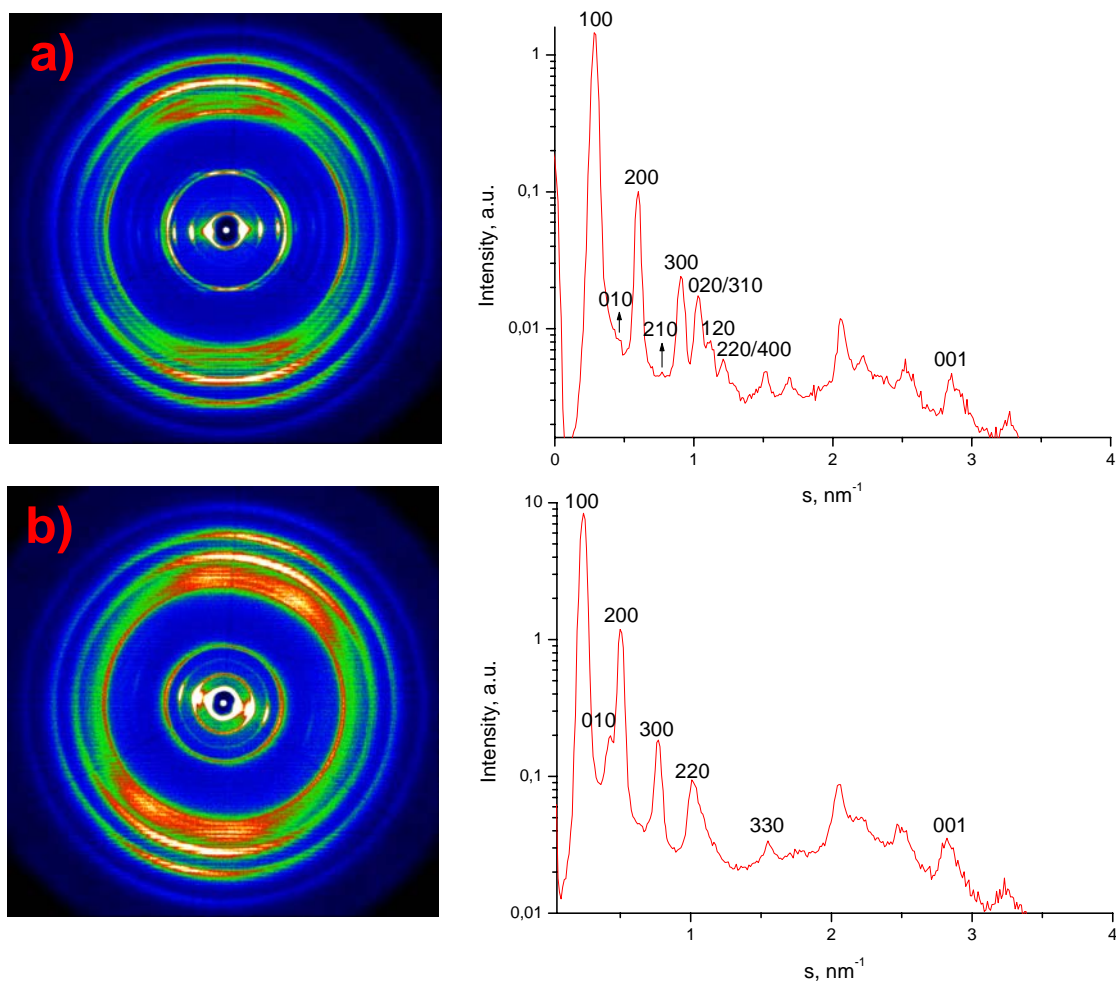


Figure 5: 2D-WAXS patterns and equatorial intensity distribution of precursors a) **35** and b) **36** at room temperature.

The meridional reflections for **35** and **36** revealed strong reflections according to a π -stacking distance of 0.35 nm. Additional meridional higher order reflections were characteristic for the pronounced intracolumnar packing of the molecules.

Heating over the phase transition was accompanied by a significant structural rearrangement for both materials (**35** and **36**). The compounds exhibited a typical mesophase organization where the columns are arranged in a hexagonal lattice ($a' = 2.33$ nm for **35** and $a' = 2.63$ nm for **36**) with periodic non-tilted stacking.

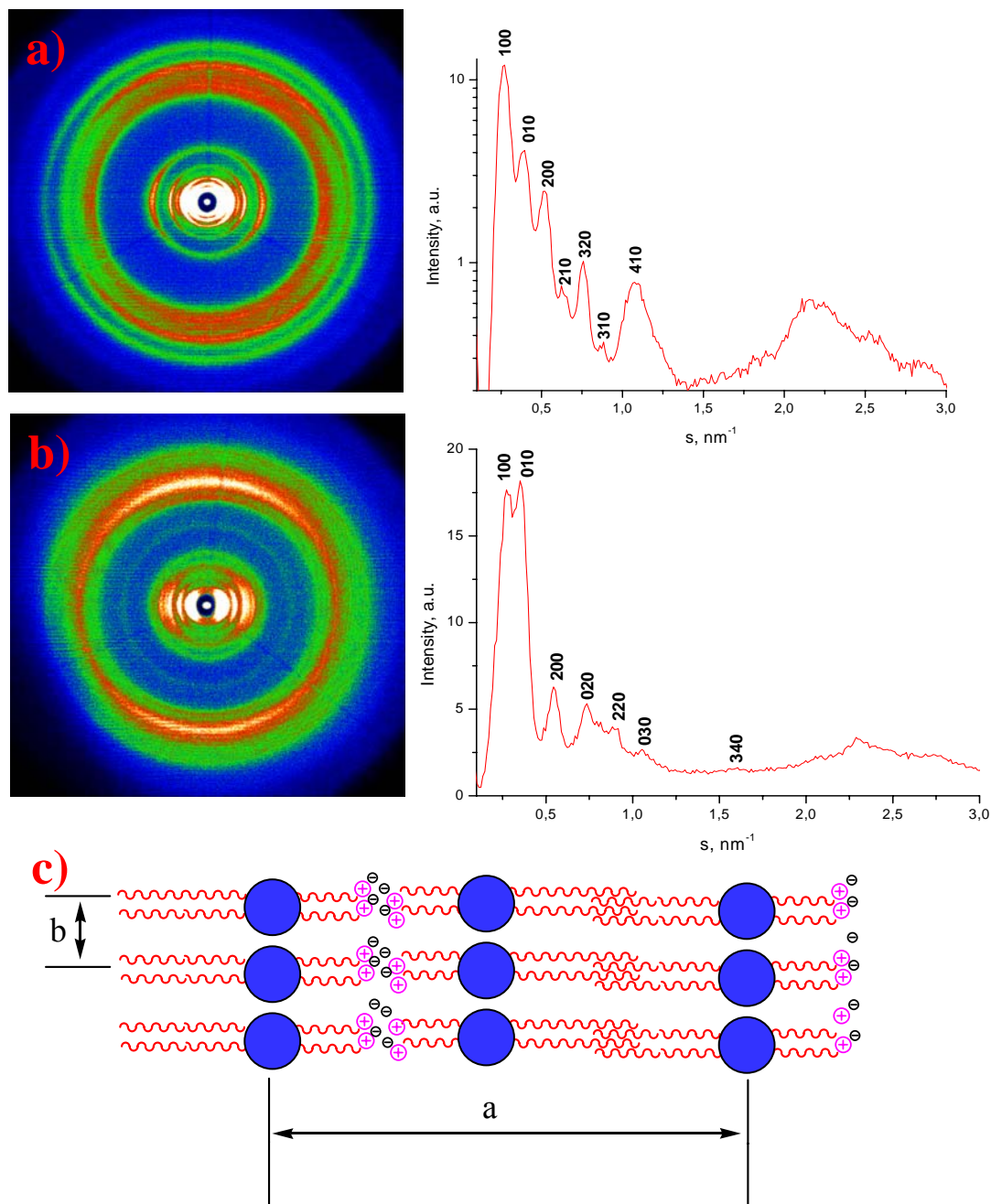


Figure 6: X-ray diffractogram and intensity distribution for a) **38a** and b) **37a** at room temperature; c) suggested packing model of molecules in solid-state (Top view).

The temperature dependent X-ray diffractions of HBC derivatives **37a** and **38a** were measured. The diffraction pattern showed a rectangular columnar phase that did not significantly change for either HBC **37a** or **38a** when the temperature was varied (Figure 6). This suggested that the

imidazolium and HBC units were locked in a single phase up to the isotropization temperature at 270 °C, as determined by polarized optical microscopy. This has been additionally supported by DSC, where no thermal transition occurred in the range of -100 °C to 250 °C.

Integration along the equatorial reflections resulted in a series of reflections correlated to a 2D rectangular ordered lattice with parameters $a = 4.18$ nm, $b = 2.87$ nm for **38a** and $a = 3.51$ nm, $b = 2.72$ nm for **37a** (Figure 6). In both compounds, the (001) off-meridional reflection observed at about 0.36 nm and a periodic non-tilted stacking of the molecules within the columns was observed.

The relatively large spacing of 4.18 nm could reasonably be explained by a lateral lamellar arrangement of HBC columns. The reflection at 2.87 nm corresponds to the spacing typically observed between neighboring columns of HBC's. The phase segregation induced by the hydrophilic imidazolium salts and hydrophobic alkyl chains rendered these C_{2v} symmetric molecules into layer-like structures. The parameter "a" is therefore correlated to the distance between the layers and "b" is correlated to the inter-disc distance at the direction perpendicular to the layer axis. The layer-to-layer distance for molecule **37a** is shorter and can be explained by the shorter spacer between the HBC core and imidazolium units. In the meridional plane, reflections characteristic for π - π overlap in aromatic systems, corresponding to the periodicity along the fiber axis, suggested that the discs stack along the columnar axis, which indicated that the HBC discs are non-tilted with respect to the columnar axes.

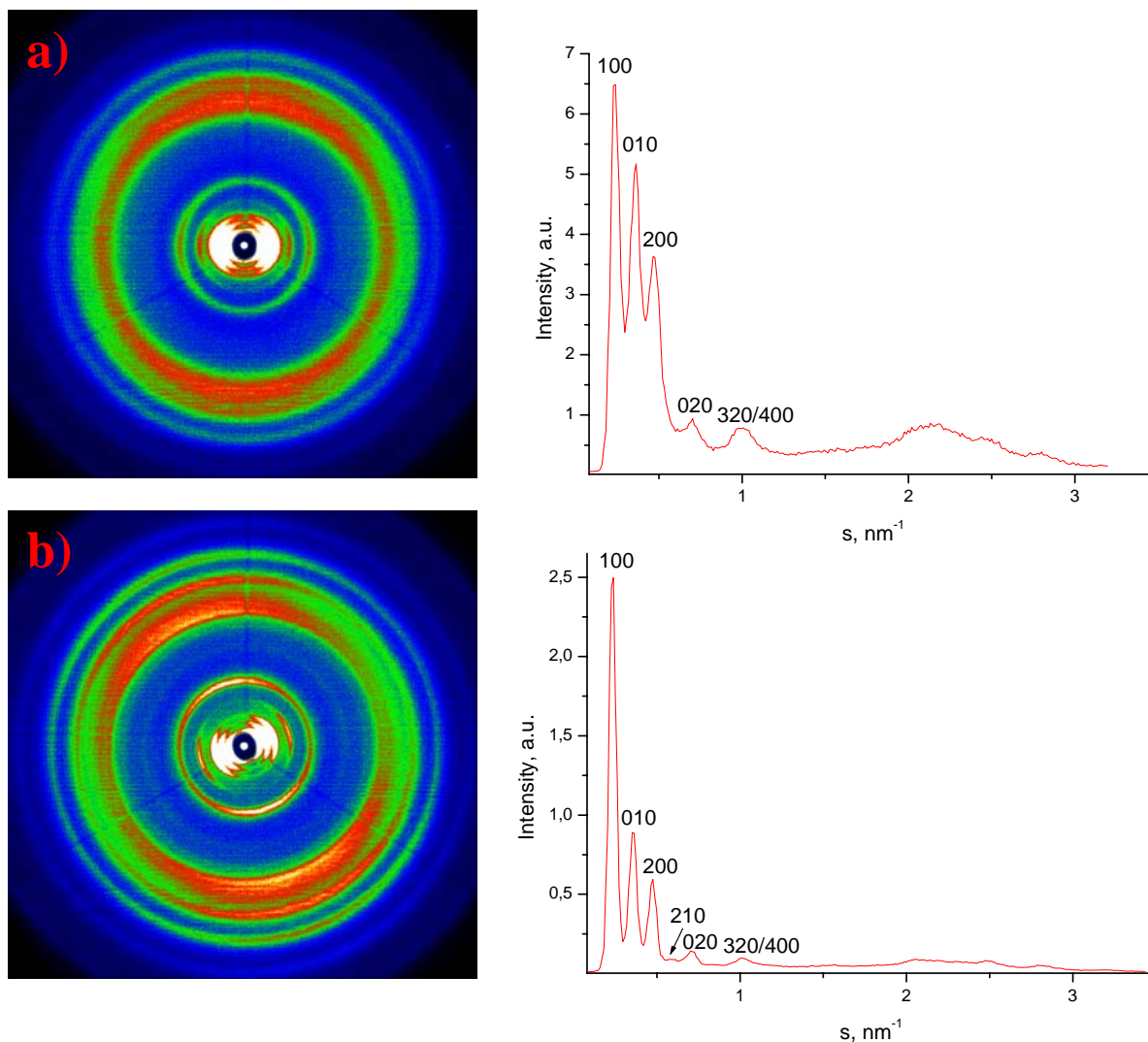


Figure 7: X-ray diffractogram and intensity distribution pattern for a) **38b** and b) **38c**, at room temperature.

It seems reasonable to assume that the shorter linkage of the HBC discs promotes a higher intercolumnar order. The phase forming obtained by **37a** and **38a** between the HBC core and the imidazolium ring confirmed that there is a substantial effect on the columnar packing. As previously shown for alkyl-chain-linked triphenylene dimers, the phase behavior is strongly dependent on the spacer length between discs.²⁶ A mesophase could be observed after reaching an inter-triphenylene alkyl link length of eight carbon atoms. However with **37a** and **38a**, it was possible to reach a linker length of eleven carbon atoms between the HBC and the imidazolium ring without transition from the crystalline phase up to the isotropization

temperature. This phase locking is assumed also to be supported by the presence of hydrogen-bonding and ionic interactions between the imidazolium salts of neighboring HBC columnar structures. We therefore hypothesize that the alkyl spacer length between the HBC core and the imidazolium ring plays an important role by varying the interaction between the HBC units in two adjacent columns and dictating their phase behavior.

The 2D WAXS patterns of HBCs **38b** and **38c** revealed a series of reflections correlated to an orthorhombic lattice with parameters of $a = 4.10$ and $b = 2.80$ for **38b** and $a = 4.09$ and $b = 2.79$ for **38c** (figure 7). This indicates that lattice parameters did not change compared to those of **38a**. The substitution of the chloride atoms with BF_4^- or PF_6^- showed no difference regarding the intermolecular properties of the HBC columns, with isotropization temperature above 270 °C. Upon increasing the temperature, no significant structural change appeared. In the meridional plane, the aromatic π -stacking of the HBC cores was found to be 0.36 nm. This is not surprising since the counter ion is not directly connected to the HBC core, but only to the imidazolium cation through ionic interaction. Unfortunately, it was not possible to assign reflections corresponding to the imidazolium rings for all the HBC derivatives.

3.3.3. Infrared Spectroscopy

The two-dimensional wide angle X-ray scattering showed no difference in the packing behavior of the different HBC-imidazolium derivatives. To have a closer look at the bulk properties and the effect of the counter ion exchange, IR measurements were conducted. An important aspect of the imidazolium salts is the existence of the interactions among the ion-pairs present in the medium. IR spectroscopy should reveal the extent to which a hydrogen bonding between the imidazolium hydrogens and the counter ions can occur.

The bands at 2848 and 2918 cm^{-1} of all HBC-imidazolium derivatives **37-38** corresponded to the alkyl chains CH_2 stretching. The weak band at 3055 cm^{-1} for **38a**, assigned to a hydrogen bonding between the chloride and the hydrogen of the imidazolium salt, was present, but it disappeared when the counter ions were replaced by PF_6^- (**38b**) and BF_4^- (**38c**) (Figure 8, and inset). The "nitrogen stretching" ranging from 3200 and 3400 cm^{-1} were hidden by the broad peak from water between 3130 and 3723 cm^{-1} . As previously shown by crystallographic and IR²⁷ studies of imidazolium chloride derivatives, the chloride anion was observed to participate in hydrogen bonding with H-C(2) of the imidazolium ring. The obvious feature of the IR spectrum is the presence of the Cl^- interaction band²⁸ around 3050 cm^{-1} , which is assigned to the stretching vibrations of Hd-C(2), hydrogen bonded to the chloride anion. The infrared spectrum of the **38b** showed a band at 3172 cm^{-1} . This band corresponded to the C-H of the imidazolium ring, not present in the HBC with chloride (**38a**). The absence of hydrogen bonding in the presence of fluorinated counter ions was also observed in 1-alkyl-3-methylimidazolium halides derivatives due to the weak electronegativity of these anions, compared to chloride.²⁹

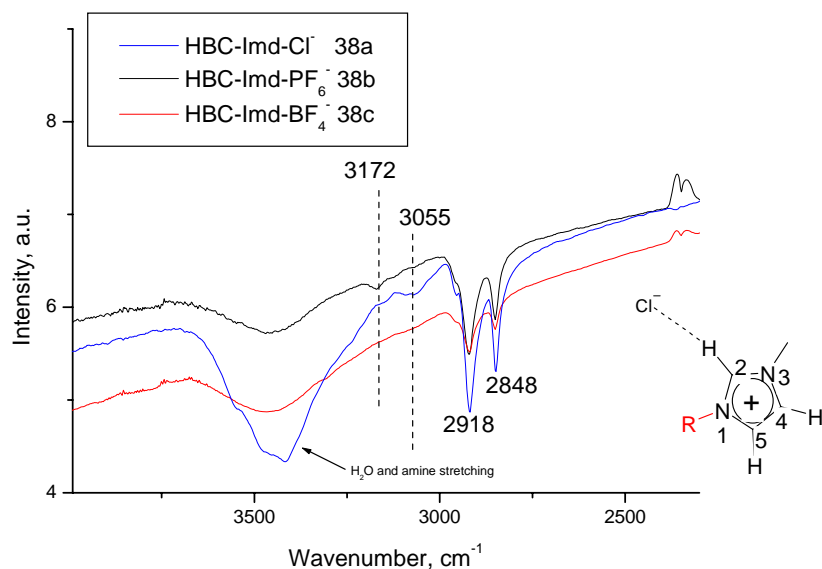
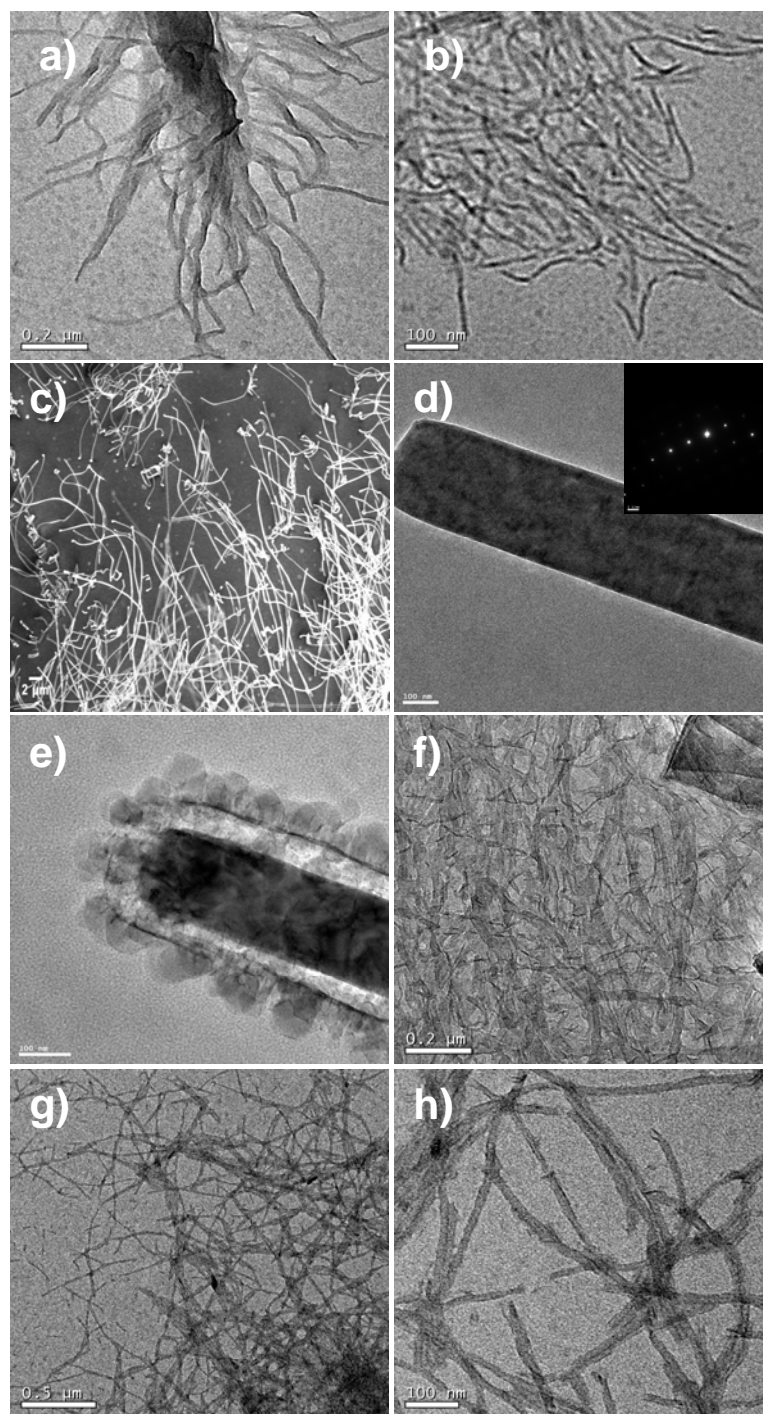


Figure 8: Infrared spectrum of **38a**, **38b** and **38c** in KBr, inset shows a schematical representation of hydrogen bonding of imidazolium with chloride.

3.3.4. Self-assembled nanostructures studied by electron microscopy

To investigate the effect of self-association and the morphology of the HBC derivatives on surface, their organization after deposition from solution and solvent evaporation was investigated by electron microscopy. Therefore, several samples were prepared under different preparation procedures. The preparation method of the HBC films consisted of drop-casting of the HBC solution on a silicon wafer substrate and the evaporation of the solvent was done at ambient temperature conditions. After the material on surface was dried, the prepared sample was studied by electron microscopy. Slow evaporation of a droplet of compound **38a** in DMSO (3×10^{-4} mol/L) on a silicon wafer resulted in tree-like fiber structures. Unfortunately, the structure size was irregular (Figure 9a). Ethanol was added to the DMSO solution and after a few days, a cloudy precipitate appeared. A small portion of the obtained suspension was taken up with a Pasteur pipette, deposited and dried (under ambient atmosphere) on a silicon wafer. Scanning electron microscopy (SEM) measurements showed fiber-like nanostructures, which were further confirmed by transmission electron microscopy (TEM) measurements (Figure 9b). Individual nanofibers with diameters of about 6 nm were observed. By using water as a hydrophilic solvent which also possesses higher polarity than DMSO, the film from HBC **38a** prepared after solution drop-casting and solvent evaporation exhibited pronounced anisotropy in the structure such as fibrous features. Similar results were observed from both concentrations 7×10^{-4} M and 3.5×10^{-4} M. The obtained objects were on the order of several hundred of nanometers in length with diameter ranging around 100 nm (Figure 9c, 9d). These fibers were sensitive to the electron beam, but occasionally, an electron diffraction analyses could be rapidly done under low electron beam intensity (inset 9d). The latter pattern exhibited highly ordered structure, but afterwards, the fiber started to decompose (figure 9e).



Figures 9: all the images were taken upon deposition of the HBC solutions on SiO_2 substrates. a) TEM image of **38a** after heating and cooling to room temperature from DMSO; b) TEM images of **38a** after addition of ethanol to the DMSO solution; c) SEM image of **38a** after deposition from water solution; d) and e) TEM pictures (from c)) of **38a** after short and long

time exposure under low electron beam respectively; (inset shows the electron diffraction pattern of the corresponding fiber of image d) immediately after focusing); f) TEM picture of 37a showing fiber-like structures from water solution under hexane vapor; g) and h) TEM images of 38a after deposition from water solution under hexane vapor.

When **37a** and **38a** were dissolved in water and then placed in a saturated hexane vapor chamber, ordered nanostructures in a fiber-like shape were observed (figure 9g) with diameters ranging between 10-15 nm and their length up to several micrometers. These nanoobjects were aggregated in bundles composed of several nanofibers, and some of them were broken probably due to the sonification of the suspension before dropping on the TEM grid (Figure 9h).

3.3.5 Discussion

Disc-like molecules such as triphenylene,³⁰ metallophthalocyanines³¹ and hexa-*peri*-hexabenzocoronenes (HBC) have attracted interest because of their high tendency to aggregate into columnar superstructures. All these discs are substituted with alkyl chains to provide solubility and to induce the phase separation between the aliphatic and the aromatic moieties. Amphiphilic HBC derivatives substituted by branched oligo(ethylene glycol) chains¹⁴ showed ordered columnar superstructures in the bulk state. The HBC imidazolium compounds described here are the first examples of HBCs bearing two charges on the periphery. Moreover, the length of the alkyl chain between the core and the imidazolium salt could be varied and the counter ions could be exchanged. The change of these parameters allowed an albeit coarse tuning of the structure formation. The effect of the counter ion variation was observable in the ¹H NMR and the infrared spectroscopy.

At identical concentrations in DMSO-*d*₆, the chemical shifts of the ring proton H(d) of **38a** increased with increasing anion's electronegativity and charge density. This indicated that

the acidity of this hydrogen increased due to the presence of chloride counter ions³² and suggested a hydrogen bonding ability of the chloride anions toward the H(d). In contrast, PF_6^- and BF_4^- are weak donor anions with a low charge density, and thus are only weak coordinating anions. However, the chloride did not make any hydrogen-bond interactions with other alkyl chain hydrogens due to their low acidity. This could be confirmed by the presence of the C-H stretching bands around 2900 cm^{-1} therefore indicating the acidity of the Hd-C2 protons. This effect could be also observed and studied with other imidazolium halide salts where the chloride anions performed hydrogen bonds only with imidazolium hydrogens but not with those attached to the imidazolium alkyl chains.³³ It is thus concluded that the chloride anion had a stronger interaction with the imidazolium cation and forms a hydrogen bond H(d). It was reported by Dymek et al. and Turner et al.^{27,28,34} using IR, crystallographic studies and calculations that different anions were observed to perform hydrogen bonds with Hd-C2, He-C4 and Hf-C5 of the imidazolium ring. Computations revealed that the chloride anion was positioned in the plane of the imidazolium ring (ab initio HF and MP2)³⁴ for various imidazolium chloride derivatives. These calculations showed that the position of the halogen, regarding the imidazolium ring, is a local minimum on the potential energy surface of the isolated molecules. The lowest energy was found when the halogen was positioned at the most acidic hydrogen C2-(Hd).

After attaching the imidazolium cations to the HBC alkyl chains, no transition up to the isotropization temperature occurred. This phenomenon could be explained as follows: at room temperature the HBC is crystalline and the mobility of the core is low. This behavior has been observed for various other HBCs such as HBC-C₁₂ by solid state NMR spectroscopy.³⁵ Upon raising the temperature, the rotational mobility around the columnar axis of the HBC molecules increases due to the increase in thermal energy. Such behavior has also been observed using

solid state NMR spectroscopy.³⁶ For example, HBC-C₁₂ exhibits enhanced dynamics upon increasing the temperature to 130 °C. This compartment is accompanied by a transition from the crystalline phase to the mesophase.³⁵ Because of the repulsion between the imidazolium cations, they can be speculated to be separated within the columnar superstructures established by the HBCs. The dynamic behavior induced by the high rotation of the HBC cores destroys the supramolecular architecture and thus no organized mesophase develops. Therefore, the compound directly becomes isotropic. Additionally, the charges in the corona reduce the isotropization temperature due to the columbic repulsion. This is in contrast to the HBC-imidazolium precursors **(35)** and **(36)**, which bear no charged species and exhibit mesophase formation at high temperatures. On the other hand, the replacement of the chloride atoms by PF₆⁻ and BF₄⁻ did not induce any change on the macroscopic level. The intermolecular packing remained unchanged as observed by 2D-WAXS of the extruded filaments. In comparison to HBC-C₁₂, all discussed new derivatives packed into smaller unit cells due to the lack of substituents in the 2 and 11 positions of the HBC core.

UV-vis and fluorescence measurements of the HBC-imidazolium derivatives showed an aggregation behavior in DMSO whereas the addition of water as a "bad solvent" increased aggregate formation. This was not surprising since other HBCs such as HBC-C₁₂ have been observed to aggregate increasingly upon methanol addition.^{12b,15} It is assumed that organic solvents such as DMSO reduce the π -stacking between aromatic solutes (compared to water), because interactions between the solute and solvent (solvation) effectively competes with or prevails over those between solutes. It was evident that the length and the nature of the side chains played an important role in determining the aggregation tendency. This behavior correlates well with that observed for HBC-C₁₂, supporting the notion that solvophobicity induced π -stacking interactions are a driving force for the formation of higher aggregation

states.^{12b,15} Additionally, the substituents (four alkyl chains at positions 2, 5, 11 and 14 and two hydrogens at 8 and 17 of the HBC core) possess as a whole, a relatively small steric demand in the periphery of the aromatic disc, which allow the molecules to approach one another more easily, resulting in a higher degree of association compared to HBC-C₁₂ and branched alkyl chain substituted HBCs.^{12b,37}

Both the structure of the HBC-imidazolium derivatives and the self-assembly conditions are important to prepare defined objects on surfaces. Upon decreasing the spacer length between the imidazolium salt and the hydrophobic HBC core, preparation of nanostructures became more difficult. This might be explained by the fact that whenever the ionic moiety is further away from the hydrophobic part, the better the phase separation and thus the nanostructure formation. The critical role of the assembling conditions on solid substrates, such as surface spreading, was confirmed by the absence of one-dimensional supramolecular structures upon drop-casting of **37a** (compared to **38a**) from solution. However, it was possible to control the self-assembly of the HBC derivatives on surface by varying the length of the alkyl chains and the nature of the solvent.^{12b} This allowed the formation of fiber-like structures upon addition of ethanol as another bad solvent to the HBC-imidazolium DMSO solution (Figure 9a and 9b). Given that the size of the nanostructure is about two times the lateral size of the HBC molecule, the formed nanofibers could be constituted of two single columns assembled together, probably via hydrophobic-hydrophobic and hydrophilic-hydrophilic interactions. The addition of a bad solvent induced precipitation after a few days, reflecting the slow kinetics of the structure formation. The general π -stacking of the HBC discs further stabilized the fiber structures and the diameters obtained were fairly close to the molecular dimensions estimated from the models.^{12b,15}

In a good solvent such as DMSO, HBC-imidazolium existed as monomeric species at low concentrations (Figure 4). The addition of water as a bad solvent induced higher aggregation at the same concentration. We can further speculate that the higher the water content, the more shielded is the hydrophobic part in the medium. This would allow the formation of fibers where the hydrophobic units lie in the inner part and the hydrophilic polar heads (the imidazolium salts) remain outside in the hydrophilic medium. Therefore, the presence of water induced phase separation of the hydrophobic-hydrophilic units. As a result, the drop casting of the charged HBCs from a water solution revealed the formation of nanofibers depending on the preparation conditions. The observed electron diffraction pattern of the fiber shown in figure 9d exhibited well-ordered packing, similar to inorganic crystals such as sodium chloride.³⁸ However, inorganic materials are not sensitive under the presence of electron beam, which support that these fibers consist of organic materials. Therefore, this nanoobjects should arise from the self-assembly of **38a** by π -stacking of the HBC-cores in the presence of the imidazolium salt. Moreover, inorganic material (such as sodium chloride) never formed similar fiber-like features under similar preparation conditions. This suggests that **38a** is unique in its self-assembly properties and would open the way toward further investigations over the packing behavior of the HBC cores and the ionic interactions among the present ions of the nanofibers.

These ordered objects (from **38a** in water) resembled those obtained from nanofibers prepared by self-assembly of hyperbranched dendrimers by the Longmuir-Blodgett technique.³⁹ However, no one-dimensional supramolecular nanostructures were formed when drop-casting these dendrimers from solution was used to deposit molecules on the solid substrate, but only long fibrillar structures on a microscopic level. This reflects the importance of the chemical structure: either large aromatic discs or hyperbranched dendrimers possessing

weak interactions are important to drive them to aggregate and form ordered nanoobjects in comparison to the HBC-Imidazolium derivatives.

The mere presence of a large aromatic disc does not guarantee the formation of ordered nanoobjects. For example, C₉₆-C₁₂ was a candidate for self-assembly on surfaces after solution drop-casting.⁴⁰ Like the HBC-Imidazolium systems, C₉₆-C₁₂ also consists of a graphene core, but the size is larger. However, from solution drop-casting of C₉₆-C₁₂, yielded only percolated networks without forming defined nanoobjects. By comparison, the presence of imidazolium units on the periphery of the HBCs influenced their self-assembly behavior and conducted the formation of fibrillous objects. This result points toward the importance of the presence of functionalities on the periphery of the graphene moiety such as ionic imidazolium salts which improved the nanophase separation and thus the formation of anisotropic features such as nanofiber.

The ethylene glycol amphiphilic HBC prepared by Aida et al.¹⁶ consists of a disc with functionality on the periphery and it forms well defined nanotubes. By comparison, the HBC-imidazolium derivatives could self-assemble into different sized fibers depending on the preparation conditions. The presence of alkylated salts attached to the HBC core gives them the ability to interact with other ionic species such as polyelectrolytes and potentially form materials with properties such as ionic conductivity. This would open the way for the study of the self-assembly on ionic surfaces. All these possibilities do not exist for ethylene glycol substituted HBCs due to the absence of ionic units attached to the ends of the alkyl chains. Furthermore, HBC-imidazolium chloride exhibited no phase transition to the mesophase before reaching the isotropization temperature, unlike the ethylene glycol HBC, which melts at 203 °C. This phase stabilization could be due to the inter-ionic interactions among the imidazolium salts between neighboring HBCs as similarly described for alkyl-imidazolium

substituted triphenylenes where the latter showed no phase transition from crystalline to liquid crystalline up to the isotropization temperature.^{19b}

3.4. Conclusion

In summary, we have synthesized new type of amphiphilic HBCs where the core is connected to the imidazolium salt via alkyl chains. These charged species could even dissolve the HBC core in polar solvents such as water. The counter ion could be varied from chloride to hexafluorophosphate or tetrafluoroborate in good yields. However, no change on the macroscopic level was observed by 2D-WAXS of mechanically extruded fibers. On the other hand, NMR and IR showed the formation of hydrogen-bonding between the chloride anion and the hydrogen of the imidazolium ring, but not for the other anions. After attaching the imidazolium salt to the HBC, the mesophase disappeared probably due to the repulsion of the positively charged species and high molecular dynamics at elevated temperature. Drop-casting from DMSO or water solution exhibited various nanostructures, where the morphology of the prepared nanoobjects could be varied due to the different aggregation behavior in various solvents.

For future work, the plan is to attach the imidazolium groups to DNA via columbic interactions of the charged imidazolium and the anionic phosphate units in the DNA double helical chain. The aim is to study the effect of the supramolecular arrangement and the order of the HBC derivatives after the formation of the DNA-HBC complex, and find out if such systems can form 1D-semiconducting materials which could have better charge carrier mobility. On the other hand, the absence of the side chains at positions 2 and 11 increased the concentration of the chromophores (HBC core) and would allow intercolumnar charge transport due to the closer distance between HBC columns.⁴¹ One more possibility is to

synthesize hexasubstituted imidazole-HBC bearing NH groups on the imidazole rings and measures the proton conductivity along the HBC columns.

-
- ¹ a) G. M. Whitesides, J. P. Mathias, C. T. Seto, *Science* **1991**, *254*, 1312; b) D. Philip, J. F. Stoddart, *Angew. Chem. Int. Ed.* **1996**, *35*, 1155; d) J. C. MacDonald, G. M. Whitesides, *Chem. Rev.* **1994**, *94*, 2383.
- ² a) C. G. Claessens, J. F. Stoddart, *J. Phys. Org. Chem.* **1997**, *10*, 254; b) R. S. Lokey, B. I. Iverson, *Nature* **1995**, *375*, 303; M. M. Conn, J. Rebek, *Chem. Rev.* **1997**, *97*, 1647; d) Z. Wang, C. J. Medforth, J. A. Shelnutt, *J. Am. Chem. Soc.* **2004**, *126*, 15954; e) M. D. Watson, A. Fechtenkötter, K. Müllen, *Chem. Rev.* **2001**, *101*, 1267; f) B. Eisenberg, *Acc. Chem. Res.* **1998**, *31*, 117.
- ³ F. J. M. Hoeben, P. Jonkheijm, E. W. Meijer, A. P. H. J. Schenning, *Chem. Rev.* **2005**, *105*, 1491.
- ⁴ a) D. C. Tully, J. M. J. Frechet, *Chem. Commun.* **2001**, 1229; b) T. Bjornholm, T. Hassenkam, N. Reitzel, *J. Mater. Chem.* **1999**, *9*, 1975; c) C. F. van Nostrum, R. J. M. Nolte, *Chem. Commun.* **1996**, 2385.
- ⁵ a) F. S. Schoonbeek, J. H. van Esch, B. Wegewijs, D. Rep, M. de Haas, T. M. Klapwijk, R. M. Kellogg, B. L. Feringa, *Angew. Chem. Int. Ed.* **1999**, *38*, 1393; b) L. Qin, H. Li, L. Wu, D. Qui, X. Zhang, J. Shen, *Chem. Lett.* **2003**, *32*, 390; c) H. Wang, W. You, P. Jiang, L. Yu, H. H. Wang, *Chem. Eur. J.* **2004**, *10*, 986; d) B. W. Messmore, J. F. Hulvat, E. D. Sone, S. I. Stupp, *J. Am. Chem. Soc.* **2004**, *126*, 14452.
- ⁶ a) J. Liu, E. Sheina, T. Kowalewski, R. D. McCullough, *Angew. Chem. Int. Ed.* **2002**, *41*, 329; b) T. Bjørnholm, T. Hassenkam, D. R. Greve, R. D. McCullough, M. Jayaraman, S. M. Savoy, C. E. Jones, J. T. McDevitt, *Adv. Mater.* **1999**, *11*, 1218; c) Ph. Leclère, E. Hennebicq, A. Calderone, P. Brocorens, A. C. Grimsdale, K. Müllen, J. L. Brédas, R. Lazzaroni, *Prog. Poly. Sci.* **2003**, *28*, 55; d) Y.-H. Luo, H.-W. Liu, F. Xi, L. Li, X.-G. Jin, C. C. Han, C.-M. Chan, *J. Am. Chem. Soc.* **2003**, *125*, 6447.
- ⁷ A. P. H. J. Schenninh and E. W. Meijer, *Chem. Commun.* **2005**, 3245.
- ⁸ F. S. Schoonbeek, J. H. van Esch, B. Wegewijs, D. B. A. Rep, M. P. de Haas, T. M. Klapwijk, R. M. Kellogg, B. L. Feringa, *Angew. Chem. Int. Ed.* **1999**, *38*, 1393.
- ⁹ P. Jonkheijm, A. Miura, M. Zadanowska, F. J. M. Hoeben, S. De Feyter, A. P. H. J. Schenning, F. C. De Schryver, E. W. Meijer, *Angew. Chem. Int. Ed.* **2004**, *43*, 74.
- ¹⁰ a) M. D. Watson, A. Fechtenkötter, and K. Müllen, *Chem. Rev.* **2001**, *101*, 1267; b) A. C. Grimsdale and K. Müllen, *Angew. Chem. Int. Ed.* **2005**, *44*, 5592.
- ¹¹ C. D. Simpson, ; J. Wu, M. D. Watson, K. Müllen, *J. Mater. Chem.* **2004**, *14*, 494.
- ¹² a) J. Wu, A. Fechtenkötter, J. Gauss, M. D. Watson, M. Kastler, C. Fechtenkötter, M. Wagner, K. Müllen, *J. Am. Chem. Soc.* **2004**, *126*, 11311; b) M. Kastler, W. Pisula, D. Wasserfallen, and K. Müllen *J. Am. Chem. Soc.* **2005**, *127*, 4286; c) D. Adam, P. Schuhmacher, J. Simmerer, L. Häußling, K. Siemensmeyer, K. H. Etzbach, H. Ringsdorf, D. Haarer, *Nature* **1994**, *371*, 141; d) J. Wu, K. Müllen, "Carbon-rich Compounds: From Molecules to Electronics" (Eds. M. M. Haley, R. R. Tykwinski), Wiley-VCH: Weinheim **2006**, 90-139.
- ¹³ J. Wu, M. D. Watson, L. Zhang, Z. Wang and K. Müllen, *J. Am. Chem. Soc.* **2004**, *126*, 177.
- ¹⁴ M Lee, J.-W. Kim, S. Peleshanko, K. Larson, Y.-S. Yoo, D. Vaknin, S. Markutsya, V. V. Tsukruk, *J. Am. Chem. Soc.* **2002**, *124*, 9121.

- ¹⁵ J. Wu, J. Li, U. Kolb, K. Müllen, *Chem. Commun.* **2006**, 48.
- ¹⁶ J. P. Hill, W. Jin, A. Kosaka, T. Fukushima, H. Ichihara, T. Shimomura, K. Ito, T. Hashizume, N. Ishii, T. Aida, *Science* **2004**, *304*, 1481.
- ¹⁷ W. Jin, T. Fukushima, A. Kosaka, M. Niki, N. Ishii, T. Aida, *J. Am. Chem. Soc.* **2005**, *127*, 8284
- ¹⁸ a) W.-F. Lee, Y.-J. Chen, *J. Appl. Pol. Sci.* **2001**, *105*, 10942; b) S. Kumar, S. K. Pal, *Tetra. Lett.* **2005**, *46*, 2607.
- ¹⁹ a) G. Maruccio, P. Visconti, V. Arima, S. D'Amico, A. Biasco, E. D'Amone, R. Cingolani, R. Rinaldi, S. Masiero, T. Giorgi, G. Gottarelli, *Nano Letters* **2003**, *3*, 479; b) L. Cui, J. Miao, L. Zhu, *Macromolecules* **2006**, *39*, 2536; c) L. Cui, L. Zhu, *Langmir* **2006**, *22*, 5982; d) K. K. Ewert, H. M. Evans, N. F. Boussein, C. R. Safinya, *Bioconjugate Chem.* **2006**, *17*, 877; e) I. Tranchant, B. Thompson, C. Nicolazzi, N. Mignet, D. Scherman, *J. Gene Med.* **2004**, *6*, S24-S35.
- ²⁰ a) H. J. Barber, R. J. Slack, *R. J. Chem. Soc.* **1944**, 612; b) D. Wasserfällen, I. Fischbach, N. Chebotareva, M. Kastler, W. Pisula, F. Jäckel, M. D. Watson, I. Schnell, J. P. Rabe, H. J. Spiess, K. Müllen, *Adv. Funct. Mater.* **2005**, *15*, 1585.
- ²¹ a) A. G. Avent, P. A. Chaloner, M. P. Day, K. R. Seddon, T. Welton, *J. Chem. Soc. Dalton Trans.* **1994**, 3405; b) K. R. Seddon, A. Stark, M.-J. Torres, *Pure Appl. Chem.* **2000**, *72*, 2275.
- ²² D. Wasserfällen, M. Kastler, W. Pisula, W. A. Hofer, Y. Fogel, Z. Wang, K. Müllen, *J. Am. Chem. Soc.* **2006**, *128*, 1334.
- ²³ a) C. Bao, R. Lu, M. Jin, P. Xue, C. Tan, T. Xu, G. Liu, Y. Zhao, *Chem. Eur. J.* **2006**, *12*, 3287.
- ²⁴ W. Pisula, Ž. Tomović, C. Simpson, M. Kastler, T. Pakula, K. Müllen, *Chem. Mater.* **2005**, *17*, 4296.
- ²⁵ W. Pisula, Ž. Tomović, B. El Hamaoui, M. D. Watson, T. Pakula, K. Müllen *Adv. Funct. Mater.* **2005**, *15*, 893.
- ²⁶ N. Boden, R. J. Bushby, A. N. Cammidge, A. El-Mansoury, P. S. Martin, Z. Lu, *J. Mater. Chem.* **1999**, *9*, 1391.
- ²⁷ C. M. Dymek Jr, D. A. Grossie, A. V. Fratini, W. W. Adams, *J. Mol. Struct.* **1989**, *213*, 25.
- ²⁸ K. M. Dieter, C. M. Dymek Jr, N. E. Heimer, J. W. Rowang, J. S. Wilkes, *J. Am. Chem. Soc.* **1988**, *110*, 2722.
- ²⁹ a) A. Downard, M. J. Earle, C. Hardacre, S. E. J. McMath, M. Nieuwenhuzen, S. J. Teat, *Chem. Mater* **2004**, *16*, 43; b) L. Cammarata, S. G. Karazian, P. A. Salter, T. Welton, *Phys. Chem. Chem. Phys.* **2001**, *3*, 5192.
- ³⁰ a) D. Adam, P. Schuhmacher, J. Simmerer, L. Haussling, K. Siemensmeyer, K. H. Etbach, H. Ringsdorf and D. Haarer, *Nature* **1994**, *371*, 141; b) S. Chandrasekhar and S. K. Prasad, *Contemp. Phys.* **1999**, *40*, 237.
- ³¹ a) C. Piechoki, J. Simon, A. Skoulios, D. Guillon and P. Weber, *J. Am. Chem. Soc.* **1982**, *104*, 5245; b) S. Chandrasekhar, *Mol. Cryst. Liq. Cryst.* **1981**, *63*, 171.
- ³² P. Bonhôte, A.-P. Dias, N. Papageorgiou, K. Kalyanasundaram, M. Grätzel, *Inorg. Chem.* **1996**, *35*, 1168.
- ³³ K. Dong, S. Zhang, D. Wang, X. Yao, *J. Phys. Chem. A* **2006**, *110*, 9775.
- ³⁴ E. A. Turner, C. C. Pye, R. D. Singer, *J. Phys. Chem. A* **2003**, *107*, 2277.
- ³⁵ I. Fischbach, T. Pakula, P. Minkin, A. Fechtenkötter, K. Müllen, H. W. Spiess, *J. Phys. Chem. B* **2002**, *106*, 6408.
- ³⁶ S. P. Brown, I. Schnell, J. D. Brand, K. Müllen, H. W. Spiess, *J. Am. Chem. Soc.* **1999**, *121*, 6712.
- ³⁷ A. S. Shetty, J. S. Zhang, J. S. Moore, *J. Am. Chem. Soc.* **1996**, *118*, 1019.
- ³⁸ I. Marklund, S. Andersson, *Surf. Sci.* **1966**, *5*, 197.

³⁹ M. Ornatska, S. Peleshanko, K. L. Genson, B. Rybak, K. N. Bergman, and V. V. Tsukruk, *J. Am. Chem. Soc.* **2004**, *126*, 9675.

⁴⁰ V. Palermo, M. Palma, Z. Tomović, M. D. Watson, K. Müllen, P. Samori, *Syn. Met.* **2004**, *147*, 117.

⁴¹ S. Xiao, M. Myers, Q. Miao, S. Sanaur, K. Pang, M. L. Steigerwald, C. Nuckolls, *Angew. Chem. Int. Ed.* **2005**, *44*, 7390.

Chapter 4

*Control of the homeotropic order of discotic hexa-*peri*-hexabenzocoronenes*

In this chapter, thermal properties and self-organization of hexa-*peri*-hexabenzocoronene derivatives with dove-tailed alkyl chains of various lengths **45a-b** have been investigated using polarized optical microscopy and X-ray scattering. It is shown that the size related increase of steric interactions among the side chains in the aromatic core periphery leads to a lowered isotropization temperature. Additionally, the introduction of ether groups within the side chains enhances the affinity of the discotic molecules towards polar surfaces resulting in homeotropic self-assembly when the compounds are processed from the isotropic state between two surfaces or on one surface as a thin film. Structure analysis of the latter film revealed an identical supramolecular order between the dendritic structures and their periphery, observed by optical microscopy, where the three-dimensional confocal surface measurements demonstrated that both structures resulted from a dewetting during crystallization from the isotropic phase. It is thus established that the degree of homeotropic order is influenced by the phase behavior, the supramolecular order in the bulk and the surface affinity of the corresponding derivatives.

4.1 Processability and alignment on surfaces

Various device configurations require specific alignment between the electrodes which can be accomplished by different processing techniques.^{1,2} The main charge transport in field-effect transistors takes place parallel to the insulating substrate and therefore requires an edge-

on arrangement (Figure 1a) of the discotic molecules with uniaxial columnar orientation in charge transport direction. Langmuir-Blodgett deposition,³ zone-casting technique,⁴ zone-crystallization^{5,6} or solution casting onto pre-oriented polytetrafluoroethylene PTFE⁷ are suitable methods for obtaining highly ordered surface layers with the desired columnar orientation. During solution processing of alkylated HBC on molybdenum disulfide⁸ or highly oriented pyrolytic graphite⁹ the interaction between the aromatic core and the surfaces plays an important role during the alignment, leading to monolayer formation with molecules lying flat on the substrate. On the other hand, examples of homeotropic alignment from the isotropic state of triphenylenes¹⁰ and phthalocyanines¹¹ bearing heteroatoms in the side chains imply a strong influence of the substituents on the arrangement of the molecules.

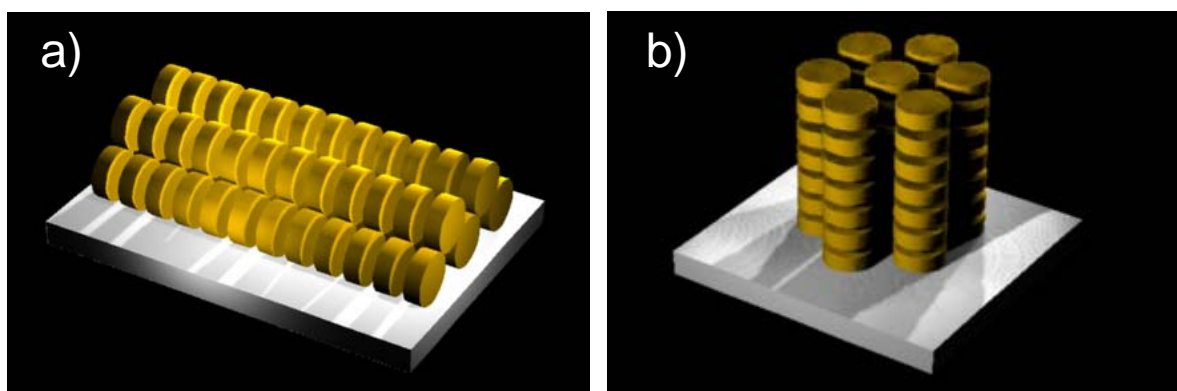


Figure 1: Schematic representation of the different type of supramolecular arrangement on surfaces with a) edge-on orientation of the molecules, where the columnar axis is oriented parallel to the substrate and b) face-on arrangement resulting in homeotropical order

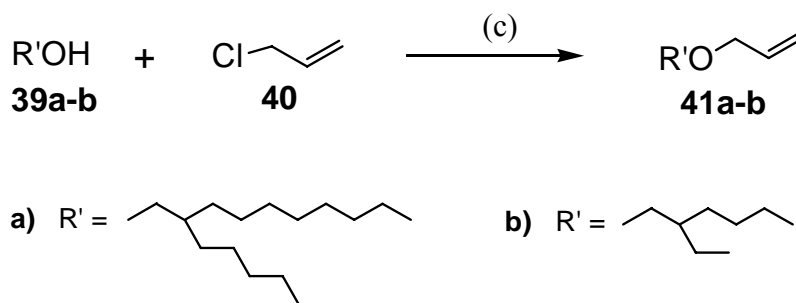
The homeotropic alignment from the isotropic state of discotic systems consisting of larger aromatic cores has not been extensively investigated, due to their prohibitively high isotropization temperatures (T_i) until recently, the high thermal stability of the columnar phases of alkylated HBCs precluded their thermal processing within configurations suitable for electronic evaluation.¹² Substitution of the HBC core with 3,7,11,15-tetramethylhexadecyl

(HBC-C_{16,4}) led to successful isotropization temperature decrease to 231 °C compared to Ti of 420 °C of the alkylated HBCs.¹³ The lowered processing temperature allowed homeotropic alignment of this material between two ITO surfaces and the investigation of the relationship between photoconductivity and columnar alignment.

The exact mechanism leading to homeotropic order is still not clear. The example of HBC-C_{16,4} on ITO confirms that specific molecular affinity for the surfaces is not a prerequisite for the face-on arrangement. On the other hand, the increase of attraction towards specific surfaces has been reported for other discotic systems.¹⁰ These results prompted us to combine the two advantageous properties discussed above: substitution of the discs with branched alkyl chains and insertion of heteroatoms, such as oxygen, into these alkyl chains which might have an influence on the mesomorphic properties of discotic liquid crystalline HBC. Therefore, the aim of the present study is to examine two essential requirements for photovoltaic applications of HBC derivatives. First, the processibility from the isotropic state at reasonable temperatures was induced via long dove-tailed side chains that lowered the isotropization temperature of the HBC derivatives.⁶ Second, the supramolecular order and molecular orientation, by improving the molecular affinity towards specific surfaces leading to homeotropic alignment of the discs. The homeotropic arrangement was monitored by two-dimensional wide-angle X-ray scattering (2D-WAXS) measurements and variable-temperature polarized optical microscopy (POM). In the following pages of this chapter, synthesis, characterization, as well as homeotropic self-assembly (results obtained in cooperation with W. Pisula in the group of Prof. Müllen) of such alkyl-ether derivatives are presented.

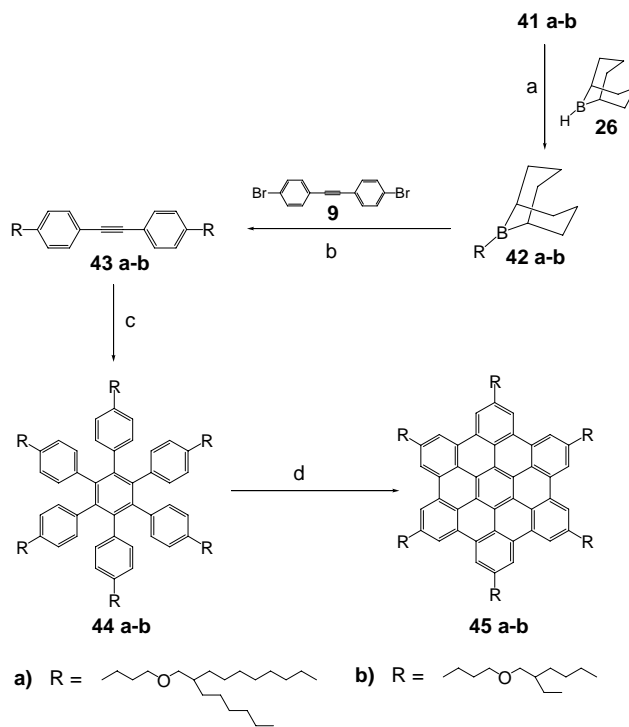
4.2 Synthesis.

Two different derivatives of hexa-*peri*-hexabenzocoronene (HBC) (**45a** and **45b**), substituted at the periphery by six branched alkyl ether chains, 3-(2-hexyldecyloxy)propyl (**a**), and 3-(2-ethylhexyloxy)propyl (**b**), have been synthesized.



Scheme 1: Synthesis 3-(2-hexyldecyloxy)propene (**41a**) and 3-(2-ethylhexyloxy)propene (**41b**), (c) Tetrabutylammonium hydrogen sulphate, NaOH (aq.), 45 °C, overnight.

3-(2-Hexyldecyloxy)propene (**41b**) and 3-(2-ethylhexyloxy)propene (**41c**) were prepared by Williamson ether synthesis (Scheme 1) between allyl chloride (**40**) and the corresponding alcohol (**39a-b**) in 70–80% yield. The synthesis was carried out in aqueous sodium hydroxide solution at 45 °C and in the presence of the phase-transfer catalyst tetrabutylammonium hydrogen sulphate (TBAH).¹⁴



Scheme 2. Synthesis of hexa(3-(2-hexyldecyloxy)propyl)-HBC (**45a**) and hexa(3-(2-ethylhexyloxy)propyl)-HBC (**45b**). (a) RT, overnight; (b) NaOH(aq.), PdCl₂(dppf), RT, 5 h; (c) Co₂(CO)₈, dioxane, 125 °C, 5h; (d) FeCl₃/nitromethane, CH₂Cl₂, RT.

The synthesis of hexa(3-(2-hexyldecyloxy)propyl)-HBC (**45a**) and hexa(3-(2-ethylhexyloxy)propyl)-HBC (**45b**) is outlined in Scheme 2. The disubstituted diphenylacetylenes (**43a-b**) were easily synthesized in a one-pot reaction from 4,4'-dibromodiphenylacetylene (**16**), prepared according to a literature procedure.¹⁵ First, hydroboration¹⁶ of (**41a-b**) with 9-borabicyclo[3.3.1]nonane in THF (9-BBN, **26**) at room temperature, overnight, gave the corresponding intermediate organoboranes (**42a-b**), which were then directly used in the subsequent Suzuki coupling¹⁷ with 4,4'-dibromodiphenylacetylene (**16**), in the presence of catalytic PdCl₂(dppf). The reaction was complete after 5 hours at room temperature, and the corresponding disubstituted diphenylacetylenes (**43a-b**) were isolated in 60–70% yield, following column chromatographic

purification. $\text{Co}_2(\text{CO})_8$ mediated cyclotrimerization¹⁸ of (**43a-b**) afforded hexaphenylbenzene derivatives (**44a-b**) in 60 – 80% yield, after workup. The final step for this reaction sequence was the oxidative planarization of the six pendant phenyl rings in (**44a-b**) with concurrent loss of twelve hydrogens. The cyclodehydrogenation¹⁹ was achieved by FeCl_3 in nitromethane to afford (**45a-b**) where the oxygen atoms are located at the δ position of the alkyl chain. Isolated yields after purification using column chromatography were in the order of 80%. The resulting HBC derivatives are yellow in the bulk state, show very good solubility in common organic solvents, and have been characterized by ^1H and ^{13}C NMR spectroscopies, and matrix-assisted laser desorption ionization time-of-flight (MALDI-TOF) mass spectrometry.

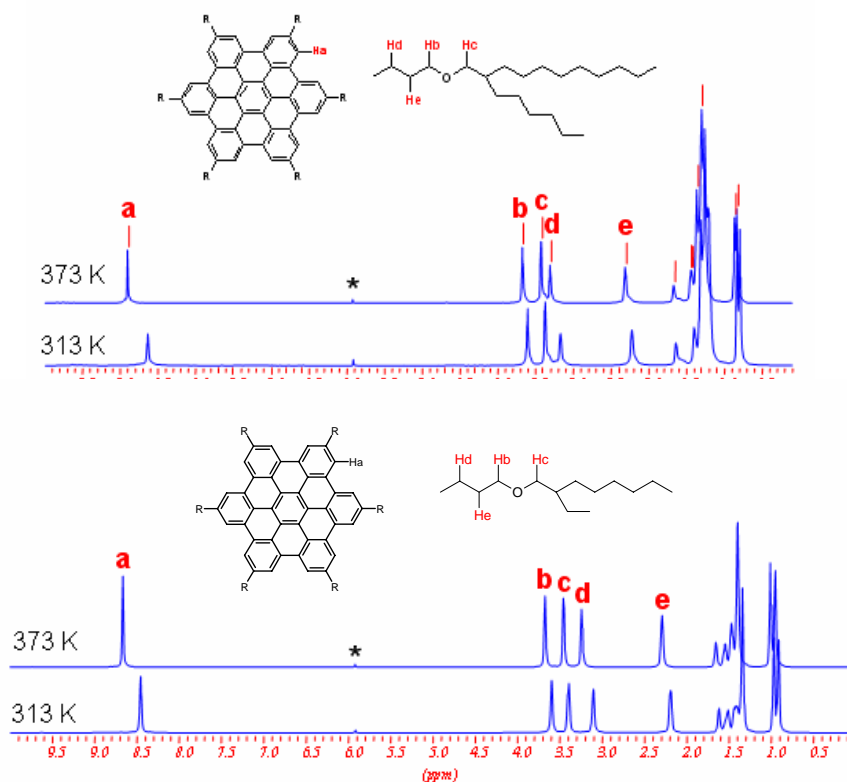


Figure 2: ^1H NMR spectra of hexa(3-(2-hexyldecyloxy)propyl)-HBC (**45a**) and hexa(3-(2-ethylhexyloxy)propyl)-HBC (**45b**) in tetrachloroethane- d_4 (*) at 313 and 373 K.

The ^1H NMR spectra of (**45a-b**) in solution, at 313 and 373 K, are shown in Figure 2. As can be seen, on heating from 313 K to 373 K, the relevant aromatic signals experience a downfield shift of $\Delta\delta = 0.25$ (from $\delta = 8.88$ to $\delta = 8.63$) for (**45a**) and $\Delta\delta = 0.21$ (from $\delta = 8.45$ to $\delta = 8.66$) for (**45b**). A less pronounced shift to low fields can be observed for the protons of the alkyl side chains. It is clear that an increase in the temperature leads to smaller aggregates in solution, a phenomenon widely observed in the HBC and other disc-like systems. The observed shift to lower field by the resonances in the aggregates of (**45a**) and (**45b**) with the increase of the temperature can be explained by the slight increase of the π - π distance during the heating or the decrease of the size of the aggregate where the protons in one HBC molecule localize in the electromagnetic field of the neighboring aromatics, resulting in shielding effects.

4.3 Thermal properties of compounds 45a and 45b

The influence of the substituents on the thermal behavior of the HBC derivatives was followed by using differential scanning calorimetry (DSC). The results were derived from the DSC traces (**45a-b**, Figure 3) and are summarized in Table 1. The phase behavior of the HBC compounds differs significantly, indicating a strong dependence of the thermal behavior on the length and structure of the side chains.

Table 1: Thermal behavior determined by DSC of the investigated HBC derivatives **45a-b**. The recrystallization temperatures and the enthalpies during cooling are given in brackets.

Compound	Temperature [°C]	Enthalpy [J/g]	Phase transition [a]
45a	-1 (-5)	13.8 (12.9)	$\text{Col}_p - \text{Col}_{\text{hd}}$
	162 (155)	2.9 (3.5)	$\text{Col}_{\text{hd}} - \text{I}$
45b	55 (17)	10.5 (8.8)	$\text{Col}_p - \text{Col}_{\text{hd}}$
	~420 (~370)	-	$\text{Col}_{\text{hd}} - \text{I}$

[a] Col_p – plastic crystalline phase, Col_{hd} – hexagonal disordered columnar phase, I – isotropic phase.

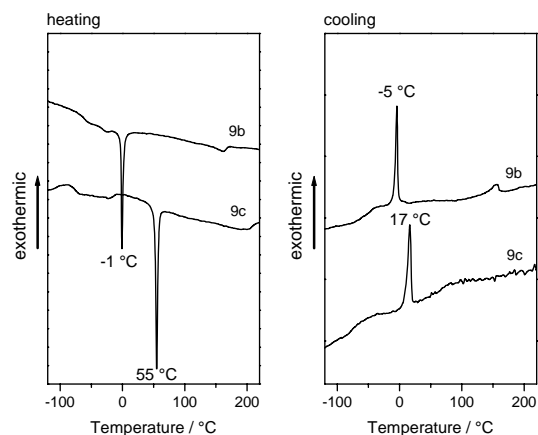


Figure 3: Differential scanning calorimetry traces of (45a-b).

Both compounds (45a-b) investigated were assigned to a plastic crystalline phase in their low temperature state due to their plastic deformation and short-range ordering at room temperature. The T_i of (45a) appeared to be at 162 °C as illustrated in Figure 3. By reducing the length of the side chains, T_i was identified at considerably higher temperature as exemplified by compound (45b). The latter material entered a disordered columnar phase above 55 °C.

4.4 Structure investigation by X-ray scattering of compounds 45a and 45b

The supramolecular organization of columnar systems is particularly important for the one-dimensional charge carrier mobility. Therefore, the intra- and intercolumnar arrangement were investigated using both powder X-ray diffraction of bulk materials and 2D-WAXS experiments of extruded filaments. The pronounced macroscopic alignment of columns along the filaments was indicated by the intense and sharp equatorial reflections corresponding to the intercolumnar arrangement, strongly correlated to the phase of the compounds.

For both compounds (**45a**) and (**45b**), an identical supramolecular order, a hexagonal disordered columnar phase (Col_{hd}) was obtained in the higher temperature solid-state. Based on X-ray scattering results, the intercolumnar arrangement of the two materials was assigned to a two-dimensional, lateral, hexagonal disordered columnar phase, Col_{hd} and showed significant dependence of the packing parameters on the length of the side chains. The bulk hexagonal lattice dimensions decreased from $a = 3.07$ nm for (**45a**) to $a = 2.65$ nm for (**45b**). Figure 4a shows a typical intensity distribution of the derivative (**45a**) in the higher temperature solid-state phase. The material, as obtained from solution, revealed a well-organized, two-dimensional, lateral hexagonal intercolumnar structure as implied by the large number of higher order reflections with peak positions corresponding to a relationship $1 : \sqrt{3} : 2 : \sqrt{7} : 3$. The intracolumnar arrangement was specified by temperature dependent 2D-WAXS experiments. Figure 5 presents examples of characteristic patterns of (**45a**) as an extruded filament. In the mesophase, diffuse meridional reflections in the pattern (Figure 5b) resulted from the disordered intracolumnar packing. Weak off-meridional peaks suggested a slightly tilted intracolumnar arrangement of the disc; whereby the core plane was tilted with respect to the columnar axis. Similar patterns were obtained for compound (**45b**) in its Col_{hd} mesophase. The supramolecular order of bulk (**45a**), however, was considerably influenced by the thermal treatment when heated to the optically isotropic phase. In the isotropic state a small-angle reflection appeared at $s = 0.385 \text{ nm}^{-1}$ as derived from the maximum peak in the X-ray diffraction (Figure 4b). A reflection of this kind can be attributed to positional correlation of molecular aggregates possessing electron density contrast between the aromatic core stacks and the aliphatic substituents. Assuming only nearest-neighbor relations, the correlation distance should be taken as $d = \frac{1.23}{s_{\text{max}}}$.²⁰ This value allows to estimate the number of stacking molecules

in the aggregates as a spherical unit of volume $\frac{\pi}{6}d^3$ which is related to the molecular mass M

by the following equation:

$$\frac{\pi}{6}d^3 = \frac{M \cdot n}{\rho \cdot N_A} \quad (1),$$

where n is the number of molecules; ρ is the density, assumed here to be $1 \text{ g}\cdot\text{cm}^{-3}$ for both nanophases (the aromatic core and the alkyl shell) and N_A is the Avogadro's number by using equation (1), the most probable stacking number of 4.7 molecules was determined for **(45a)** indicating that the molecules in the isotropic state were not isolated as previously assumed, but still form columnar aggregates consisting of several discs.

After slow cooling the sample from the isotropic state, a supplementary small angle reflection appeared due to the enhanced higher-order structure (Figure 4c). Two unit cells were identified from the peak positions and could be assigned to a pseudo-hexagonal arrangement. A hexagonal lattice with twice the dimensions as before the thermal treatment and an orthorhombic unit cell with $a = 5.34 \text{ nm}$ and $b = 3.2 \text{ nm}$, where $a \approx b\sqrt{3}$, can be alternatively be assigned to the observed scattered intensity distributions. The relationship between the packing parameters a and b of the orthorhombic lattice did not fit exactly to the pseudo-hexagonal model because the central column could be displaced slightly from the center of the cell.²¹

The phase transition from the Col_{hd} to the plastic crystalline phase was accompanied by a considerable structural change for the compounds **(45a)** and **(45b)**. During cooling, the degree of intracolumnar order improved leading to a significant intensity increase of the off-meridian reflections in the 2D-WAXS patterns which corresponded to molecular tilting towards the columnar axes.²² Figure 5a illustrates a characteristic, 2D-WAXS result of extruded **(45a)** in the Col_{p} phase. The meridional peak corresponds to the intracolumnar

periodicity of 0.43 nm; whereas the off-meridional reflections are attributed to the cofacial distance of 0.34 nm. Therefore, it was possible to assume a molecular tilting angle between of 30° and 40° similarly observed for compound (**45b**).

The intercolumnar arrangement was determined from the low-angle reflection distribution in the powder X-ray diffraction. The lattice of (**45a**) fitted well to a two-dimensional orthorhombic unit cell with $a = 2.75$ nm and $b = 2.52$ nm as illustrated in the powder diffraction in Figure 4d. The wide-angle part of the scattered intensity distribution revealed discrete periodicities at distances below 0.5 nm which suggests high intracolumnar correlation between the discotic molecules. A two-dimensional monoclinic unit cell with $a = 2.80$ nm, $b = 2.00$ nm, $\gamma = 65^\circ$ was found for (**45a**). Interestingly, an exceptional phase behavior was observed for the molecule **86a** (hexa(3-(2-decyltetradecyloxy)propyl)-hexa-*peri*-hexabenzocoronene in the PhD thesis of Dr. Željko Tomović) for which no intermediate state between the plastic crystalline phase and the isotropic-state phase was detected, in strong contrast to **45a** and other discotic compounds. But in a similar behavior to (**45a**), at the quasi-isotropic state of (**86a**), an aggregation size of nearly five molecules was calculated by means of equation (1).

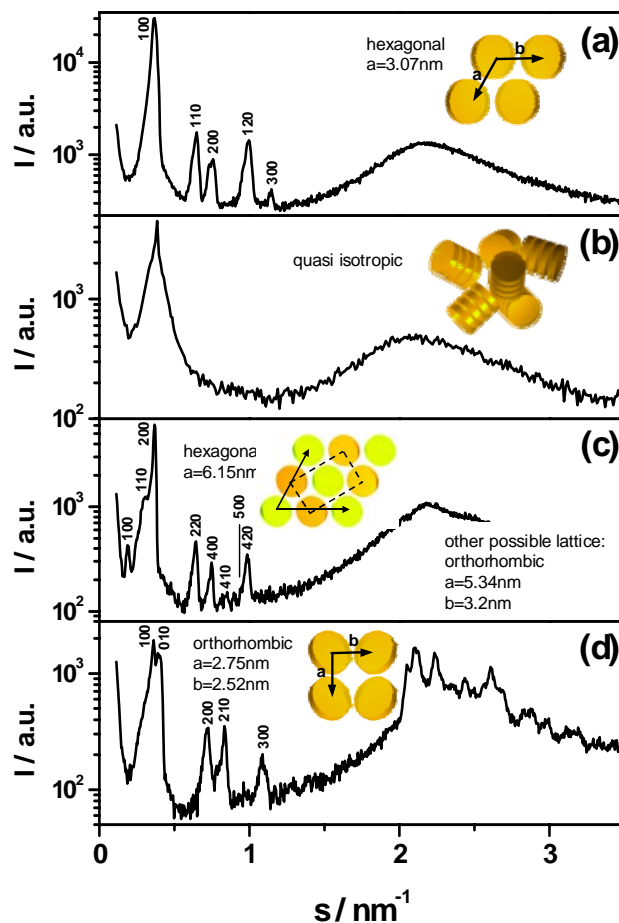


Figure 4: Phase dependent powder diffraction of (45a); the intensity distribution is plotted against scattering vector; a) at room temperature Col_{hd} phase, b) at the isotropic state (inset drawing illustrates schematically the aggregation behavior in this phase), c) cooled back to room temperature (inset presents the two unit cells, arrows indicate the hexagonal lattice and dashed line the orthorhombic unit cell), d) cooled to the plastic crystalline phase. Reflections are indexed by using the Miller's indexes (hk0).

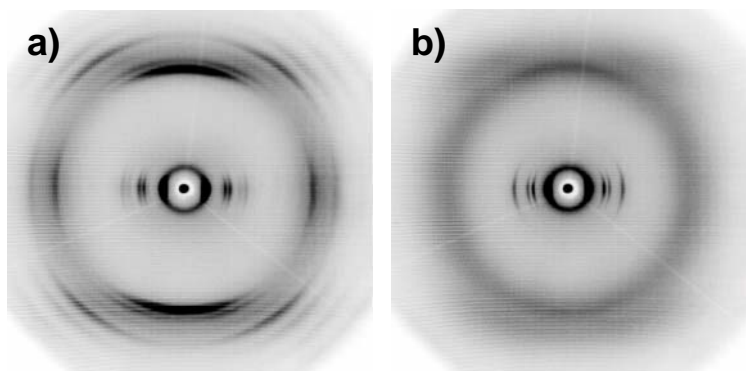


Figure 5: Typical 2D-WAXS pattern of (45a), prepared as an extruded filament, at a) the plastic crystalline phase, and b) in the Col_{hd} phase.

4.5 Homeotropic arrangement of compounds 45a and 45b

Spontaneous homeotropic alignment can be formed for small discotic systems such as triphenylenes and phthalocyanines, bearing alkoxy chains in their core periphery, when crystallized from the isotropic state, whereas HBC-C_{16,4} was the only HBC derivative that successfully oriented in this way,¹³ suggesting that the introduction of the peripheral alkoxy units is not sufficient for the alignment. To enhance the ability to align HBC materials homeotropically the control of homeotropic supramolecular order by the introduction of heteroatoms into the side chains was investigated.

When slowly crystallized from their isotropic state between two polar surfaces as a thin film, both compounds (**45a-45b**) revealed similar morphological behavior. Examples of textures observed by means of the optical microscope are presented in Figure 6 for compound (**45a**). Dendritic textures with a weak contrast with respect to the disordered material were observed in transmitted non-polarized light. However, when cross-polarizers were applied the image became black (Figure 6b). This observation is characteristic for the homeotropic phase where the columnar axis is perpendicular to the substrate, or for an isotropic state. In the first case, since the light propagation coincides with the optical axis, the transmitted light intensity is always zero for all positions of the sample with respect to the analyzer/polarizer axis and there is no anisotropy in the second case. The POM in such configuration does not allow, therefore, these two cases to be uniquely distinguished. By tilting the sample with respect to the light beam by nearly 45°, however, the dendritic areas of the homeotropically aligned sample appeared birefringent, whereas no effect for the isotropic parts was observed. Images from thermally controlled POM in Figure 6a display dendritic structures of (**45a**) formed during crystallization. Interestingly, the angle between the branching was about 60°,

characteristic for hexagonal packing. Despite the directional propagation of these textures, no birefringence was observed in cross-polarized optical microscopy indicating homeotropic arrangement and this was verified by 2D-WAXS measurements. In Figure 7a, the 2D-WAXS recorded with the incident beam perpendicular to the film surface is shown for compound **(45a)**. The diffraction pattern with the six intense, point-like first order reflection maxima uniquely indicates the hexagonal order extending uniformly at least over the area of the X-ray beam cross-section. This is attributed to the hexagonal arrangement of the columns with axes normal to the film surfaces with discs perpendicular to the axes of columns (homeotropic arrangement). An orientational disorder within the hexagonal packing even for areas at large distances would lead to a smearing of the six point diagram to a ring. The observed diffraction indicates a hexagonal monodomain within the scattering volume. It is interesting that this monodomain reveals a two-dimensional dendritic form. With an appropriate exposure, less intense, but distinct higher-order reflections can be visualized (second, third and fourth order reflections) which correspond to hexagonal order as well, and indicate a long-range order in the hexagonal lattice. The first reflection appeared at 3.07 nm, followed by the higher-order peaks which are consistent with the typical relationship of hexagonal packing $1 : \sqrt{3} : 2 : \sqrt{7}$ (Figure 7b). Since the disc axes were orthogonal to the columnar axis, which in turn coincided with the incident beam, the typical reflections corresponding to the π - π stacking did not appear. A schematic drawing of the homeotropic organization between the two surfaces is presented in the inset of Figure 7b.

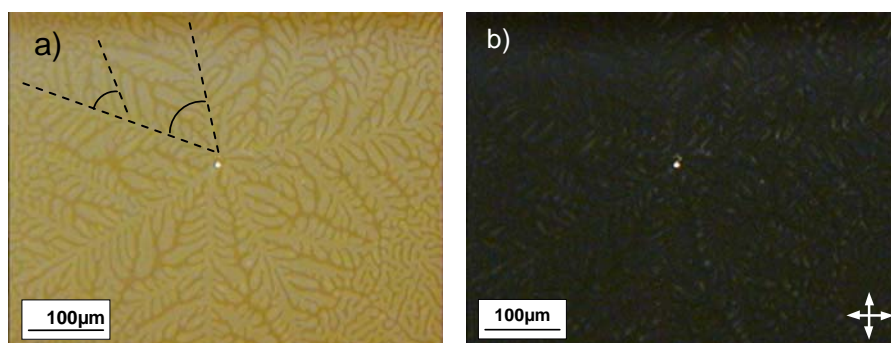


Figure 6: Optical microscopy images of (45a) homeotropically aligned during controlled crystallization between two glass slides a) without and b) with cross-polarizers (dashed lines indicate the propagation direction of the dendritic structures).

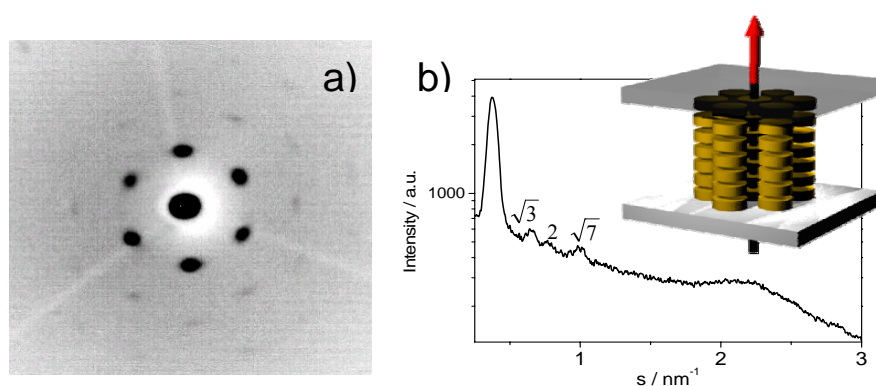


Figure 7: a) Room temperature 2D-WAXS pattern of (45a) crystallized between two thin aluminum foils, showing only the most essential intermediate 2θ range of 2° - 10° ; b) the intensity distribution as a function of the scattering vector. Inset: schematic presentation of the homeotropic alignment between two surfaces during the X-ray experiment. The discs represent the rigid molecular and the red arrow assigns the X-ray beam direction).

The optical axis is oriented along the incident light beam of the microscope and the refractive index of the sample is equal in all lateral directions leading to a black image in the POM. Therefore, the in-plane rotation of the film with respect to the cross-polarizers did not change this observation. In contrast to a hexagonal unit cell possessing one main axis, the arrangement of the columns in a monoclinic resulted in birefringence with high optical anisotropy.²³

Tilting the sample by *ca* 40° with respect to the incident beam resulted in an image with birefringence in the POM. The tilting changed the columnar organization with respect to the incident light and thus the orientation of the optical axis (figure 8).

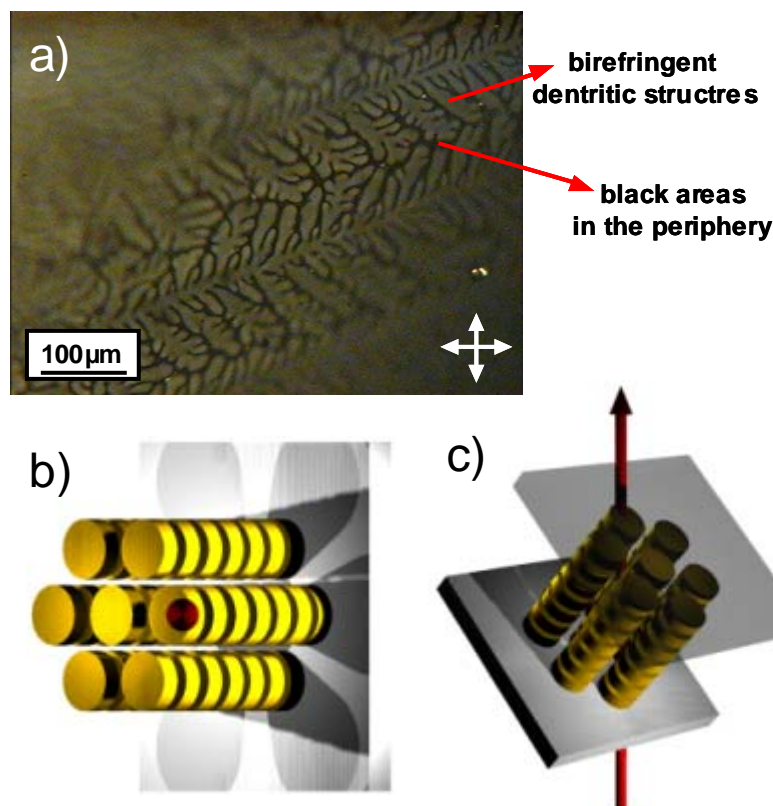


Figure 8: a) Homeotropically aligned film of (45a) tilted with respect to the incident light beam, schematic illustration of the supramolecular organization with respect to the light with b) top and c) perspective view.

Surprisingly, in this case the birefringence appeared homogeneously only on the dendritic structures, whereas the periphery remained black indicating an obvious distinction of alignment and order between these two parts. A rotation of the sample in the plane of the film around the light beam did not change the brightness distribution. The high birefringence of the dendritic morphology was correlated with pronounced order, whereas the black parts in the periphery might imply poor order or even amorphous domains.

This supramolecular organization is in accordance with the results obtained for the bulk sample by powder diffraction. The first appearance of the homeotropic phase of **(45a)** was observed by temperature-dependent 2D-WAXS measurements at 135 °C and remained stable until room temperature. Besides a facile homeotropic alignment between two surfaces, it was of interest to design a molecule which could be ordered in the same manner on one surface. Therefore, films of different thickness of compound **(45a)** were prepared on one glass slide and each sample was identically subjected to thermal treatment. Large differences in the optical textures of these films were revealed by optical images shown in Figure 9. When processed as a thicker film, colorful dendritic-like textures appeared, whereas a characteristic strongly birefringent fan-shaped morphology was obtained with thinner surface layers. The 2D-WAXS (Figure 9d) presented edge-on alignment in both films shown in Figures 9a and 9b. The 360° azimuthal intensity distribution of the first-order reflection corresponding to the "a" cell parameter, as well as the appearance of the wide-angle reflection corresponding to the intracolumnar period, indicated a significant deviation from vertical columnar alignment, whereby the columnar axes were randomly distributed relative to the surface normal. At an appropriately small film thickness (1 μm), dendritic structures were observed (Figure 9c) which did not show any birefringence in cross-polarizers. Further structural investigations using X-ray scattering experiments (Figure 9e) proved an identical intercolumnar arrangement on one surface to be identical to the above-described, characteristic homeotropic, hexagonal order attained between two surfaces.

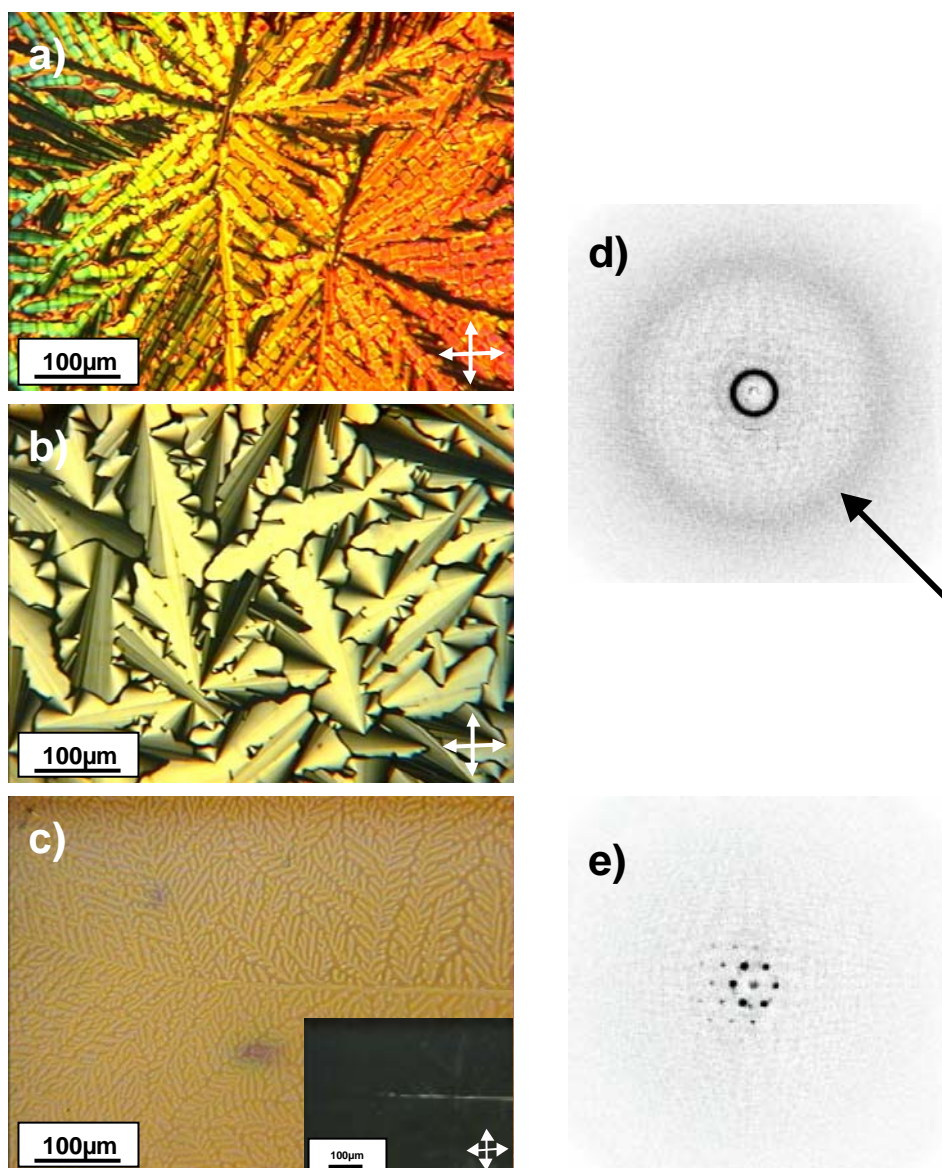


Figure 9: Examples of the characteristic optical textures as a function of film thickness of (45a) crystallized on one glass surface at a cooling rate of 1 °C/min from the isotropic state. POM images a) and b) show the optical textures of the film with different film thickness; whereby a) presents the thickest surface layer. The optical image in c) exhibits characteristic dendritic textures formed on one surface. The same image in cross-polarizers is shown in the inset. The 2D-WAXS pattern in d) reveals the supramolecular structure within the films, which are presented in the POM images a) and b). The arrow indicates the reflection corresponding to the disordered intracolumnar disc stacking. The alignment of the layer in c) is demonstrated by the typical hexagonal 2D-WAXS pattern. Both 2D-WAXS patterns in d) and e) were recorded at identical conditions.

4.6 Synchrotron radiation Microfocus diffractometry of the dendritic morphology

To gain a deeper insight into the local structure synchrotron radiation (SR) microfocus 2D wide-angle X-ray scattering (2D-WAXS) experiments were carried out at the Microfocus beamline (ID13) of the European Synchrotron Radiation Facility (ESRF), Grenoble, France.

The homeotropically oriented film of (45a) was placed perpendicular to the incident X-ray beam. The experiments were carried out in transmission by using a beam spot size at the focal position of approximately $0.8 \times 0.8 \mu\text{m}^2$; the investigated parts of the sample were first monitored by a reflected light dark-field optical microscope. Slice scans of $40\mu\text{m}$ length, covering both fragments the dendritic structures and the non-birefringent periphery, were performed, whereby for each μm an X-ray pattern was recorded. Various parts of the sample were chosen for the structural study to gain a whole picture of the sample. An example of two representative scans is shown in Figure 10. Surprisingly, both fragments revealed an identical hexagonal pattern, which is typical for a homeotropically aligned mesophase, with a packing parameter of 3.07 nm being similar in the bulk state.¹² Moreover, the strong similarity of lateral orientation of the unit cell in different regions indicated a remarkably large monodomain. But it is even more outstanding that the lateral arrangement of the columns was equal in areas which were obviously not related to each other. This phenomenon cannot be explained yet. On the other hand, the intensity distribution of the reflections differed from part to part and could not be correlated to a corresponding area of the sample. Conclusively, both fractions contributing to a high optical contrast revealed the same supramolecular alignment and belonged to a single domain. It was not possible to find grain boundaries.

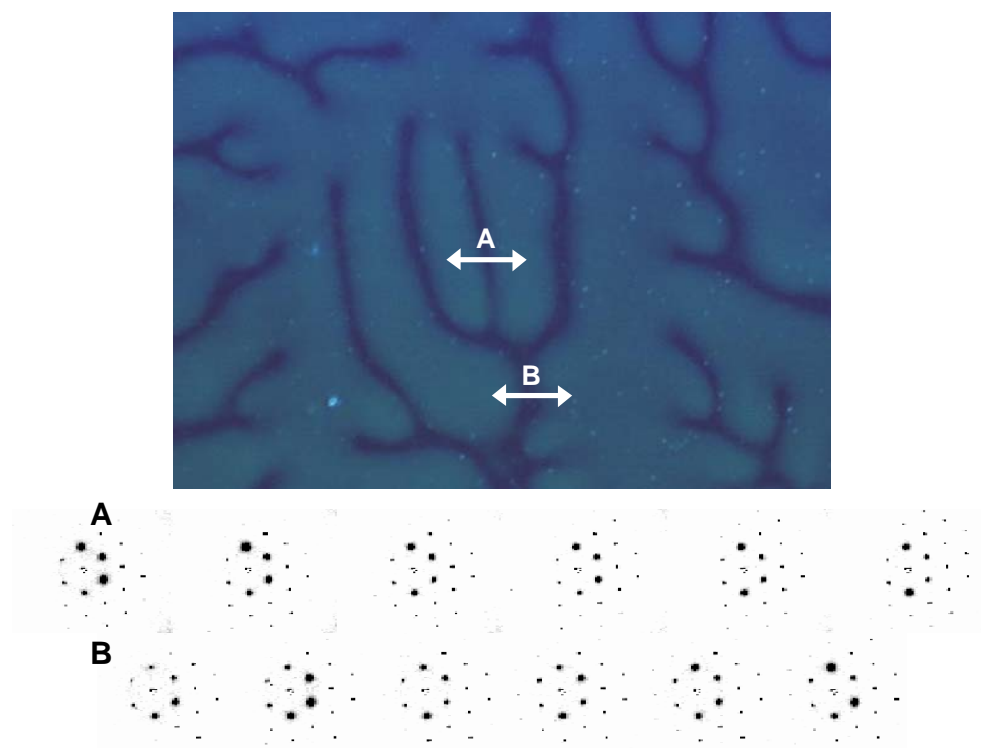


Figure 10: Representative two examples of characteristic SR microfocus X-ray patterns obtained from a slice scan along A and B indicated in the reflected light dark-field optical image. Each μm a pattern was recorded at a scan length of $40 \mu\text{m}$. Due to simplification each 7th pattern of the slice scans in A and B is shown.

For the investigation of the surface contact of both fractions the homeotropically oriented film, which was prepared between two glass slides, was carefully cleaved. Therefore, the sample was cooled down below $-20 \text{ }^\circ\text{C}$ into its plastic crystalline phase to lower the material's viscosity.²⁴ Figure 11a shows the optical microscopy image of one of both glass slides. The dendritic structures were still obvious on the substrate, but not covering the whole glass area and the parts between these assemblies displayed the plain uncovered glass. The second counter glass revealed the same structure distribution. The topography of these microstructures in three dimensions was studied in more detail by using a 3D confocal surface measurement system. For this purpose, the samples were prepared in a slightly different way. After aligning

the material between a glass slide and an aluminum foil, and the aluminum surface was removed in diluted hydrochloric acid. The remaining structures on the glass substrate revealed dendritic shapes with a height up to 3 μm , whereby no material was found in between the residues (Figure 11b,c).

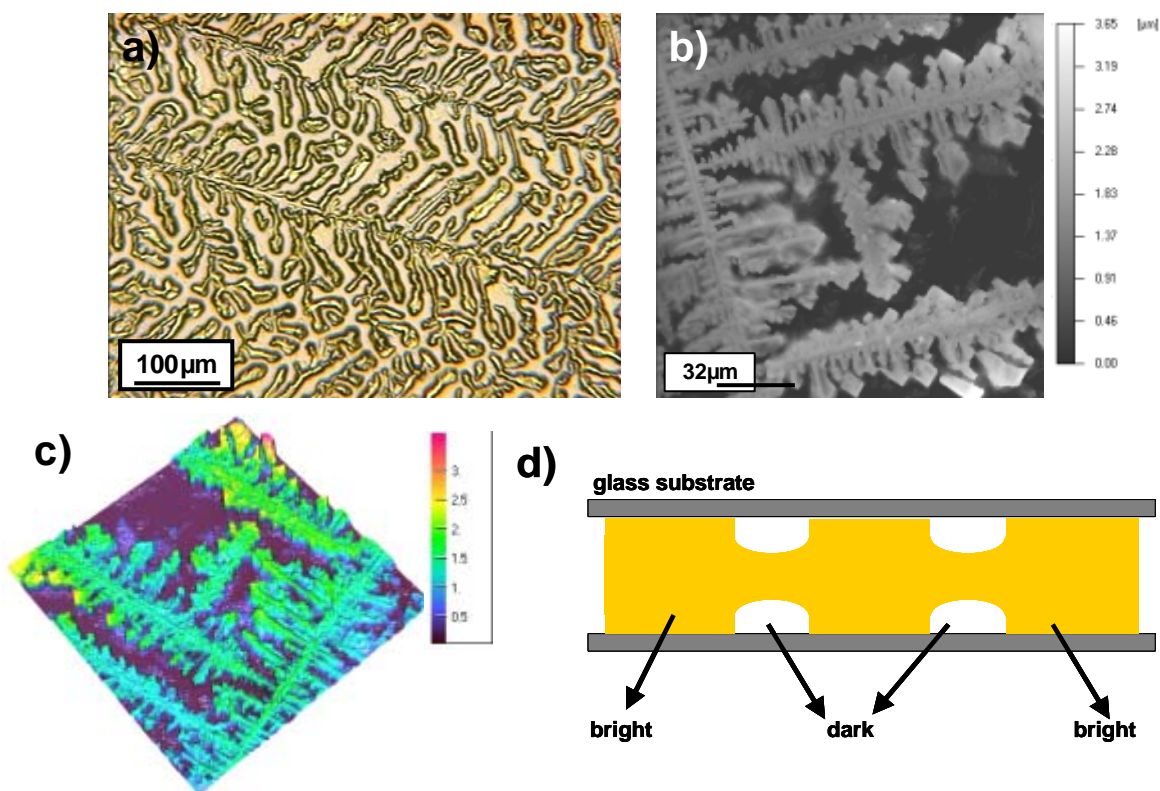


Figure 11: a) Optical image of a homeotropically aligned sample after cleavage, b) height image of the dendritic microstructures on one surface, c) 3D view of the dewetted areas on the glass substrate, d) schematic illustration of the material distribution of a sandwiched sample after cooling from the isotropic phase and the resulting optical contrast in the optical image.

On the basis of the above described results it was concluded that the dendritic morphology observed in the optical microscopy resulted from a dewetting process during crystallization. It can be assumed that the density changed during the solidification at the phase transition between the isotropic phase and the mesophase. A variation of density is accompanied by a

change of volume. Since the sandwiched material was incorporated in a confined volume between the two glass slides, the increase in density and in turn the decrease of volume during crystallization provoked the creation of free macroscopic space leading to the dewetting effect. The optical contrast between areas with and without surface contact was responsible for the appearance of the dendritic structures (Figure 11d). During passing the sample, the light was probably scattered significantly stronger at the thinner dewetted parts and less light reached the optical lens. Consequently, these areas appeared darker, in comparison to the more thicker dendritic structures, in the optical microscopy in transmission, and did not show any birefringence between cross-polarizers. But it should be mentioned that this process did not influence the homeotropic alignment which is remarkably uniform within the film including the dewetted areas.

4.7 Discussion

In order to obtain a highly processible compound, the isotropization temperature had to be lowered considerably. Therefore, the aggregation of the molecules had to be reduced by overcoming the π - π interaction of the aromatic cores. The introduction of bulky, space-filling side chains induced strong steric interactions at the core periphery and modulated the disc's stacking propensity.

Although the branching site was not directly at the aromatic core, the substitution of branched alkyl chains induced a drastic lowering of the isotropization temperature. Additionally, the introduction of strong steric interactions by using space-filling side chains influenced the stacking behavior of the molecules to such a high extent that intracolumnar disorder was generated and the degree of intracolumnar disorder was more significant in the liquid-crystalline phase when the molecular dynamics increased. X-ray scattering experiments

showed that especially in the liquid crystalline phase, the exceptionally long side chains occupy a large volume due to their high mobility in the periphery and disturb the strong interaction between the aromatic cores. As a result of the additional lateral rotation and longitudinal fluctuations in this high-temperature phase, molecules (**45a-45b**) adopted a tilted arrangement towards the columnar axis. The disturbed π - π interaction and increased intracolumnar disorder are disadvantageous because of their dramatic influence on the charge carrier mobility along the columns. This suggestion has to be proven by additional experiments such as time-of-flight measurements. In general, a compromise must be made between lowering the isotropization temperature and maintaining high columnar order at room temperature. For this reason, the branch point was slightly displaced from the core.

Supramolecular orientation and long-range, defect-free order are additional essential characteristics for the design of nano-electronic devices based on one-dimensional self-organized organic materials. One way for obtaining long-range order and alignment is to introduce polar groups into the side chains to increase the affinity of the molecules towards surfaces such as glass. During crystallization from the isotropic state, the molecules first arrange “face-on” towards the substrate, providing seeds for homeotropic growth. It is assumed that this alignment should enhance the electronic performance of intracolumnar charge carrier pathways in photovoltaic cells.

Indeed, the introduction of ether groups in the side chains essentially improved the affinity of the HBC derivatives investigated towards face-on arrangement at the corresponding surface and facilitated a control of the homeotropic alignment. The presence of these polar ether units in the HBC core periphery had a fundamental influence on the self-organization behavior of the molecules on polar surfaces. During controlled cooling between two glass or aluminum surfaces, the materials yielded uniform homeotropic alignment, even at cooling rates

as fast as 20 °C.min⁻¹, proving the high attraction of the polar groups to this kind of surfaces. This can be attributed to the rigid spacer between the aromatic core and the branching site of the side chains as well as to the δ position of the oxygen atom. The spacer induces stability at the δ position from the steric hindrance of the space-filling, dove-tailed side chains and ensures the high affinity of the molecules to the corresponding surfaces. Due to a strong affinity for both studied HBC compounds (**45a-b**) to the applied surfaces, the side chain architecture seems to be most important for the processibility of the material.

Moreover, the strong affinity towards the surface was clearly demonstrated by the successful homeotropic orientation of (**45a**) on only one surface. Thicker films could not be aligned in this geometry. There is evidently some critical thickness above which the governing influence of the surface layer is lost within the bulk of the film or the upper surface, whereby random columnar growth becomes dominant. In contrast, the all-hydrocarbon HBC-C_{16,4}, which showed homeotropic alignment between two surfaces, could not be aligned on one single surface at any of the investigated film thickness or processing conditions. Therefore, while homeotropic alignment is in fact the thermodynamically preferred orientation and does not require heteroatoms for specific molecule-surface interactions, it is greatly enhanced by their presence.

Due to its distinct characteristics, the self-orientation behavior of (**45a**) deserves attention. During cooling between two glass surfaces, the material created dendritic textures which nucleated sporadically and grew at structure edges with columns arranging perpendicular with respect to the growing front, in contrast to other cases with directional growth.⁶ The appearance of the dendritic textures of a homeotropically aligned discotic compound is the effect of the optical contrast between areas with surface contact and dewetted parts. But both fractions possess an identical supramolecular organization and belong to the

same monodomain. The dewetting effect reduces the surface contact of the organic semiconductor, which is critical for the device performance, since the transfer of charge carriers between the active layer and the electrodes might be disturbed. A performance might be expected due to the formation of the dendritic morphology. This is an essential point in the consideration of discotic liquid crystals for the application in organic electronics. The 2D-WAXS and (SR) microfocus 2D-WAXS confirmed the hexagonal homeotropic arrangement which indeed was totally related to the optical texture. Therefore, the structure evaluation suggested an extremely uniform and quasi defect-free hexagonal order without apparent replacements of the lattice over the whole investigated range of the sample. On the other hand, this is in excellent correlation with powder diffraction experiments, which showed that even the bulk material at room temperature forms a well-ordered supramolecular structure with a strong dependence on thermal processing. The only relationship between the macro- and nanoscopic organization is the characteristic 60° angle which appears in both hexagonal two-dimensional lattice and the dendritic morphology.

The homeotropic phase of **(45a)** was stable upon cooling to room temperature, but at 0°C the material underwent structural changes at the solid-solid transition that were related to alterations in the inter- and intracolumnar packing. Since the homeotropic order is formed during the transition from the isotropic state to the mesophase, a hexagonal, two-dimensional lateral columnar arrangement appears, which is characteristic for the liquid-crystalline state. Any change in this intercolumnar arrangement induces defects in the homeotropic alignment which could be observed by POM by cooling the sample below 0°C . At the low temperature, the morphology and macroscopic orientation of the homeotropically aligned sample diminished. Therefore, the absence of significant thermal and structural transitions between the orientation process and application is another important requirement for this kind of

supramolecular order. These requirements are fulfilled for **(45a)**, which was confirmed to be in the Col_{hd} phase at room temperature. However, the low extent of birefringence below 0 °C indicated the high stability of the homeotropic alignment. This suggests a strong and tight surface contact of the molecules, since the bulk compound revealed a considerable structural change at this solid – solid phase transition. Heating the sample back to the higher temperature phase revealed a significant decrease in the birefringent defects and a reversible appearance of the homeotropical texture, thus proving the structure reversibility and confirming the strong interaction of the molecules with the surface.

The observed intracolumnar disorder in the liquid crystalline phase highlights another crucial problem. On the one hand, the space filling side chains provoke this disorder in the intracolumnar packing, which poses considerable disadvantages for applications in electronic devices, since the majority of charge-carrier transport takes place along the columns. On the other hand, however, these bulky substituents are necessary to decrease the aggregation of the molecules and therefore to lower the processing temperature which is essential for processing. This problem is a challenge for the design of new, single building blocks which include both the facile processing from the isotropic state resulting in the desired alignment of the material and the strong self-association leading a high supramolecular order.

4.8 Conclusion

The prohibitively high isotropization temperatures of alkylated hexa-*peri*-hexabenzocoronene derivatives can be overcome by substitution with long, dove-tailed side chains, ensuring the processability of these materials from the isotropic state. Despite the increased peripheral steric contribution from the side chains, both compounds displayed

long-range supramolecular columnar organization in both bulk samples and as thin films in sandwich geometries between two polar surfaces leading to homeotropic alignment. Specific molecule-surface interactions are sufficient, but not necessary, as proven by the previously published alignment of an all-hydrocarbon alkylated HBC between two ITO surfaces. However the tendency toward homeotropic alignment is greatly enhanced by incorporating heteroatoms in the side chains, as they can interact with glass and aluminum surfaces. This allows face-on alignment even at fast cooling rates and, more significantly, on a single surface, which has until now been unattainable with all hydrocarbon HBCs. The latter supramolecular alignment is most likely nucleated at, and grows from, face-on monolayers at surfaces. Homogeneous nucleation and growth of non-oriented columns occurs away from the surface in thicker films, and in films of the weakly interacting discs when not sandwiched between two surfaces. Alignment on single surfaces should enable construction of multilayer devices via the subsequent processing of additional layers. These two issues, practical processability and control over alignment of charge-carrier pathways connecting large area flat electrodes (e.g. in solar cells), are essential to the optimal potential application of columnar-type materials in electronic devices.

Further research activities in our group have resulted in new HBC derivatives whose thermal properties can be effectively controlled by dove-tailed alkyl ether chains (prepared by Ž. Tomović), and investigations concerning their phase behavior and surface interaction are prepared in cooperation with W. Pisula in the group of Prof. Müllen).

¹a) D. Adam, P. Schuhmacher, J. Simmerer, L. Haussling, K. Siemensmeyer, K. H. Etzbach, H. Ringsdorf, D. Haarer, *Nature* **1994**, *371*, 141; b) N. Boden, R. J. Bushby, J. Clements, B. Movaghar, K. J. Donovan, T. Kreouzis, *Phys. Rev. B* **1995**, *52*, 13274 .

² A. M. van de Craats, J. M. Warman, *Adv. Mater.* **2001**, *13*, 130.

³ a) O. Karthaus, H. Ringsdorf, V. V. Tsukruk, J. H. Wendorff, *Langmuir* **1992**, *8*, 2279; b) N. Reitzel, T. Hassenkam, K. Balashev, T. R. Jensen, P. B. Howes, K. Kjaer, A. Fechtenkotter, N. Tchibotareva, S. Ito, K.

- Müllen, T. Bjornholm, *Chem.-Eur. J.* **2001**, *7*, 4894; c) P. Smolenyak, R. Peterson, K. Nebesny, M. Torker, D. F. O'Brien, N. R. Armstrong, *J. Am. Chem. Soc.* **1999**, *121*, 8628.
- ⁴ a) A. Tracz, J. K. Jeszka, M. D. Watson, W. Pisula, K. Müllen, T. Pakula, *J. Am. Chem. Soc.* **2003**, *125*, 1682; b) J. Piris, W. Pisula, A. Tracz, T. Pakula, K. Müllen, J. Warman, *Liq. Cryst* **2004**, *31*, 993.
- ⁵ C. Y. Liu, A. J. Bard, *Chem. Mater.* **2000**, *12*, 2353.
- ⁶ W. Pisula, M. Kastler, D. Wasserfallen, T. Pakula, K. Müllen, *J. Am. Chem. Soc.* **2004**, *126*, 8074.
- ⁷ a) A. M. van de Craats, N. Stutzmann, O. Bunk, M. M. Nielsen, M. Watson, K. Müllen, H. D. Chanzy, H. Siringhaus, R. H. Friend, *Adv. Mater.* **2003**, *15*, 495; b) O. Bunk, M. M. Nielsen, T. I. Solling, A. M. van de Craats, N. Stutzmann, *J. Am. Chem. Soc.* **2003**, *125*, 2252; c) S. Zimmermann, J. H. Wendorff, C. Weder, *Chem. Mater.* **2002**, *14*, 2218.
- ⁸ R. Friedlein, X. Crispin, D. Simpson, M. D. Watson, F. Jäckel, W. Osikowicz, S. Marciniak, M. P. d. Jong, P. Samori, S. K. M. Jönsson, M. Fahlman, K. Müllen, J. P. Rabe, W. R. Salaneck, *Phys. Rev. B* **2003**, *68*, 195414.
- ⁹ P. Samori, M. Keil, R. Friedlein, J. Birgerson, M. Watson, K. Müllen, W. R. Salaneck, J. P. Rabe, *J. Phys. Chem. B* **2001**, *105*, 11114.
- ¹⁰ a) N. Terasawa, H. Monobe, K. Kiyohara, Y. Shimizu, *Chem. Commun.* **2003**, 1678; b) A. N. Cammidge, H. Gopee, *J. Mater. Chem.* **2001**, *11*, 2773.
- ¹¹ K. Hatsusaka, K. Ohta, I. Yamamoto, H. Shirai, *J. Mater. Chem.* **2001**, *11*, 423.
- ¹² a) P. Herwig, C. W. Kayser, K. Müllen, H. W. Spiess, *Adv. Mater.* **1996**, *8*, 510; b) S. Ito, M. Wehmeier, J. D. Brand, C. Kubel, R. Epsch, J. P. Rabe, K. Müllen, *Chem.-Eur. J.* **2000**, *6*, 4327.
- ¹³ C. Y. Liu, A. Fechtenkötter, M. D. Watson, K. Müllen, A. J. Bard, *Chem. Mater.* **2003**, *15*, 124.
- ¹⁴ a) C. Brondino, B. Boutevin, Y. Hervaud, N. Pelaprat, A. Manseri, *J. Fluorine Chem.* **1996**, *76*, 193; b) B. Boutevin, B. Youssef, S. Boileau, A. M. Garnault, *J. Fluorine Chem.* **1987**, *35*, 399; c) D. B. Sharp, T. M. Patrick, *J. Org. Chem.* **1961**, *26*, 1389; d) W. L. Devaney, G. W. Panian, *J. Am. Chem. Soc.* **1953**, *75*, 4836.
- ¹⁵ H. J. Barber, R. J. Slack, *R. J. Chem. Soc.* **1944**, 612.
- ¹⁶ a) H. C. Brown, E. F. Knights, C. G. Scouten, *J. Am. Chem. Soc.* **1974**, *96*, 7765; b) H. C. Brown, R. Liotta, C. G. Scouten, *J. Am. Chem. Soc.* **1976**, *98*, 5297; c) R. Liotta, H. C. Brown, *J. Org. Chem.* **1977**, *42*, 2836; d) H. C. Brown, R. Liotta, L. Brener, *J. Am. Chem. Soc.* **1977**, *99*, 3427; e) H. C. Brown, R. Liotta, G. W. Kramer, *J. Org. Chem.* **1978**, *43*, 1058; f) A. Suzuki, *Acc. Chem. Res.* **1982**, *15*, 178; g) A. Suzuki, R. S. Dhillon, *Topics in Current Chemistry* **1986**, *130*, 23.
- ¹⁷ a) N. Miyaura, T. Ishiyama, M. Ishikawa, A. Suzuki, *Tetrahedron Lett.* **1986**, *27*, 6369; b) N. Miyaura, T. Ishiyama, H. Sasaki, M. Satoh, A. Suzuki, *J. Am. Chem. Soc.* **1989**, *111*, 314; c) M.R. Netherton, C. Dai, K. Neuschütz, G. C. Fu, *J. Am. Chem. Soc.* **2001**, *123*, 10099; d) N. Miyaura, A. Suzuki, *Chem. Rev.* **1995**, *95*, 2457; e) A. Suzuki, *J. Organomet. Chem.* **1999**, *576*, 147; f) A. Suzuki, In *Metal – Catalyzed Cross – Coupling Reactions*; Diederich, F.; Stang, P. J., Eds.; Wiley – VCH: New York, **1998**; Chapter 2.
- ¹⁸ K. P. C. Vollhardt, *Acc. Chem. Res.* **1977**, *10*, 1.
- ¹⁹ S. P. Brown, I. Schnell, J. D. Brand, K. Müllen, H. W. Spiess, *J. Am. Chem. Soc.* **1999**, *121*, 6712.
- ²⁰ A. Guinier, *X-ray Diffraction in Crystals, Imperfect Crystals and Amorphous Bodies*; W. H. Freeman & Co.: San Francisco, CA, 1963.

²¹ M. D. Watson, M. G. Debye, J. M. Warman, K. Müllen, *J. Am. Chem. Soc.* **2003**, *126*, 766.

²² I. Fischbach, T. Pakula, P. Minkin, A. Fechtenkötter, K. Müllen, H. W. Spiess, K. Saalwachter, *J. Phys. Chem. B* **2002**, *106*, 6408.

²³ Kastler, M.; Pisula, W.; Laquai, F.; Kumar, A.; Davies, R. J.; Balushev, S.; Garcia-Gutiérrez, M.-C.; Wasserfallen, D.; Butt, H.-J.; Riekel, C.; Wegner, G.; Müllen, K. *submitted*.

²⁴ W. Pisula, Ž. Tomović, B. El Hamaoui, M. D. Watson, T. Pakula, K. Müllen *Adv. Funct. Mater.* **2005**, *15*, 893.

Chapter 5

Solid-state synthesis of carbon nanotubes and other carbon nanostructures by thermolysis of 2D and 3D cobalt complexes

This chapter is composed of two parts, the first includes the preparation and solid-state pyrolysis of hexa-*peri*-hexabenzocoronene-cobalt complex **50** as a model compound, and the second details the synthesis, characterization and solid-state thermolysis of various graphene and three-dimensional cobalt complexes. All cobalt complexes were characterized by NMR and IR spectroscopy. The powder X-ray analysis of the new hexa-*peri*-hexabenzocoronene-cobalt complex **50** revealed that after complexing HBC with cobalt, no more aggregation was found. The corresponding solid-state pyrolysis afforded multi-walled carbon nanotubes (CNTs) in high carbon-conversion yield. "Bamboo-like" and straight CNTs were obtained under controlled heating procedures. Thermolysis of the graphene precursors afforded mainly CNTs in different ratios, under various heating programs. Similar treatment of tolane (diphenylacetylene) derivatives yielded various carbon nanostructures depending on structure, geometry of precursors and heating conditions. Such novel strategy toward solid-state synthesis of CNTs has promising applications in CNT based nanoelectronics.

5.1 Introduction

Carbon materials in the form of charcoal or soot have been known for a long time. For more than 6000 years carbon materials have been used for the reduction of metal oxides. Nevertheless, only in the year 1779 was the graphite discovered by Scheele to consist of pure carbon. Furthermore, he identified diamond as another allotropic form of carbon. All these “old forms of carbon” are formed either by nature or artificially, under thermodynamic control. The discovery of carbon nanotubes (CNTs) in 1991¹ has stimulated intensive research into the characterization of their structure and the determination of their physical properties,² and their exploitation in a wide range of application forms. However, the controllable solid-state pyrolysis of organometallic precursors, emerged as an alternative method for preparing carbon nanostructures (CNTs), would combine the ease and the low cost synthesis.

Earlier work from the groups of Vollhardt et al.³ and Bunz et al.⁴ showed that the solid-state pyrolysis of metal-dehydro[n]annulene complexes afforded a mixture of carbon onions, tubes, graphite and amorphous carbon.^{4,5} More recently, they have found that solid-state pyrolysis of the tolane-Co complex **46** (Chart 1) afforded carbon nanotubes in nearly quantitative yield.⁶ Later, Müllen et al. observed that pyrolysis of Fe- and Co-phthalocyanines **47a-b** produced nitrogen-containing carbon nanotubes or nanocables with iron-carbide wires within the tubes.⁷ Additionally, the solid-state thermolysis of the dendronized carbon-Co complex affords uniform carbon-Co nanorods which can be subsequently converted into carbon nanotubes under slow heating rates.⁸ All these results show that ultimate carbon nanostructure can be controlled by choosing appropriate organometallic precursors and by controlled thermal treatment.

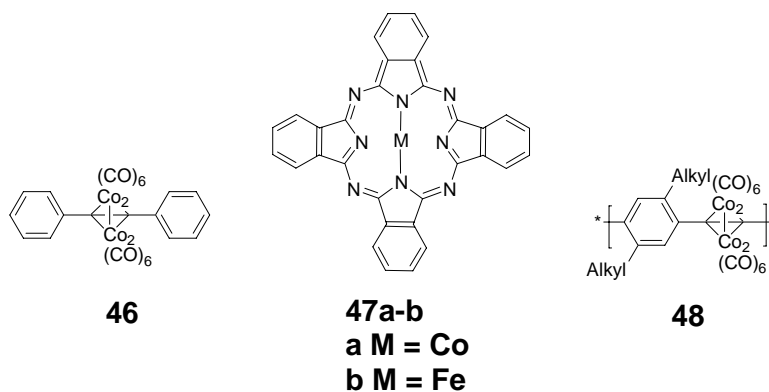


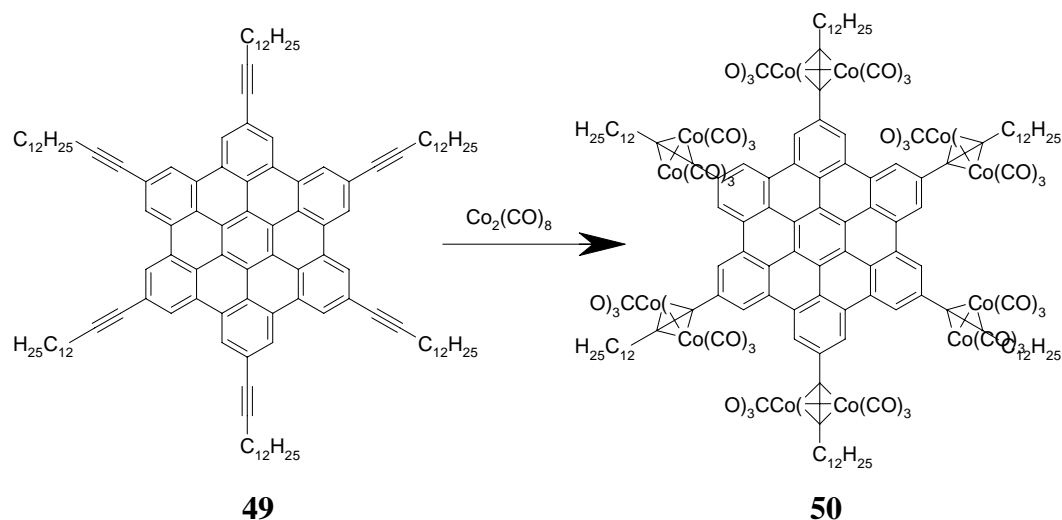
Chart 1

5.2 Preparation and solid-state pyrolysis of complex 50 as a model compound

Herein, we chose large graphitic disk-like molecules such as hexa-*peri*-hexabenzocoronenes (HBCs)⁹ as the model compound, and report that the thermolysis of the HBC-cobalt complex **50** (see Scheme 1) in the solid state affords: 1) multiwalled CNTs in near-quantitative carbon conversion yield, and 2) either uniform “bamboo-like” or straight CNTs selectively by controlling the heating process. Complex **50** contains a graphene segment which is expected to play an important role in the high-yield synthesis of carbon nanotubes.

5.2.1 Synthesis and characterization of complex 50

The choice of organometallic precursor appears to be the key issue for controlling the morphologies (shape and uniformity) and the conversion yield into ordered carbon nanostructures. CNTs with special shapes such as “bamboo” or “Y-shaped” structures are extremely interesting for applications in electronic devices. The Y-junction functions electronically as a semiconductor heterojunction, where a rectifying diode behavior, expected of such a semiconductor heterojunction, has been observed at room temperature.¹⁰



Scheme 1: Synthesis of the complex 50.

Our recent progress¹¹ in the synthesis and functionalization of HBCs allowed the facile synthesis of the cobalt-HBC complex **50** by treating the hexa(1-dodecylethynyl)-perihexabenzocoronenes **49**¹² with excess $[\text{Co}_2(\text{CO})_8]$ in dichloromethane (Scheme 1). After purification by column chromatography, compound **50** was obtained in 50 % yield as an amorphous black powder and characterized by NMR, IR and mass spectroscopic techniques (Figure 1). While the normal alkylated HBCs show ordered columnar structures due to the strong π - π interactions between the aromatic cores, compound **50** exists as an amorphous material because the bulky substitutions suppress the π - π stacking (Figure 2).

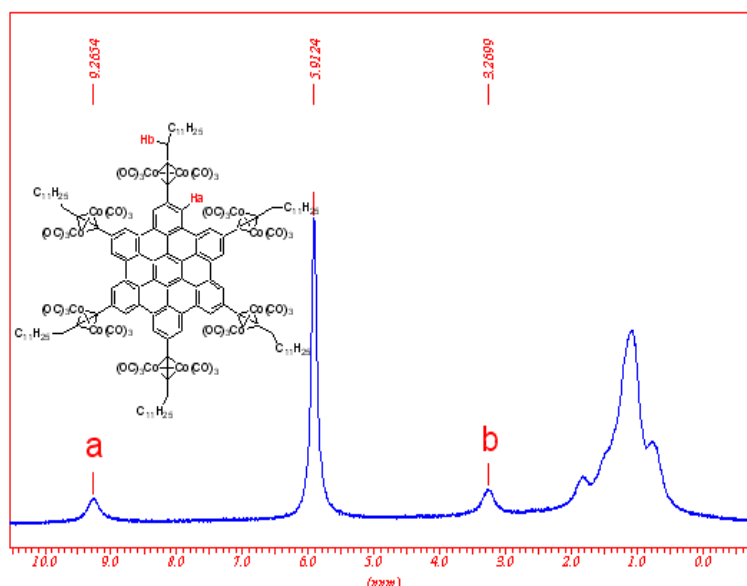


Figure 1: ^1H NMR spectrum of **50**

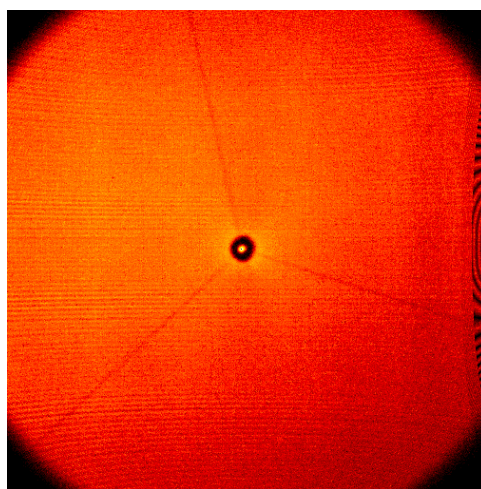


Figure 2: 2D-Wide Angle X-ray pattern of **50**

The powder of compound **50** (typically 10–40 mg) was placed in a quartz tube sealed under high vacuum and different heating processes were used to perform the thermolysis in an oven. The samples were first heated slowly to 250 °C over 2 h and then kept at this temperature for 2 h to ensure complete decomposition of the cobalt complex (According to thermogravimetric analysis (TGA), the cobalt carbonyl $[\text{Co}_2(\text{CO})_6]$ decomposed above 200 °C during the heating

process), Subsequently, the sample was heated to either 600, 800, or 1000 °C over 3 h and maintained at these temperatures for 8 h. After slow cooling to room temperature, a black powder was obtained, which was then analyzed by scanning electron microscopy (SEM) and transmission electron microscopy (TEM).

5.2.2 Results and discussion

The SEM micrographs of the respective materials (Figure 3a, 6a, and 7) show carbon nanotubes with different aspect ratios obtained in high yield, that is, without any other graphitic carbon nanostructures such as carbon onions. They exhibit a cylindrical structure without any obvious compartment layer. Low- and high-resolution TEM images of the material obtained at 800 °C and 1000 °C are displayed in (Figure 3b, 4, 5a, 6b,c, and 9). Interestingly, the sample obtained upon thermolysis at 800 °C mainly yielded bamboo-like carbon nanotubes (Figure 3, 4 and 5) with an average length of up to several micrometers. In Figure 5, the particles of higher contrast visible within the nanotubes were identified as cobalt by EDX (Energy dispersive X-ray spectroscopy) investigation. The metal catalysts were mainly located at the tip of the tube and sometimes were also observed in the separated tube units of the bamboo structure.

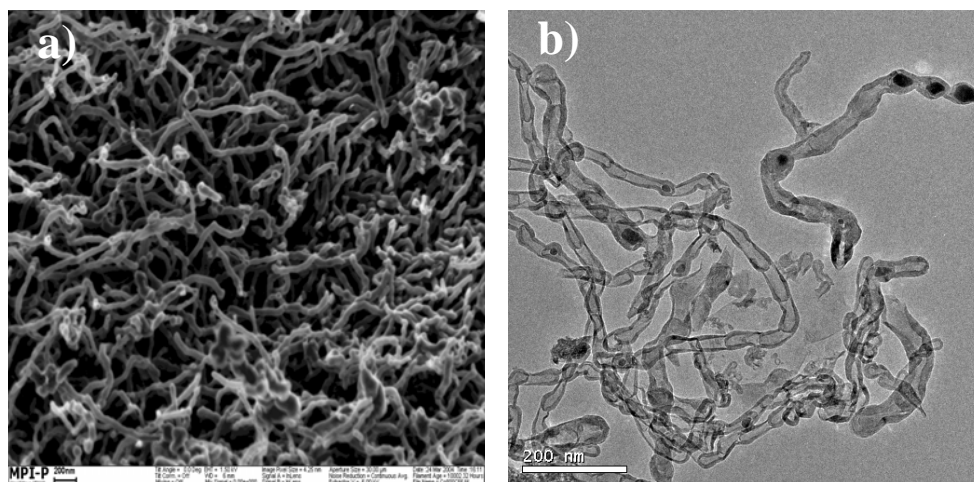


Figure 3: a) SEM and b) TEM pictures of HBC-Co pyrolysed at 800 °C for 8 hours.

A high-resolution TEM image (Figure 4) disclosed that the bamboo-like structures comprised well-ordered graphene layers (normally 10–20 layers in the wall) with an outer diameter of about 20–35 nm and an inner-diameter of about 15–20 nm. The compartments of the bamboo structure also possessed graphene layer structures, which are actually an extension of the graphene layers of the wall. Most of the nanotubes have closed-ended tips, and the curvature observed in the compartment layers is at its greatest at these tips. The bamboo-shaped structures are remarkable and have been previously observed in the nitrogen-doped CNTs^{13,14} or vertically aligned carbon nanotubes prepared by the vapor deposition of acetylene onto iron nanoparticles,¹⁴ in contrast to pyrolysis results from precursor **46**.¹⁵ The mechanism of the formation of bamboo structures is still unknown.¹⁵ The thermolysis of precursor **50** at 1000 °C yielded uniform straight carbon nanotube structures with average tube lengths of several micrometers (Figure 6b and 6c); the catalysts were mainly located at the tip of the tubes. High-resolution TEM characterization identified a narrow diameter distribution of the tubes with outer diameters of about 33 ± 2 nm and inner diameters of about 16 ± 1 nm.

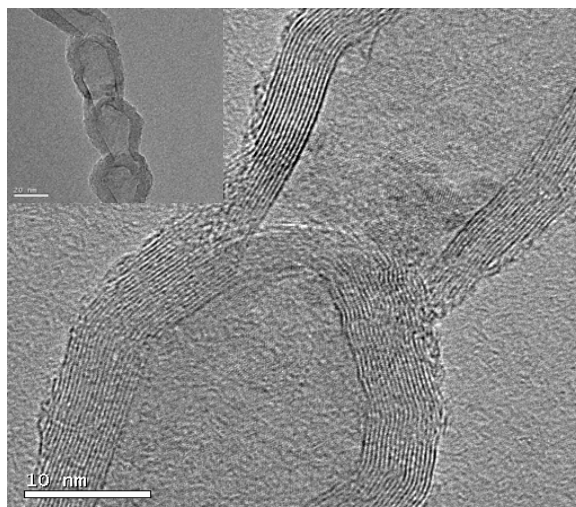


Figure 4: High-resolution TEM picture of HBC-Co heated at 800 °C for 8 hours

The walls of the CNTs comprised 26 graphene layers which were oriented parallel to the tube axis. The highly ordered graphitic structures obtained at this higher temperature indicated the importance of temperature for the ordered wall structures of the CNTs.

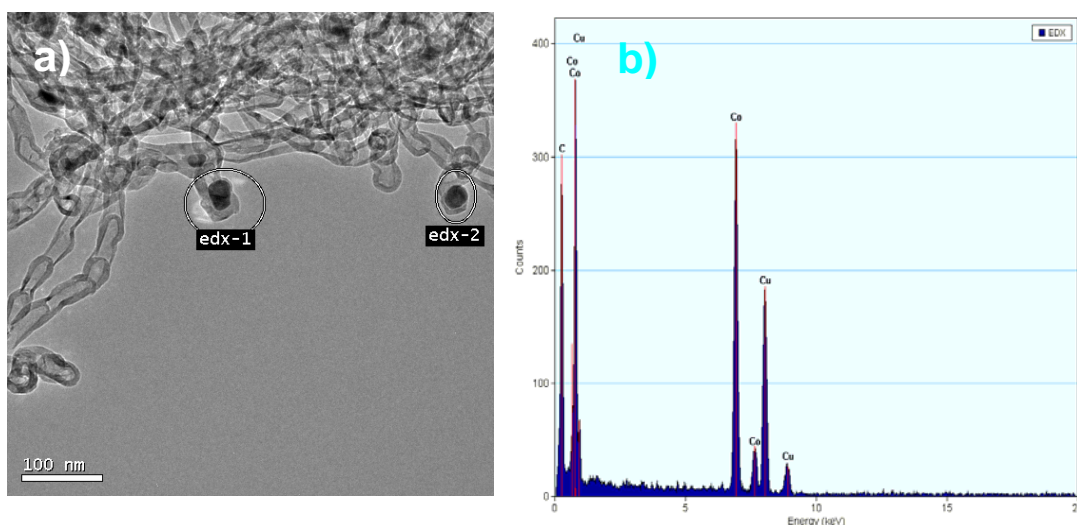


Figure 5: a) TEM picture showing cobalt nanoparticles on the top of the carbon nanotubes grown at 800 °C, b) EDX spectrum of the corresponding cobalt nanoparticles.

The uniform size of the nanotubes is related to the formation of uniformly sized metallic catalysts from the amorphous precursors.

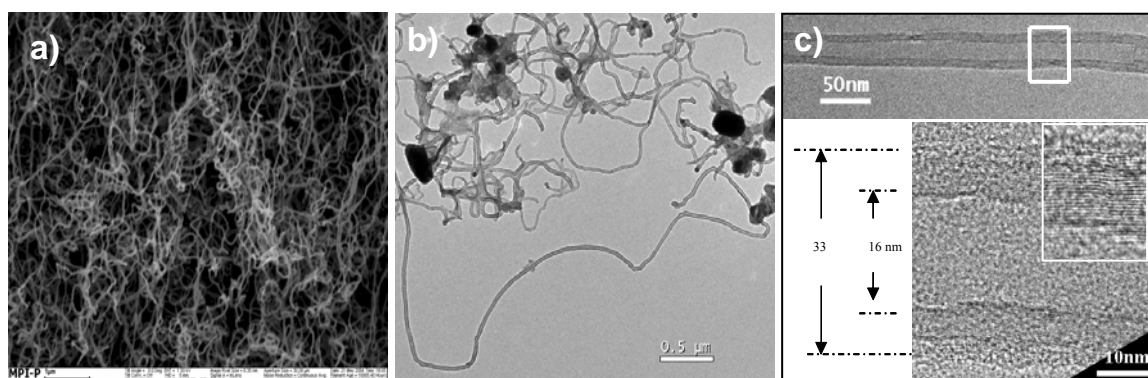


Figure 6: a) SEM and b) TEM pictures of HBC-Co thermolysed at 1000 °C for 8 hours, c) HR-TEM picture disclosing the ordered graphene sheets of the CNT at 1000 °C.

In contrast, the sample treated at 600 °C for 8 h showed short wormlike structures with average lengths less than 200 nm and diameters of about 20–40 nm (Figure 7a). Extending the thermolysis time to 24 h at 600 °C dramatically improved CNT formation (Figure 7b) in terms of length and uniformity, and a mixture of bamboo-like and straight CNTs with an average outer diameter of 44 ± 2 nm and a length of several hundred nanometers was obtained.

To study the effect of the covalent bonding of the cobalt clusters on the HBC core, we thermolysed unsubstituted hexa-*peri*-hexabenzocoronene in the presence of dicobalt octacarbonyl where the latter and HBC have a similar proportion compared to compound **50** (and identical heating procedure). As it was expected, most of the obtained black powder consisted of amorphous carbon and cobalt particles. Only very few carbon nanotubes were obtained (figure 7c). This indicates the importance of the covalent bonding of the cobalt carbonyl with the HBC which allows a uniform distribution of the catalyst precursors in the amorphous solid compared with a simple mixing of the HBC and $[\text{Co}_2(\text{CO})_8]$.

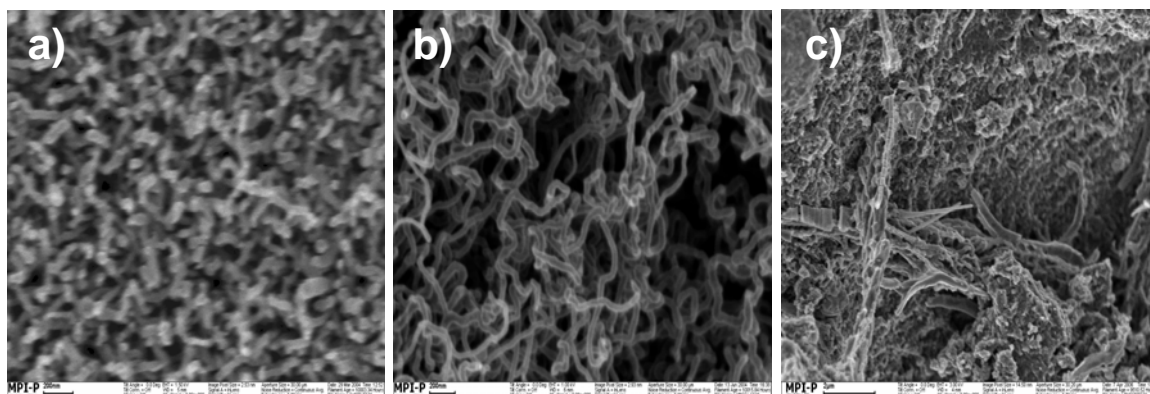


Figure 7: a) and b) SEM pictures of HBC-Co pyrolyzed at 800 °C for 8 and 24 hours respectively; c) SEM picture of the pyrolyzed non-covalent mixture of HBC and dicobaltoctacarbonyl.

To further characterize the CNTs, Raman spectroscopy was used. First-order Raman spectra for the CNTs (from precursor **50**) grown from CNTs obtained at 800 °C and 900 °C are displayed in Figure 8a. Both spectra show mainly two Raman bands at $\sim 1580\text{ cm}^{-1}$ (G band) and $\sim 1350\text{ cm}^{-1}$ (D band). The G band is originated from the Raman active E_{2g} mode due to in-plane atomic displacements. The origin of D has been explained as disorder-induced features due to the finite particle size effect or lattice distortion.¹⁶ It was noted that the intensity ratio of D band to G band (I_D/I_G) has a linear relation with the inverse of the in-plane crystallite dimension.^{16a} the values of I_D/I_G are 1.249, and 1.226, respectively, for the CNTs grown at 800 °C and 1000 °C. This indicates that the degree of long-range ordered crystalline perfection can be smoothly higher for the CNTs grown using 1000 °C compared to those grown at 800 °C. The Raman spectra of CNTs grown at 800 °C and 1000 °C show an increase of the I_D/I_G values with temperature increase.

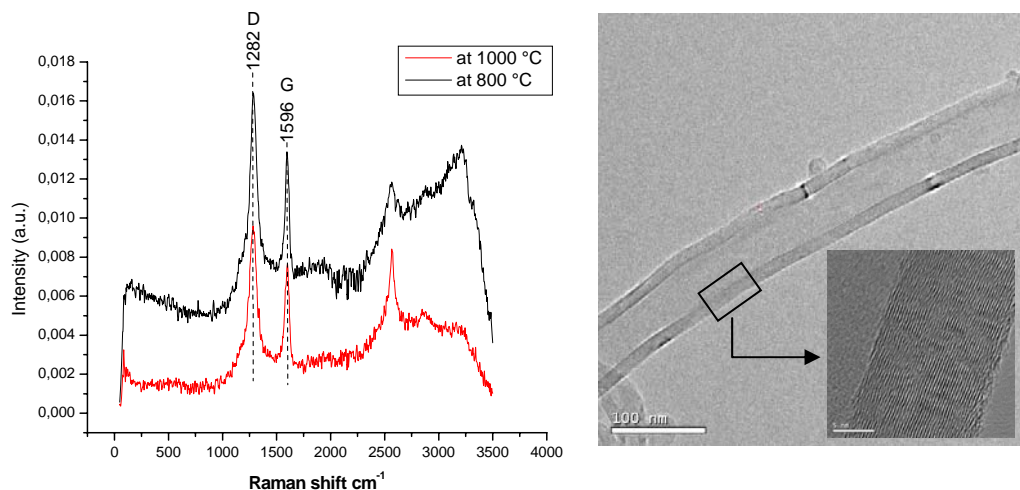


Figure 8: a) Raman spectra of CNTs grown via pyrolysis at 800 °C and 1000 °C, b) TEM of straight CNT grown at 1000 °C. inset is a HR-TEM magnification image.

Figure 8b shows a High-resolution TEM image for typical CNTs grown using CNTs prepared at 1000 °C. The graphitic sheets are aligned parallel to the tube axis. The CNT grown at 1000 °C exhibit a high degree of crystalline perfection in accordance to what is mentioned in the literature.¹⁷ In general the degree of perfection of the graphitic sheets increases progressively with temperature and the outer graphitic sheets are usually less crystalline than the inner graphitic sheets.

In conclusion, efficient solid-state synthesis of carbon nanotubes from graphite islands (HBCs) with a near-quantitative carbon conversion yield have been performed. The obtained carbon nanostructures (either bamboo-shaped or straight CNTs) depend on the heating process employed. Potential applications of this solid-state CNT synthesis include the selective growth of nanotubes by printing precursors onto certain surfaces followed by thermolysis, or pyrolysis of the precursors in porous templates,^{2d,18} the modification of SPM tips,¹⁹ and the fabrication of heterostructures of CNTs and metal carbides.²⁰ The non-volatility of the graphite island in the precursor complexes and the capability of CNT formation in the solid state may allow the in situ monitoring of CNT growth by TEM at high temperature without contamination.²¹

5.3 Cobalt complexes with various structures and geometries

To gain further understanding of the role of molecular structure on the carbon nanoobject formation, we herein represent the preparation of a series of systemically varied organometallic molecules carrying carbon-rich moieties and metal-centers, and the investigation of their solid-state pyrolysis products (Chart 2). Given the facile synthesis of the Co-carbonyl complexes and the efficiency of the cobalt catalyst for nanotube formation, most of the organometallic precursors that have been designed (**52**, **55**, **57**, **59**, **61**, **63** and **67**) contain $[\text{CCCo}_2(\text{CO})_6]$ moieties, with the exception of compound **67** in which ruthenium is incorporated. Precursors with carbon-rich frameworks based on linear and branched oligophenylenes, in contrast to disc-shaped graphene-containing precursors (such as **50**), have been studied; and that allow us to further probe the importance of the graphitic fragments on the formation of graphitic CNTs.

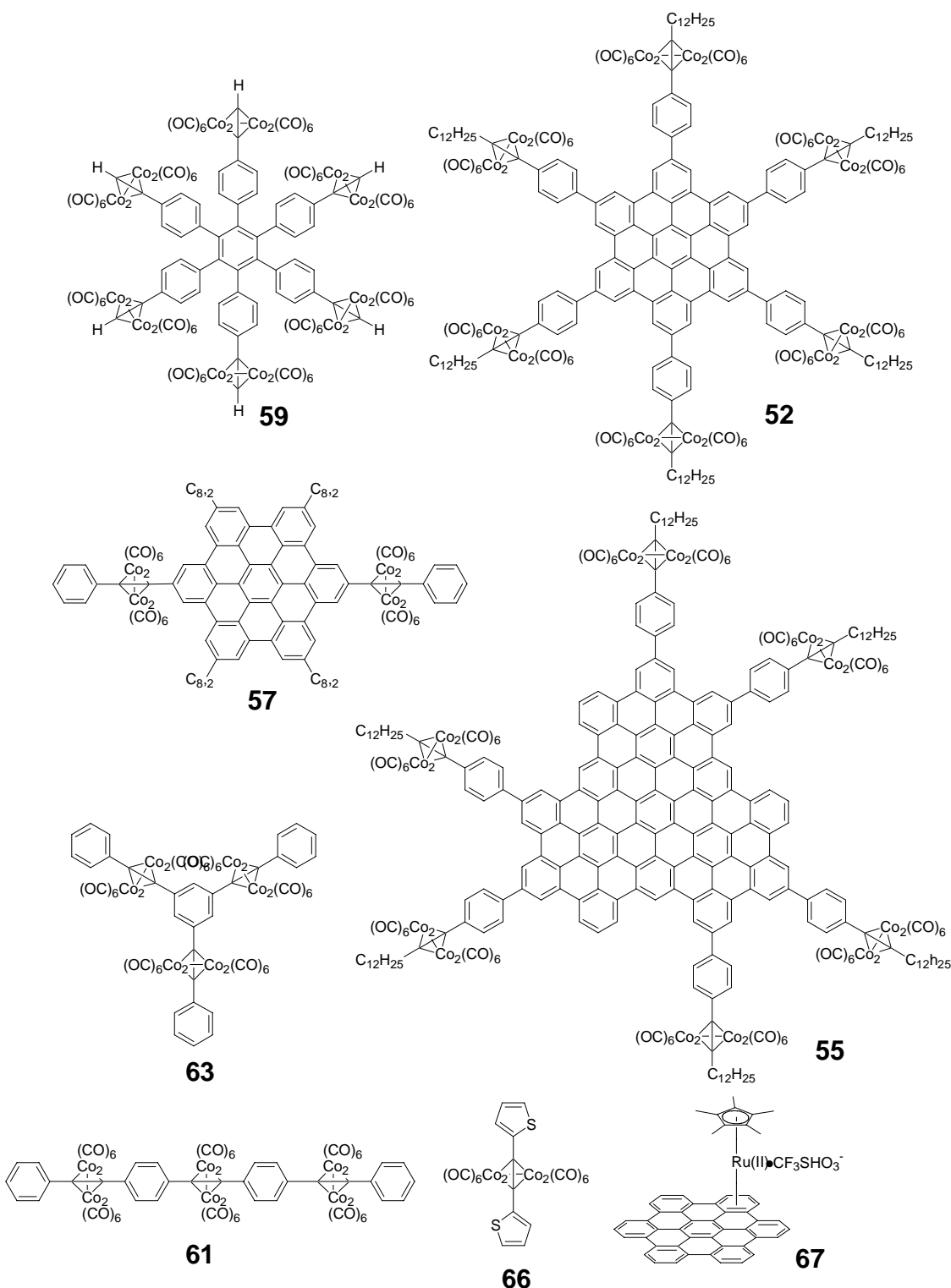


Chart 2: chemical structures for complexes **52**, **55**, **57**, **59**, **61**, **63**, **66** and **67**

The metal loading of organometallic precursors has also been varied (compare **59**, with only two $[\text{CCCo}_2(\text{CO})_6]$ moieties, to **50**, **52**, or **55** which contain six), and this helps to better

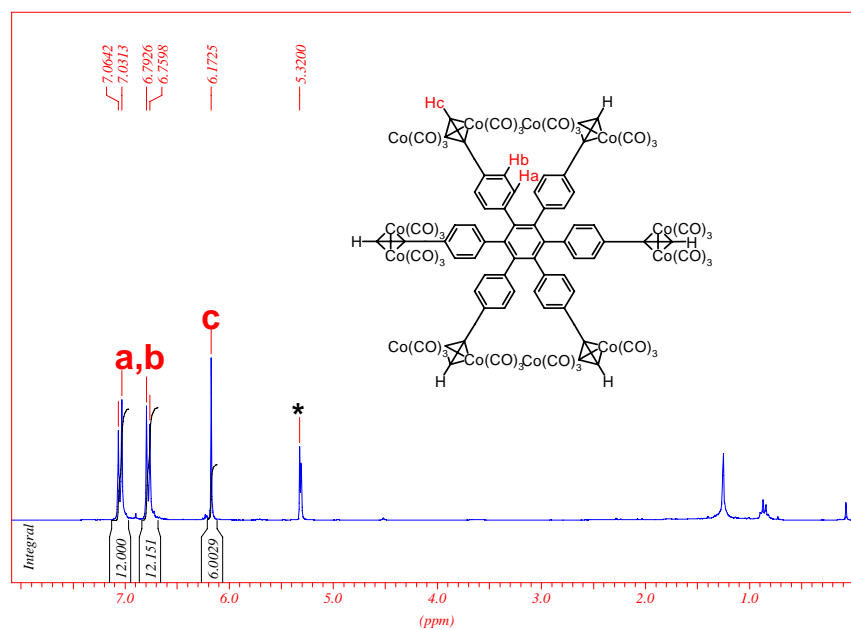
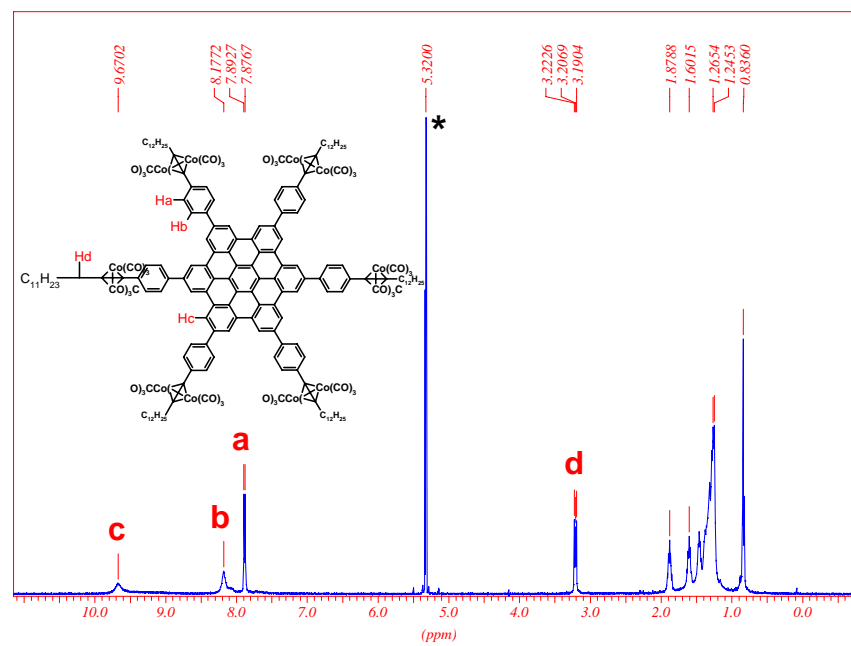
understand the importance of the carbon-catalyst ratio. The high-yielding synthesis of CNTs from the simple diphenylacetylene-Co complex **46** also encourages us to study in more detail some related structures; compounds **63** and **61** having identical elemental compositions but different geometries have been prepared. Further **66**, a simple dithionyl analogue of compound **46**, has been investigated to understand the effect of sulfur heteroatoms. Finally, the sandwich complex **67**, in which the HBC core ligates a Ru atom provides further variation, not only to metal type, but also its mode of attachment to the carbon reservoir.

5.3.1 Synthesis and characterization

The dicobalthexacarbonyl complexes were all prepared by reaction of an ethynyl-functionalized organic framework with excess $[\text{Co}_2(\text{CO})_8]$ to afford $[\text{CCCo}_2(\text{CO})_6]$ -containing complexes. Both IR and NMR spectroscopy indicate complete occupancy of the alkyne sites by dicobalt hexacarbonyl fragments. The synthesis of compounds **52**, **55**, **57** and **59** is shown in Scheme 2. Compound **59** was prepared by simple complexation of hexakis(4-ethynylphenyl)benzene (**58**) with $[\text{Co}_2(\text{CO})_8]$ in 25% yield.²² The incorporation of six cluster units was clearly established from the diagnostic shift in the ^1H NMR spectrum of the alkyne proton signal from $\delta = 3.02$ ppm in **58** to $\delta = 6.17$ ppm in **59** (figure 9). Similarly, complex **52** was prepared from the star-shaped hexakis[4-(dodecylethynyl)phenyl]-*peri*-hexabenzocoronene (**51**)^{11a} in 60% yield. The singlet resonances from the protons attached to the HBC core and the doublets resonances from the attached phenyl protons shifts to lower fields (figure 10) upon complexation of the acetylenic bonds with cobalt (from 8.00, 7.51 and 7.34 to 9.67, 8.17 and 7.88 ppm respectively). Additionally, (**52**) is soluble in most organic solvents, even hexane (typically used to precipitate HBC materials like (**51**)). Because of the

high deshielding effect and the high enhanced solubility, we suggested that the clustering of the cobalt atoms on the triple bonds around the HBC core decreases dramatically the aggregation effect of the HBC core. We recently reported the giant D_{3h} symmetric graphitic disc and although insoluble in most of organic solvents, it can be functionalized by Pd-catalyzed Hagihara-Sonogashira coupling reactions (prepared and provided by Ž. Tomović).²³ The coupling reactions between **53** and 1-tetradecyne proceeded smoothly and gave the partially soluble compound **54** in 76% yield. Complexation of **54** with $[\text{Co}_2(\text{CO})_8]$ afforded the readily good soluble complex **55** in 47% yield.

In the ^1H NMR spectrum of hexadodecyl-C96,^{23c} regardless of solvent and temperature (up to 170°C), resonances arising from the mobile alkyl side chains could be resolved, but not those of the aromatic-core protons due to low mobility and the multitude of local environments associated with dynamic aggregation. Herein it was possible for compound (**55**) to obtain an aromatic signal between 6 and 7 ppm, probably due to the presence of the adjacent phenyl protons of the aromatic core. The presence of cobalt clusters around the big aromatic core helped to allow the visualization of the aromatic protons probably due to a decrease in the aggregation, since the precursor **54** was poorly soluble in most organic solvents and became, after complexation and purification with column chromatography, highly soluble in dichloromethane and THF. The broad signals between 4 and 0.5 ppm correspond to the alkyl chain protons. Compound **56** was prepared from the '*para*'-dibromo-substituted HBC **21**,²⁴ by a Hagihara coupling reaction with phenylacetylene. The corresponding compound **57** was obtained in 48% yield upon mixing with $\text{Co}_2(\text{CO})_8$ in dichloromethane at room temperature for 36 hours.

Figure 9: ^1H NMR spectrum of 59Figure 10: ^1H NMR spectrum of 52

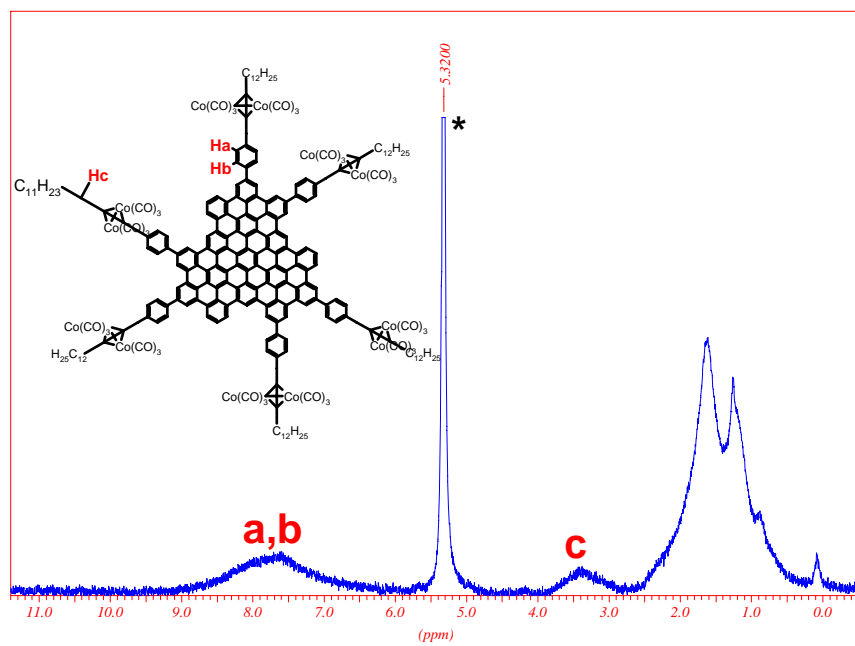
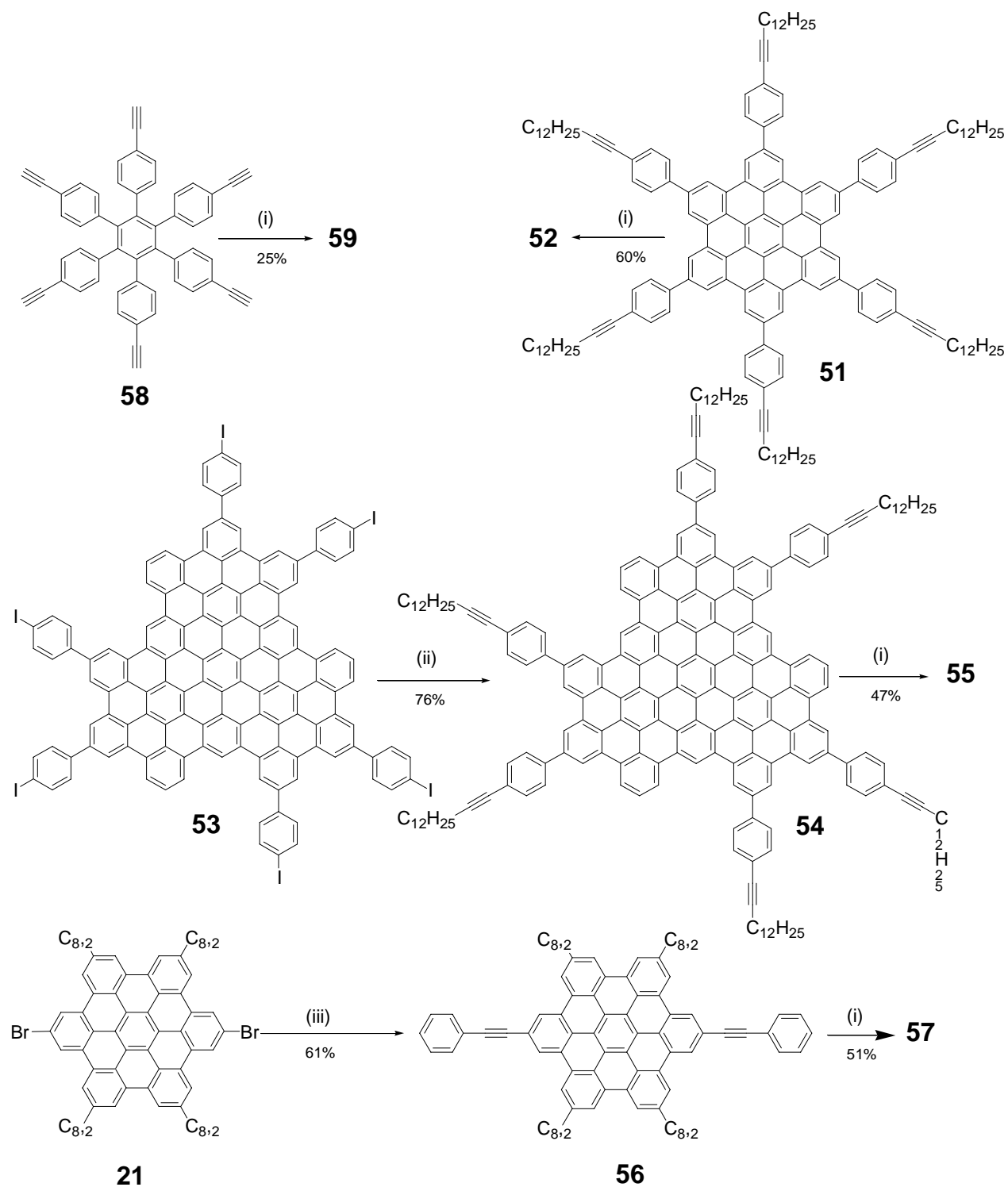
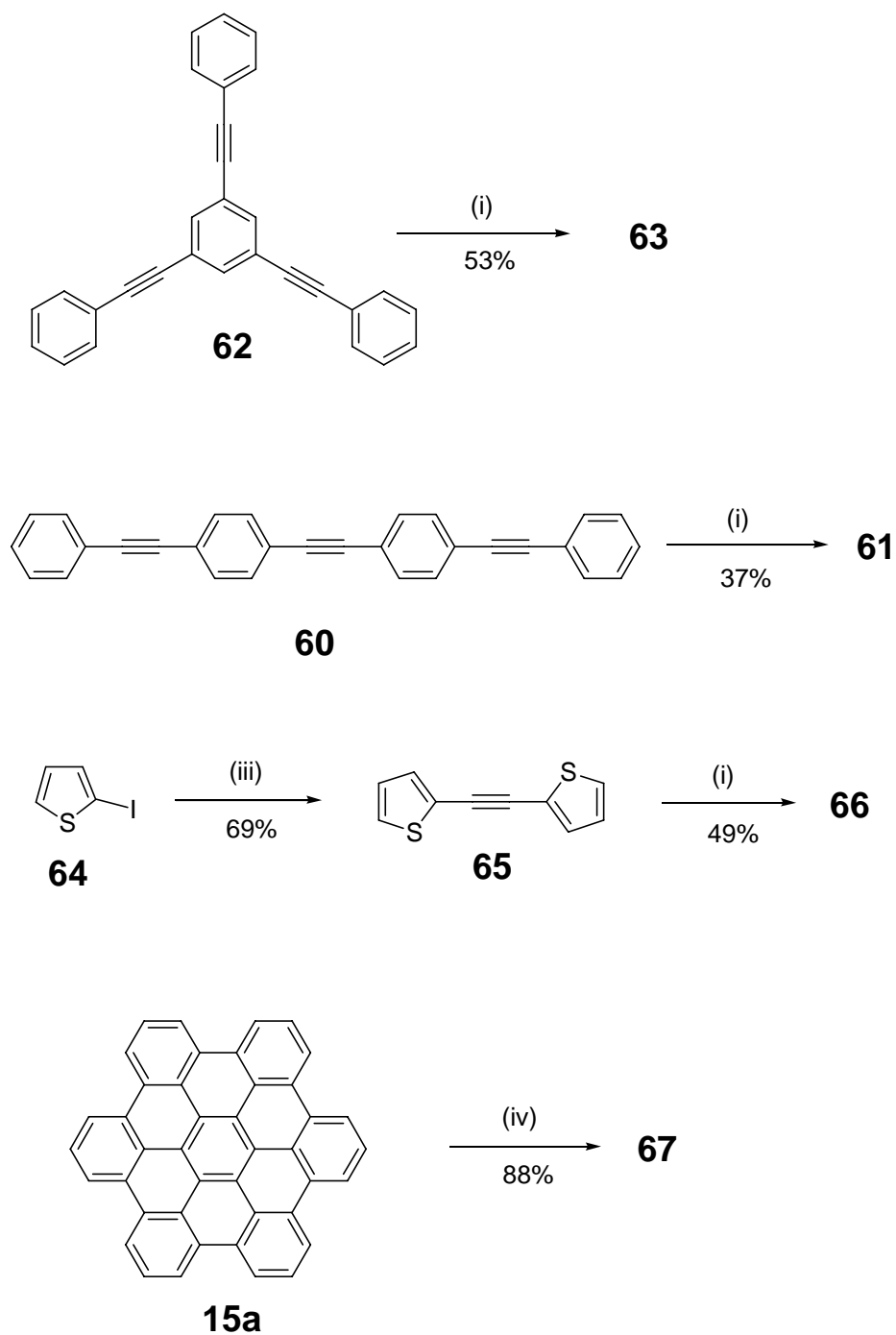


Figure 11: ^1H NMR spectrum of 55



Scheme 2: (i) $\text{Co}_2(\text{CO})_8$, CH_2Cl_2 , rt, 2 days; (ii) 1-tetradecyne, $\text{Pd}(\text{PPh}_3)_4$, CuI , PPh_3 , piperidine, 50°C ; (iii) phenylacetylene, $\text{Pd}(\text{PPh}_3)_4$, CuI , PPh_3 , piperidine, 80°C , overnight.



Scheme 3: (i) $\text{Co}_2(\text{CO})_8$, CH_2Cl_2 , rt, 2 days; (iii) 2-iodothiophene, $\text{PdCl}_2(\text{PPh}_3)_2$, CuI , DBU, trimethylsilylethyne, water, 18 hours, rt; (iv) $[\text{RuCp}^*(\text{NCMe})_3](\text{OTf})$, CH_2Cl_2 , reflux, 24 h. (Cp^* = pentamethylcyclopentadiene)

The non-PAH compounds **61**, **63** and **66** were prepared via the same method described above (Scheme 3). Complexation reactions of **60**²⁵ and **62** with $[\text{Co}_2(\text{CO})_8]$ afforded **61** (53% yield) and **63** (37% yield), respectively. A single-step Hagihara coupling reaction of 2-iodothiophene (**64**) with trimethylsilylacetylene, with *in situ* desilylation, provided 2,2'-dithiophenylacetylene **65** in 69% yield.²⁶ Complexation of **65** with $[\text{Co}_2(\text{CO})_8]$ afforded compound **66** in 49% yield.

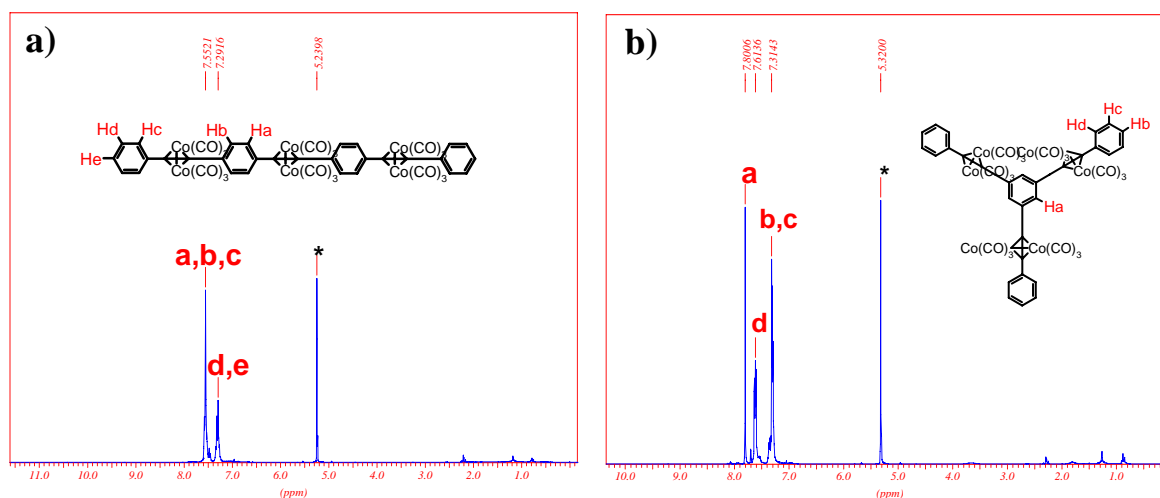


Figure 12: ¹H NMR spectra of a) **61** and b) **63**

The poorly soluble HBC-Ru complex **67** was prepared in 88 % yield by reaction of hexa-*peri*-hexabenzocoronene (**15a**) with the reactive $[\text{RuCp}^*(\text{NCMe})_3](\text{OTf})$ complex in refluxing dichloromethane. The RuCp^* moiety is thought to coordinate to one of the outer phenyl rings of the HBC by analogy with a related complex that has been characterized by single-crystal analysis (synthesized by N. Lucas).²⁷

The complexation of ethynyl moieties with $[\text{Co}_2(\text{CO})_8]$ was confirmed by NMR, FT-IR and mass spectroscopic analysis of the complexes. In the FT-IR spectra, three strong absorption bands in the region of 2019-2094 cm^{-1} (ν_{CO}), typical for $[\text{Co}_2(\text{CO})_6\text{RCCR}]$ clusters, were observed. The ¹H and ¹³C NMR spectra disclosed distinct signal shifts for the protons and

carbons of the ethynyl groups, indicating complete complexation at these sites. Poor solubility of the ruthenium complex **67** precluded solution spectroscopic characterization. A positive ion MALDI-TOF spectrum of the reaction product indicated complete consumption of HBC **15a** and a signal centered at $m/z = 759$ corresponding to the molecular ion $[\text{RuCp}^*(\text{HBC})]^+$.

The powder of the metal complexes (typically 20-100 mg) was sealed in a quartz tube under vacuum, and submitted to different heating programs in an oven. The samples were first heated to their decomposition temperature (usually 200-250 °C as predetermined by TGA analysis), held for 2 hours or more to ensure the complete decomposition of the cobalt complexes, and then heated to a higher temperature for several hours with a controlled heating rate. After slow cooling to room temperature, the black powder was submitted to scanning electron microscopy (SEM) and Transmission Electron Microscopy (TEM).

5.3.2 Results and discussion

Slow heating (~ 1 °C/min) of the HBC-Co complex **52** to 800 °C and holding at this temperature for 24 hours yielded uniform multi-walled CNTs in high yield. Interestingly, at the surface of the quartz substrate, the CNTs tended to epitaxial growth (Figure 13a and 13b). Despite the structure similarity of precursors **52** and **50**, **52** was expected to produce high yield of CNTs under similar heating conditions, but it seems that the presence of the phenyl ring between the HBC core and the cobalt nanoclusters diminishes the influence of the metal activity toward the HBC core upon heating to high temperatures (if compared to the main precursor **50**). Moreover, it seems surprising that the chemical structure promoted a unidirectional CNTs growth. Obviously, the quartz tube is working as supporting substrate to provide unilateral growth of the homogeneously dispersed carbon nanofibers on surface. TEM

analysis showed that the average outer diameter is around 21 nm (Figure 13c). The distribution of the inner diameter is in the range 7-10 nm. Accordingly, the tube wall thickness varied between 1.25 and 5.5 nm. It was also observed that some of the nanotubes were attached with small cobalt nanoparticles (~ 15 nm) located in the end of their tips. The similarity in size of these encapsulated cobalt nanoparticles clearly indicates that the dimensions of the nanotubes are determined by the size of the catalytic particles (figure 13d). The Co particles have a diameter of 15-50 nm, some of which were observed at the tip of the tubes. On the other hand, under a fast heating rate ($10^\circ\text{C}/\text{min}$), only a very small amount of carbon nanotubes was observed, underscoring the importance of a slow heating rate on the carbon nanotube formation.

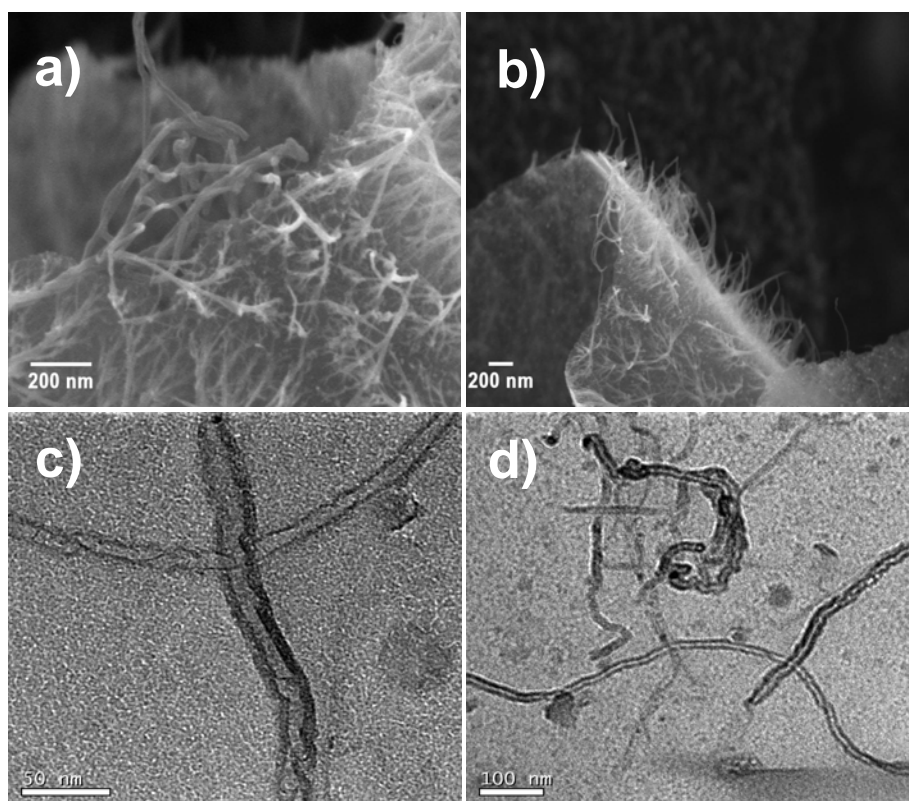


Figure 13: a),b) SEM and c),d)TEM pictures showing epitaxially grown CNTs by thermolysis of compound **52** at $2.9^\circ\text{C}/\text{min}$ from rt to 200°C , holding at 200°C for 2 hrs, then heating to 800°C at rate of $\sim 1^\circ\text{C}/\text{min}$, and then holding for 24 hrs.

Heating of the larger graphene molecule-Co complex **55** at 800 °C for 8 or 24 hours also afforded multi-walled CNTs in high yield (Figure 14a and 14b), suggesting that 8 hours is sufficient to afford a high yield of carbon nanotubes. The crystalline Co catalyst particles were mainly located at the tip of the CNTs and wrapped in ordered graphene layers (Figure 14c). Electron diffraction analysis of the Co particles demonstrated that the Co crystal formed here has a regular hexagonal lattice parameters of 2.5 and 16 Å, which is a new Co crystal other than cubic closed-packed (ccp) and hexagonal close-packed (hcp)^{7b,8} (Figure 15). The carbon nanotubes have a uniform size with an inner diameter of ~14 nm and an outer diameter of ~30 nm (Figure 14d). The uniform size of the nanotubes is related to the uniform formation of the metallic catalyst from the amorphous precursor. Interestingly, unlike the wall structures of normal multi-walled carbon nanotubes which usually have long-range oriented graphene layers along the tube axis, here the wall of CNTs are constituted from tilted graphene segments.

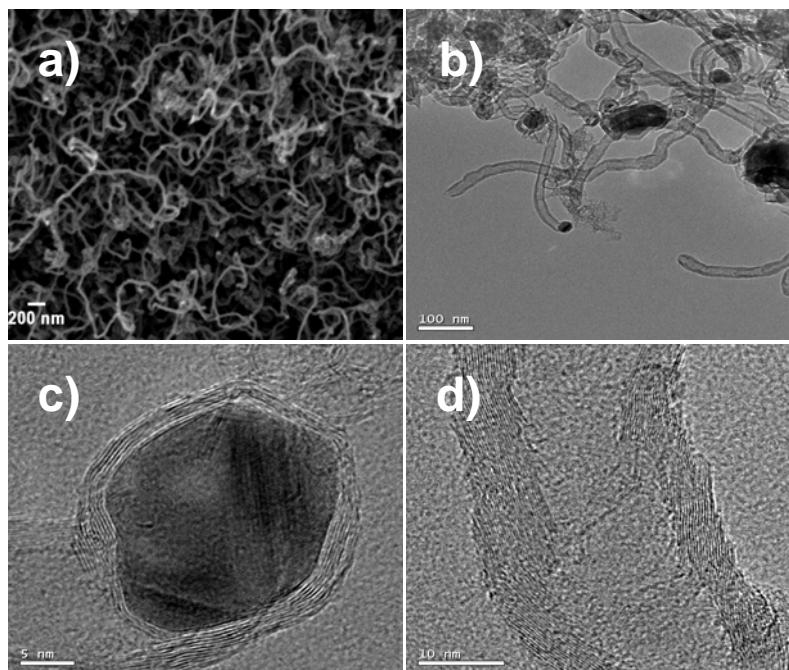


Figure 14: a) SEM of CNTs and b), c), d) TEM images of CNTs and cobalt nanoparticles, of compound **55** after thermolysis at 2.9 °C/min from rt to 200 °C, holding at 200 °C for 2 hrs, then heating to 800 °C at rate of ~ 5 °C/min, and then holding for 24 hrs.

These graphene segments are probably formed from several of the graphene cores of the precursors. The inter-graphitic distance is around 0.34 nm, similar to that of normal CNTs. Heating of compound **55** at lower temperature (600 °C) for short time (8 hours) afforded minor yield of CNTs. Moreover, extending the thermolysis time at 600 °C for 24 hours dramatically improved the yield of multi-walled CNTs. The enhancement of the CNT's growth should be related to the catalyst activity at this temperature as well as to the required time needed to achieve the nanotubes formation.

Owing to the structural similarity of compound **57** to **50** and **52**, the lower cobalt/carbon ratio containing compound **57** was subjected to thermolysis at 800 °C. Unlike **50** and **52**, few isolated islands of CNTs were obtained, with mainly the formation of carbon/cobalt amorphous materials (figure 16a and 16b). The lack of CNTs formation was

assigned to the low amount of cobalt-cobalt clusters in **57**, compared to compounds **50**, **52** and **55** under different heating conditions. These studies provide evidence for the importance of a high ratio of cobalt/carbon in the pyrolytic-starting compounds to promote high yield of CNTs.

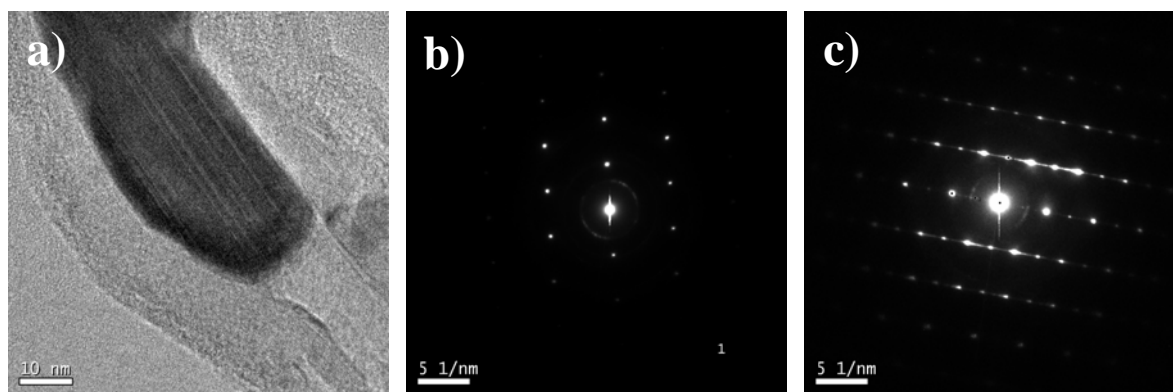


Figure 15: Compound **55** after pyrolysis at 800 °C showing a) TEM image of cobalt nanoparticle embedded inside a nanotube; b) and c) electron diffraction patterns of the cobalt crystal in a) measured from different angles.

All the complexes containing a graphene fragment and $[\text{CCCo}_2(\text{CO})_6]$, i.e., compounds **50**, **52** and **55**, can be used as good precursors for the high-yielding carbon nanotubes formation under controlled heating procedures. To understand the role of the graphene structure on the yield of the CNTs, we thermolysed the hexaphenylbenzene-cobalt complex **59**, an analogue of molecule **50** with a non-planar core. The pyrolysis of compound **59** under various heating conditions gave only some micro-sized ill-defined structures (Figure 16c) and CNTs were rarely found. Additionally, most of the CNTs were catalyst-filled (Figure 16d) similar to what was obtained by Zhi et al.^{7b} This confirms the importance of the graphene structure in the precursors. One may assume that at high temperatures, the graphene molecules may cross-link to form large graphene layers and in the presence of the Co catalyst, these graphene layers can curve and finally form the tube-like structures.

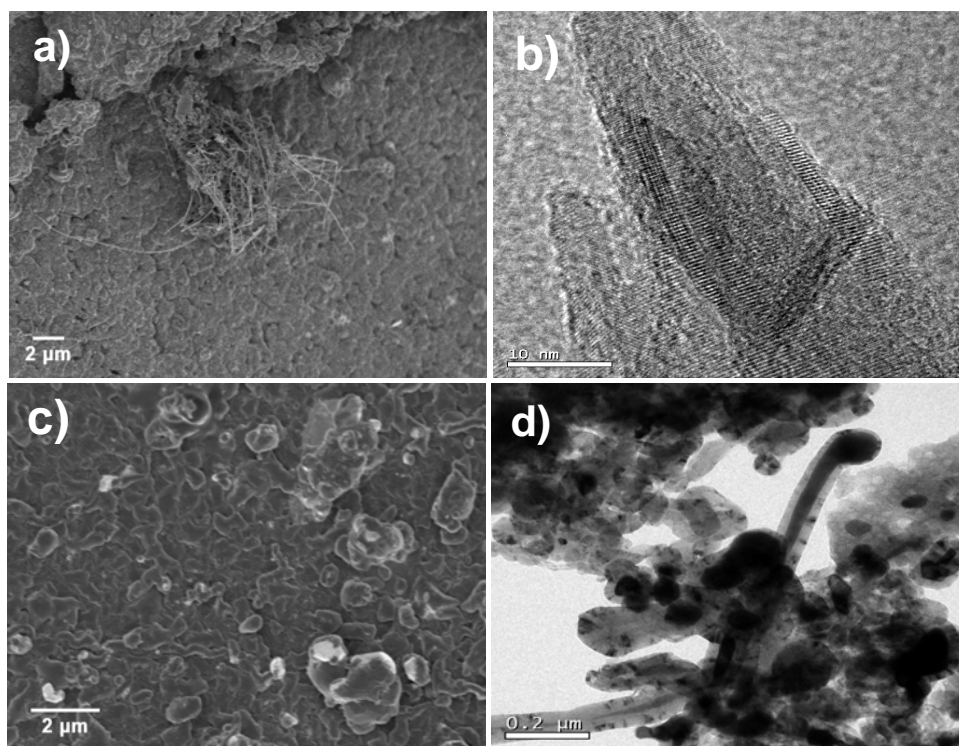


Figure 16: a-b) SEM and TEM images of the carbon-cobalt product after pyrolysis of precursor **59** at $4^{\circ}\text{C}/\text{min}$ from rt to 230°C , holding for 2 hrs, then heating to 500°C at rate of $4.5^{\circ}\text{C}/\text{min}$, holding for 4 hours, and then heating to 800°C ($3^{\circ}\text{C}/\text{min}$) and holding for 24 hrs; c-d) SEM and TEM pictures of compound **57** showing very few CNTs and graphitic structures respectively, after pyrolysis at $3.3^{\circ}\text{C}/\text{min}$ from rt to 200°C , holding at 200°C for 3 hours, then heating to 800°C at rate of $\sim 5^{\circ}\text{C}/\text{min}$ and holding for 36 hours.

The successful synthesis of CNTs from the diphenylacetylene-Co complex **46** encouraged us to further investigate the role of molecular structures in the precursors upon pyrolysis into carbon nanostructures. As observed in solution, **46** was expected to first undergo cyclotrimerization when heated, therefore forming a hexagonal symmetric hexaphenylbenzene intermediate which underwent further carbonization at higher temperatures to give carbon nanotubes.

The molecules **63** and **61** have three and four tolane-Co units with different geometries, however, pyrolysis of **61** under various conditions afforded irregular carbonaceous materials together with large agglomerates of cobalt; nanotube formation was not observed. This behavior may be ascribed to the symmetry of molecule **61** which cannot form symmetric structures (e.g., hexaphenylbenzene), ready for *in situ* subsequent graphene layer formation.

Heating **63** at 700 °C for 8 hours led to carbon-cobalt nanospheres in high yield. TEM pictures showed that the cobalt nanoparticles (diameters are around 10-50 nm) were embedded in semi-crystalline carbons (figure 17a and 17b). Increasing temperature to 850 °C for similar holding time, however, afforded fiber-like nanostructure with diameters of 5-10 nm in high yield and lengths up to hundreds of nanometers (Figure 17c). TEM images disclosed that the fibers are not carbon nanotubes, but crystalline graphitic carbon nanorods (Figure 17d). A regular inter-graphene sheet distance of 0.36 nm was measured by electron diffraction (Figure 17e). It is obvious that the increase of the temperature resulted in the improvement of graphitization of the carbon nanorods. The cobalt nanoparticles with diameters ranging from 30 to 100 nm were surrounded with carbon nanorods and little amorphous carbon.

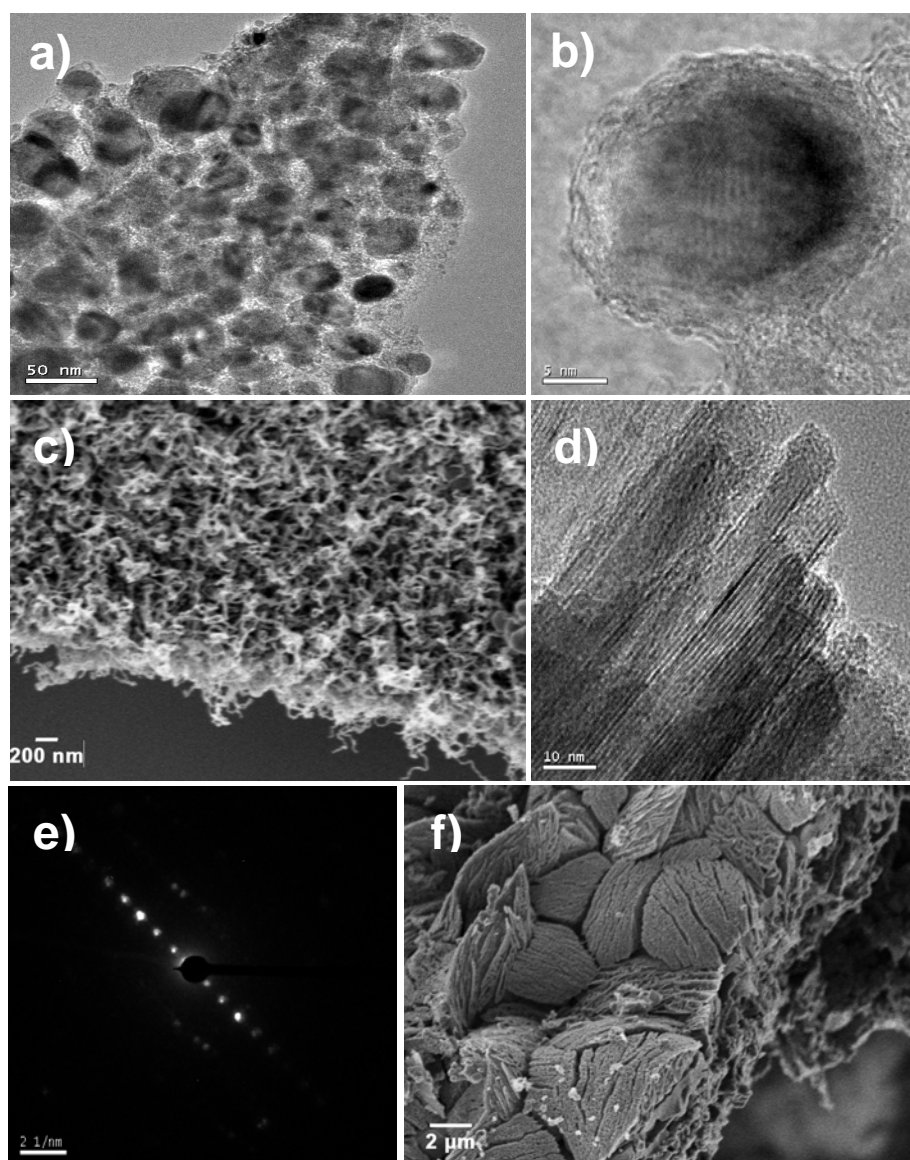


Figure 17: a-b) TEM pictures, showing cobalt nanoparticles embedded in semi-crystalline carbon, obtained after thermolysis of compound **63** at 2.4 °C/min from rt to 170 °C, holding at 170 °C for 2 hrs, then heating to 700 °C at rate of ~ 2.9 °C/min, and then holding for 8 hrs; c) SEM and d) TEM images disclosing graphitic carbon nanorods in high yield after pyrolysis of compound **63** at 2.1 °C/min from rt to 150 °C, holding at 150 °C for 2 hrs, then heating to 850 °C at rate of ~ 5.8 °C/min, and then holding for 8 hrs; e) electron diffraction pattern of the carbon nanorods of **63** at 850 °C; f) ice-cream-like material afforded after heating compound **66** at 2.8 °C/min from rt to 170 °C, holding at 170 °C for 2 hrs, then heating to 370 °C (3.3

$^{\circ}\text{C}/\text{min}$) and holding for 2 hours, and then heating to 700°C ($6.7^{\circ}\text{C}/\text{min}$) and holding for 24 hrs.

Upon temperature increase, the diameter of the cobalt nanoparticles increases due to the coalescence. Additionally, the high-yield production of the crystalline carbon nanorods is surprising and shows the influence of the geometric structure of the precursors on nanostructure formation. Although the formation mechanism of the ordered nanostructures is still unknown, the dicobalt octacarbonyl is a known catalyst for the cyclotrimerization reaction of triple bonds and forms benzene rings upon heating. The same principle is applied here; we believe that upon heating, cyclodi- or tri-merization reactions between the different clustered triple bonds begin and increase with temperature. This mechanism should afford large frameworks of metal-organic materials with increasing temperature, which is the key issue for nanostructures formation. As previously mentioned for **63**, the temperature difference between 700 and 850°C was an important issue toward improving the yield of large amounts of graphitic nanorods. At 700°C , only cobalt particles surrounded with semi-crystalline carbon were obtained. Thus, we think that the importance of the precursor lies in its structure, geometry, and the thermal conditions, that are crucial for producing nice ordered carbon nanostructures.

Replacement of the benzene rings in molecule **46** by the five-membered thiophene rings was thought to be a logical method for the generation of novel carbon nanostructures containing sulfur atoms. However, thermolysis of **66** at 800°C under regular and slow heating rate did not produce carbon nanotubes, instead, some micrometer sized structures (Figure 17f). One explanation for this behavior is that the sulfur atom weakens the bonding of the organic molecules towards the cobalt as a catalyst and inhibits their activity, an essential process for the formation of nanostructures.

For the molecules **50**, **52**, **55**, and **57**, the metal moieties are located at the periphery and approximately in the plane of the graphene molecules. In contrast, the Ru atom in molecule **67** stands on the top of the HBC. Pyrolysis of **67** at 800°C produced nanorods with different diameters (Figure 18a). TEM images disclosed rods consisting of ordered graphitic layers, instead of amorphous carbon (Figure 18b). Therefore, this change in the metal had a large effect on the catalytic activity, which in turn produced unexpected graphitic structures.

So far, it is clear that pyrolysis of the graphene-Co complexes always provide multi-walled carbon nanotubes in high yields (except molecule **57** which has a low Co loading). In contrast, with hexaphenylbenzene-Co complex **59**, very few CNTs are formed under equivalent conditions.

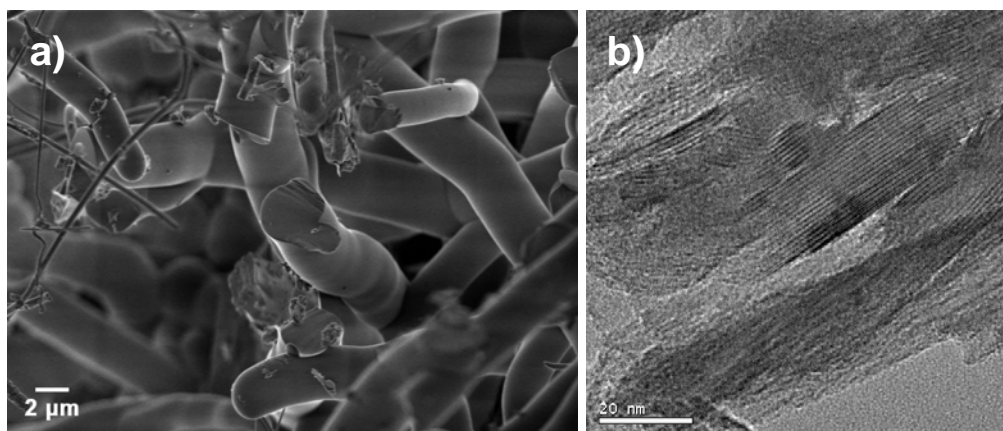


Figure 18: SEM and TEM images of the product from compound **67**: 6 °C/min from rt to 400 °C, holding at 400 °C for 8 hrs, then heating to 800 °C at rate of ~ 3.3 °C/min, and then holding for 8 hrs.

Pyrolysis of the HBC-Ru complex **67** also provided graphitic carbon nanorods. Therefore, the graphene fragment within the precursors plays a key role in the graphene layer formation. It is known that the graphitization of carbon precursors normally requires very high temperatures under inert atmosphere. However, if the precursors already contain graphite

segments, with the assistance of a metal catalyst the graphitization temperature can be significantly lowered, nevertheless, the loading of catalyst, is also important for the yield of the CNTs.

Vollhardt's work on the pyrolysis of tolane-Co complex **46** is an important example showing that small carbon-Co complexes can also be used as precursors for the high-yield synthesis of carbon nanotubes. This reflects the effect of the symmetry on the cyclotrimerization reaction which occurs upon heating cobalt nanoclusters above their decomposition temperature under controlled heating conditions. Besides this molecule, all the other complexes (except **50**) containing the $[\text{CCCO}_2(\text{CO})_8(\text{Ph})_2]$ (and other systems in literatures) do not afford CNTs in good yield. The success of molecule **46** is perhaps due to its capability to form 6-fold symmetric hexaphenylbenzene intermediates which were further carbonized into the graphitic structures at higher temperature. However, the synthesis of graphitic carbon nanorods from molecule **63** provided very interesting crystalline graphitic structure which might be useful in lithium-ion batteries.

Besides the structural properties of the precursors, the thermolysis heating program (such as heating rate, temperature and holding time) is also important. To achieve a high-yielding synthesis of certain nanostructures, slow heating, high temperature ($< 1000\text{ }^\circ\text{C}$) and longer holding time usually help. During pyrolysis, the precursors were usually heated to the decomposition temperature of the Co-carbonyl at a slow heating rate and then held at this temperature for several hours to ensure uniform Co particle formation. Fast heating from room temperature normally resulted in less well-defined structures. Compared to the CNTs obtained by other methods, the CNTs produced here typically have uniform sizes, probably due to the uniform Co catalytic particles formed from the covalently bonded organometallic precursors.

SEM and TEM pictures were obtained in cooperation with Dr. Jishan Wu and Dr. Linjie Zhi. They also provided valuable discussions and ideas for concepts described in chapters 6 and 7.

5.3.3 Conclusion

In summary, the solid-state pyrolysis of different organo-metal precursors were investigated in detail and show that preformed graphitic structures within the precursors are important for the formation of uniform CNTs. In addition, the C/Co ratio and the heating program also have a significant effect on the yield. Studies on the pyrolysis of diphenylacetylene-Co based precursors suggest that molecular symmetry is an important determinant of the final pyrolyzed product. The inclusion of heteroatoms also affected the nature of the final products. The high-yielding synthesis of graphitic carbon nanorods formed from compounds **63** and **67** is an important discovery and allows us to probe their materials applications as anode in lithium-ion batteries. Since the solid-state pyrolysis is simple and the structures of the materials obtained can be well controlled, this method may be regarded as new route toward novel carbon nanomaterials synthesis and applications, such as heterogeneous catalysis. Good solubility of the precursors may also allow their ink-printing onto surfaces, which when pyrolyzed, would form selective CNT- or carbon nanorod-patterned surfaces.

¹ Iijima, *Nature* **1991**, 354, 56-58.

²a) H. Haughman, A. A. Zakhidov, W. A. de Heer, *Science* **2002**, 297, 787-792; b) S. Subramoney, *Adv. Mater.* **1998**, 10, 1157; c) H. Dai, *Surf. Sci.* **2002**, 500, 218; d) S. Fan, M. G. Chapline, N. R. Franklin, T. W. Tombler, A. M. Cassell, H. Dai, *Science* **1999**, 283, 512; e) P. Chen, X. Wu, J. Lin, K. L. Tan, *Science* **1999**, 285, 91; f) H. Dai, E. W. Wong, C. M. Lieber, *Science* **1996**, 272, 523; g) J. Kong, N. R. Franklin, C. Zhou, M. G. Chapline, S. Peng, K. Cho, H. Dai, *Science* **2000**, 287, 622; h) C. Liu, Y. Y. Fan, M. Liu, H. T. Cong, H. M. Cheng, M. S. Dresselhaus, *Science* **1999**, 286, 1127; i) S. B. Sinnott, R. Andrews, *Crit. Rev. Solid State Mater. Sci.* **2001**, 26, 145; g) T. W. Ebbesen, *Acc. Chem. Res.* **1998**, 31, 558; k) R. Andrews, D. Jacques, D. Qian, T. Rantell, *Acc. Chem. Res.* **2002**, 35, 1008; l) H. Dai, *Acc. Chem. Res.* **2002**, 35, 1035.

- ³ a) P. I. Dosa, A. Schleifenbaum, K. P. C. Vollhardt, *Org. Lett.* **2001**, *3*, 1017; b) P. I. Dosa, C. Erben, V. S. Iyer, K. P. C. Vollhardt, I. M. Wasser, *J. Am. Chem. Soc.* **1999**, *121*, 10430; c) R. Boese, A. J. Matzger, K. P. C. Vollhardt, *J. Am. Chem. Soc.* **1997**, *119*, 2052;
- ⁴ a) M. Laskoski, W. Steffen, J. G. M. Morton, M. D. Smith, U. H. F. Bunz, *J. Am. Chem. Soc.* **2002**, *124*, 13814; b) U. H. F. Bunz, *J. Organomet. Chem.* **2003**, *683*, 269.
- ⁵ S. Scholz, P. J. Leech, B. C. Englert, W. Sommer, M. Weck, U. H. F. Bunz, *Adv. Mater.* **2005**, *17*, 1052.
- ⁶ V. S. Iyer, K. P. C. Vollhardt, R. Wilhelm, *Angew. Chem.* **2003**, *115*, 4515; *Angew. Chem. Int. Ed.* **2003**, *42*, 4379.
- ⁷ a) L. Zhi, T. Gorelik, J. Wu, U. Kolb, K. Müllen, *J. Am. Chem. Soc.* **2005**, *127*, 12792; b) L. Zhi, T. Gorelik, R. Friedlein, J. Wu, U. Kolb, R. Salaneck, K. Müllen, *Small* **2005**, *1*, 798.
- ⁸ B. El Hamaoui, L. Zhi, U. Kolb, J. Wu, K. Müllen, *Adv. Mater* **2005**, *17*, 2957.
- ⁹ a) J. Wu, A. Fechtenkötter, J. Gauss, M. D. Watson, M. Kastler, C. Fechtenkötter, M. Wagner, K. Müllen, *J. Am. Chem. Soc.* **2004**, *126*, 11311; b) M. D. Watson, A. Fechtenkötter, K. Müllen, *Chem. Rev.* **2001**, *101*, 1267; c) C. Simpson, J. Wu, M. D. Watson, K. Müllen, *J. Mater. Chem.* **2004**, 494.
- ¹⁰ Abstracts of Papers, 223rd ACS National Meeting, Orlando, FL, United States, April 7-11, **2002**, PHYS-112
- ¹¹ a) J. Wu, M. D. Watson, K. Müllen, *Angew. Chem. Int. Ed.* **2003**, *42*, 5329; b) J. Wu, M. Watson, L. Zhang, Z. Wang, K. Müllen, *J. Am. Chem. Soc.* **2004**, *126*, 177; c) J. Wu, M. Baumgarten, M. G. Debije, J. Warman, *Angew. Chem.* **2004**, *116*, 5445; *Angew. Chem. Int. Ed.* **2004**, *43*, 5331.
- ¹² J. Wu, A. Fechtenkötter, J. Gauss, M. D. Watson, M. Kastler, G. Fechtenkötter, M. Wagner, K. Müllen, *J. Am. Chem. Soc.* **2004**, *126*, 11311.
- ¹³ a) P. Hu, K. Xiao, Y. Liu, G. Yu, X. Wang, L. Fu, G. Cui, D. Zhu, *Appl. Phys. Lett.* **2004**, *84*, 4932; b) R. Czerw, M. Terrones, J. Charlier, X. Blase, B. Foley, R. Kamalakaran, N. Grobert, H. Terrones, D. Tekleab, P. M. Ajayan, W. Blau, M. Rühle, D. L. Carroll, *Nano Lett.* **2001**, *1*, 457.
- ¹⁴ Y. T. Lee, J. Park, Y. S. Choi, H. Ryu, H. J. Lee, *J. Phys. Chem. B* **2002**, *106*, 7614.
- ¹⁵ C. J. Lee, J. Park, *J. Phys. Chem. B* **2001**, *105*, 2365.
- ¹⁶ a) F. Tuinstra, J. L. Koenig, *J. Chem Phys.* **1970**, *53*, 1126; b) H. Wilhelm, M. Lelaurain, E. McRae, B. Humbert, *J. Appl. Phys.* **1998**, *84*, 6552.
- ¹⁷ N. S. Kim, Y. T. Lee, J. Park, J. B. Han, Y. S. Choi, S. Y. Choi, J. Choo, A. H. Lee, *J. Phys. Chem. B* **2003**, *107*, 9249.
- ¹⁸ a) E. J. Bae, W. B. Choi, K. S. Jeong, J. U. Chu, G. S. Park, S. Song, I. K. Yoo, *Adv. Mater.* **2002**, *14*, 277; b) A. Cao, G. Meng, P. M. Ajayan, *Adv. Mater.* **2004**, *16*, 40; c) J. Li, C. Papadopoulos, J. Xu, *Nature* **1999**, *402*, 253; d) J. Kong, H. T. Soh, A. M. Cassell, C. F. Quate, H. Dai, *Nature* **1998**, *395*, 878.
- ¹⁹ P. Kim, C. M. Lieber, *Science* **1999**, *286*, 2148.
- ²⁰ Y. Zhang, T. Ichihashi, E. Landree, F. Nihey, S. Iijima, *Science* **1999**, *285*, 1719.
- ²¹ M. Terrones, H. Terrones, F. Banhart, J. Charlier, P. M. Ajayan, *Science* **2000**, *288*, 1226.
- ²² E. C. Constable, O. Eich, D. Fenske, C. E. Housecroft, L. A. Johnston, *Chem. Eur. J.* **2000**, *6*, 4364.
- ²³ Ž. Tomović, M. D. Watson, K. Müllen, *Angew. Chem. Int. Ed.* **2004**, *43*, 775; b) Ž. Tomović, J. Wu, K. Müllen, in preparation, c) PhD thesis of Dr. Ž. Tomović **2004**, Johannes-Gutenberg universität, mainz.

²⁴ A. Fechtenkötter, N. Tchegotareva, M. D. Watson, K. Müllen, *Tetrahedron* **2001**, *57*, 3769-3783.

²⁵ A. Orita, K. Miyamoto, M. Nakashi, ma, F. Ye, J. Otera, *Adv. Synth. Catal.* **2004**, *346*, 767.

²⁶ M. J. Mio, L. C. Kopel, J. B. Braun, T. L. Gadzikwa, K. L. Hull, R. G. Brisbois, C. J. Markworth, P. A. Grieco, *Org. Lett.* **2002**, *4*, 3199.

²⁷ N. T. Lucas, J. Wu, K. Müllen, V. Enkelmann, A. C. Willis, manuscript in preparation.

Chapter 6

Uniform carbon and carbon-cobalt nanostructures by solid-state thermolysis of polyphenylene dendrimer-cobalt complexes

In this chapter, uniform carbon/cobalt nanorods with unique cross-sections, Co-carbon core-shell nanospheres and multi-walled carbon nanotubes are described, and were selectively prepared in high yield by solid-state thermolysis of polyphenylene dendrimer-cobalt complexes (e.g., **71**) under controlled heating procedures. Acidic treatment of the carbon/cobalt nanorods followed by their magnetic property measurements were performed. The obtained materials have potential catalytic^{1,2} and magnetic applications such as hydroformylation catalysis (this reaction will be further studied in the near future) and hard permanent magnets for media storage respectively.

6.1 Introduction

The discovery of fullerenes and carbon nanotubes^{3,4} sparked interest in the research of carbon-rich materials and led to the renaissance of alkyne chemistry. Consequently a plethora of novel carbon-rich compounds has been generated during the last 15 years (Figure 1). These new carbon materials attracted particular interest due to a wide variety of their structures⁵ and potential applications.⁶

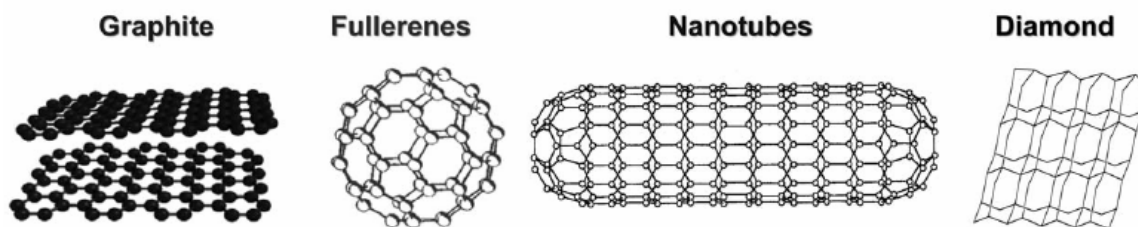


Figure 1: Known allotropes of Carbon

The catalytic decomposition of hydrocarbons is a promising way for the production of carbon nanotubes on large scales.^{7,8} Therefore, the subsequent interaction of carbon with the catalyst (transition metals or their alloys) leads to graphitization which occurs at lower temperatures (600 – 900 °C).⁹ Encapsulation of foreign metal nanoparticles, especially magnetic Fe, Co and Ni, inside carbon spheres prevented environmental degradation and opened the opportunities of using magnetic carbon-metal nanoparticles in information storage and as co-catalyst in medicinal chemistry.¹⁰ The solid-state pyrolysis of organometallic complexes, done in vacuum without substrate, has recently emerged as an alternative route toward novel carbon and carbon-metal nanostructures, however, mixtures of metal nanoparticles with carbon nanotubes, carbon onions and amorphous carbons were usually obtained.^{11,12,13} Thus, ethynyl functionalized polyphenylene dendrimers can serve as precursors because of their carbon-rich character and facile complexation with cobalt carbonyl at the peripheries.¹⁴ Herein, we demonstrate that the solid-state thermolysis of polyphenylene dendrimer-cobalt complexes (Chart 1) affords (i) uniform carbon/cobalt nanorods with special cross-sections never reported before, (ii) carbon-cobalt nanospheres and (iii) carbon nanotubes depending on the molecular structures of the precursors and heating procedures.

[Co₂(CO)₆RCCR] clusters (Figure 2). The NMR spectra disclose obvious signal shifts for the protons and carbons of the ethynyl groups, indicating a complete complexation (Figure 3). Confirmation of complete functionalization came from ¹H and ¹³C NMR spectroscopy data which revealed the presence of symmetrical products in solution. In the ¹H NMR spectrum, a shift in the signal due to the terminal C-H proton from $\delta = 3.07$ ppm in **68** to $\delta = 6.44$ ppm in **71** was consistent with the coupling of the dicobalt carbonyl fragment to each alkyne moiety (Figure 3).

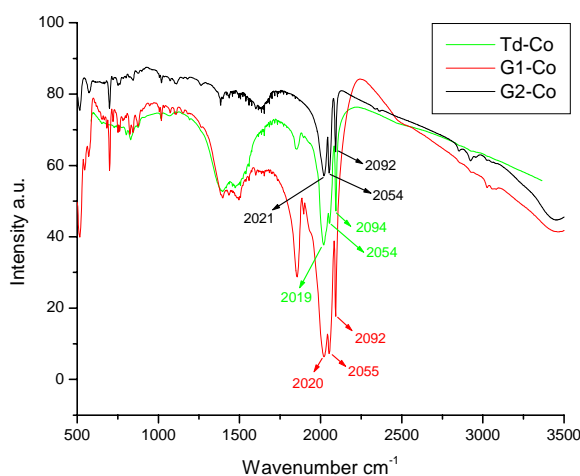


Figure 2: Infra-red spectra of **71**, **72** and **73** showing typical C≡O in-cluster absorptions

Two diagnostic features in terms of confirming cluster formation at each of the alkyne units in ¹³C NMR spectrum are the presence of the signal at $\delta = 199.97$ ppm corresponding to the cobalt-carbonyl groups and signals assigned to the clustered C≡C from $\delta = 83.6$ and 78.4 ppm in **68** to $\delta = 90.00$ and 73.71 ppm in **71** (Figure 4).

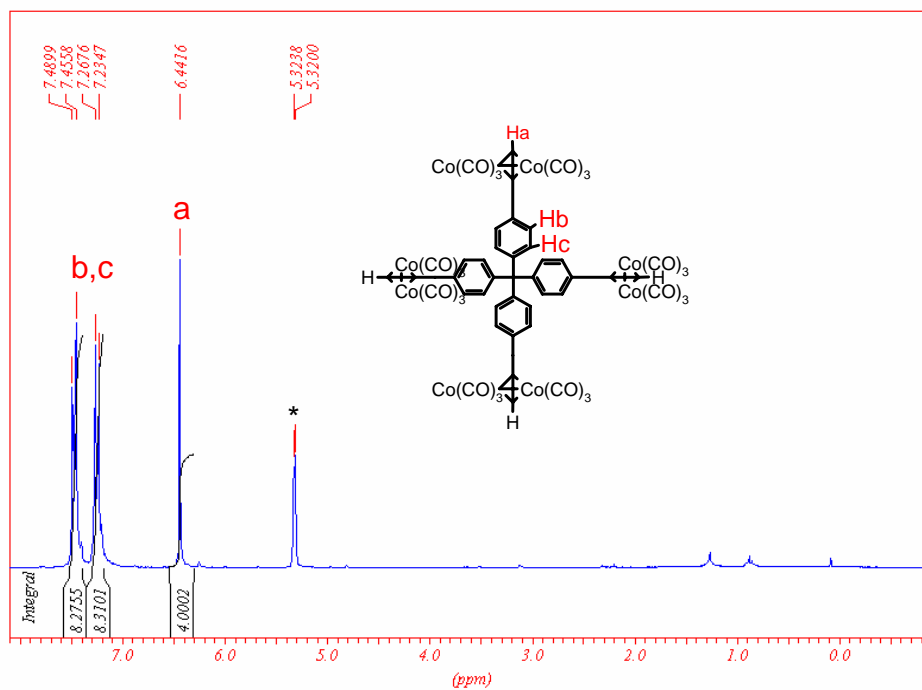


Figure 3: ^1H NMR spectrum of **71** in dichloromethane

The same reasoning can be applied for the higher generation **72** and **73** dendrimer cobalt complexes regarding the NMR characterization. In the ^1H NMR spectrum, complexation was completed when the signals around 3 ppm (acetylenic hydrogens) in both compounds was totally shifted to values between 6.2-6.3 ppm. In the ^{13}C NMR spectrum, carbonyl values appeared around 200 ppm and the acetylenic carbon clusters shifted to values of 90 and 73 ppm for both compounds **72** and **73**. FD-Mass or MALDI-TOF measurements were not possible to access due to the instability of the cobalt complexes in the mass measurement conditions.

Powders of **71**, **72** or **73** were placed in a quartz tube and sealed under vacuum. Each compound was firstly heated to the decomposition temperature (determined by thermogravimetric analysis), and kept at this temperature for about two hours, then heated to higher temperatures with different heating rates and kept at these temperatures for different

times. After cooling to room temperature, the solid samples obtained were submitted to scanning electron microscopy (SEM) and transmission electron microscopy (TEM) analysis.

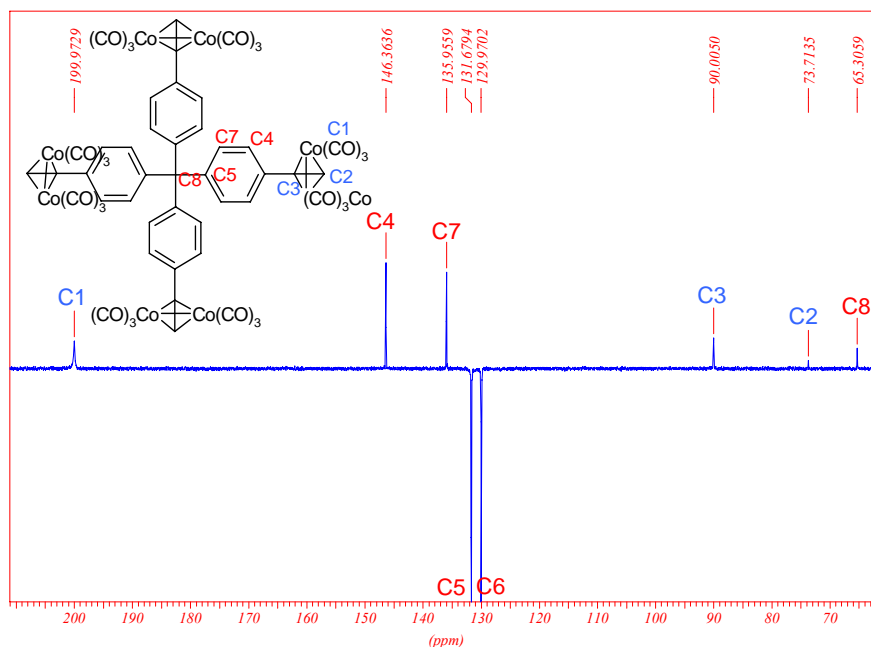


Figure 4: ^{13}C NMR spectrum of **71** in dichloromethane at room temperature

6.3 Solid-state thermolysis of cobalt complex **71**

6.3.1 Results and discussion

Compound **71** burns in the solid-state upon slight scratching. Surprisingly, heating at 130°C for two hours in a quartz tube resulted in regular rod-like structures in high yield with diameters ranging from 200 nm to 500 nm (Figure 5b). TEM images show that the rod-like structures are composed of uniformly dispersed amorphous carbon and Co nanoparticles with diameters around 1~2 nm (Figure 5a, 5c). The monodispersed Co nanoparticles arise from the decomposition of $[\text{C}_2\text{Co}_2(\text{CO})_6]$ clusters as previously reported by Vollhardt et al.^{11d} Similar nanorod structures were also obtained by further heating at 300 °C under a relatively slow heating rate (Figure 6). TEM images disclosed rod-like structures containing dispersed carbon and cobalt.

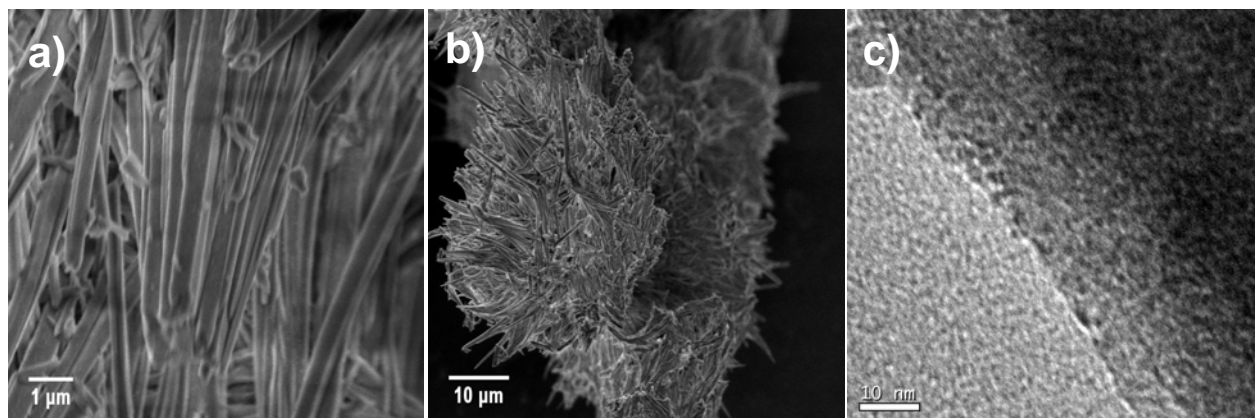


Figure 5: (a),(b) SEM and (c) TEM images of the obtained carbon-Co materials from **71** heated at 130°C for two hours (2.2°C/ min from RT).

After rapid heating ($> 5^\circ\text{C}/\text{min}$) and further pyrolysis at 600 °C for 8 hours, nanorods with both rectangular and cylindrical cross-sections were formed with diameters of 200-300 nm and lengths of up to tens of μm (Figure 7).

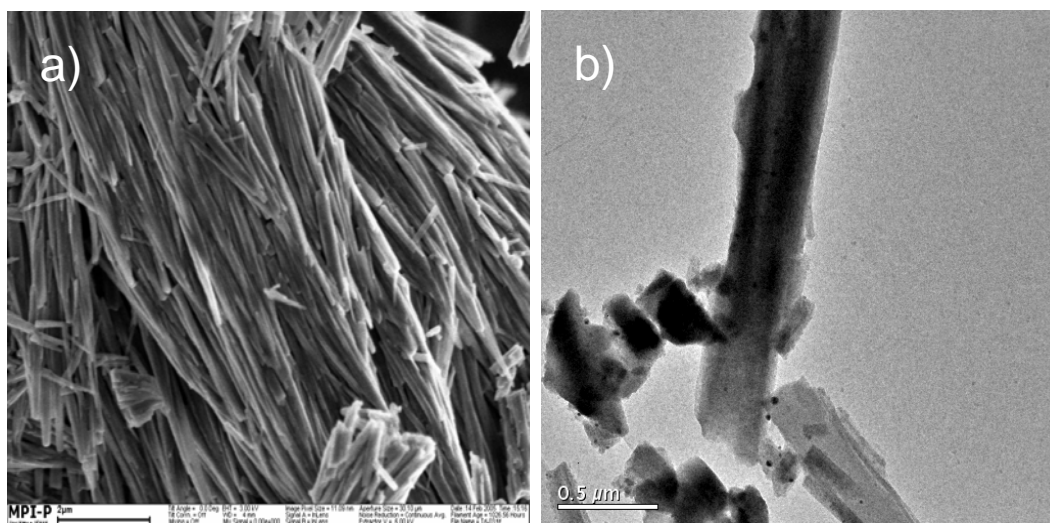


Figure 6: (a) SEM and (b) TEM images of the obtained carbon-Co materials from **71** heated at 300 °C for two hours (2.8 °C/ min from 130 °C).

Upon heating **71** at 800 °C for 8 hours, SEM images showed that uniform nanorods with unique rectangular cross-sections and with a cross-section width of 0.8-2 μm were obtained in high yield (Figure 8a).

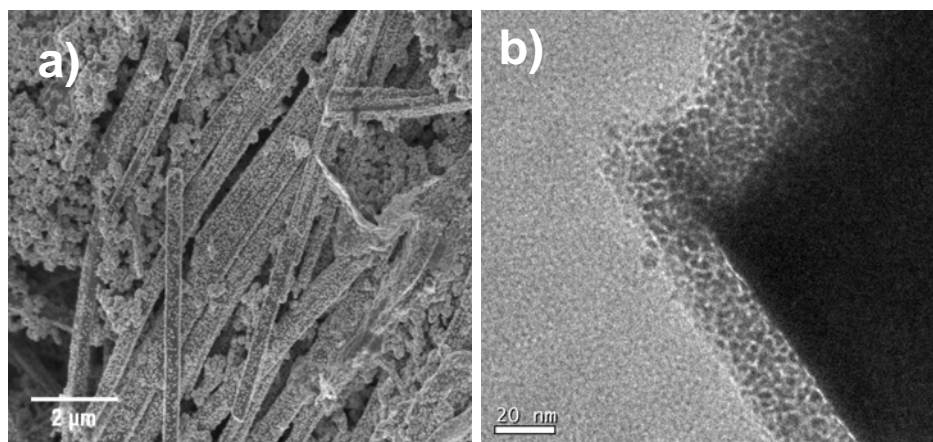


Figure 7: a) SEM and b) TEM pictures of the obtained carbon-Co materials from **71** heated at 600 °C for two hours (5 °C/ min from 130 °C).

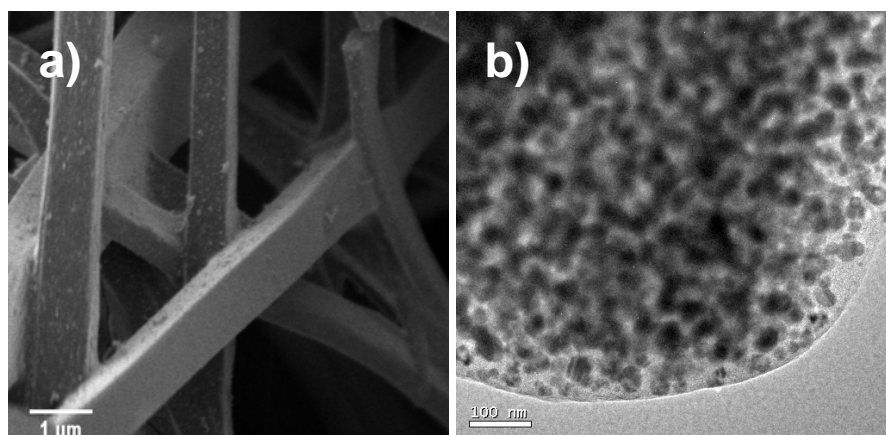


Figure 8: a) SEM and b) TEM pictures of the obtained carbon-Co materials from **71** heated at 800 °C for two hours (5.6 °C/ min from 130 °C).

TEM analysis disclosed that the rods formed at both 600°C and 800°C were still composed of well-dispersed carbon and Co nanoparticles; however, the diameters of the particles are

larger for the latter (20-40 nm) (Figure 8b). The formation of unique nanorods with rectangular cross-section is surprising and should be related to the original morphology during the “exothermic” decomposition of **71** at 130°C. The sizes of the Co nanoparticles increase with increasing heating time and temperature probably due to the coalescence of the small nanoparticles during the heating.

The nanorods are composed of both carbon source and catalytically active Co nanoparticles which suggested us to fabricate novel carbon or carbon-cobalt nanostructures under slow heating procedures (1.5 °C/min). This led to the “growth” of carbon nanotubes randomly from the surface of the nanorods where the cobalt particles (catalyst) are located on the tip of the formed nanotubes (Figure 9). The interior of the rods is still composed of carbon and cobalt nanoparticles. The growth of carbon nanotubes indicated that the nanorods serve as a feedstock of both carbon and catalyst and as a support for the growth. It was then proposed that addition of more carbon source would increase the formation of carbon nanotubes on the surface of the nanorods instead of using the embedded carbon, thus increasing the amount of nanotubes on the surface (aligned in one direction if possible) and keeping the rectangular cross-sections intact. Therefore, the thermolysis of **71** was carried out in the presence of tetraphenylmethane (**74**) as additional carbon source, which increases the amount of CNTs. When **71/74** ratios were between 1:1 and 1:2, few CNTs were grown on the surface of the nanorods and led to rectangular cross-sections with indiscretions (Figure 10). Upon increasing the carbon amount, a **71/74** ratio of 1:4 afforded irregular tree-like nanostructures, in which small carbon-cobalt nanorods were grown from the main “trunk” (Figure 11a, 11b), while 1:8 afforded large amounts of uniform carbon nanotubes accompanied by amorphous materials (Figure 11c, 11d). Thus, the formed carbon-cobalt nanorods from **71** can indeed be used as catalytic centers as well as templates for further carbon nanotube formation from the rods.¹⁷ Extension of the

heating time at 800 °C from 10 hours to 4 days using identical equivalents of **74** provided similar results. It is thus clear that addition of bulk carbon source for the growth of aligned CNTs on the surface of the nanorods is not a good choice. Future work will focus on using carbon sources from vapor, such as methane, acetylene and hexane, in a chemical vapor deposition oven.

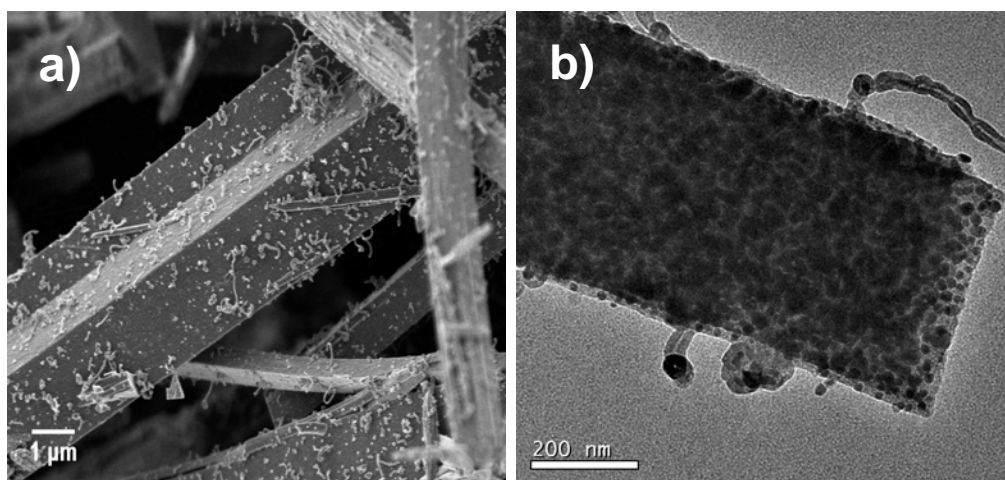


Figure 9: a) SEM and b) TEM pictures of the obtained carbon-Co materials from **71** heated at 800 °C for two hours (1 °C/ min from 130 °C).

6.3.2 Acidic treatment and magnetic properties of cobalt nanoparticles of **71** prepared at 800 °C

Metallic nanoparticles such as Fe, Co, and Ni, are useful in various application fields of magnetism, including magnetic data storage, ferrofluids, and biotechnology.¹⁸ The main difficulty for the use of pure metals arises from their instability towards oxidation in air and dissolution in acid, which becomes much easier as the size gets smaller. It is thus highly important to develop methods to improve the chemical stability of such particles. One approach is to use the core-shell strategy to deposit a protecting shell on the nanoparticle's external surface that prevents the oxidation reaction.¹⁹ Presently, most studies are focused on polymer and silica shells. Compared to these, however, carbon exhibits a much higher stability

in various chemical and physical environments such as acid or base media, and at high temperature and pressure. In order to meet the demands of nanoparticle applications, the synthesis of carbon protected metallic nanoparticles was explored in this study.

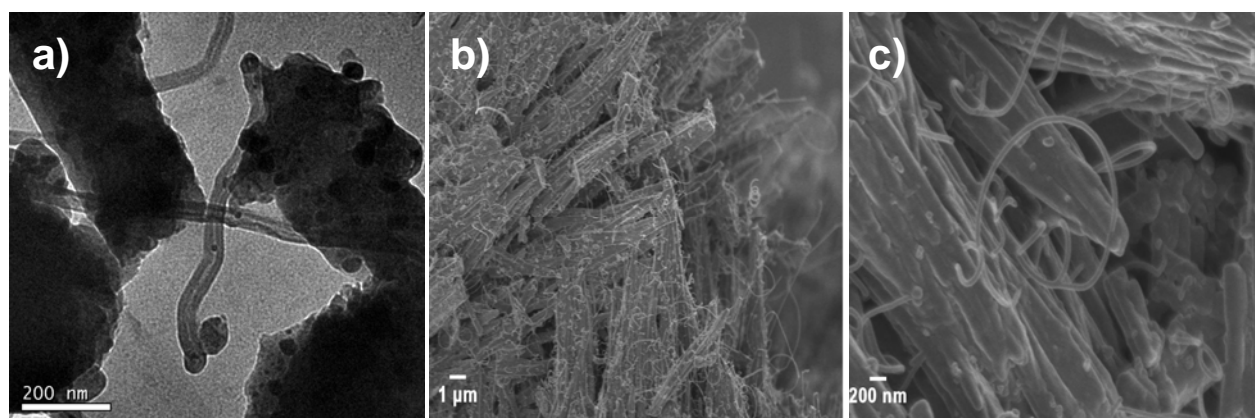


Figure 10: (a) TEM and (b), (c) SEM images of the obtained carbon-Co materials from **71** after slow heating to 800 °C and holding for 8 hours; pictures of materials after thermolysis of mixture of **71/74** with different ratios: (a) and (b) 1:1, (c) 1:2 (heating from RT to 130°C at 2.2°C/min for 2 hours, then to 800°C at 1.1°C/min for 8 hours).

Immersing the nanorods produced at 300 °C, 600 °C and 800 °C in an excess amount of highly concentrated nitric acid HNO₃ (53 wt%) solution for one month at room temperature showed high acid resistance for the sample heated to 600 °C, without destroying its regular structures, suggesting these well-dispersed carbon-Co materials as candidates for magnetic applications such as ferrofluids²⁰, and ultra-high-density storage media.²¹ A short study on the magnetic properties of these structures will be mentioned.^{10b,22}

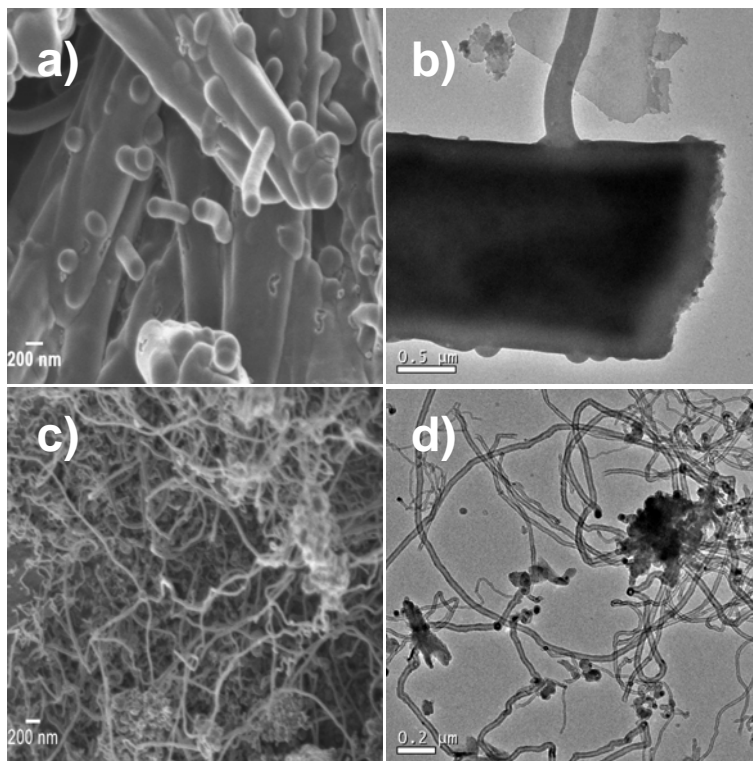


Figure 11: (a), (c) SEM and (b), (d) TEM images of the obtained carbon-Co materials from **71** after slow heating to 800 °C and holding for 8 hours; pictures of materials after thermolysis of mixture of **71/74** with different ratios: (a) and (b) 1:4, (c) and (d) 1:8 (heating from RT to 130°C at 2.2°C/min for 2 hours, then to 800°C at 1.1°C/min for 8 hours).

Although after the 600 °C harsh treatment, some empty shells were found in the TEM images, most of the cobalt particles were well protected by dense carbon (Figure 12). In Figure 12, TEM images show the cobalt nanoparticles with an average size between 10-15 nm surrounded with carbon throughout the sample. This demonstrates that the carbon-coated cobalt nanoparticles were protected against acid erosion. At 300 °C and 800 °C, no cobalt nanoparticles could be observed after two weeks of highly concentrated HNO₃ (53 wt%) treatment (Figure 13).

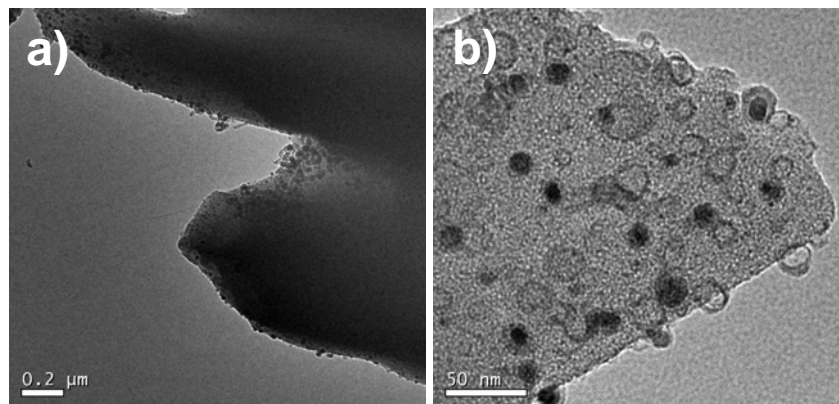


Figure 12: TEM image of Carbon protected carbon-Cobalt nanorods at 600 °C after 1 month treatment in 53% HNO_3 (the dark spots correspond to the cobalt nanoparticles and the light material is carbon)

The color of the solution after acid treatment became lightly dark indicating the leaching of the cobalt particles by acid without destroying the regular structures of the carbon nanorods.

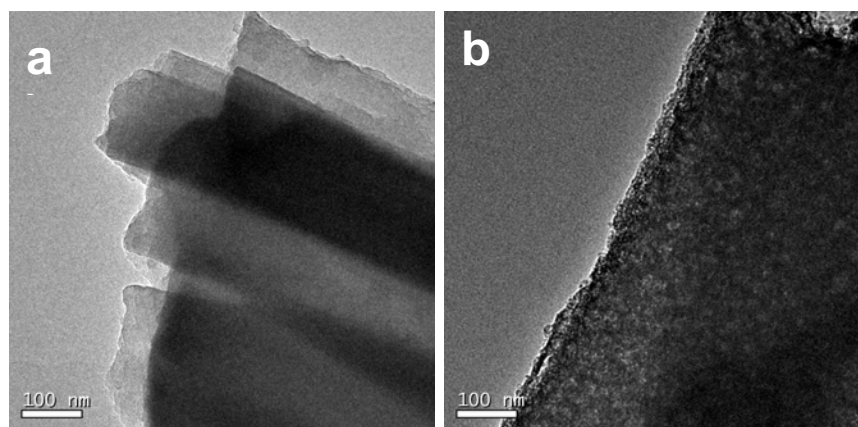


Figure 13: TEM image of Carbon protected carbon-Cobalt nanorods at a) 300 °C and b) 800 °C after 1 month treatment in 53% HNO_3 .

This implies that the pyrolysis conditions of the same carbon-cobalt precursor play an important role in the formation of carbon-shell structures and protection against acid erosion.

The magnetic separability of the carbon-Co materials obtained after pyrolysis at 600 °C and 800 °C was tested by placing a bar magnet near the glass vial as well as by systematic study.

The black powder was attracted by the magnet demonstrating that these materials are magnetic.²³

For this experiment, the powder sample was packed, and the measured weight of the cobalt/carbon nanorods was 43 mg. The magnetic measurement was carried out as a function of magnetic field in the range from -8000 to 8000 Oe at room temperature (300 K). The magnetization curve of the carbon-coated cobalt particles is shown in Figure 14.

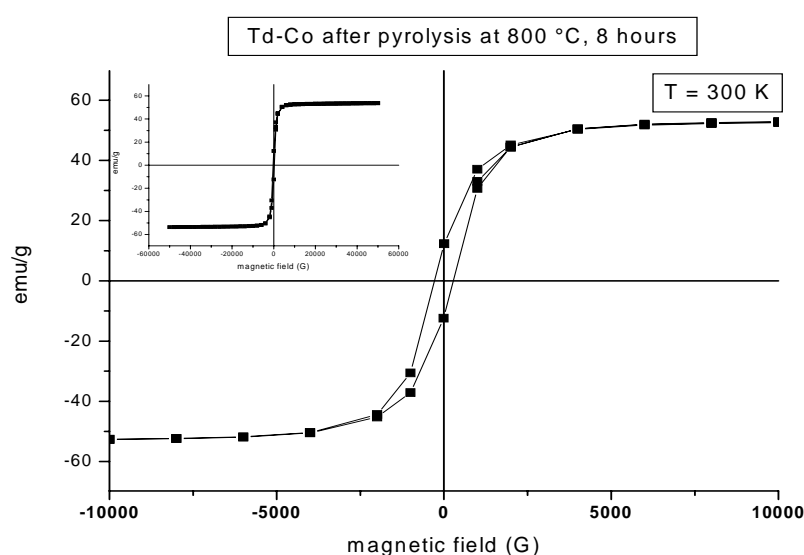


Figure 14: Magnetic hysteresis loop of cobalt nanoparticles embedded in the carbon nanorods after the pyrolysis of 1b at 800 °C for 8 hours. Inset is the larger hysteresis domain.

The cobalt sample shows a medium coercive field of about 300 Oe. The coercivity, also called the coercive field, of a ferromagnetic material is the intensity of the applied magnetic field required to reduce the magnetization of that material to zero *after* the magnetization of the sample has been driven to saturation (Such magnets can find application in magnetic recording media²⁴ and magnetic separation). The ferromagnetic character of these samples was characterized by a ratio of remnant to saturation magnetization $M_R/M_S \sim 0.23$. Our results also showed that the cobalt sample has a value of saturation magnetic moment per gram of 53.5

emu/g. Previous work of Jiao et al.²² regarding coercive field measurements performed on carbon-coated metal nanoparticles, afforded a values of 200 Oe and 240 Oe for coated cobalt (average size 40 nm) and coated nickel nanoparticles (average size 37 nm) respectively. In addition, the saturation magnetization was found to be 114 and 35 emu/g for cobalt and nickel respectively.²² Comparing these results to what we obtained, it is clear that our carbon-coated cobalt nanoparticles present better coercive field properties, and lower saturation magnetization. The features that the larger the particle size, the stronger the coercive field have been observed and studied in single domain magnetic particles and we suggest that the sizes of these particles are close to those of single domain particles. At this time we can only speculate on reasons for the deviation of the saturation magnetization from bulk values²⁵.

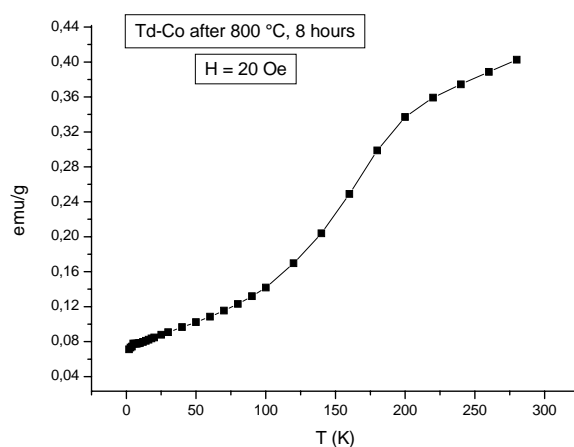


Figure 15: Temperature dependence of the magnetization obtained in Zero-field Cooled (ZFC) process with applied field $H = 20$ Oe.

They may include geometric factors such as shape factors, size anisotropy, coating-shell effect as well as surface effects. Additionally, comparing our data with the values of bulk ferromagnetic elements, the cobalt particles have 33% of the value of the bulk element²⁵ with a bulk-like behavior at room temperature.

In Figure 15, a Zero-field-cooled (ZFC) measurement in a 20 Oe applied field was conducted. The aim was to obtain the value of the blocking temperature (T_B) of the cobalt-coated nanoparticles. The blocking temperature is the point where the transition between the superparamagnetic state (unordered) and the ferromagnetic (ordered) state occurs. It can be related to the nanoparticle size and how well the particles are dispersed in the sample. To measure the T_B , the sample is cooled from room temperature to 2 K without applying an external magnetic field. This implies that by decreasing the temperature, the nanoparticle moments are blocked progressively along their anisotropy direction. After reaching $T = 2$ K, a field of 20 Oe is applied and the magnetization is recorded on warming. Since the nanoparticles reveal a long-range magnetic order at room temperature, no blocking behavior has been observed (no T_B appeared). In conclusion, the nanoparticles are magnetic at room and low temperatures, and may be of a single domain (single domain for fcc-Co is ca 10 nm). This is not surprising as the particle size distribution lies between 10 and 40 nm (Figure 14). Given the relatively high coercive field, the particle anisotropy field induced by the shape of the cobalt nanoparticles is also not low. (The anisotropy field is the smallest when the coercivity is the lowest; this happens when the metal nanoparticles are nearly sphere).

(These magnetic studies were done by Dr. Elena-Lorena Salabas and Dr. An-Hui Lu in the Max-Planck-Institute for Coal Research in Mülheim Germany).

6.4 Thermolysis of the higher generation dendrimer cobalt complexes 72 and 73.

SEM images of the pyrolysis products from the higher generation dendrimers **72** and **73** under fast heating rate (>4 °C/min) disclosed uniform spherical structures, which contain both cobalt nanoparticles and carbon (Figure 16a and Figure 17c). TEM images revealed that the spheres consisted of cobalt nanoparticles covered with semi-crystalline carbon shells with an average

diameter of 100-200 nm, and metal-free graphitic onions present in the empty space between the metal nanospheres (inset Figure 17c). Upon slower heating, multi-walled carbon nanotubes grow at the surface of the nanospheres. TEM showed that most of the multi-walled CNTs had an open end with a diameter of 8-15 nm and a wall thickness of 2-5 nm (Figure 16b, 16c and Figure 17a, 17b).

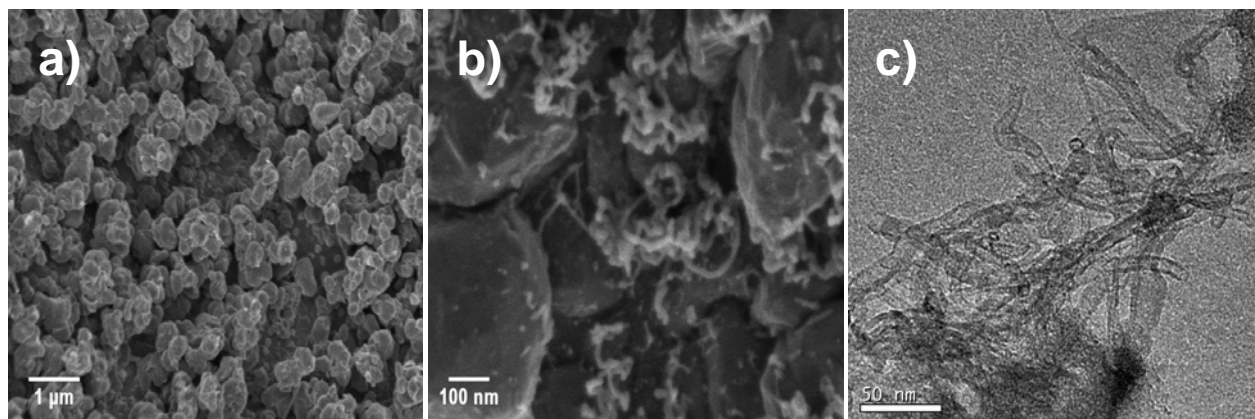


Figure 16: (a) SEM picture of the thermolysis product from **72** under fast heating from 250°C to 900°C at 4.3 °C/min and holding for 8 hours; (b) SEM and (c) TEM images of the thermolysis product from **72** under slow heating from 220°C to 900°C at 2°C/min and holding for 24 hours; (rt to 250(220) °C (2h) at 2 °C/min)

This implies that the cobalt nanoparticles were left out of the nanotubes. CNTs formation on the surface of the coated cobalt nanoparticles is due to the slow heating rate, which provided enough time and temperature to improve diffusion of the carbon over the Co nanoparticles. The uniform size of the carbon nanotubes is related to the uniform formation of the catalyst from the amorphous precursor. As a result, the carbon-cobalt nanoparticles are playing the role of carbon feedstock and catalysis, as well as substrate.

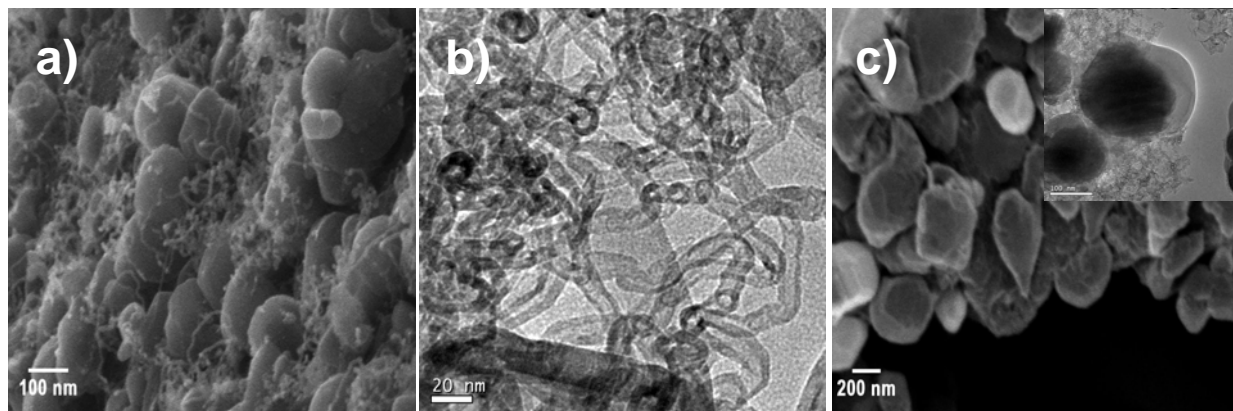


Figure 17: (a) SEM and (b) TEM images of the thermolysis product from **73** under slow heating from 200° C to 900°C at 2°C/min and holding for 24 hours; and (c) SEM picture of the thermolysis product from **73** under fast heating from 220°C to 900°C at 2°C/min and holding for 8 hours; Inset is the corresponding TEM image.

Electron diffraction analysis of the Co particles formed in this work disclosed a new cobalt crystal formation other than ccp and hcp. A regular hexagonal lattice structure with parameters of 2.5 Å and 16 Å was observed. These new structured Co crystals were reported recently when solid state pyrolysis of Co-phthalocyanine was studied in our group.²⁶

6.5 Summary

In conclusion, polyphenylene dendrimer-cobalt complexes were subjected to solid-state thermolysis under vacuum to yield (i) carbon-Co nanorods with unprecedented cross-sections, (ii) carbon-Co nanospheres under fast heating rates and (iii) carbon nanotubes under slow heating rates. Nanorods with this shape and composition have never been reported before. These carbon-metal materials could be regarded as carbon sources and template for carbon nanotube formation from the surface of the rod or sphere under controlled heating procedures. The unique carbon nanorods are candidates as nano-electrodes as well as templates for growth of novel carbon nanostructures.

- ¹ E. L. Rodrigues, J. M. C. Bueno, *Appl. Catal. A: Gen* **2002**, 232, 147.
- ² H. Hou, D. H. Reneker, *Adv. Mater.* **2004**, 16, 69.
- ³ a) L.T. Scott, M.M. Boorum, B.J. McMahon, S. Hagen, J. Mack, J. Blank, H. Wegner, A. de Meijere, *Science* **2002**, 295, 1500; b) M. Terrones, W.K. Hsu, H.W. Kroto, D.R.M. Walton, *Top. Curr. Chem.* **1999**, 199, 189; c) P.M. Ajayan, *Chem. Rev.* **1999**, 99, 1787; d) For novel fullerenes containing four membered rings see, S.-C. Qian, R.B. Chuang, T. Amador, M. Jarrosson, S. Sander, S.I. Pieniazek, Y.R. Rubin Khan, *J. Am. Chem. Soc.* **2003**, 125, 2066; e) H. Kroto, J. Heath, S. O'Brien, R. Curl, R. Smalley, *Nature* **1985**, 318, 162.
- ⁴ a) T. W. Ebbesen, *Acc. Chem. Res.* **1998**, 31, 558; b) H. Dai, *Surf. Sci.* **2002**, 500, 218; c) C. N. R. Rao, B. C. Satishkumar, A. Govindaraj, M. Nath, *Chem. Phys. Chem.* **2001**, 2, 78.
- ⁵ T. Fujimoto, A. Fukuoka, S. Iijima, M. Ichikawa, *J. Phys. Chem.* **1993**, 97, 279.
- ⁶ a) J. Bernholc, C. Roland, B.I. Yakobson, *Curr. Opin. Solid State Mater. Sci.* **1997**, 2, 706; b) R. H. Baughman, A. A. Zakhidov, W. A. de Heer, *Science* **2002**, 297, 787; c) V. N. Popov, *Mater. Sci. Eng., R: Reports* **2004**, R43, 61.
- ⁷ a) P. M. Ajayan, T. W. Ebbesen, *Nature* **1992**, 358, 6383; b) J. Liu, M. Shao, X. Chen, W. Yu, X. Liu, Y. Qian, *J. Am. Chem. Soc.* **2003**, 125, 8088.
- ⁸ N.I. Maksimova, O.P. Krivoruchko, *Chem. Eng. Sci.* **1999**, 54, 4351.
- ⁹ O.P. Krivoruchko, V.I. Zaikovskii, *Mendeleev Commun.* **1998**, 3, 97.
- ¹⁰ a) R. S. Tuoff, D. C. Lorents, B. Chan, R. Malhotra, S. Subramoney, *Science* **1993**, 259, 346; b) J. Hormes, H. Modrow, H. Bönemann, C. S. S. R. Kumar, *J. Appl. Phys.* **2005**, 97, 10R102; c) f) A.-H. Lu, W. Li, A. Kiefer, W. Schmidt, E. Bill, G. Fink and F. Schüth, *J. Am. Chem. Soc.* **2004**, 126, 8616; d) A.-H. Lu, W. Schmidt, N. Matoussevitch, H. Bönemann, B. Spliethoff, B. Tesche, E. Bill, W. Kiefer and F. Schüth, *Angew. Chem. Int. Ed.* **2004**, 43, 4303; e) P.-Z. Si, Z.-D. Zhang, D.-Y. Geng, C.-Y. You, X.-G. Zhao, W.-S. Zhang, *Carbon* **2003**, 41, 247. f) V. G. Pol, S. V. Pol, A. Gedanken, V. G. Kessler, G. A. Seisenbaeva, M.-G. Sung, S. Asai, *J. Phys. Chem. B.* **2005**, 109, 6121; g) M. Abe, *Electrochimica. Acta* **2000**, 45, 3337.
- ¹¹ a) P. I. Dosa, C. Erben, V. S. Iyer, K. P. C. Vollhardt, I. M. Wasser, *J. Am. Chem. Soc.* **1999**, 121, 10430; b) R. Boese, A. J. Matzger, K. P. C. Vollhardt, *J. Am. Chem. Soc.* **1997**, 119, 2052; c) P. I. Dosa, A. Schleifenbaum, K. P. C. Vollhardt, *Org. Lett.* **2001**, 3, 1017; d) V. S. Iyer, K. P. C. Vollhardt, R. Wilhelm, *Angew. Chem. Int. Ed.* **2003**, 42, 4379.
- ¹² a) U. H. F. Bunz, *J. Organomet. Chem.* **2003**, 683, 269; b) M. Laskoski, W. Steffen, J. G. M. Morton, M. D. Smith, U. H. F. Bunz, *J. Am. Chem. Soc.* **2002**, 124, 13814; c) S. Scholz, P. J. Leech, B. C. Englert, W. Sommer, M. Weck, U. H. F. Bunz, *Adv. Mater.* **2005**, 17, 1052.
- ¹³ a) J. Wu, B. EL Hamaoui, J. Li, L. Zhi, U. Kolb, K. Müllen, *Small* **2005**, 1, 210; b) T. M. Keller, S. B. Qadri, *Chem. Mater.* **2004**, 16, 1091.
- ¹⁴ A. J. Berresheim, M. Müller, K. Müllen *Chem. Rev.* **1999**, 99, 1747.
- ¹⁵ a) O. Mongin, A. Gossauer, *Tetrahedron* **1997**, 53, 6835; c) U. -M. Wiesler, K. Müllen, *Chem. Comm.* **1999**, 2293.
- ¹⁶ E. C. Constable, O. Eich, D. Fenske, C. E. Housecroft, L. A. Johnston, *Chem. Eur. J.* **2000**, 6, 4364.
- ¹⁷ H. Hou, D. H. Reneker, *Adv. Mater.* **2004**, 16, 69.

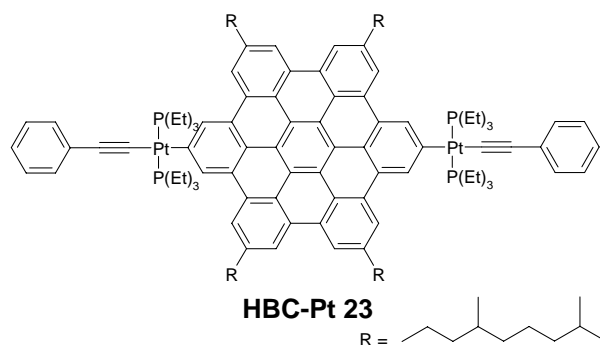
-
- ¹⁸ P. Tartaj, M. P. Morales, S. Veintemillas-Verdaguer, T. Gonzalez- Carreno and C. J. Serna, *J. Phys. D: Appl. Phys.* **2003**, *36*, R182.
- ¹⁹ D. K. Kim, M. Mikhaylova, Y. Zhang and M. Muhammed, *Chem. Mater.* **2003**, *15*, 1617.
- ²⁰ J. Wagner, T. Autenrieth, R. Hempelmann, *J. Magn. Magn. Mater.* **2002**, *252*, 4.
- ²¹ a) S. Sun, C. B. Murray, D. Weller, L. Folks, A. Moser, *Science* **2000**, *287*, 1989.
- ²² b) J. Jiao, S. Seraphin, X. Wang, J. C. Withers, *J. Appl. Phys.* **1996**, *80*, 103.
- ²³ A. H. Lu, W. C. Li, N. Matoussevitch, B. Spliethoff, H. Bönemann, F. Schüth. *Chem. Comm.* **2005**, *1*, 98
- ²⁴ G. Bottoni, D. Candolfo, A. Cecchetti, *J. Magn. Magn. Mater.* **1995**, *140-144*(Pt. 3), 2205-6.
- ²⁵ CRC Handbook of Chemistry and Physics, 76th ed., edited by D. R. Lide (chemical Robber, Boca Raton, FL, 1995-1996), pp. 117-122.
- ²⁶ L. Zhi, T. Gorelik, R. Friedlein, J. Wu, U. Kolb, W. R. Salaneck, K Müllen, *Small* **2005**, *1*, 798.

Chapter 7

Summary and Outlook

The results of this work can be summarized as follows:

I-a A new, organometallic HBC carrying two platinum metal units in the para positions was prepared by subsequent double oxidative addition of platinum to compound **21** in 36% yield followed by CuI-catalyzed dehydrohalogenation with phenyl acetylene to give the desired molecule **HBC-Pt 23** in 44% yield. This molecule showed phosphorescence lifetime three orders of magnitude lower than **HBCC_{8,2} 24** due to the fast ISC and enhanced spin-orbit coupling of **HBC-Pt 23** (figure 1a). The latter molecule **23** revealed unique phosphorescence emission at room temperature and 77K (Figure 1b) opposite to all HBC molecules studied before whereas **HBCC_{8,2} 24** yielded phosphorescence emission at low temperature but delayed fluorescence at room temperature. In contrast to **HBC-Pt 18**, **HBC-PhC₁₂ 25** emits only delayed fluorescence at room and low temperature. The synthesis concept allows functionalization of the HBC core which greatly broaden the scope of functionalities that can be introduced, thus paving the way to new photoluminescent materials on HBC π -systems.



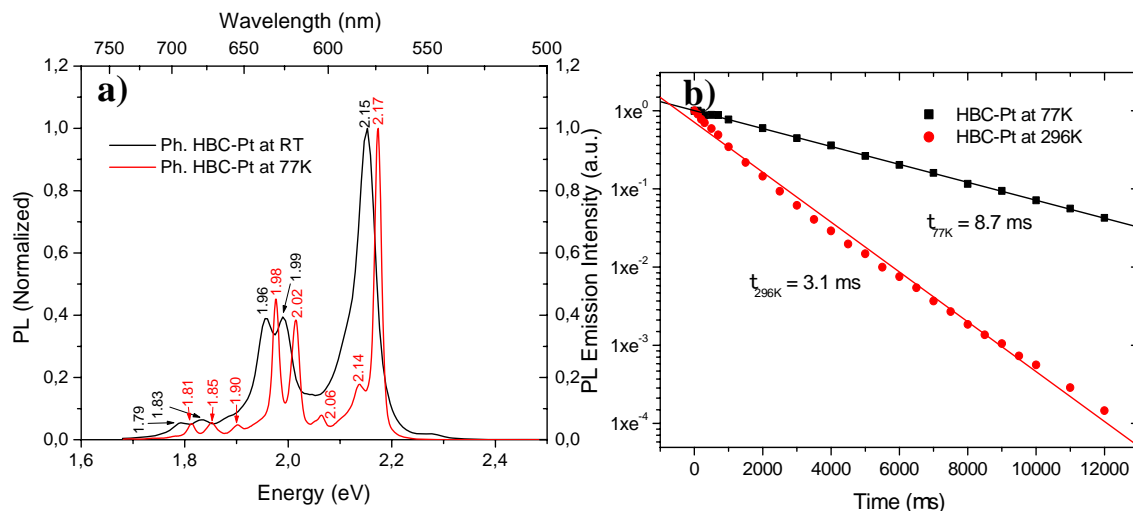


Figure 1: Molecular structure of HBC-Pt; **a)** Fluorescence and phosphorescence spectra of HBC-Pt 23 in *m*-THF (1.0×10^{-6} M) at room temperature and 77K; **b)** the phosphorescence decay plots for HBC-Pt 23 at RT and 77K.

I-b New amphiphilic columnar discotic materials based on hexa-peri-hexabenzocoronene with imidazolium fragments have been prepared (Figure 2). Hence, the idea of our straight-forward synthetic approach toward amphiphilic discotics has been reached.

The tetrasubstituted **37a** and **38a** π -systems were prepared by oxidative cyclodehydrogenation of suitable HPB precursors with FeCl₃. These precursors were built-up via Diels-Alder reaction followed by Suzuki or Negishi cross-coupling depending on the chloride-ended chains with N-methyl-imidazole provided the final materials as orange waxy solids. They could be dissolved only in water or DMSO after gentle heating. Structure and purity were proven by NMR and Maldi-TOF measurements. The chloride counter ions could be exchanged by PF₆⁻ or BF₄⁻ and could be detected by ¹H NMR and infra-red spectroscopy. The maximum absorption in DMSO and water is $\lambda_{\max} = 360$ nm, almost typical for usual HBCs. Upon increasing the water/DMSO ratio, the intensity of the bands at 342, 360 and 389 decreased and an increase at 418 nm pointed toward formation of aggregates. 2D-WAXS measurements revealed an orthorombic columnar lattice without change upon temperature variation or counter ion variation. The discs

were not tilted but orthogonal relatively to the columnar axis. The meridional reflections are relatively intense, suggesting large intracolumnar order. The self-assembly from solution on surface for both HBCs, using drop casting and slow precipitation techniques were investigated. Compound **38a** revealed ordered carbon nanofibers in different solvents under different treatment conditions unlike compound **37a** which showed that water is a better solvent than DMSO for growing of carbonaceous ordered nanostructures.

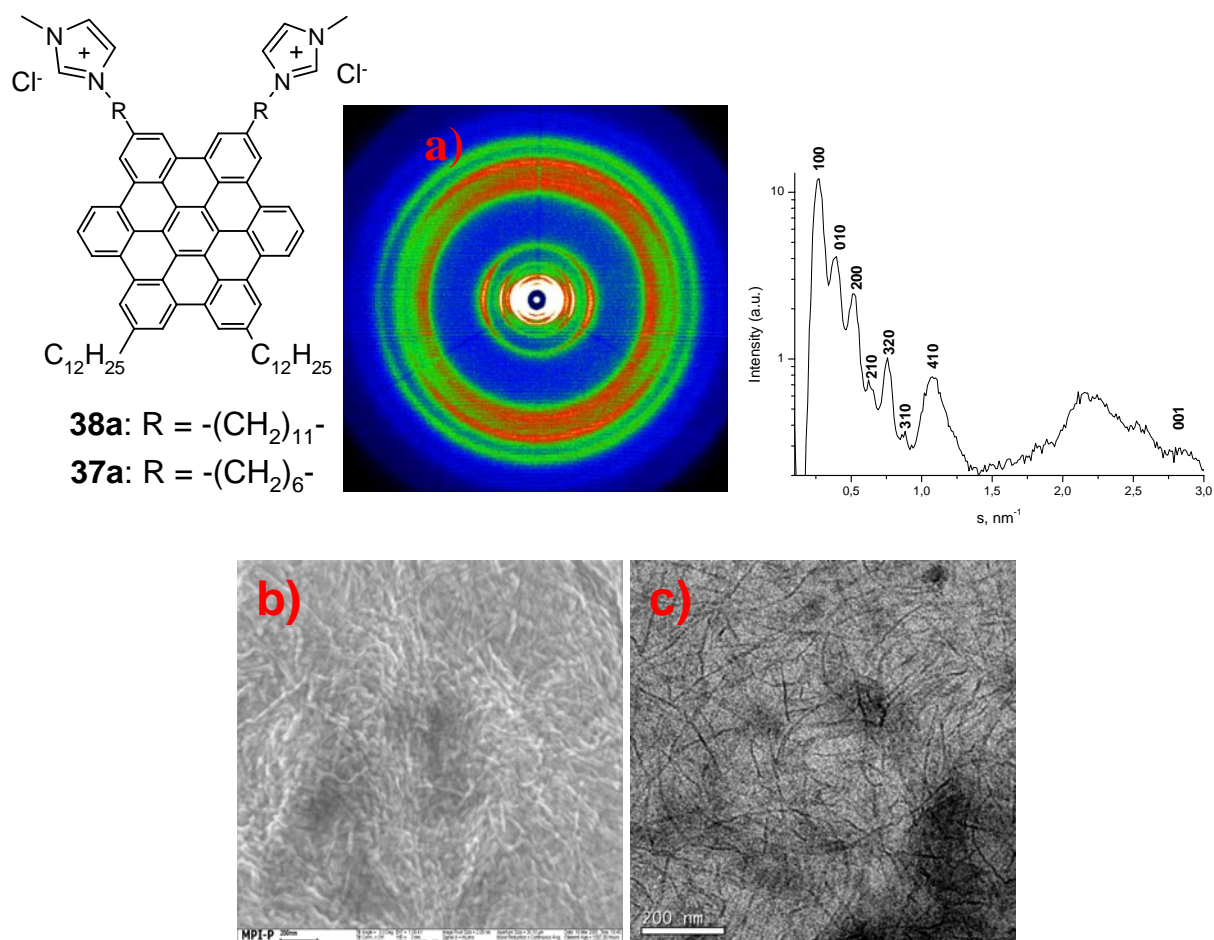


Figure 2: Chemical structure of **37a** and **38a**; **a)** X-ray diffraction and intensity distribution pattern for **1** at room temperature; SEM **b)** and TEM **c)** images showing fibers formation of compound **38** after precipitation with ethanol in DMSO.

I-c HBC derivatives, such as **45a-b**, substituted at the periphery by six branched alkyl ether chains were synthesized (Figure 3). It was shown that effective lowering of the isotropisation temperature could be achieved by introduction of bulky and space filling side chains,¹ which induce steric interactions at the core periphery and dominate the stacking ability of the discs. Additionally, the introduction of ether groups within the side chains enhances the affinity of the discotic molecules towards polar surfaces, resulting in homeotropic self-assembly when the compounds are processed from the isotropic state between one and two surfaces (Figure 3). These results are important for the design of photovoltaic cells based on HBC derivatives.

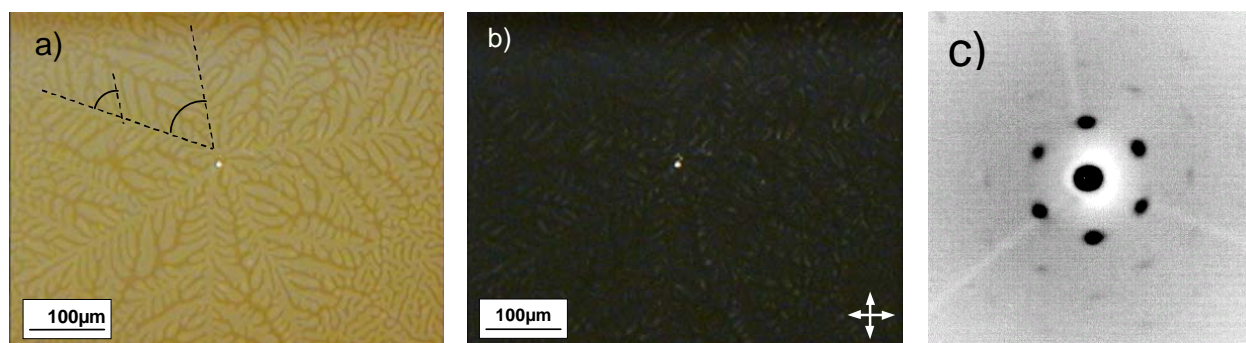
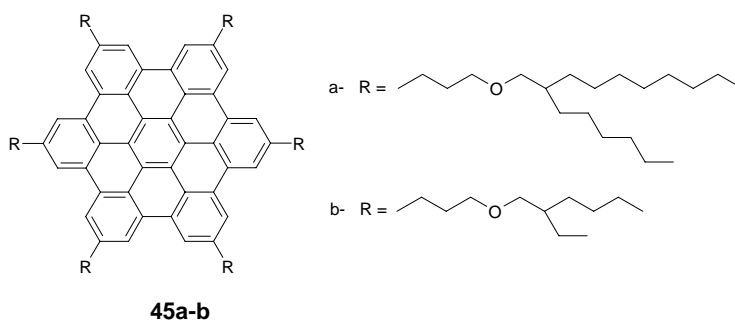


Figure 3: Molecular structures of alkyl ether substituted HBCs **45a-b**; a), b) optical microscopy images of **45a** homeotropically aligned during controlled crystallization between two glass slides; c) 2D-WAXS pattern of **45a** at room temperature crystallized between two thin aluminum foils.

II-a A new family of organometallic dendritic, graphitic and linear organometallic precursors where cobalt metal clusters at the peripheral ethynyl bonds have been prepared. The synthesis of these metal-organic frameworks is readily made in high yield, easy to purify and these materials are soluble in most organic solvents. Heating to the decomposition temperature, holding for two hours or more, and then increasing temperature, are common procedures for all molecules but the heating programs depend on every compound's decomposition temperature. The G₀ **71** dendrimer cobalt complex afforded carbon cobalt nanorods with different shape cross-sections depending on temperature (Figure 4a), and also was used as catalyst with tetraphenylmethane (as a carbon source) for CNTs formation. 1st and 2nd generation complexes, **72** and **73** respectively, provided carbon-cobalt nanospheres under fast heating rate and CNTs under slow heating rate.

C₉₆ **55** and all HBC cobalt complexes **50**, **52**, **57** and **67** revealed the formation of CNTs under slow and fast heating rates depending on the molecular structures, carbon/cobalt ratio and temperature procedure. HBC-(Co-Co)₆ **50** (Figure 4b) and C96-(Co-Co)₆ **55** (Figure 4c) exhibited high yields of CNTs under fast heating whereas **52**, **57** and **67** needed slower heating rate to obtain CNTs.

II-b Similarly to the diphenylacetylene cobalt complex, a series of linear and triangular organo-cobalt precursors (compounds **61**, **63** and **66**) were tested but none of them provided CNTs. The linear tolane-cobalt complex **61** afforded mostly amorphous carbon-cobalt materials, probably due to its symmetry. However, the 1,3,5-triethynylphenylbenzene-tris(dicobalt hexacarbonyl) complex **63** exhibited high yield of straight and curved carbon nanorods where cobalt is present as nanoparticles outside the rods (Figure 4d). Attempts to synthesize CNTs including sulfur atoms in the graphitic structure failed when di(2-thienyl)acetylene-dicobalt hexacarbonyl complex **66** was pyrolysed, probably due to the coordination of sulfur with

cobalt and decreasing its activity upon thermolysis. All these new materials could be used in the field of catalysis into carbon nanostructures as well as their potential applications in synthesis and growth of nanotubes by printing precursors onto certain surfaces, and fabrication of heterostructures of CNTs and metal carbides.

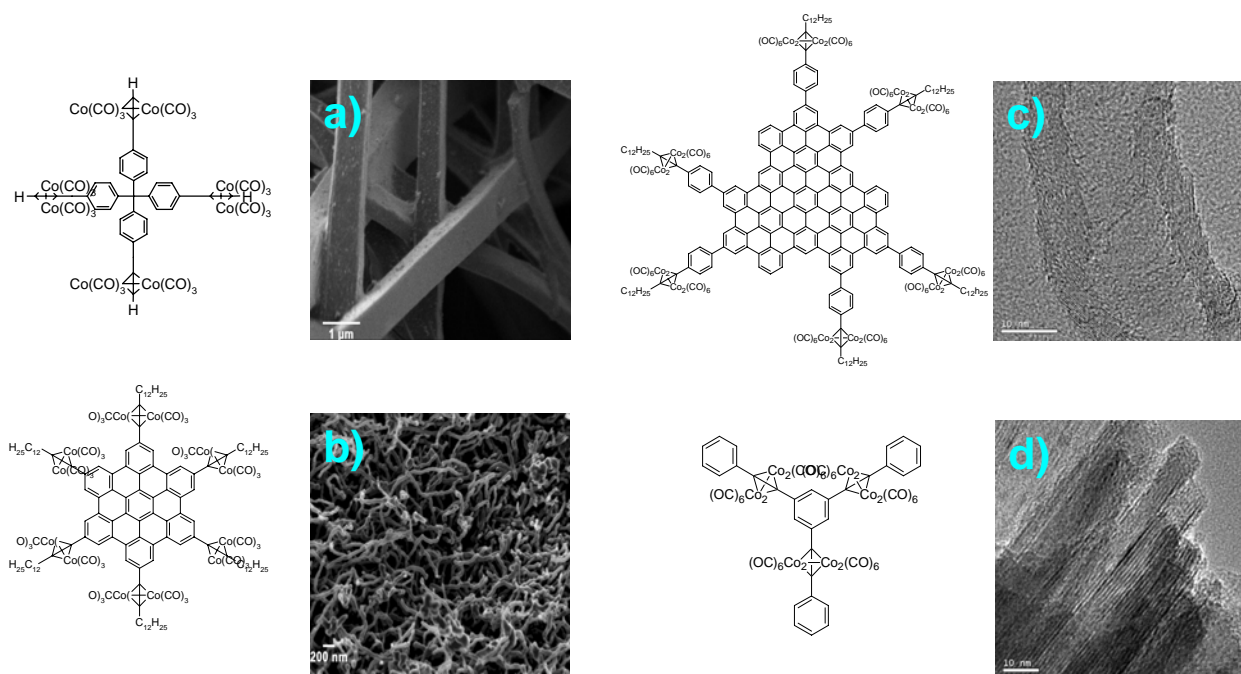


Figure 4: molecular structures of a variety of cobalt complexes; **a)** SEM picture of Td-Co **71** at 800 °C, **b)** SEM picture of HBC-(Co-Co)₆ **50** at 800 °C; **c)** TEM image of compound **55** at 800 °C; **d)** TEM picture of compound **63** at 850 °C.

In the future, various electroactive π -system moieties such as rylene dyes or thiophene² oligomers (dimers or trimers) can be attached to the platinum metal of the HBC-Pt **22** precursor via an acetylenic bond. The structures may induce higher spin-orbit coupling and therefore enhances the intersystem crossing. Indeed, this would decrease the probability of the non-radiative decay channels and thus increase the emission from the triplet excited state to singlet ground state. Because of the low emission quantum yields of the symmetric HBC **23**, the idea is to attach groups with high quantum efficiencies where electron and energy transfer

may happen. This principle can be investigated with N-(2,6-diisopropylphenyl)-9-ethynyl-3,4-perylene dicarboxmonoimide dye (PMI) through an ethynyl linker. The fluorescence of the HBC (donor) overlaps with the absorption band of the PMI (acceptor) additionally to the electron transfer through the platinum site. These organometallic compounds have increased interest due to their large potential for new photophysical and photochemical applications such as organic light emitting diodes.³ The self-assembly of amphiphilic HBCs is interesting because of their capability to organize into well-defined aggregates. Varying the ionic or the hydrophilic units attached to the HBC core by substitution with sulfonyl ions (simultaneously pyridylium groups on another HBC molecule) on the end of the alkyl chains and mixing the oppositely charged moieties may afford ordered nanostructures similarly to the nanotubes obtained with porphyrin molecules.⁴ This strategy could be very useful for applications in electronic devices such as semiconductor materials for FET mobility. The combination of hydrogen bonding π - π interaction allows creating ordered structures. The thermally reversible character of the H-bonding makes the system able to correct structure defects and provide order within bulk. One can also think of HBC core with sugar units, which may allow phase separation into well-ordered supramolecular architectures.

As shown in chapters five and six, organometallic precursors are of importance because of their ability to transform into well-defined pyrolytic structures such as carbon nanotubes, nanorods and nanoparticles, and their further functionalization. As mentioned previously, the cobalt nanoparticles embedded in the carbon nanorods (from precursor **71**) are ferromagnetic, which provide application opportunities in media storage. Various functionalization of these nanostructures are possible; pyrolysis of **71** at 200 °C together (PMI) in a certain ratio (to conserve the morphology of the nanorods) would lead to the formation of fluorescent carbon-cobalt nanorods in a similar way to the preparation of fluorescent carbon nanotubes (currently

in preparation in cooperation with Dr. Linjie Zhi). Moreover, thermolysis of **71** with stable, positively charged salts, such as 2-chloro-imidazolium, may lead to positively charged carbon nanostructures. The obtained materials would be interesting because of the possibility to further functionalize with DNA for biological purposes.

¹ such as the molecule **86b**, $T_{\text{isotropisation}} = 160\text{ }^{\circ}\text{C}$ in the PhD Thesis of Dr. Željko Tomović.

² N. Chawdhury, A. Köhler, R. H. Friend, W. -Y. Wong, J. Lewis, M. Younes, R. P. Raithby, T. C. Corcoran, M. R. A. Al-Mandhary, M. S. Khan *J. Chem. Phys.* **1999**, *110*, 4963.

³ Y.-Y. Lin, S. C. Chan, M. C. W. Chan, Y. -J. Hou, N. Zhu, C. -M. Che, Y. Liu, Y. Wang *Chem. Eur. J.* **2003**, *9*, 1263

⁴ Z. Wang, C. Medforth, J. Shelnett, *J. Am. Chem. Soc.* **2004**, *126*, 15954.

Chapter

8

Experimental section

8.1 General methods

NMR spectroscopy:

^1H NMR and ^{13}C NMR spectra were recorded in CD_2Cl_2 , $\text{C}_2\text{D}_2\text{Cl}_4$, THF- d_8 or CDCl_3 on a Bruker DPX 250, Bruker AMX 300, Bruker DRX 500 or Bruker DRX 700 spectrometer with use of the solvent proton or carbon signal as an internal standard.

Mass spectrometry:

FD mass spectra were obtained on a VG Instruments ZAB 2-SE-FPD spectrometer. MALDI-TOF mass spectra were measured on a Bruker Reflex ITOF spectrometer using a 337 nm nitrogen laser and 7,7,8,8-tetracyanoquinodimethane (TCNQ) as matrix. The mass instrument is not dedicated to isotopic measurements, and the deviations of relative intensities of peaks, from those calculated, can be more than 10%.

UV/Vis spectroscopy:

UV/Vis spectra were recorded at room temperature on a Perkin-Elmer Lambda 9 spectrophotometer.

Fluorescence spectroscopy:

Fluorescence spectra were recorded on a SPEX-Fluorolog II (212) spectrometer.

Melting points:

Melting points were determined using a Büchi B-545 apparatus in open capillaries and are uncorrected.

Elemental analysis:

Elemental analyses[*] were carried out on a Foss Heraeus Vario EL as a service of the Institute for Organic Chemistry, Johannes-Gutenberg-University of Mainz. [*] Because of the high

carbon content of large PAHs, combustion may be incomplete (soot formation), resulting in values lower than expected for the carbon content.

Differential scanning calorimetry (DSC):

DSC was measured on a Mettler DSC 30 with heating and cooling rates of 10 °C/min in the range from -150 °C to 250 °C.

Polarization microscopy:

A Zeiss Axiophot with a nitrogen flushed Linkam THM 600 hot stage was used to perform polarization microscopy.

X-ray:

Powder X-ray diffraction experiments were performed using a Siemens D 500 Kristalloflex diffractometer with a graphite-monochromatized CuK α X-ray beam, emitted from a rotating Rigaku RV-300 anode. 2D WAXS measurements of oriented filaments were conducted using a rotating anode (Rigaku 18 kW) X-ray beam (CuK α , pinhole collimation, double graphite monochromator) and CCD camera. The patterns were recorded with vertical orientation of the filament axis and with the beam perpendicular to the filament.

Solid-state thermolysis reaction:

The thermolysis was carried in a sealed quartz tube and the temperature was controlled by an electromagnet oven.

Scanning and Transmission Electron Microscopy:

SEM measurements were performed on a LEO 1530 field emission scanning electron microscope. TEM studies were conducted on a CM20 electron microscope at an operating voltage of 200kv. The sample was dispersed in ethanol using ultrasonic water bath and the suspension was dropped onto a copper grid.

Thermogravimetric Analysis:

TGA measurement was performed on a METTLER TOLEDO TS0801R0 device with a heating of 10K/min between 0 and 900 °C under inert atmosphere.

8.2 Materials

Chemicals and solvents:

The chemicals and solvents were obtained from the companies ABCR, Lancaster, Merck, Riedel-de Haen, Sigma-Aldrich, Fluka and Strem and used as obtained, unless otherwise mentioned. THF was freshly distilled over potassium prior to use in chemical reactions.

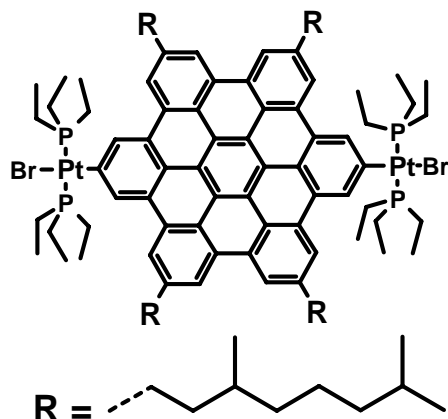
Chromatography:

Preparative column chromatography was performed on silica gel from Merck with a particle size of 0.063-0.200 mm (Geduran Si 60). For analytical thin layer chromatography (TLC) silica gel coated substrates 60 F254 from Merck were used. Compounds were detected by fluorescence quenching at 254 nm and self-fluorescence at 366 nm.

N. B. When more than one of the same branch is present, the prefixes *di*, *tri*, *tetra*, etc. are used for simple branches and *bis*, *tris*, *tetrakis*, etc. for branches containing numbers, are added just after the numbers locating the branch on the parent chain.

8.3 Synthesis

2,11-Bis[trans-bromobis(triethylphosphine)platinum]-5,8,14,17-tetrakis(3,7-dimethyloctyl)-hexa-*peri*-hexabenzocoronene (22)



2,11-Dibromo-5,8,14,17-tetrakis(3,7-dimethyloctyl)-hexa-*peri*-hexabenzocoronene (**21**) (100 mg, 0.08 mmol) and Pt(PEt₃)₄ (163 mg, 0.24 mmol) were dissolved in dry toluene under argon atmosphere. The mixture was heated at 60°C for 40 h. After cooling, an excess of methanol was added and the product was precipitated and collected. The residue was purified by column chromatography on silica gel, using petroleum ether/dichloromethane (4/6) and dichloromethane as eluents to afford 61 mg as green solid in 36% yield.

¹H NMR (250 MHz, CD₂Cl₂, 298K): δ_{ppm} = 9.32 (s, 4H, CH_{arom}), 9.05 (s, 4H, CH_{arom}), 8.98 (s, 4H, CH_{arom}), 3.26 (m, 8H, CH₂), 2.2-1.1 (overlapped, 112H, CH, CH₂, CH₃), 0.88 (d, ³J(H,H) = 6.59 Hz, 24H, CH₃),

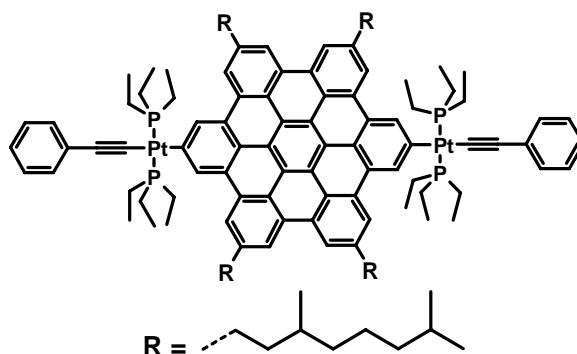
¹³C NMR (75 MHz, CD₂Cl₂, 298K): δ_{ppm} = 142.11, 140.4, 131.45, 131.13, 130.93, 129.42, 124.21, 122.32, 122.04, 120.97, 120.26, 39.97, 39.78, 37.75, 34.96, 33.15, 28.39, 25.14, 22.85, 22.77, 19.95, 14.75, 8.07.

³¹P{¹H} NMR (CD₂Cl₂, 202 MHz, 298K): δ_{ppm} = 6.51 (s, ¹J_{ppt} = 2740 Hz),

MS (MALDI-TOF): *m/z* (%) = 2104.5 (100) [*M*⁺], (calcd. for C₁₀₆H₁₅₆Br₂P₄Pt₂: 2104.27).

Elemental analysis: calcd. for C₁₀₆H₁₅₆Br₂P₄Pt₂: C 60.50%, H 7.47%, Found C 60.95%, H 8.05%.

2,11-Bis[trans-bis(triethylphosphine)-(phenylethynyl)platinum]-5,8,14,17-tetrakis(3,7-dimethyloctyl)-hexa-*peri*-hexabenzocoronene (23)



2,11-Bis[trans-bromobis(triethylphosphine)platinum]-5,8,14,17-tetrakis(3,7-dimethyloctyl)-hexa-*peri*-hexabenzocoronene (**22**) (20 mg; 0.0095 mmol) and phenylacetylene (4.85 mg, 0.0474 mmol) were dissolved in diisopropylamine (3 ml) under argon atmosphere. CuI (0.5 mg; 0.0027 mmol) was then added and the mixture was stirred overnight at room temperature. After adding an excess of methanol, the obtained precipitate was filtered and purified by column chromatography on silica gel using petroleum ether/dichloromethane mixture (7/3) then (4/6) as eluents to afford 9 mg in 44% yield.

^1H NMR (700 MHz, CD_2Cl_2 , 298K): δ_{ppm} = 9.38 (s, 4H, CH_{arom}), 9.04 (2s, 8H, CH_{arom}), 7.38 (br s, 4H, CH_{arom}), 7.27 (br s, 4H, CH_{arom}), 7.16 (br s, 2H, CH_{arom}) 3.4-3.15 (m, 8H, CH_2), 2.2-1.1 (overlapped, 112H, CH, CH_2 , CH_3), 0.88 (d, $^3\text{J}(\text{H},\text{H}) = 6.6$ Hz, 24H, CH_3);

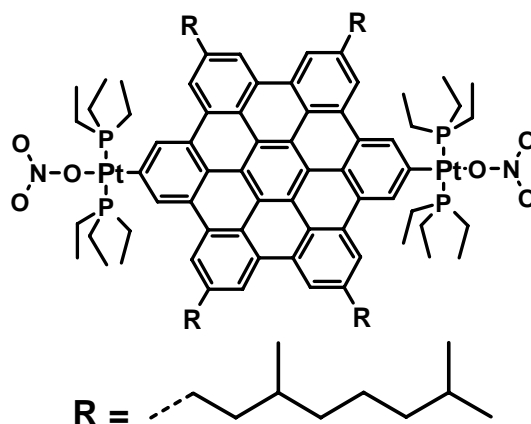
^{13}C NMR (125 MHz, CD_2Cl_2 , 298K): δ_{ppm} = 156.6, 141.92, 133.8, 131.72, 131.21, 131.05, 130.05, 128.75, 128.4, 125.08, 124.33, 122.38, 122, 121.71, 121.12, 120.24, 113.07, 110.70, 40.07, 39.87, 37.84, 35.07, 33.25, 28.44, 25.21, 22.90, 22.81, 20.01, 15.95, 8.38.

$^{31}\text{P}\{^1\text{H}\}$ NMR (CD_2Cl_2 , 202 MHz, 298K): δ_{ppm} = 4.65 (s, $^1\text{J}_{\text{ppt}} = 2606$ Hz).

MS (MALDI-TOF): m/z (%) = 2146.1 (100) [M^+], (calcd. for $\text{C}_{122}\text{H}_{166}\text{P}_4\text{Pt}_2$: 2146.7)

Elemental analysis: calcd. for $\text{C}_{122}\text{H}_{166}\text{P}_4\text{Pt}_2$: C 68.26%, H 7.79%, Found C 62.07%, H 7.32%.

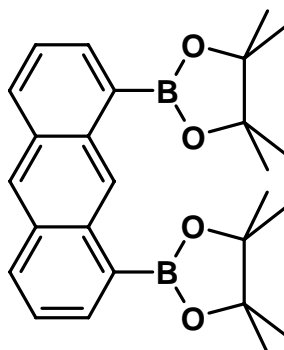
2,11-Bis[trans-nitratobis(triethylphosphine)platinum]-5,8,14,17-tetrakis(3,7-dimethyloctyl)-hexa-*peri*-hexabenzocoronene (26)



2,11-Bis[trans-bromobis(triethylphosphine)platinum]-5,8,14,17-tetrakis(3,7-dimethyloctyl)-hexa-*peri*-hexabenzocoronene (**22**) (25 mg, 0.012mmol) and a large excess (20.2 mg, 0.12 mmol, 10 equiv) of AgNO₃ were placed in a small two-neck-flask followed by 2 ml of dichloromethane. The reaction was stirred in the dark at room temperature for 24 h under inert atmosphere. A clear solution with a creamy precipitate resulted; the solution was carefully decanted, the solvent was removed under a flow of argon to afford 9 mg as yellow solid in 38% yield.

¹H NMR (700 MHz, CD₂Cl₂, 298K): δ_{ppm} = 9.26 (s, 4H, CH_{arom}), 9.06 (s, 4H, CH_{arom}), 8.99 (s, 4H, CH_{arom}), 3.40-3.21 (m, 8H, CH₂), 2.15-1.13 (m, 112H, CH, CH₂, CH₃), 0.87 (d, ³J(H,H) = 6.58 Hz, 24H, CH₃).

³¹P{¹H} NMR (CD₂Cl₂, 202 MHz): δ_{ppm} = 13.46 (s, ¹J_{ppt} = 2864 Hz).

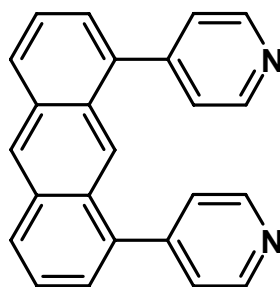
1,8-Bis(pinacolboronate)anthracene (28)

A dry 50 ml two-neck round flask was charged with $\text{Pd}_2(\text{dba})_3$ (42 mg, 0.046 mmol), tricyclohexylphosphine (52 mg, 0.19 mmol), 1,8-dichloroanthracene (**27**) (248 mg, 1.00 mmol), bis(pinacolato)diboron (564 mg, 2.22 mmol), potassium acetate (306 mg, 3.64 mmol) and dioxane (6 ml). The mixture was heated to reflux for five days, then after cooling, was transferred to a separation funnel. The organic phase was washed with water, extracted with dichloromethane, dried over MgSO_4 and the solvent was removed under vacuum. The residue was purified by column chromatography on silica gel with dichloromethane/hexane 1/1 mixture and then pure dichloromethane as eluents to afford 258 mg as green solid in 60% yield.

$^1\text{H-NMR}$ (250 MHz, CD_2Cl_2 , 298K): $\delta_{\text{ppm}} = 9.72$ (s, 1H, CH_{arom}), 8.44 (s, 1H, CH_{arom}), 8.17-8.06 (m, 4H, CH_{arom}), 7.48, 7.44 (2d, $^3\text{J}(\text{H,H}) = 6.6$ Hz, 2H, CH_{arom}), 1.48 (s, 12H, CH_3).

$^{13}\text{C-NMR}$ (62.5 MHz, CD_3Cl , 298K): $\delta_{\text{ppm}} = 136.81, 134.98, 132.25, 131.51, 128.16, 127.78, 124.67, 84.02, 25.27$.

MS (FD, 8 kV): m/z (%): 430.8 (100) [M^+] (calcd for $\text{C}_{26}\text{H}_{32}\text{B}_2\text{O}_4$: 430.16).

1,8-Bis(4-pyridyl)anthracene (29)

A dry 50 ml two-neck round flask was charged with 1,8-bis(pinacolboronate)anthracene (**28**) (190 mg, 0.44 mmol), Pd(PPh₃)₄ (51 mg, 0.044 mmol), 4-bromopyridine (429 mg, 2.2 mmol) and toluene (5 ml). K₂CO₃ (244 mg, 1.76 mmol) dissolved in water (0.6 ml) was added and the mixture was heated to 80 °C overnight. After cooling, the organic phase was washed with water, extracted with dichloromethane, dried over MgSO₄ and the solvent was removed under vacuum. The crude product was purified by column chromatography on silica gel with dichloromethane/triethylamine 1/1 mixture to yield light yellow solid in 65 %.

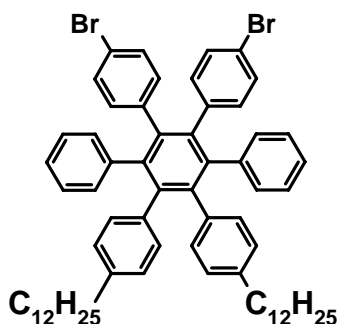
¹H-NMR (250 MHz, CD₂Cl₂, 298K): δ_{ppm} = 8.65 (d, 4H, ³J(H,H) = 5.9 Hz, CH_{arom}), 8.63 (s, 1H, CH_{arom}), 8.46 (s, 1H, CH_{arom}), 8.13 (d, 2H, ³J(H,H) = 8.43 Hz, CH_{arom}), 7.60 (d, 1H, ³J(H,H) = 8.3 Hz, CH_{arom}), 7.57 (d, 1H, ³J(H,H) = 8.5 Hz, CH_{arom}), 7.46 (d(overlapped), 2H, CH_{arom}), 7.42 (d, ³J(H,H) = 6.0 Hz, 4H, CH_{arom}).

¹³C-NMR (75 MHz, C₂D₂Cl₄, 323K): δ_{ppm} = 149.87, 148.48, 137.71, 132.03, 129.52, 129.32, 127.89, 127.21, 125.76, 125.05, 122.38.

MS (FD, 8 kV): m/z (%): 332.9 (100) [M⁺] (calcd for C₂₄H₁₆N₂: 332.4).

For single crystal X-ray results, see attached appendix

1,2-Bis(4-bromophenyl)-3,6-diphenyl-4,5-bis(4-dodecylphenyl)benzene (**31**)



3,4-Bis(4-dodecyl)phenyl-2,5-diphenylcyclopentadienone (**30**) (1g, 1.387 mmol) and 1,2-bis(4-bromophenyl)acetylene (**16**) (560 mg, 1.664 mmol) were suspended in a minimal amount of diphenyl ether (2.5 ml) and refluxed overnight under argon atmosphere. After cooling, diphenylether was removed under reduced pressure and the residue was purified by column chromatography on silica gel, with petroleum ether/dichloromethane 9/1 as eluent to afford 0.97 g as colorless solid in 68% yield.

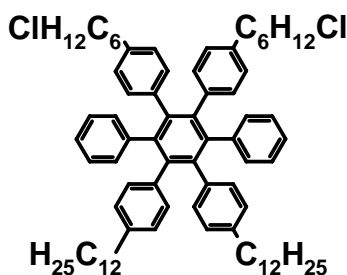
^1H NMR (250 MHz, CD_2Cl_2 , 298K): $\delta_{\text{ppm}} = 7.07\text{-}6.98$ (m, 4H, CH_{arom}), $6.93\text{-}6.78$ (m, 10H, CH_{arom}), $6.77\text{-}6.6$ (m, 12H, CH_{arom}), $2.39\text{-}2.28$ (m, 4H, CH_2), $1.6\text{-}1.0$ (m, 40H, CH_2), $0.95\text{-}0.8$ (m, 6H, CH_3).

^{13}C NMR (125 MHz, CD_2Cl_2 , 298K): $\delta_{\text{ppm}} = 141.55, 140.91, 140.84, 140.23, 140.19, 139.06, 138.10, 133.50, 131.75, 131.51, 130.27, 127.10, 127.01, 125.79, 119.91, 35.65, 32.36, 31.59, 30.13, 30.08, 29.90, 29.79, 29.24, 23.11, 14.27$.

MS (FD, 8 kV): m/z (%): 1028.8 (100) [M^+] (calcd for $\text{C}_{66}\text{H}_{76}\text{Br}_2$: 1029.15).

Elemental analysis: calcd. for $\text{C}_{66}\text{H}_{76}\text{Br}_2$: C 77.03%, H 7.44%, Found C 77.24%, H 7.39%.

1,2-Bis(4-(6-chlorohexyl)phenyl)-3,6-diphenyl-4,5-bis(4-dodecylphenyl)benzene (33)



To a solution of 1,2-bis(4-bromophenyl)-3,6-diphenyl-4,5-bis(4-dodecylphenyl)benzene (**31**) (500 mg, 0.48 mmol) and (6-chlorohexyl)zinc bromide (19.4 ml, 9.7 mmol in 0.5M THF solution) was added $\text{Pd}(\text{dppf})\text{Cl}_2$ (40 mg, 0.048 mmol). The mixture was left stirring at room temperature overnight under argon atmosphere and then quenched with water. The organic phase was washed with water three times, extracted with dichloromethane, dried over MgSO_4 and solvent was removed under vacuum. The crude product was purified by column chromatography on silica gel using petroleum ether/dichloromethane 9/1 as eluent to afford 300 mg as colorless solid in 55% yield.

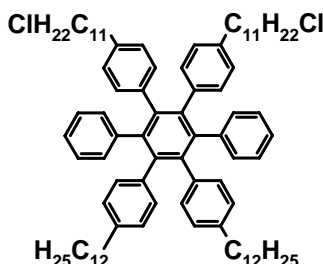
^1H NMR (250 MHz, CD_2Cl_2 , 298K): $\delta_{\text{ppm}} = 6.84$ (s, 10H, CH_{arom}), $6.75\text{-}6.61$ (m, 16H, CH_{arom}), 3.50 (t, $^3\text{J}(\text{H},\text{H}) = 6.75$ Hz, 8H, CH_2), $2.41\text{-}2.29$ (m, 8H, CH_2), $1.77\text{-}1.01$ (m, 56H, CH_2), 0.88 (t, $^3\text{J}(\text{H},\text{H}) = 6.62$ Hz, CH_3).

^{13}C NMR (125 MHz, CD_2Cl_2 , 353K): $\delta_{\text{ppm}} = 141.49, 140.73, 140.69, 140.61, 139.91, 139.58, 138.60, 138.45, 131.85, 131.64, 131.57, 126.86, 126.73, 125.26, 45.63, 35.59, 35.38, 32.99, 32.31, 31.59, 31.29, 30.09, 30.04, 29.86, 29.75, 29.18, 28.27, 26.98, 23.07, 14.26$.

MS (FD, 8 kV): m/z (%): 1110.1 (100) [M^+] (calcd for $\text{C}_{78}\text{H}_{100}\text{Cl}_2$: 1108.57).

Elemental Analysis: calcd. for $C_{78}H_{100}Cl_2$: C 84.51%, H 9.09%, found C 84.01%, H 9.95%.

1,2-Bis(4-(11-chloroundecyl)phenyl)-3,6diphenyl-4,5-bis(4-dodecylphenyl)benzene (34)



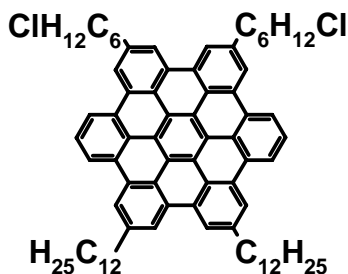
In a dry 100 mL two-necked round-bottomed flask 4.27 mL of a 0.5 M solution of 9-borabicyclo[3.3.1]nonane (9-BBN) in THF was added slowly to (367 mg, 1.943 mmol) of 11-chloro-1-undecene under an argon atmosphere, and the resulting mixture (**32**) was stirred overnight at room temperature. To this solution, at first, 0.65 mL of 3M aqueous K_2CO_3 solution was added via a syringe and then, after 15 min, 1,2-bis(4-bromophenyl)-3,6-diphenyl-4,5-bis(4-dodecylphenyl)benzene (**31**) (500 mg, 0.485 mmol) and 40 mg of $[PdCl_2(dppf)]$, respectively. The reaction mixture was stirred under argon at room temperature overnight. The organic phase was washed with water three times, extracted with CH_2Cl_2 , dried over $MgSO_4$ and the solvent was removed under vacuum. The residue was then purified by column chromatography on silica gel with petroleum ether / CH_2Cl_2 (9:1) as eluent to afford 360 mg as colorless solid in 60% yield.

1H NMR (500 MHz, CD_2Cl_2 , 298K): δ_{ppm} = 6.87-6.81 (m, 10H, CH_{arom}), 6.73-6.69 (m, 8H, CH_{arom}), 6.65 (d, $^3J(H,H)$ = 8.03 Hz, 8H, CH_{arom}), 3.54 (t, $^3J(H,H)$ = 6.08 Hz, 4H, CH_2), 2.35 (t, $^3(H,H)J$ =7.45 Hz, 8H, CH_2), 1.8-1.73 (m, 4H, CH_2), 1.54-1.06 (m, 72H, CH_2), 0.88 (t, $^3J(H,H)$ = 6.9 Hz, 6H, CH_3).

^{13}C NMR (125 MHz, CD_2Cl_2 , 298K): δ_{ppm} = 141.61, 140.78, 139.95, 138.57, 131.95, 131.68, 126.92, 126.79, 125.32, 45.71, 35.66, 33.16, 32.36, 31.62, 30.2, 30.14, 30.09, 29.91, 29.80, 29.34, 29.25, 27.34, 23.12.

MS (FD, 8 kV): m/z (%): 1248.0 (100) [M^+] (calcd for $C_{88}H_{120}Cl_2$: 1248.84).

Elemental analysis: calcd. for $C_{88}H_{120}Cl_2$: C 84.64%, H 9.69%, Found C 84.54%, H 9.74%.

2,5-Bis(6-chlorohexyl)-11,14-didodecyl-hexa-*peri*-hexabenzocoronene (35)

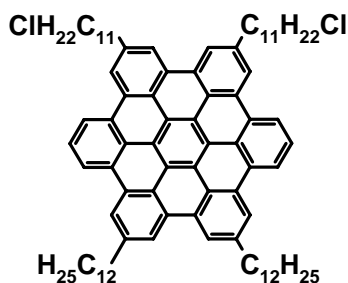
A 250 ml two-neck round bottomed flask was charged with 154 mg (0.123 mmol) of **(33)** and 60 ml CH_2Cl_2 . Using a glass capillary, a constant stream of argon was bubbled through the solution. Then, 600 mg (3.67 mmol) of FeCl_3 dissolved in CH_3NO_2 (6 ml) was added dropwise using a syringe. After 30 minute, the reaction was quenched with a large excess of methanol. The product was filtrated and washed several times with methanol. The residue was purified using column chromatography on silica gel with petroleum ether/dichloromethane (8/2) and then with toluene as eluents, to afford 120 mg as yellow solid in 55% yield.

^1H NMR (250 MHz, $\text{THF-d}_8/\text{CS}_2$, 298K): $\delta_{\text{ppm}} = 8.56$ (d, $^3\text{J}(\text{H,H}) = 9.2$ Hz, 4H, CH_{arom}), 8.54 (d, $^3\text{J}(\text{H,H}) = 8.9$ Hz, 4H, CH_{arom}), 8.38 (2s, 4H, CH_{arom}), 8.34, 8.31 (2s, 4H, CH_{arom}), 7.72 (t, $^3\text{J}(\text{H,H}) = 7.5$ Hz, 2H, CH_{arom}), 3.60 (t, $^3\text{J}(\text{H,H}) = 6.6$ Hz, 4H, CH_2), 3.01, 3.00 (two overlapped t, 8H, CH_2), 2.02-1.22 (m, 56H, CH_2), 0.94-0.81 (t, 6H, $^3\text{J}(\text{H,H}) = 6.5$ Hz, CH_3).

^{13}C NMR (125 MHz, $\text{C}_2\text{D}_2\text{Cl}_4$, 343K): $\delta_{\text{ppm}} = 143.19, 142.75, 132.53, 132.43, 128.64, 127.60, 125.79, 125.79, 124.21, 124.12, 124.04, 123.94, 123.89, 122.53, 122.43, 122.36, 48.12, 39.94, 39.73, 35.66, 34.82, 34.79, 34.55, 32.79, 32.69, 32.64, 32.56, 32.20, 31.90, 29.88, 25.51, 16.92$.

MS (MALDI-TOF): m/z (%) = 1096.59 (100) [M^+], (calcd. for $\text{C}_{78}\text{H}_{88}\text{Cl}_2$: 1096.48).

Elemental analysis: calcd. for $\text{C}_{78}\text{H}_{88}\text{Cl}_2$: C 85.44%, H 8.09%, Found C, 85.03%, H 8.44%.

2,5-Bis(11-chloroundecyl)-11,14-didodecyl-hexa-*peri*-hexabenzocoronene (36)

A 250 ml two necked round bottomed flask was charged with 50 mg (0.04 mmol) of **(34)** and 25 ml of CH_2Cl_2 . Using a glass capillary, a constant stream of argon was bubbled through the solution. Then, 117 mg (0.72 mmol) of FeCl_3 dissolved in CH_3NO_2 (1.5 ml) was added dropwise using a syringe. After 30 minutes, the reaction was quenched with a large excess of methanol. The product was filtrated and washed several times with methanol. The residue was purified using column chromatography on silica gel with petroleum ether/dichloromethane (8/2) and then with toluene as eluents, and dried under vacuum to afford 25 mg as a yellow solid in 51% yield.

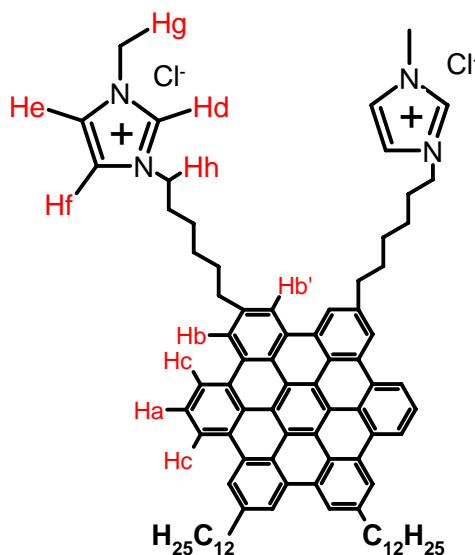
^1H NMR (250 MHz, $\text{THF-d}_8/\text{CS}_2$, 298K): δ_{ppm} = 8.79 (d, 4H, CH_{arom}), 8.61, 8.59 (2s, 8H, CH_{arom}), 7.87 (t, $^3\text{J}(\text{H,H}) = 7.9$ Hz, 2H, CH_{arom}), 3.46 (t, $^3\text{J}(\text{H,H}) = 6.68$ Hz, 4H, CH_2), 3.08 (t, $^3\text{J}(\text{H,H}) = 7.7$ Hz, 8H, CH_2), 2.08-1.92 (m, 8H, CH_2), 1.82-1.08 (m, 68H, CH_2), 0.91-0.81 (m, 6H, CH_3).

^{13}C NMR (175 MHz, $\text{C}_2\text{D}_2\text{Cl}_4$, 343K): δ_{ppm} = 140.48, 140.44, 129.92, 129.86, 129.79, 125.97, 124.95, 123.13, 121.53, 121.46, 121.24, 119.82, 119.68, 45.48, 37.32, 32.96, 32.21, 32.17, 30.18, 30.15, 30.10, 30.08, 30.02, 29.94, 29.91, 29.77, 29.59, 29.19, 27.21, 22.90, 14.31.

MS (MALDI-TOF): m/z (%) = 1236.1 (100) [M^+], (calcd. for $\text{C}_{88}\text{H}_{108}\text{Cl}_2$: 1236.75).

Elemental analysis: calcd. for $\text{C}_{88}\text{H}_{108}\text{Cl}_2$: C 85.46%, H 8.80%, Found C 85.27%, H 8.95%.

2,5-bis[6-(3-methyl-1-imidazoliumyl)]-11,14-didodecylhexa-*peri*- hexabenzocoronene dichloride (37a)



A dry 25 ml two-neck round flask was charged with 100 mg (0.09 mmol) of (**35**) and excess of N-methylimidazol (3 ml). The mixture was heated to 135 °C for 24 hours. After cooling, an excess of hexane was added. The precipitate was filtered and washed with hexane to afford 90 mg as orange waxy solid in 78% yield.

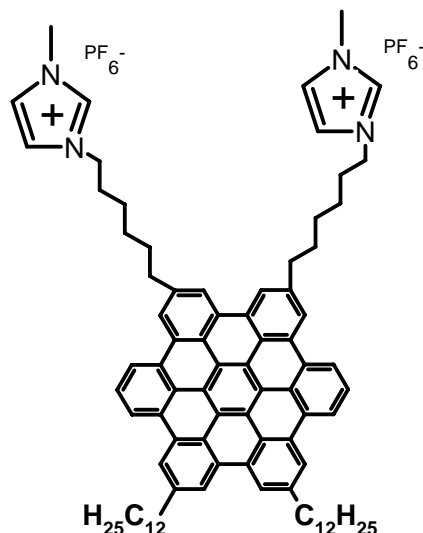
¹H NMR (500 MHz, DMSO, 373K): δppm = 9.18 (s, 2H, H_d, CH_{arom}), 9.10, 9.08 (2d, 4H, H_c, ³J(H,H) = 7.6 Hz, CH_{arom}), 8.95, 8.94 (2s, 4H, H_{b,b'}, CH_{arom}), 8.87, 8.86 (2s, 4H, H_{b,b'}, CH_{arom}), 8.11 (t, ³J(H,H) = 7.4 Hz, 2H, H_a, CH_{arom}), 7.72 (s, 2H, H_{e,f}, CH_{imid}), 7.62 (s, 2H, H_{e,f}, CH_{imid}), 4.24 (t, ³J(H,H) = 7.1 Hz, 4H, CH₂), 3.85 (s, 6H, CH₃), 3.25 (t, ³J(H,H) = 7.3 Hz, 4H, CH₂), 3.19 (t, ³J(H,H) = 7.3 Hz, 4H, CH₂), 2.12-1.10 (m, 58H, CH₂), 0.84-0.75 (m, 6H, CH₃).

¹³C NMR (125 MHz, DMSO, 393K): δppm = 140.53, 136.96, 136.11, 129.05, 128.98, 126.90, 126.04, 123.72, 123.48, 122.98, 122.82, 122.55, 121.99, 121.84, 121.50, 121.27, 120.94, 118.89, 118.74, 48.57, 35.46, 35.41, 35.10, 30.44, 30.30, 28.93, 28.70, 28.29, 28.27, 28.25, 28.21, 27.80, 27.74, 25.11, 25.03, 21.11, 12.77.

MS (MALDI-TOF): *m/z* (%) = 1188.88 (100) [*M*⁺], (calcd. for C₈₆H₁₀₀N₄: 1188.77).

Elemental analysis: calcd. for C₈₆H₁₀₀N₄Cl₂ : C 81.93%, H 7.99%, N 4.44%, Found C 78.36%, H 8.26%, N 4.52%.

2,5-bis[6-(3-methyl-1-imidazoliumyl)]-11,14-didodecylhexa-*peri*-hexabenzocoronene bis(hexafluorophosphate) (37b)



37a (15 mg, 0.011 mmol) was dissolved in a minimal amount of hot water. A solution of NH_4PF_6 (19.4 mg, 0.118 mmol) in 3 ml of water was added dropwise. The resulting yellow precipitate was filtrated and washed with water to give 13 mg of **37b** in 79% yield.

^1H NMR (500 MHz, DMSO, 353K): $\delta_{\text{ppm}} = 9.10$ (d, 2H, H_{c} , $^3\text{J}(\text{H},\text{H}) = 8.1$ Hz, CH_{arom}), 9.08 (d, 2H, H_{c} , $^3\text{J}(\text{H},\text{H}) = 8.1$ Hz, CH_{arom}), 9.06 (s, 2H, H_{d} , CH_{arom}), 8.95 (d, 4H, $^3\text{J}(\text{H},\text{H}) = 8.8$ Hz, $\text{H}_{\text{b,b'}}$, CH_{arom}), 8.85 (d, 4H, $^3\text{J}(\text{H},\text{H}) = 8.6$ Hz, $\text{H}_{\text{b,b'}}$, CH_{arom}), 8.10 (t, $^3\text{J}(\text{H},\text{H}) = 7.8$ Hz, 2H, H_{a} , CH_{arom}), 7.72 (t, $^3\text{J}(\text{H},\text{H}) = 1.7$ Hz, 2H, $\text{H}_{\text{e,f}}$, CH_{imid}), 7.63 (t, 2H, $^3\text{J}(\text{H},\text{H}) = 1.7$ Hz, $\text{H}_{\text{e,f}}$, CH_{imid}), 4.20 (t, $^3\text{J}(\text{H},\text{H}) = 7.3$ Hz, 4H, CH_2), 3.82 (s, 6H, CH_3), 3.23 (t, $^3\text{J}(\text{H},\text{H}) = 7.7$ Hz, 4H, CH_2), 3.15 (t, $^3\text{J}(\text{H},\text{H}) = 7.6$ Hz, 4H, CH_2), 2.09-1.13 (m, 56H, CH_2), 0.77 (t, $^3\text{J}(\text{H},\text{H}) = 6.9$ Hz, 6H, CH_3).

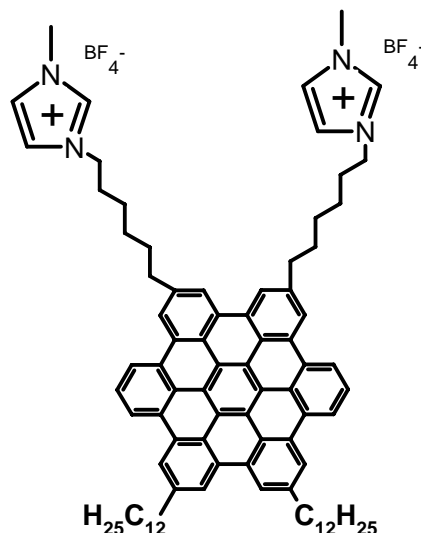
^{13}C NMR (75 MHz, DMSO, 393K): $\delta_{\text{ppm}} = 139.79, 139.69, 135.95, 128.68, 128.61, 128.51, 128.42, 125.42, 123.35, 123.05, 122.64, 121.70, 121.65, 121.46, 120.78, 120.64, 118.35, 118.24, 48.48, 35.72, 35.51, 35.17, 30.65, 30.44, 28.73, 28.61, 28.49, 28.41, 28.31, .28.21, 28.03, 27.83, 25.03, 24.14, 21.34, 13.04$.

MS (MALDI-TOF): m/z (%) = 1188.85 (100) [M^+], (calcd. for $\text{C}_{86}\text{H}_{100}\text{N}_4$: 1188.77).

MS (MALDI-TOF): m/z (%) = 143.6 (100) [M^-], (calcd. for (PF_6^-) : 144.96).

Elemental analysis: calcd. for $\text{C}_{86}\text{H}_{100}\text{N}_4\text{P}_2\text{F}_{12}$: C 69.80%, H 6.81%, N 3.78%, Found C 69.81%, H 6.74%, N 3.79%.

2,5-bis[6-(3-methyl-1-imidazoliumyl)]-11,14-didodecylhexa-*peri*-hexabenzocoronene bis(tetrafluoroborate) (37c)



37a (15 mg, 0.011 mmol) was dissolved in a minimal amount of hot water. A solution of NH_4BF_4 (12.5 mg, 0.118 mmol) in 3 ml of water was added dropwise. The resulting yellow precipitate was filtrated and washed with water to give 12 mg of **37c** in 80% yield.

^1H NMR (500 MHz, DMSO, 353K): $\delta_{\text{ppm}} = 9.14$ (d, 2H, H_c , $^3\text{J}(\text{H,H}) = 8.7$ Hz, CH_{arom}), 9.12 (d, 2H, H_c , $^3\text{J}(\text{H,H}) = 8.7$ Hz, CH_{arom}), 9.06 (s, 2H, H_d , CH_{arom}), 8.99 (d, 4H, $^3\text{J}(\text{H,H}) = 8.8$ Hz, $\text{H}_{b,b'}$, CH_{arom}), 8.90 (d, 4H, $^3\text{J}(\text{H,H}) = 5.7$ Hz, $\text{H}_{b,b'}$, CH_{arom}), 8.13 (t, $^3\text{J}(\text{H,H}) = 7.8$ Hz, 2H, H_a , CH_{arom}), 7.72 (t, $^3\text{J}(\text{H,H}) = 1.7$ Hz, 2H, $\text{H}_{e,f}$, CH_{imid}), 7.63 (t, 2H, $^3\text{J}(\text{H,H}) = 1.7$ Hz, $\text{H}_{e,f}$, CH_{imid}), 4.20 (t, $^3\text{J}(\text{H,H}) = 7.3$ Hz, 4H, CH_2), 3.82 (s, 6H, CH_3), 3.24 (t, $^3\text{J}(\text{H,H}) = 7.7$ Hz, 4H, CH_2), 3.17 (t, $^3\text{J}(\text{H,H}) = 7.7$ Hz, 4H, CH_2), 2.09-1.13 (m, 56H, CH_2), 0.77 (t, $^3\text{J}(\text{H,H}) = 6.9$ Hz, 6H, CH_3).

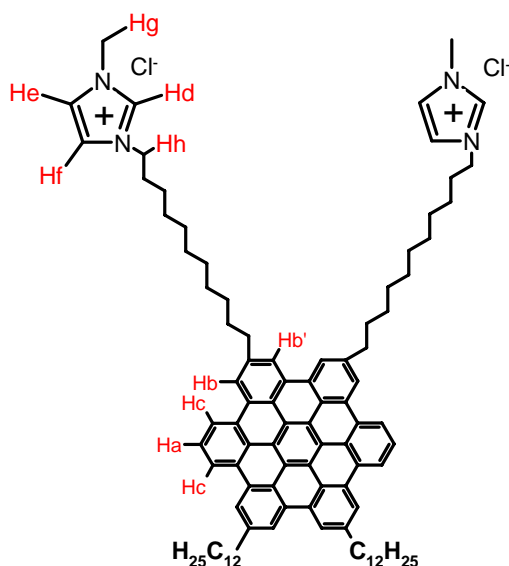
^{13}C NMR (75 MHz, DMSO, 393K): $\delta_{\text{ppm}} = 140.68, 140.52, 136.06, 129.17, 129.10, 129.01, 128.96, 128.83, 123.82, 123.13, 122.12, 121.93, 121.82, 121.59, 121.43, 119.04, 118.97, 118.87, 48.63, 35.65, 35.35, 35.24, 30.61, 30.54, 28.86, 28.42, 28.35, 27.97, 27.94, 25.17, 21.30, 13.01$.

MS (MALDI-TOF): m/z (%) = 1188.86 (100) [M^+], (calcd. for $\text{C}_{86}\text{H}_{100}\text{N}_4$: 1188.77).

MS (MALDI-TOF): m/z (%) = 85.68 (100) [M^-], (calcd. for (BF_4^-) : 86.80).

Elemental analysis: calcd. for $\text{C}_{86}\text{H}_{100}\text{N}_4\text{B}_2\text{F}_8$: C 74.58% H 7.27%, N 4.04%, Found C 73.96%, H 7.37%, N 4.39%.

2,5-bis[11-(3-methyl-1-imidazoliumyl)]-11,14-didodecylhexa-*peri*-hexabenzocoronene dichloride (38a)



A dry 25 ml two-neck round flask was charged with 18 mg (0.0145 mmol) of **(36)** and excess of N-methylimidazol (2 ml) were added. The mixture was heated to 135 °C for 24 hours. After cooling, excess of hexane was added. The precipitate was filtered and washed with hexane to afford 15 mg as orange waxy solid in 74% yield.

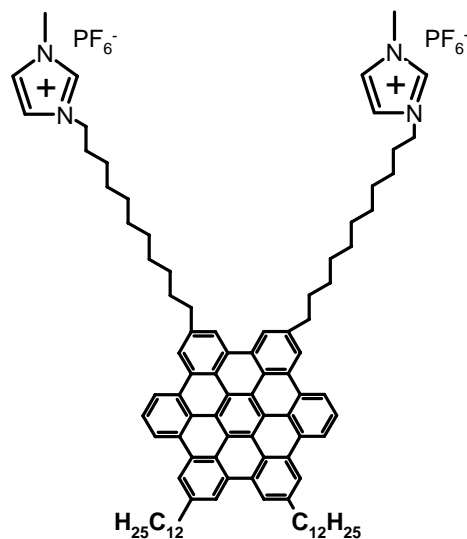
¹H NMR (500 MHz, DMSO, 373K): δ_{ppm} = 9.01 (s, 2H, H_d, CH_{Imid}), 8.95, 8.92 (2d, 4H, H_c, CH_{arom}), 8.79, 8.78 (2s, 4H, H_{b,b'}, CH_{arom}), 8.72, 8.70 (2s, 4H, H_{b,b'}, CH_{arom}), 8.00 (t, ³J(H,H)= 7.7 Hz, 2H, H_a, CH_{arom}), 7.58 (m, 2H, H_{e,f}, CH_{Imid}), 7.55 (m, 2H, CH_{Imid}), 4.06 (t, ³J(H,H)= 7.3 Hz, 4H, CH₂), 3.79 (s, 6H, CH₃), 3.19 (t, ³J(H,H)= 7.6 Hz, 4H, CH₂), 3.14 (t, ³J(H,H)= 7.6 Hz, 4H, CH₂), 2.08-1.08 (m, 76H, CH₂), 0.84-0.78 (m, 6H, CH₃).

¹³C NMR (125 MHz, DMSO, 393K): δ_{ppm} = 139.70, 139.62, 136.11, 128.62, 128.56, 128.48, 128.39, 125.41, 123.32, 123.02, 121.69, 121.62, 121.44, 120.72, 120.69, 120.59, 118.30, 118.20, 48.44, 35.70, 35.51, 35.17, 30.65, 30.42, 28.76, 28.61, 28.51, 28.48, 28.41, 28.31, 28.03, 27.84, 25.06, 21,33, 13.04.

MS (MALDI-TOF): m/z (%) = 1330.09 (100) [M^+], (calcd. for C₉₆H₁₂₀N₄: 1330.05).

Elemental analysis: calcd. for $C_{96}H_{120}N_4Cl_2$: C 82.30%, H 8.63%, N, 3.99%, Found C 77.30%, H 9.76%, N, 4.95%.

2,5-bis[11-(3-methyl-1-imidazoliumyl)]-11,14-didodecylhexa-*peri*-hexabenzocoronene bis(hexafluorophosphate) (38b)



Prepared as described above for compound (37b). yellow precipitate, yield: 78%.

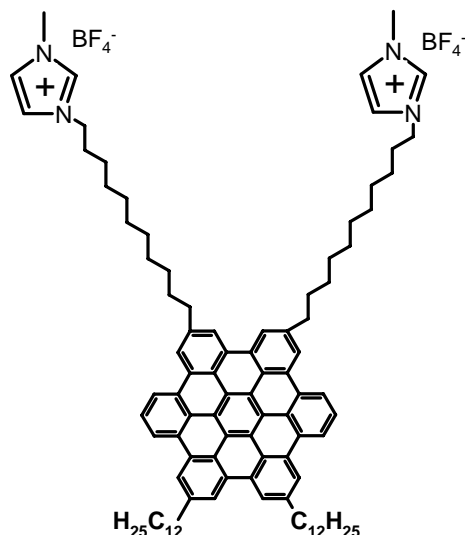
1H NMR (500 MHz, DMSO, 353K): δ_{ppm} = 8.97 (s, 2H, H_d , CH_{arom}), 8.76 (d, 2H, H_c , $^3J(H,H)$ = 8.2 Hz, CH_{imid}), 8.70 (d, 2H, H_c , $^3J(H,H)$ = 8.0 Hz, CH_{arom}), 8.59 (s, 4H, $H_{b,b'}$, CH_{arom}), 8.48, 8.43 (2s, 4H, $H_{b,b'}$, CH_{arom}), 7.85 (t, $^3J(H,H)$ = 7.6 Hz, 2H, H_a , CH_{arom}), 7.63 (t, $^3J(H,H)$ = 1.7 Hz, 2H, $H_{e,f}$, CH_{imid}), 7.59 (t, 2H, $^3J(H,H)$ = 1.7 Hz, $H_{e,f}$, CH_{imid}), 4.04 (t, $^3J(H,H)$ = 7.3 Hz, 4H, CH_2), 3.76 (s, 6H, CH_3), 3.10 (t, $^3J(H,H)$ = 7.6 Hz, 4H, CH_2), 3.00 (t, $^3J(H,H)$ = 7.6 Hz, 4H, CH_2), 2.04-1.13 (m, 76H, CH_2), 0.78 (t, $^3J(H,H)$ = 6.9 Hz, 6H, CH_3).

^{13}C NMR (75 MHz, DMSO, 393K): δ_{ppm} = 139.78, 139.69, 135.95, 128.68, 128.61, 128.51, 128.42, 125.46, 123.35, 123.05, 121.70, 121.65, 121.46, 120.86, 120.78, 120.65, 118.35, 118.24, 48.48, 35.72, 35.52, 35.17, 30.65, 30.44, 28.73, 28.60, 28.51, 28.49, 28.41, 28.31, 28.03, 27.83, 25.05, 21.34, 13.04.

MS (MALDI-TOF): m/z (%) = 1330.11 (100) [M^+], (calcd. for $C_{96}H_{120}N_4$: 1330.05).

MS (MALDI-TOF): m/z (%) = 143.55 (100) [M^+], (calcd. For (PF_6^-) : 144.96).

2,5-bis[11-(3-methyl-1-imidazoliumyl)]-11,14-didodecylhexa-*peri*-hexabenzocoronene bis(tetrafluoroborate) (38c)



Prepared as described above for compound (37c). yellow precipitate, yield: 84%.

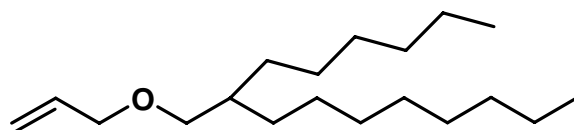
^1H NMR (500 MHz, DMSO, 353K): δ_{ppm} = 8.98 (s, 2H, H_d , CH_{arom}), 8.76 (d, 2H, H_c , $^3\text{J}(\text{H,H}) = 7.9$ Hz, CH_{imid}), 8.70 (d, 2H, H_c , $^3\text{J}(\text{H,H}) = 7.4$ Hz, CH_{arom}), 8.58 (s, 4H, $\text{H}_{b,b'}$, CH_{arom}), 8.47, 8.41 (2s, 4H, $\text{H}_{b,b'}$, CH_{arom}), 7.84 (t, $^3\text{J}(\text{H,H}) = 7.3$ Hz, 2H, H_a , CH_{arom}), 7.64 (t, $^3\text{J}(\text{H,H}) = 1.7$ Hz, 2H, $\text{H}_{e,f}$, CH_{imid}), 7.60 (t, 2H, $^3\text{J}(\text{H,H}) = 1.7$ Hz, $\text{H}_{e,f}$, CH_{imid}), 4.03 (t, $^3\text{J}(\text{H,H}) = 7.3$ Hz, 4H, CH_2), 3.76 (s, 6H, CH_3), 3.10 (t broad, 4H, CH_2), 3.00 (t broad, 4H, CH_2), 2.04-1.12 (m, 76H, CH_2), 0.77 (t, $^3\text{J}(\text{H,H}) = 6.8$ Hz, 6H, CH_3).

^{13}C NMR (125 MHz, DMSO, 393K): δ_{ppm} = 139.64, 139.54, 135.92, 128.60, 128.53, 128.43, 128.34, 125.33, 123.28, 123.03, 121.67, 121.59, 121.40, 120.65, 120.51, 118.25, 118.14, 48.47, 35.68, 35.47, 35.14, 30.62, 30.36, 28.69, 28.57, 28.48, 28.45, 28.38, 28.27, 27.99, 27.80, 25.03, 21.29, 12.98.

MS (MALDI-TOF): m/z (%) = 1330.12 (100) [M^+], (calcd. for $\text{C}_{86}\text{H}_{100}\text{N}_4$: 1330.05).

MS (MALDI-TOF): m/z (%) = 85.64 (100) [M^-], (calcd. for (BF_4^-) : 86.80).

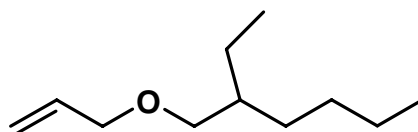
Elemental analysis: calcd. for $\text{C}_{96}\text{H}_{120}\text{N}_4\text{B}_2\text{F}_8$: C 75.59% H 7.93%, N 3.67%, Found C 75.06%, H 8.10%, N 4.24%.

3-(2-Hexyldecyloxy)propene (41a)

(As an example of the synthesis of alkyl allyl ethers) Into a 500 mL three-neck round bottomed flask, equipped with a condenser, a magnetic stirring bar and a dropping funnel, was introduced a mixture of 6.335 g (0.026 mol) of 2-hexyl-1-decanol (**39a**), 21 mL of 10M (0.210 mol) aqueous NaOH solution and 0.9 g (2.623 mmol) of tetrabutylammonium hydrogen sulphate, while 7.96 g (0.104 mol) of allyl chloride (**40**) were added dropwise with stirring at 30 °C. The resulting mixture was heated to 45 °C and stirred in an inert atmosphere overnight. After cooling, the product was extracted with petrol ether, washed three times with water, and the solvent removed under reduced pressure. Purification using column chromatography on silica gel with petrol ether as the eluent afforded **3a** (5.625 g, 76%) as a colorless liquid.

¹H-NMR (250 MHz, C₂D₂Cl₄, 298K): δ_{ppm} = 5.90-5.75 (m, 1H, =CH-), 5.25-5.13 (m, ³J (H,H)_{trans} = 17.4 Hz, 1H, C=CH₂), 5.12-5.03 (m, ³J (H,H)_{cis} = 10.4 Hz, 1H, C=CH₂), 3.86 (d, ³J (H,H) = 5.4 Hz, 2H, O-CH₂-), 3.20 (d, ³J (H,H) = 6.0 Hz, 2H, O-CH₂-), 1.47 (br, 1H, CH), 1.18 (m, 24H, CH₂), 0.85-0.75 (m, 6H, CH₃);

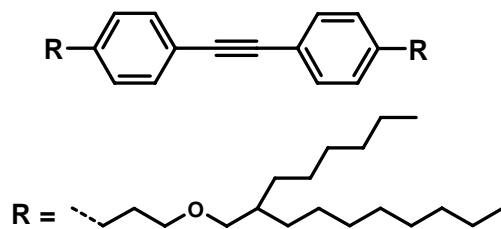
¹³C-NMR (62.5 MHz, C₂D₂Cl₄, 298K): δ_{ppm} = 135.82, 116.48, 73.93 (O-CH₂-), 72.03 (O-CH₂-), 38.50, 32.23, 32.21, 31.72, 30.42, 30.08, 29.95, 29.67, 27.14, 27.11, 23.03, 14.52.

3-(2-Ethylhexyloxy)propene (41b).

Prepared as described above for compound (**39a**). Colorless liquid, yield: 70%.

¹H-NMR (250 MHz, C₂D₂Cl₄, 298K): δ_{ppm} = 5.90-5.74 (m, 1H, =CH-), 5.24-5.12 (m, ³J (H,H)_{trans} = 17.4 Hz, 1H, C=CH₂), 5.11-5.02 (m, ³J (H,H)_{cis} = 10.4 Hz, 1H, C=CH₂), 3.86 (d, ³J (H,H) = 5.4 Hz, 2H, O-CH₂-), 3.21 (d, ³J (H,H) = 6.0 Hz, 2H, O-CH₂-), 1.49-1.15 (m, 9H, CH, CH₂), 0.85-0.74 (m, 6H, CH₃);

¹³C-NMR (75 MHz, C₂D₂Cl₄, 298K): δ_{ppm} = 135.78, 116.52, 73.49 (O-CH₂-), 72.05 (O-CH₂-), 39.89, 30.86, 29.41, 24.17, 23.43, 14.48, 11.41.

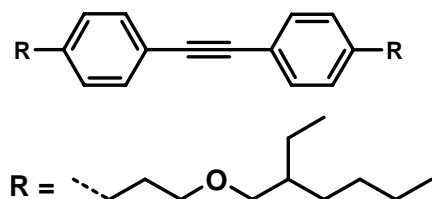
4,4'-Bis(3-(2-hexyldecyloxy)propyl)diphenylacetylene (43a).

(As an example of the synthesis of substituted diphenyl-acetylenes) In a dry 100 mL two-necked round-bottomed flask 68 mL of a 0.5 M solution of 9-borabicyclo[3.3.1]nonane (9-BBN) (**26**) in THF was added slowly to 5.624 g (19.9 mmol) of 3-(2-hexyldecyloxy)propene (**41a**) under an argon atmosphere, and the resulting mixture was stirred overnight at room temperature. To this solution, at first, 13.0 mL of 3M aqueous NaOH solution was added via a syringe and then, after 15 min, 1.672 g (4.97 mmol) of 4,4'-bis(bromophenyl)acetylene (**16**) and 205 mg of [PdCl₂(dppf)], respectively. The reaction mixture was stirred under argon at room temperature for another 5 hours. The product was extracted with CH₂Cl₂, washed with water three times and dried over magnesium sulfate. After evaporating the solvent, the residue was purified by column chromatography on silica gel with petroleum ether / CH₂Cl₂ (7:3) to afford (**43a**) (2.574 g, 70%) as a colorless oil.

¹H-NMR (250 MHz, C₂D₂Cl₄, 298K): δ_{ppm} = 7.37 (d, ³J (H,H) = 8.2 Hz, 4H, CH_{arom}), 7.10 (d, ³J (H,H) = 7.9 Hz, 4H, CH_{arom}), 3.29 (t, ³J (H,H) = 6.0 Hz, 4H, O-CH₂-), 3.17 (d, ³J (H,H) = 5.7 Hz, 4H, O-CH₂-), 2.62 (t, ³J (H,H) = 7.4 Hz, 4H, α-CH₂), 1.85-1.70 (m, 4H, β-CH₂), 1.55 - 1.40 (m, 2H, CH), 1.30 - 1.10 (br, 48H, CH₂), 0.85 - 0.72 (m, 12H, CH₃);

¹³C-NMR (75 MHz, C₂D₂Cl₄, 298K): δ_{ppm} = 143.03, 131.85, 128.89, 120.81, 89.35, 74.37 (O-CH₂-), 69.99 (O-CH₂-), 38.43, 32.59, 32.22, 31.75, 31.38, 30.45, 30.10, 29.97, 29.67, 27.14, 27.11, 23.04, 14.56;

MS (FD, 8 kV): m/z (%): 744.8 (100) [M⁺] (calcd for C₅₂H₈₆O₂: 743.3).

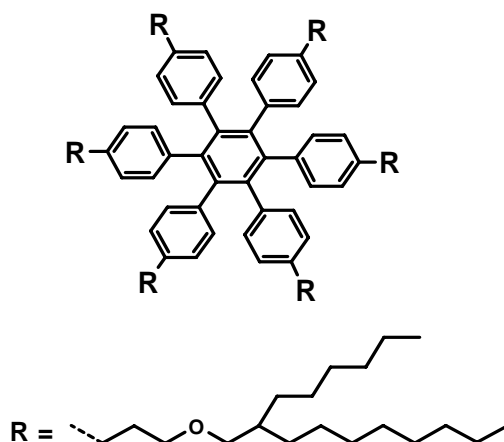
4,4'-Bis(3-(2-ethylhexyloxy)propyl)diphenylacetylene (43b).

Prepared as described above for compound (43a). Colorless oil, yield: 62%.

$^1\text{H-NMR}$ (250 MHz, $\text{C}_2\text{D}_2\text{Cl}_4$, 298K): $\delta_{\text{ppm}} = 7.37$ (d, ^3J (H,H) = 7.9 Hz, 4H, CH_{arom}), 7.11 (d, ^3J (H,H) = 8.2 Hz, 4H, CH_{arom}), 3.30 (t, ^3J (H,H) = 6.3 Hz, 4H, O- CH_2 -), 3.18 (d, ^3J (H,H) = 5.7 Hz, 4H, O- CH_2 -), 2.62 (t, ^3J (H,H) = 7.4 Hz, 4H, α - CH_2), 1.90-1.72 (m, 4H, β - CH_2), 1.56 (br, 2H, CH), 1.40 - 1.12 (m, 16H, CH_2), 0.95 - 0.75 (m, 12H, CH_3);

$^{13}\text{C-NMR}$ (75 MHz, $\text{C}_2\text{D}_2\text{Cl}_4$, 298K): $\delta_{\text{ppm}} = 143.02$, 131.87, 128.91, 120.80, 89.35, 73.95 (O- CH_2 -), 70.00 (O- CH_2 -), 39.81, 32.58, 31.40, 30.86, 29.39, 24.20, 23.47, 14.57, 11.48;

MS (FD, 8 kV): m/z (%): 518.3 (100) [M^+] (calcd for $\text{C}_{36}\text{H}_{54}\text{O}_2$: 518.8).

Hexakis-4-(3-(2-hexyldecyloxy)propyl)hexaphenylbenzene (44a).

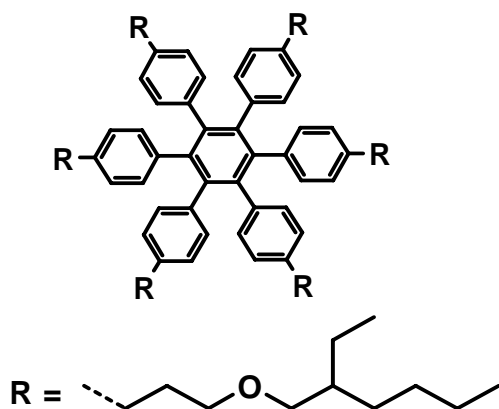
(As an example of the cyclotrimerization reaction). 75 mg (0.219 mmol) $\text{Co}_2(\text{CO})_8$ was added under argon to a degassed solution of 1.98 g (2.66 mmol) 4,4'-bis(3-(2-hexyldecyloxy)propyl)diphenylacetylene (43a) in 170 mL of dioxane in a 250 mL round bottomed flask equipped with a reflux condenser. After refluxing for 5 hours, the solvent was evaporated under vacuum, and the residue was purified using column chromatography on silica gel with petrol ether / CH_2Cl_2 (4:6) as the eluent, yielding (44a) as Colorless oil, yield: 62%.

$^1\text{H-NMR}$ (250 MHz, $\text{C}_2\text{D}_2\text{Cl}_4$, 298K): $\delta_{\text{ppm}} = 6.59$ (d, $^3J(\text{H,H}) = 8.2$ Hz, 12H, CH_{arom}), 6.53 (d, $^3J(\text{H,H}) = 8.2$ Hz, 12H, CH_{arom}), 3.10 – 2.96 (m, 24H, O-CH_2-), 2.39 – 2.27 (m, 12H, $\alpha\text{-CH}_2$), 1.54-1.50 (m, 12H, $\beta\text{-CH}_2$), 1.41 (br, 6H, CH), 1.25 - 1.10 (br, 144H, CH_2), 0.79 (t, $^3J(\text{H,H}) = 6.3$ Hz, 36H, CH_3);

$^{13}\text{C-NMR}$ (175 MHz, $\text{C}_2\text{D}_2\text{Cl}_4$, 298K): $\delta_{\text{ppm}} = 140.27, 138.79, 138.24, 131.71, 126.74, 74.24$ (O-CH_2-), 69.65 (O-CH_2-), 38.52, 32.21, 31.95, 31.74, 31.40, 30.43, 30.09, 29.95, 29.65, 27.13, 27.09, 23.01, 14.53, 14.48, ;

MS (FD, 8 kV): m/z (%): 2231.3 (100) [M^+] (calcd for $\text{C}_{156}\text{H}_{258}\text{O}_6$: 2229.8).

Hexakis-4-(3-(2-ethylhexyloxy)propyl)hexaphenylbenzene (44b).

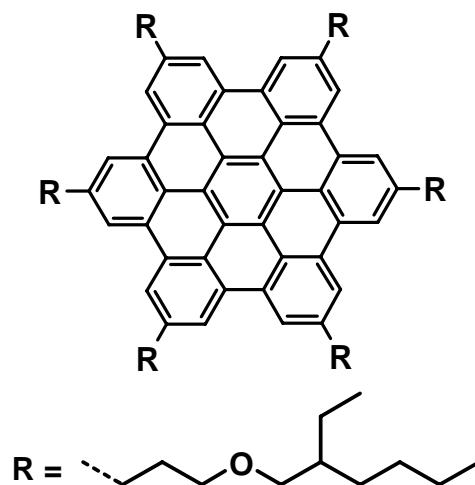


Prepared as described above for compound (44a). Colorless oil, yield: 72%.

$^1\text{H-NMR}$ (250 MHz, $\text{C}_2\text{D}_2\text{Cl}_4$, 298K): $\delta_{\text{ppm}} = 6.60$ (d, $^3J(\text{H,H}) = 8.2$ Hz, 12H, CH_{arom}), 6.54 (d, $^3J(\text{H,H}) = 7.9$ Hz, 12H, CH_{arom}), 3.10 – 2.96 (m, 24H, O-CH_2-), 2.40 – 2.25 (m, 12H, $\alpha\text{-CH}_2$), 1.57-1.50 (m, 12H, $\beta\text{-CH}_2$), 1.42 – 1.32 (m, 6H, CH), 1.30 - 1.10 (m, 48H, CH_2), 0.86 – 0.71 (m, 36H, CH_3);

$^{13}\text{C-NMR}$ (175 MHz, $\text{C}_2\text{D}_2\text{Cl}_4$, 298K): $\delta_{\text{ppm}} = 140.28, 138.80, 138.23, 131.71, 126.77, 73.79$ (O-CH_2-), 69.65 (O-CH_2-), 39.88, 31.93, 31.40, 30.85, 29.37, 24.18, 23.44, 14.54, 14.48, 11.45, 11.39;

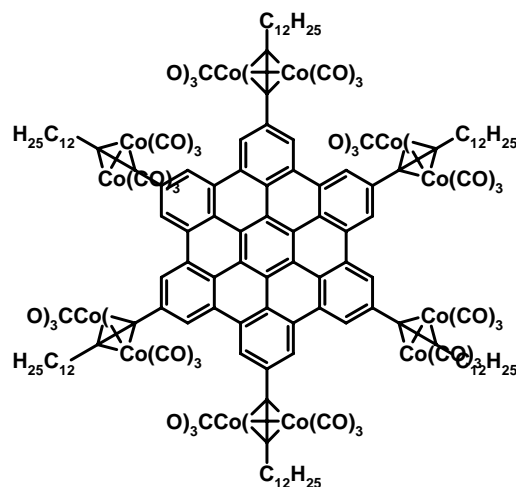
MS (FD, 8 kV): m/z (%): 1154.7 (100) [M^+] (calcd for $\text{C}_{108}\text{H}_{162}\text{O}_6$: 1556.5).

Hexakis(3-(2-ethylhexyloxy)propyl)-hexa-*peri*-hexabenzocoronene (45b).

Prepared as described above for compound (45a), using 0.1 g (0.064 mmol) of (44b), 1.25 g (7.7 mmol) of FeCl₃, and a reaction time of 3h. (45b) was isolated as yellow waxy solid in 91% yield.

¹H-NMR (700 MHz, C₂D₂Cl₄, 373K): δ_{ppm} = 8.66 (s, 12H, CH_{arom}), 3.66 (br, 12H, O-CH₂-), 3.45 (br, 12H, O-CH₂-), 3.27 – 3.17 (m, 12H, α-CH₂), 2.34 – 2.23 (m, 12H, β-CH₂), 1.68 – 1.60 (m, 6H, CH), 1.57 – 1.32 (m, 48H, CH₂), 1.03 – 0.90 (m, 36H, CH₃);

¹³C-NMR (175 MHz, C₂D₂Cl₄, 298K): δ_{ppm} = 140.00, 129.88, 123.35, 121.64, 119.67, 74.35 (O-CH₂-), 70.70 (O-CH₂-), 39.99, 33.85, 32.53, 31.02, 29.54, 24.41, 23.52, 14.61, 11.62; **MS (MALDI-TOF):** *m/z* (%): 1544.4 (100) [*M*⁺] (calcd for C₁₀₈H₁₅₀O₆: 1544.4).

Hexakis(dodecylethynyl)-*peri*-hexabenzocoronene-hexakis(dicobalt hexacarbonyl) (50)

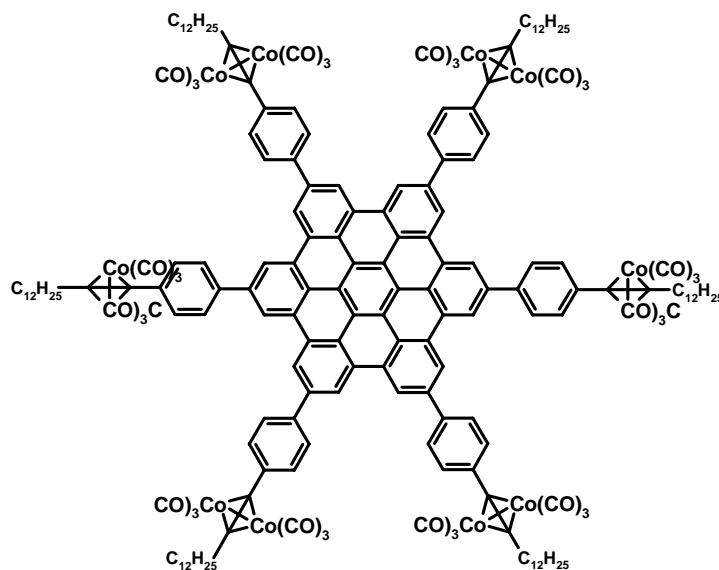
The synthesis procedure of **50** is an example for the reaction of dicobalt octacarbonyl on the peripheral ethynyl functionalities of discs, dendrimers, and diphenylacetylene derivatives: $[\text{Co}_2(\text{CO})_8]$ (500 mg, 1.46 mmol) and hexakis(dodecylethynyl)-*peri*-hexabenzocoronene (**49**) (82 mg, 0.24 mmol) were dissolved in CH_2Cl_2 (8 ml) under argon atmosphere; the mixture was stirred overnight at room temperature and the solvent was removed under vacuum at 30 °C. The residue was purified by column chromatography on silica gel with petroleum ether and petroleum ether/dichloromethane 9/1 as eluents, to afford a red waxy solid in 50% yield.

$^1\text{H NMR}$, $\delta =$ (500MHz, CD_2Cl_2 , 298 K): $\delta_{\text{ppm}} = 9.26$ (s, 12H, CH_{arom}), 1.08 (m, 150H, $\text{CH}_2\text{-CH}_3$).

MS (FD, 8 kV): m/z (%): 3392.2(100) [M^+], (calcd. for $\text{C}_{162}\text{H}_{162}\text{Co}_{12}\text{O}_{36}$: 3392.25)

FT-IR(KBr pellet) : $\bar{\nu} = 2019$ (vs), 2049 (s), 2088 cm^{-1} (s) (vs CO).

Hexakis[4-(dodecylethynyl)phenyl]-*peri*-hexabenzocoronene-hexakis(dicobalt hexacarbon-yl) (52)



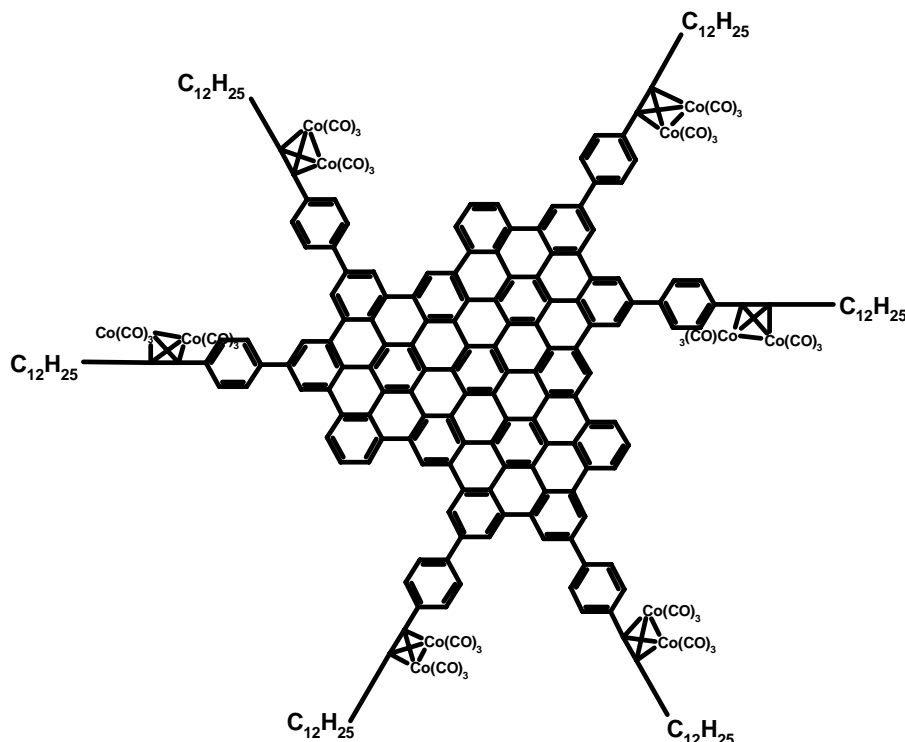
(52) is prepared as described above for compound (50). Brownish oil, yield 60%.

$\text{Co}_2(\text{CO})_8$	(51)	CH_2Cl_2	Reaction time	Eluents
385 mg, 1.125 mmol	80 mg, 0.0375 mmol	6 mL	60 hours	PE and PE/DCM ^a 9/1

^aPE : petroleum ether; DCM : dicloromethane.

¹H NMR (250 MHz, CD_2Cl_2 , 298 K): $\delta_{\text{ppm}} = 9.84\text{-}9.50$ ppm (br, 12H, $\text{CH}_{\text{arom.}}$), $8.21\text{-}8.10$ (br, 12H, $\text{CH}_{\text{arom.}}$), 7.88 (d, $^3\text{J}(\text{H,H}) = 8$ Hz, 12H, $\text{CH}_{\text{arom.}}$), 3.24-3.18 (m, 12H, CH_2), 2.0-1.15 ppm (m, 120H, CH_2), 0.89 (t, $^3\text{J}(\text{H,H}) = 6.9$ Hz, 18H, CH_3).

FT-IR(KBr pellet) : $\bar{\nu} = 2020$ (vs), 2048 (s), 2089 cm^{-1} (s, CO).

Hexakis[4-(dodecylethynyl)phenyl]-C₉₆- hexakis(dicobalt hexacarbonyl) (55)

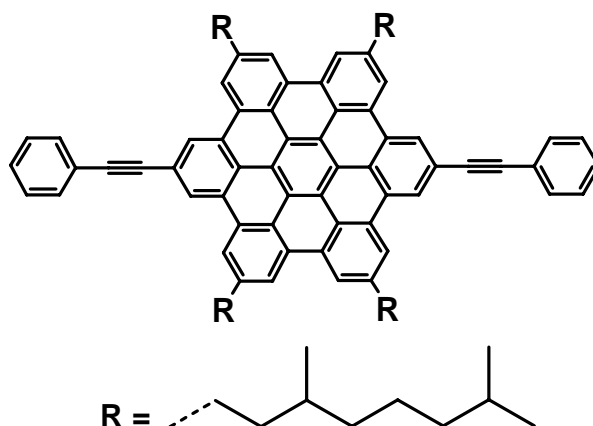
(55) is prepared as described above for compound (50). Red solid, yield 47%.

Co ₂ (CO) ₈	(54)	CH ₂ Cl ₂	Reaction time	Eluents
183 mg, 0.537 mmol	50 mg, 0.019 mmol	6 ml	three days	PE/DCM ^a 8/2

^aPE : petroleum ether; DCM : dicloromethane.

¹H NMR (250 MHz, CD₂Cl₂, 298K): δ = 6.30-8.75 (b, 24H, CH_{arom.}), 0.52-3.95 (b, 150H, CH₂, CH₃).

FT-IR(KBr pellet) : $\bar{\nu}$ = 2023 (s), 2047 (s), 2087 cm⁻¹ (vs, CO).

2,11-Bis(phenylethynyl)-5,8,14,17-tetrakis(3,7-dimethyloctyl)-hexa-*peri*-hexabenzocoronene (56)

To a frame-dried 25 ml two-neck round flask was added (**21**) (104 mg, 0.083 mmol), Pd(PPh₃)₄ (12 mg, 9.68 mmol), CuI (2 mg), and piperidine (3.5 ml). The mixture was degassed by bubbling argon for 15 min, and then phenylacetylene (172 mg, 1.65 mmol) was added. The solution was heated to 80°C overnight, cooled to RT, and excess of methanol was added. The yellow precipitate was collected and purified by column chromatography on silica gel with Petroleum ether/dichloromethane 8/2 and dichloromethane respectively, to afford 65 mg of yellow solid in 61% yield.

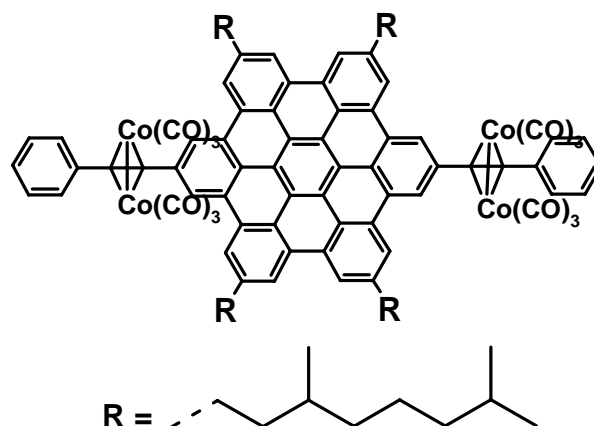
¹H NMR (500 MHz, C₂D₂Cl₄, 353 K): δ_{ppm} = 8.20 (s, 4H, CH_{arom}), 7.96-7.81 (m [3 broad signals], 12H, CH_{arom}), 7.54-7.44 (m, 6H, CH_{arom}), 3.03-2.85 (m, 8H, α-CH₂), 2.08-1.25 (m, 40H, CH, CH₂), 1.19 (d, ³J(H,H) = 6.58 Hz, 12H, CH₃), 0.95 (d, ³J(H,H) = 6.63 Hz, 24H, CH₃).

¹³C NMR (125 MHz, CD₂Cl₂, 353K): δ_{ppm} = 139.95, 132.30, 129.01, 128.82, 128.77, 128.54, 128.25, 124.40, 123.85, 123.50, 121.96, 121.28, 121.03, 119.97, 118.63, 118.14, 91.86, 89.78, 39.99, 39.82, 37.75, 34.92, 33.74, 28.32, 25.31, 23.08, 22.97, 20.14.

MS (MALDI-TOF): *m/z* (%): 1283.6 (100) [*M*⁺] (calcd for C₉₈H₁₀₆:1283.94).

Elemental analysis: calcd. for C₈₈H₁₀₈Cl₂: C, 91.68 H 8.32, Found C, 91.68 H 8.21.

2,11-Bis(phenylethynyl)-5,8,14,17-tetrakis(3,7-dimethyloctyl)-hexa-*peri*-hexabenzocoronene-bis(dicobalt hexacarbonyl) (57)



(57) is prepared as described above for compound (50). Brown wax, yield 51%.

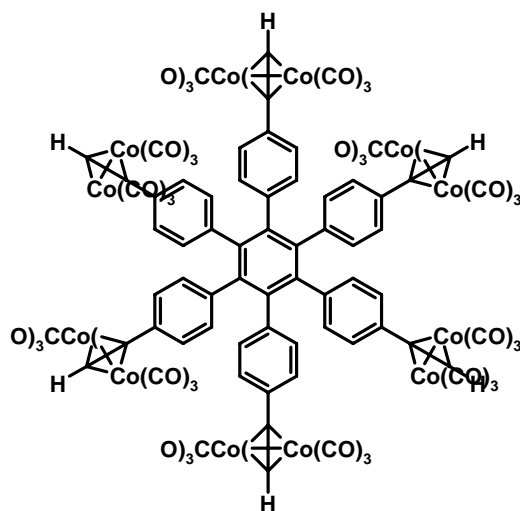
Co ₂ (CO) ₈	(56)	CH ₂ Cl ₂	Reaction time	Eluents
103mg, 0.30 mmol	39 mg, 0.03 mmol	4 ml	Two days	PE and PE/DCM ^a 9/1

^aPE : petroleum ether; DCM : dichloromethane.

¹H NMR (300 MHz, CD₂Cl₂, 298 K): δ_{ppm} = 9.43 (s, 4H, CH_{arom}), 8.94 (s, 4H, CH_{arom}), 8.82 (s, 4H, CH_{arom}) 8.00 (d, ³J(H,H) = 6.78 Hz, 4H, CH_{arom}), 7.68-7.46 (m, 6H, CH_{arom}), 3.37-3.10 (broad, 8H, α-CH₂), 2.12-1.08 (m, 52H, CH, CH₂, CH₃), 0.89 (d, ³J (H,H) = 6.01 Hz, 24H, CH₃).

¹³C NMR (75 MHz, CD₂Cl₂, 298K): δ_{ppm} = 200.08, 142.19, 139.19, 136.90, 131.29, 130.49, 130.04, 129.95, 129.61, 128.62, 125.31, 123.86, 122.97, 122.83, 122.39, 120.81, 120.45, 93.25, 93.06, 39.82, 37.74, 35.01, 33.29, 28.43, 25.21, 22.89, 22.79, 19.90.

FT-IR(KBr pellet) : $\bar{\nu}$ = 2020 (vs), 2052 (s), 2087 cm⁻¹ (s, CO).

Hexakis[4-(ethynylphenyl)]benzene-hexakis(dicobalt hexacarbonyl) (59)

(59) is prepared as described above for compound (50). Red solid, yield 25%.

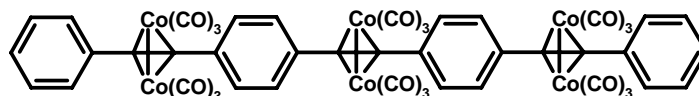
$\text{Co}_2(\text{CO})_8$	(58)	CH_2Cl_2	Reaction time	Eluents
755.6 mg, 2.21 mmol	50 mg, 0.0736 mmol	8 ml	Three days	PE/DCM ^a 9/1

^aPE : petroleum ether; DCM : dichloromethane.

¹H NMR (250 MHz, CD_2Cl_2 , 298K): $\delta_{\text{ppm}} = 7.04$ ppm (d, $^3J(\text{H},\text{H}) = 8.21$, 12H, CH_{arom}), 6.77 (d, $^3J(\text{H},\text{H}) = 8.21$ Hz, 12H, CH_{arom}), 6.17 (s, 6H, CH).

¹³C NMR (175 MHz, CD_2Cl_2 , 298K): $\delta_{\text{ppm}} = 199.97$, 140.73, 140.51, 134.99, 132.34, 129.30, 90.37, 73.04.

FT-IR(KBr pellet) : $\bar{\nu} = 2010$ (s), 2022 (s), 2032 (vs), 2051 (vs), 2094 cm^{-1} (s, CO).

4,4'-Bis(phenylethynyl)-diphenylacetylene-tris(dicobalt hexacarbonyl) (61)

(61) is prepared as described above for compound (50). Brown solid, yield 37%.

Co ₂ (CO) ₈	(60)	CH ₂ Cl ₂	Reaction time	Eluents
1355 mg, 3.963 mmol	100 mg, 0.264 mmol	10 ml	Three days	PE and PE/DCM ^a 9/1

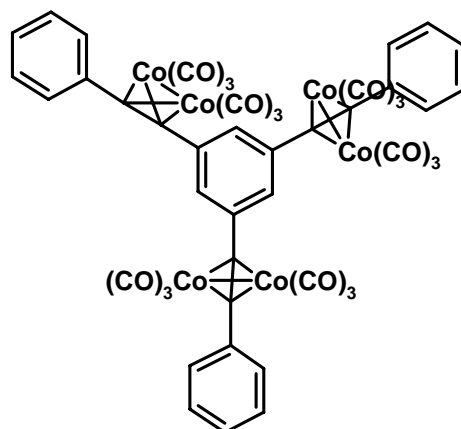
^aPE : petroleum ether; DCM : dicloromethane.

¹H NMR (300 MHz, CD₂Cl₂, 298K): δ_{ppm} = 7.67-7.53 (m, 12H, CH_{arom}), 7.43-7.32 (m, 6H, CH_{arom})

¹³C NMR (75 MHz, CD₂Cl₂, 298K): δ_{ppm} = 199.62, 138.72, 138.65, 138.57, 130.16, 129.67, 129.34, 128.34, 92.91, 91.98, 91.60.

FT-IR(KBr pellet) : $\bar{\nu}$ = 2017(vs), 2025(vs), 2049(s), 2088 cm⁻¹ (s, CO).

1,3,5-Tris(phenylethynyl)benzene-tris(dicobalt hexacarbonyl) (63)



(63) is prepared as described above for compound (50). Brown solid, yield 53%.

Co ₂ (CO) ₈	(62)	CH ₂ Cl ₂	Reaction time	Eluents
1355 mg, 3.963 mmol	100 mg, 0.264 mmol	10 ml	Two days	PE and PE/DCM ^a 9/1

^aPE : petroleum ether; DCM : dicloromethane.

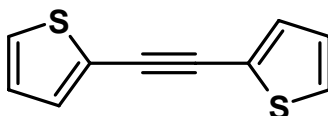
¹H NMR (250 MHz, CD₂Cl₂, 298K): δ_{ppm} = 7.80 (s, 3H, CH_{arom}); 7.66-7.58 (m, 6H, CH_{arom}), 7.36-7.26 (m, 9H, CH_{arom}).

¹³C NMR (62.5 MHz, CD₂Cl₂, 298K): δ_{ppm} = 199.45, 140.66, 138.26, 129.54, 129.35, 128.39, 92.56, 90.69.

MS (FD, 8 kV): *m/z* (%): 1237.3 (100) [*M*⁺] (calcd for C₄₈H₁₈Co₆O₆: 1236.26).

FT-IR(KBr pellet) : $\bar{\nu}$ = 2018 (s), 2054 (s), 2089 cm^{-1} (vs, CO) ;

1,2-Bis(thiophen-2-yl)acetylene (65)



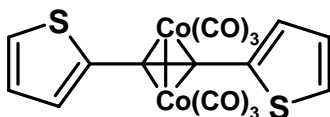
A 250 mL round bottom flask with teflon-coated magnetic stir bar is fitted with a rubber septum and flame dried under vacuum. The flask is purged with dry argon, and charged with $\text{PdCl}_2(\text{PPh}_3)_2$ (401 mg, 0.57 mmol, 6 mol%), CuI (182 mg, 0.95 mmol, 10 mol%) and 2-iodothiophene (**64**) (1 equiv, 9.52 mmol). While stirring, dry benzene (48 ml, starting material is 0.20 M in dry benzene) sparged with dry argon is added by syringe. Argon-sparged DBU (8.70 g, 57.13 mmol, 6 equiv) is then added by syringe, followed by a purge of the reaction flask with argon. Ice-chilled trimethylsilylethynylene (467.65 mg, 4.76 mmol, 0.50 equiv) is then added by syringe, followed immediately by distilled water (68.56 μl , 40 mol%). The reaction flask is covered in aluminum foil and left stirring for 18 h, at the end of which the reaction mixture is partitioned in ethyl ether and distilled water (50 mL each). The organic layer is washed with 10% HCl (3X 75 ml), saturated aqueous NaCl (1X 75 ml), dried over MgSO_4 , gravity-filtered and the solvent removed under vacuum. The crude product was purified by column chromatography on silica gel with n-Hexane as eluent to afford colorless solid in 69% yield.

^1H NMR (250 MHz, CD_2Cl_2 , 298K): δ_{ppm} = 7.35 (dd, $^3\text{J}(\text{H,H})$ = 5.1Hz, 2H, 1.1 Hz), 7.29 (dd, $^3\text{J}(\text{H,H})$ = 3.6 Hz, 2H, 1.1 Hz), 7.03 (dd, $^3\text{J}(\text{H,H})$ = 5.1Hz, 2H, 3.6 Hz).

^{13}C NMR (62.5 MHz, CD_2Cl_2 , 298K): δ_{ppm} = 132.55, 128.16, 127.63, 123.10, 86.36.

GC-MS (EI) : m/z (%): 190.2 (100) [M^+] (calcd for $\text{C}_{10}\text{H}_6\text{S}_2$: 190.29).

Elemental analysis: calcd. for $\text{C}_{10}\text{H}_6\text{S}_2$: C, 63.12 H 3.18 S 33.70, Found C, 63.21 H 3.22 S 33.60.

1,2-Bis(thiophen-2-yl)acetylene-dicobalt hexacarbonyl (66)

(66) is prepared as described above for compound (50). Brown solid, yield 49%.

$\text{Co}_2(\text{CO})_8$	65	CH_2Cl_2	Reaction time	Eluents
629 mg, 1.84 mmol	50 mg, 0.26 mmol	5 ml	Two days	PE and PE/DCM ^a 9/1

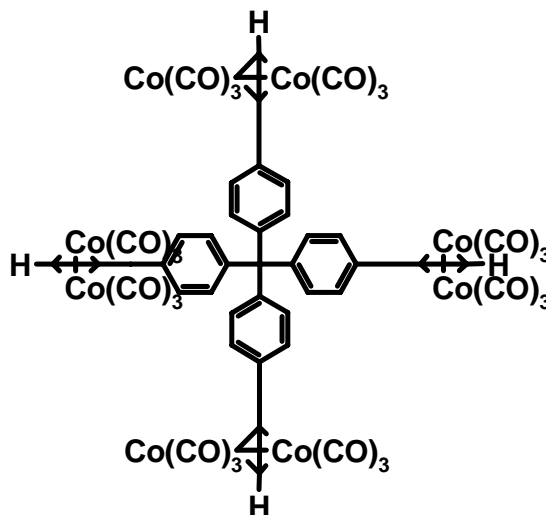
^aPE : petroleum ether; DCM : dichloromethane.

¹H NMR (250 MHz, CD_2Cl_2 , rt): $\delta_{\text{ppm}} = 7.69\text{-}7.37$ (m, 4H, CH_{thio}), $7.21\text{-}7.01$ (m, 2H, CH_{thio}).

¹³C NMR (75 MHz, CD_2Cl_2 , rt): $\delta_{\text{ppm}} = 199.25, 141.87, 129.28, 128.52, 127.52, 82.62$.

MS (FD, 8 kV): m/z (%): 475.5 (100) [M^+] (calcd for $\text{C}_{16}\text{H}_6\text{O}_6\text{S}_2\text{Co}_2$: 476.21).

FT-IR(KBr pellet) : $\bar{\nu} = 2003(\text{s}), 2019(\text{s}), 2028(\text{vs}), 2050(\text{vs}), 2090 \text{ cm}^{-1}$ (s, CO) ;

Tetrakis(4-ethynylphenyl)methane-tetrakis(dicobalt hexacarbonyl) (71)

(71) is prepared as described above for compound (50). Red solid, yield 45%.

$\text{Co}_2(\text{CO})_8$	68	CH_2Cl_2	Reaction time	Eluents
1642 mg, 4.80 mmol	100 mg, 0.24 mmol	8 ml	Three days	PE and PE/DCM ^a 9/1

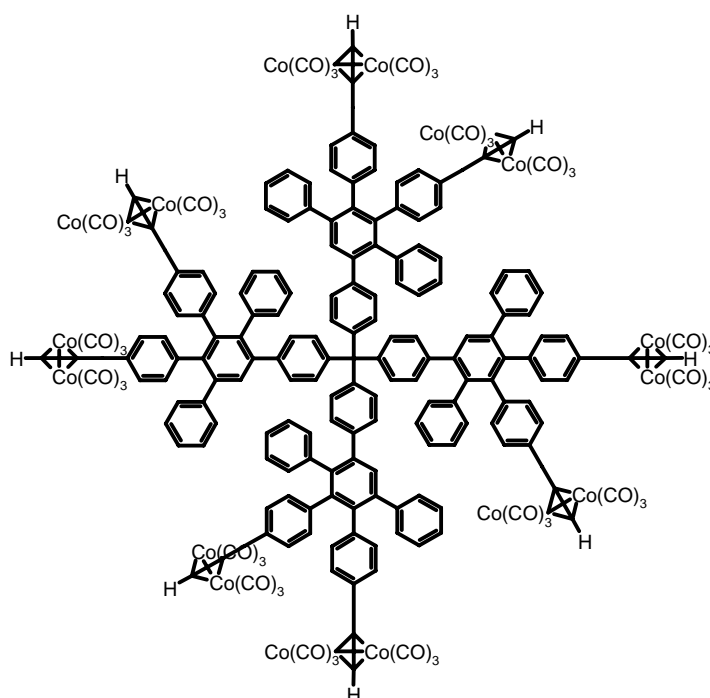
^aPE : petroleum ether; DCM : dichloromethane.

^1H NMR (250 MHz, CD_2Cl_2 , 298K): $\delta_{\text{ppm}} = 7.47$ (d, $^3J(\text{H,H}) = 8.5$ Hz, 8H, $\text{CH}_{\text{arom.}}$), 7.25 (d, $^3J(\text{H,H}) = 8.2$ Hz, 8H, $\text{CH}_{\text{arom.}}$), 6.44 (s, 4H, CH);

^{13}C NMR (75 MHz, CD_2Cl_2 , 298K): $\delta_{\text{ppm}} = 199.97$, 146.36, 135.95, 131.68, 129.97 ($\text{C}_{\text{cluster}}$), 90.00 ($\text{C}_{\text{cluster}}$), 73.71 (C_{quat}), 65.30.

FT-IR(KBr pellet) : $\bar{\nu} = 2019(\text{s})$, 2054(s), 2094 cm^{-1} (vs, CO);

8-Cascade:tetraphenylmethane[4-4,4',4'',4''']:(3',6'-diphenyl-1,1':2',1''-terphenyl-4,4',4''-triyl)1: ethynyl- octakis(dicobalt hexacarbonyl) (72)



(72) is prepared as described above for compound (50). Red solid, yield 35%:

$\text{Co}_2(\text{CO})_8$	69	CH_2Cl_2	Reaction time	Eluents
671 mg, 1.966 mmol	100 mg, 0.049 mmol	8 ml	Three days	PE and PE/DCM ^a 9/1

^aPE : petroleum ether; DCM : dichloromethane.

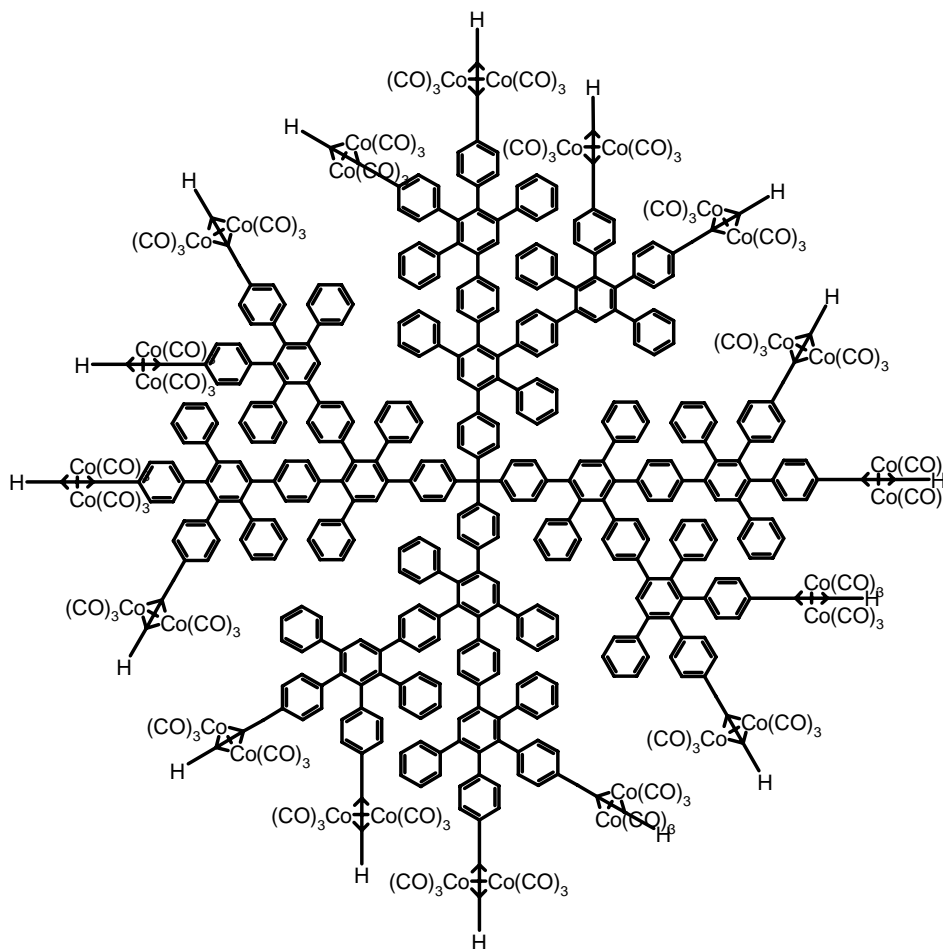
^1H NMR (250 MHz, CD_2Cl_2 , 298K): $\delta_{\text{ppm}} = 7.61$ (s, 4H, $\text{CH}_{\text{arom.}}$); 7.16-6.67 (m, 88H, $\text{CH}_{\text{arom.}}$) ; 6.28, 6.26 (2s, 8H, CH) ;

^{13}C NMR (75 MHz, CD_2Cl_2 , 298K): $\delta_{\text{ppm}} = 199.95$, 144.96, 141.78, 141.42, 141.34, 141.13, 140.93, 140.58, 140.13, 139.98, 139.79, 139.00, 135.19, 134.84, 132.42, 132.35, 132.02,

131.47, 130.73, 130.34, 129.41, 129.12, 128.02, 127.20, 126.77, 125.97, (C_{Cluster})
90.50, (C_{Cluster}) 90.40, (C_{quat}) 63.86.

FT-IR(KBr pellet) : $\bar{\nu} = 2023(\text{s}), 2054(\text{s}), 2093 \text{ cm}^{-1}$ (vs, CO) ;

16-Cascade:tetraphenylmethane[4-4,4',4'',4''']:(3',6'-diphenyl-1,1':2',1''-terphenyl-4,4',4''-triyl)²: ethynyl-hexadecakis(dicobalt hexacarbonyl) (73)



(73) is prepared as described above for compound (50). Red solid, yield 37%:

$\text{Co}_2(\text{CO})_8$	70	CH_2Cl_2	Reaction time	Eluents
520 mg, 1.52 mmol	100mg, 0.019 mmol	6 ml	8 ml	PE and PE/DCM ^a 8/2

^aPE : petroleum ether; DCM : dichloromethane.

¹H NMR (250 MHz, CD_2Cl_2 , 298K): $\delta_{\text{ppm}} = 7.51$ (s, 4H, CH_{arom}) ; 7.47 (s, 4H, CH_{arom}) ; 7.42 (s, 4H, CH_{arom}) ; 7.40-6.40 (m, 232H, CH_{arom}) ; 6.26, 6.25 (2s, 16H, CH_{arom}).

^{13}C NMR (125 MHz, CD_2Cl_2 , 298K): $\delta_{\text{ppm}} = 200.00, 144.97, 142.35, 141.97, 141.68, 141.56, 141.19, 140.75, 140.60, 140.20, 140.06, 139.77, 139.70, 139.26, 138.97, 138.57, 135.24, 134.83, 132.50, 132.44, 132.21, 132.03, 131.81, 131.59, 131.44, 130.78, 130.37, 129.42, 129.09, 128.84, 128.04, 127.32, 126.80, 126.10, \text{(C}_{\text{Cluster}}) 90.75, \text{(C}_{\text{Cluster}}) 90.60, \text{(C}_{\text{Cluster}}) 73.12, \text{(C}_{\text{Cluster}}) 73.02.$

FT-IR(KBr pellet) : $\bar{\nu} = 2021(\text{s}), 2052(\text{s}), 2092 \text{ cm}^{-1}$ (vs, CO) ;

Appendix

X-ray table for the single crystal structure of compound **29**

Atom	x/a	y/b	z/c	U(iso)	Occ
C(1)	-0.2369(2)	0.14363(19)	1.0926(2)	0.0272	
C(2)	-0.3378(3)	0.0878(2)	1.2357(2)	0.0345	
C(3)	-0.3043(3)	0.0952(2)	1.3532(2)	0.0361	
C(4)	-0.1734(2)	0.1637(2)	1.3273(2)	0.0311	
C(5)	-0.0653(2)	0.23039(19)	1.1798(2)	0.0286	
C(6)	-0.0965(2)	0.22045(18)	1.06105(18)	0.0248	
C(7)	0.0071(2)	0.28746(18)	0.91789(19)	0.0260	
C(8)	0.1397(2)	0.36323(17)	0.88928(17)	0.0221	
C(9)	0.1680(2)	0.37722(18)	1.00600(19)	0.0247	
C(10)	0.0637(2)	0.30922(18)	1.15280(18)	0.0256	
C(11)	0.2962(2)	0.46362(19)	0.9791(2)	0.0289	
C(12)	0.3921(2)	0.53100(19)	0.84039(19)	0.0285	
C(13)	0.3673(2)	0.51821(18)	0.72018(19)	0.0270	
C(14)	0.2490(2)	0.43585(18)	0.74051(19)	0.0240	
C(15)	-0.2742(2)	0.13250(18)	0.97225(19)	0.0261	
C(16)	-0.4209(2)	0.1800(2)	0.9618(2)	0.0309	
C(17)	-0.4515(3)	0.1655(2)	0.8492(2)	0.0372	
C(18)	-0.2135(3)	0.0594(2)	0.7604(2)	0.0342	
C(19)	-0.1706(3)	0.0702(2)	0.8702(2)	0.0349	
C(20)	0.2298(2)	0.42072(18)	0.61472(19)	0.0262	
C(21)	0.2265(2)	0.2883(2)	0.5981(2)	0.0340	
C(22)	0.2146(3)	0.2780(2)	0.4755(2)	0.0381	
C(23)	0.2083(2)	0.5189(2)	0.3809(2)	0.0334	
C(24)	0.2210(2)	0.5399(2)	0.4979(2)	0.0290	
N(25)	0.2047(2)	0.39430(19)	0.36342(19)	0.0402	
N(26)	-0.3542(2)	0.10809(19)	0.74934(19)	0.0392	
H(21)	-0.4306(3)	0.0411(2)	1.2543(2)	0.0307	
H(31)	-0.3744(3)	0.0527(2)	1.4502(2)	0.0385	
H(41)	-0.1504(2)	0.1683(2)	1.4057(2)	0.0352	
H(71)	-0.0130(2)	0.28157(18)	0.83847(19)	0.0179	
H(101)	0.0799(2)	0.31838(18)	1.23281(18)	0.0269	
H(111)	0.3104(2)	0.47667(19)	1.0584(2)	0.0344	
H(121)	0.4773(2)	0.58693(19)	0.82364(19)	0.0308	
H(131)	0.4341(2)	0.56745(18)	0.62384(19)	0.0282	
H(161)	-0.4957(2)	0.2212(2)	1.0298(2)	0.0326	
H(171)	-0.5496(3)	0.1983(2)	0.8415(2)	0.0385	
H(181)	-0.1423(3)	0.0197(2)	0.6893(2)	0.0313	
H(191)	-0.0736(3)	0.0331(2)	0.8779(2)	0.0387	
H(211)	0.2380(2)	0.2055(2)	0.6703(2)	0.0360	
H(221)	0.2134(3)	0.1867(2)	0.4684(2)	0.0526	

H(231)	0.2036(2)	0.5997(2)	0.3037(2)	0.0417
H(241)	0.2241(2)	0.6332(2)	0.4994(2)	0.0285

Atom	u(11)	u(22)	u(33)	u(23)	u(13)	u(12)
C(1)	0.0278(9)	0.0251(9)	0.0290(8)	-0.0071(7)	-0.0125(8)	0.0008(7)
C(2)	0.0361(11)	0.0325(10)	0.0357(10)	-0.0093(8)	-0.0156(9)	0.0004(8)
C(3)	0.0388(12)	0.0338(11)	0.0360(10)	-0.0100(8)	-0.0149(10)	-0.0009(9)
C(4)	0.0318(10)	0.0295(9)	0.0310(9)	-0.0079(7)	-0.0121(8)	-0.0003(8)
C(5)	0.0301(10)	0.0270(9)	0.0287(9)	-0.0078(7)	-0.0120(8)	0.0002(7)
C(6)	0.0270(9)	0.0233(8)	0.0250(8)	-0.0073(6)	-0.0114(7)	0.0022(7)
C(7)	0.0276(9)	0.0240(8)	0.0267(8)	-0.0061(7)	-0.0120(8)	0.0001(7)
C(8)	0.0234(9)	0.0211(8)	0.0225(8)	-0.0058(6)	-0.0101(7)	0.0006(6)
C(9)	0.0258(9)	0.0242(8)	0.0242(8)	-0.0068(6)	-0.0105(7)	0.0005(7)
C(10)	0.0278(9)	0.0238(8)	0.0265(8)	-0.0068(7)	-0.0125(8)	0.0002(7)
C(11)	0.0296(10)	0.0281(9)	0.0299(9)	-0.0074(7)	-0.0136(8)	-0.0002(7)
C(12)	0.0292(10)	0.0270(9)	0.0300(9)	-0.0077(7)	-0.0131(8)	0.0007(7)
C(13)	0.0280(9)	0.0255(9)	0.0268(8)	-0.0063(7)	-0.0114(8)	0.0001(7)
C(14)	0.0247(9)	0.0228(8)	0.0253(8)	-0.0067(6)	-0.0114(7)	0.0015(6)
C(15)	0.0287(10)	0.0235(8)	0.0263(8)	-0.0058(7)	-0.0119(8)	-0.0006(7)
C(16)	0.0309(10)	0.0293(9)	0.0310(9)	-0.0072(7)	-0.0119(8)	-0.0004(8)
C(17)	0.0376(12)	0.0348(10)	0.0398(10)	-0.0101(8)	-0.0157(10)	-0.0026(9)
C(18)	0.0357(12)	0.0319(10)	0.0346(9)	-0.0090(8)	-0.0141(9)	0.0001(8)
C(19)	0.0366(11)	0.0340(10)	0.0342(9)	-0.0099(8)	-0.0140(9)	0.0000(8)
C(20)	0.0275(9)	0.0245(9)	0.0272(8)	-0.0059(7)	-0.0125(7)	-0.0004(7)
C(21)	0.0337(11)	0.0343(10)	0.0341(10)	-0.0087(8)	-0.0145(9)	0.0000(8)
C(22)	0.0393(12)	0.0361(11)	0.0386(10)	-0.0088(8)	-0.0166(9)	-0.0013(9)
C(23)	0.0332(11)	0.0330(10)	0.0334(9)	-0.0092(8)	-0.0129(9)	-0.0003(8)
C(24)	0.0288(10)	0.0279(9)	0.0307(8)	-0.0083(7)	-0.0127(8)	0.0006(7)
N(25)	0.0405(11)	0.0394(10)	0.0405(9)	-0.0103(8)	-0.0163(9)	-0.0026(8)
N(26)	0.0401(11)	0.0379(10)	0.0406(9)	-0.0099(8)	-0.0175(9)	-0.0029(8)

C(1) - C(2)	1.384(3)
C(1) - C(6)	1.460(3)
C(1) - C(15)	1.483(3)
C(2) - C(3)	1.418(3)
C(3) - C(4)	1.355(3)
C(4) - C(5)	1.453(3)
C(5) - C(6)	1.430(3)
C(5) - C(10)	1.397(3)
C(6) - C(7)	1.410(2)
C(7) - C(8)	1.401(2)
C(8) - C(9)	1.412(2)
C(8) - C(14)	1.477(2)
C(9) - C(10)	1.439(2)

C(9) - C(11) 1.439(3)
 C(11) - C(12) 1.359(3)
 C(12) - C(13) 1.425(3)
 C(13) - C(14) 1.361(2)
 C(14) - C(20) 1.467(2)
 C(15) - C(16) 1.414(3)
 C(15) - C(19) 1.401(3)
 C(16) - C(17) 1.383(3)
 C(17) - N(26) 1.337(3)
 C(18) - C(19) 1.406(3)
 C(18) - N(26) 1.367(3)
 C(20) - C(21) 1.409(3)
 C(20) - C(24) 1.424(2)
 C(21) - C(22) 1.381(3)
 C(22) - N(25) 1.381(3)
 C(23) - C(24) 1.373(3)
 C(23) - N(25) 1.336(3)

C(2) - C(1) - C(6) 118.81(17)
 C(2) - C(1) - C(15) 120.92(18)
 C(6) - C(1) - C(15) 120.20(15)
 C(1) - C(2) - C(3) 122.20(19)
 C(2) - C(3) - C(4) 120.22(18)
 C(3) - C(4) - C(5) 120.82(18)
 C(4) - C(5) - C(6) 119.17(17)
 C(4) - C(5) - C(10) 120.84(17)
 C(6) - C(5) - C(10) 119.92(16)
 C(1) - C(6) - C(5) 118.66(15)
 C(1) - C(6) - C(7) 122.29(16)
 C(5) - C(6) - C(7) 119.04(17)
 C(6) - C(7) - C(8) 121.65(16)
 C(7) - C(8) - C(9) 119.48(15)
 C(7) - C(8) - C(14) 122.78(16)
 C(9) - C(8) - C(14) 117.68(16)
 C(8) - C(9) - C(10) 119.56(16)
 C(8) - C(9) - C(11) 120.50(16)
 C(10) - C(9) - C(11) 119.88(16)
 C(5) - C(10) - C(9) 120.29(16)
 C(9) - C(11) - C(12) 119.89(17)
 C(11) - C(12) - C(13) 120.98(17)
 C(12) - C(13) - C(14) 121.14(16)
 C(8) - C(14) - C(13) 119.75(16)
 C(8) - C(14) - C(20) 120.33(16)
 C(13) - C(14) - C(20) 119.92(15)
 C(1) - C(15) - C(16) 119.99(17)
 C(1) - C(15) - C(19) 121.99(16)
 C(16) - C(15) - C(19) 117.97(17)

C(15) - C(16) - C(17) 118.00(19)
C(16) - C(17) - N(26) 125.3(2)
C(19) - C(18) - N(26) 122.1(2)
C(15) - C(19) - C(18) 119.60(19)
C(14) - C(20) - C(21) 122.46(15)
C(14) - C(20) - C(24) 121.81(16)
C(21) - C(20) - C(24) 115.66(16)
C(20) - C(21) - C(22) 120.98(18)
C(21) - C(22) - N(25) 122.9(2)
C(24) - C(23) - N(25) 126.12(18)
C(20) - C(24) - C(23) 119.06(17)
C(22) - N(25) - C(23) 115.30(18)
C(17) - N(26) - C(18) 117.06(18)

List of Publications

(Resulting from work in the group of Prof. Dr. Klaus Müllen)

1. W. Pisula, Z. Tomović, B. El Hamaoui, M. D. Watson, T. Pakula and K. Müllen, “Control of the Homeotropic order of discotic Hexa-peri-hexabenzocoronenes”, *Adv. Funct. Mater.* **2005**, 15, 893.
2. J. Wu, B. El Hamaoui, J. Li, L. Zhi, U. Kolb and K. Müllen, “Solid State Synthesis of “Bamboo-Like” and Straight carbon Nanotubes by Thermolysis of Hexa-peri-hexabenzocoronene-Cobalt complexes” *small*, **2005**, 2, 210.
3. B. El Hamaoui, L. Zhi, J. Wu, U. Kolb and K. Müllen, “Uniform Carbon and Carbon/Cobalt Nanostructures by Solid-state Thermolysis of Polyphenylene Dendrimer/Cobalt Complexes”. *Adv. Mater.*, **2005**, 17, 2957.
4. B. El Hamaoui, F. Laquai, S. Balushev, J. Wu and K. Müllen, “Efficient Triplet Emission from Large Polycyclic Aromatic Hydrocarbons and Their Platinum Complexes”, *Synth. Met.* **2006**, 156, 1182.
5. B. El Hamaoui, L. Zhi, J. Wu, N. Lukas, U. Kolb, Z. Tomović, and K. Müllen, “Solid-state Pyrolysis of Polyphenylene-Metal Complexes: A Facile Approach Toward Carbon Nanoparticles”, *Advanced Functional Materials*, in press.
6. B. El Hamaoui, J. Wu, L. Zhi, U. Kolb and K. Müllen “synthesis of carbon nanofibers and nanorods by self-assembly of amphiphilic Hexa-peri-hexabenzocoronenes”, submitted to *Chem. Commun.*
7. W. Pisula, B. El Hamaoui, M. Kastler, M.-C. G. Gutiérrez, R. Davis, C. Riekel, K. Müllen, “Dendritic morphology in homeotropically aligned hexa-peri-hexabenzocoronene films”, submitted to *ChemPhysChem*.
8. L. Zhi, W. S. Hu, B. El Hamaoui, J. Maier, K. Müllen, “High performance carbon-metal composites for Li-ion secondary batteries” manuscript in preparation.